Coffin, M.F., Frey, F.A., Wallace, P.J., et al., 2000
Proceedings of the Ocean Drilling Program, Initial Reports Volume 183

6. Site 1138[1]

Shipboard Scientific Party[2]

BACKGROUND AND OBJECTIVES

Site 1138 lies on the central Kerguelen Plateau (CKP) ~150 km north-northwest of Site 747 and 180 km east-southeast of Heard Island (Fig. **F1**). Basalts recovered at Site 747 erupted at ~85–88 Ma, on the basis of ^{40}Ar/^{39}Ar data (Pringle et al., 1994; Storey et al., 1996) and biostratigraphy from the overlying sediments (Watkins, 1992). In contrast, Heard Island is dominated by Holocene volcanism (Barling, 1990). A major objective at Site 1138 was to determine if the age of the uppermost basaltic crust of the CKP is 85 Ma at more than one location. Also, geochemical characteristics of Site 747 basalts indicate a continental lithosphere component different from that in Site 738 basalt. Specifically, Site 747 basalts overlap in ^{87}Sr/^{86}Sr with Kerguelen Archipelago lavas, but they range to lower ^{143}Nd/^{144}Nd (Fig. **F9,** p. 59, in the "Leg 183 Summary" chapter); have the lowest ^{206}Pb/^{204}Pb found in lavas from the Kerguelen Plateau and the Kerguelen Archipelago (Fig. **F10,** p. 60, in the "Leg 183 Summary" chapter); and are outside the oceanic basalt field in a Th/Nb-La/Nb plot defining a trend to high La/Nb without a corresponding increase in Th/Nb (Fig. **F11A,** p. 61, in the "Leg 183 Summary" chapter). All of these geochemical characteristics are consistent with a continental lithosphere component such as Archean granulites (e.g., Lewisian granulites [Scotland] have very low ^{206}Pb/^{204}Pb [<14], high La/Nb, and low Th/Nb compared to primitive mantle [Dickin, 1981; Weaver and Tarney, 1984]). Archean granulites, found today along the conjugate Antarctic and Indian margins, may have been fragmented and incorporated into the embryonic Indian Ocean mantle during continental breakup and, subsequently, sampled when the Kerguelen Plateau formed. Therefore, we were especially interested in comparing the petrology and geochemistry of basaltic basement from this second CKP drill site with basalt from the southern, northern, and Elan Bank sectors, as well as Heard Island and the Kerguelen Archipelago. We

F1. Satellite-derived free-air gravity map of the Kerguelen Plateau, **p. 65.**

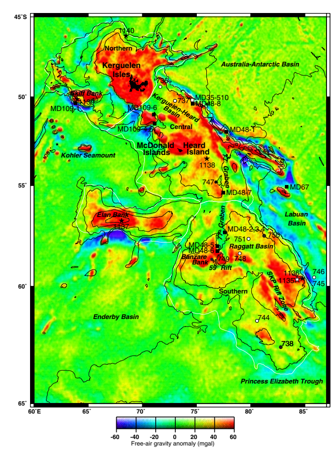

[1]Examples of how to reference the whole or part of this volume.
[2]Shipboard Scientific Party addresses.

Ms 183IR-106

located Site 1138 at a water depth of 1141 m on Australian Geological Survey Organisation *Rig Seismic* multichannel seismic (MCS) line RS179/101 (Fig. F2). The location is relatively simple structurally and seismic stratigraphically (Fig. F3). Interpreted igneous basement contains some internal reflections with a slight apparent dip to the southwest. The top of basaltic basement, however, is flat lying. Five seismic sequences overlie basement and total ~700 m in thickness.

F2. Location of Site 1138 and site-survey data, p. 66.

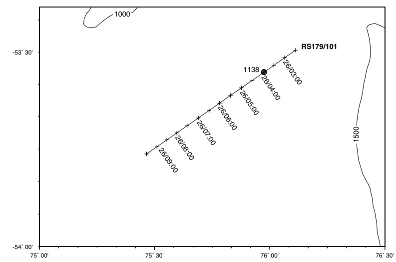

F3. *Rig Seismic* RS179/101 multichannel seismic profile across Site 1138, p. 68.

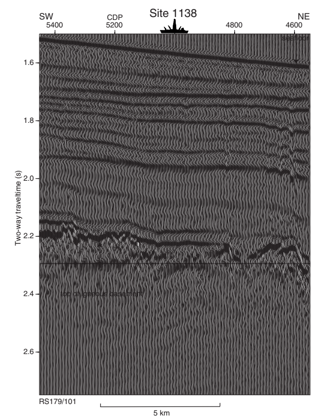

Summary of Objectives

The main objectives at this site were to

1. Characterize the petrography and compositions of the lavas, with particular focus on evaluating the presence of a continental lithosphere component and its geochemical characteristics;
2. Determine the age of the lavas, testing the hypothesis that the uppermost igneous basement of the CKP is ~85 Ma, the age yielded by basalt from Site 747 (Pringle et al., 1994; Storey et al., 1996);
3. Determine the physical characteristics of the lava flows;
4. Identify the environment of eruption (subaerial or submarine);
5. Obtain minimum estimates for the age of basement from overlying sediment;
6. Estimate the duration of possible subaerial and shallow marine environments from the sedimentary and igneous record;
7. Recover Cenozoic sediment with a significant volcanic component derived from Heard Island and its surrounding platform. Such material can provide information on the growth and composition of the volcanism that formed this edifice;
8. Determine the facies of the seismic stratigraphic sequences;
9. Define the ages of seismic sequence boundaries; and
10. Determine the paleoceanographic history of the region just south of the Polar Front.

OPERATIONS

SITE 1138

The 620-km transit to Site 1138 was made in 30.5 hr at an average speed of 11.0 kt. We arrived at Site 1138 on 7 January 1999. Weather conditions upon arrival were moderate. At 2334 hr on 7 January 1999, we deployed a beacon on the precise Global Positioning System coordinates for Site 1138.

Hole 1138A

We spudded Hole 1138A at 0445 hr on 8 January 1999. It was difficult to establish the seafloor depth because the driller did not feel a hard "tag" that could be identified as bottom. Based on recovery in the first core, a seafloor depth adjusted to the rig floor was established at 1153.0 m below rig floor (mbrf), equivalent to 1141.4 m below sea level. The 3.5-kHz precision depth recorder had indicated an adjusted seafloor depth of 1158.4 mbrf.

Continuous wireline coring proceeded in diatom clay, nannofossil clay, and nannofossil ooze through Core 183-1138A-28R to a depth of

266 mbsf. No chert was encountered. The formation then graded into nannofossil chalk with occasional chert layers. A hydraulic hose supplying the Varco top drive burst after recovering Core 183-1138A-58R from 553.6 mbsf. The ruptured hose was isolated, and a spare hose was connected in 2.25 hr. Coring continued through chalk with thin interbeds of nannofossil claystone and into reddish brown glauconite-bearing sandy packstone and brown clayey siltstone. After recovering Core 183-1138A-72R from a depth of 688.5 mbsf, coring operations were halted to wait on weather. The sea state had been deteriorating most of the day, and eventually excessive heave caused us to suspend coring in a force 8 gale. During this period swell conditions reached 9–10 m, seas were 3 m, vessel heave was 4–7 m, and the wind speed was 42 kt, gusting to 46 kt. The drill string was hung off on knobby drilling joints with the bit ~20 m above the bottom of the hole.

After waiting on weather for 16 hr, conditions improved enough to resume operations. An additional hour was required to remove the knobbies and run the pipe back to bottom. Total time lost because of the weather was 17.25 hr. Sediment coring was resumed and continued until Core 183-1138A-75R was recovered with a single hard rock jammed in the core catcher. The driller reported elevated pump pressures with the core barrel removed from the string. After four successive deployments of the bit deplugger, the last two of which were stuck briefly upon attempted recovery, coring resumed with pump pressures still abnormally high. A half core was cut and retrieved with nearly full recovery indicating that the bit throat had been cleared. Coring then continued without any additional problems. Acoustic basement was eventually contacted at ~700 mbsf in Core 183-1138A-74R. Basaltic basement was finally reached at the base of Core 183-1138A-79R at ~745 mbsf. Recovery averaged 49.8%, and the rate of penetration averaged 7.2 m/hr (ranging from 3.6 to 18.8 m/hr). Coring was terminated with the recovery of Core 183-1138A-89R from a depth of 842.7 mbsf. This was ~98 m into basaltic basement or ~123 m into acoustic basement and satisfied the scientific depth objective for this site. A total of 411.98 m of core was recovered from Hole 1138A for an overall average of 48.9%. Summaries of core numbers, depths, and recovery are given in Tables **T1** and **T2.**

T1. Coring summary, **p. 166.**

T2. Expanded coring summary, **p. 168.**

Further coring was suspended in the interest of conserving time for the remaining three primary drill sites. A variance was requested and received from the Ocean Drilling Program/Texas A&M University to forego wireline logging at the site because logging at the remaining three primary sites was deemed more important to the scientific objectives of the leg. As a result of deteriorating weather conditions, it was unlikely that logging could have been conducted in the hole without waiting on weather until the sea state and vessel heave abated. A test of the Lamont-Doherty Earth Observatory wireline compensator confirmed this when it tripped the 5-m limit switch twice, once after operating for 5 min and again after operating for 9 min.

LITHOSTRATIGRAPHY

Introduction

Site 1138 is located southeast of Heard and McDonald Islands in 1141 m of water on the CKP. Hole 1138A was rotary cored continuously to a depth of 842.7 mbsf. Sediments were recovered down to 698 mbsf.

Basalts overlain by volcaniclastic and very minor sedimentary rock layers were recovered below 698 mbsf from the lower 144 m of the hole (Fig. F4). The sedimentary section above igneous basement consists of ~655 m of pelagic ooze, chalk, and calcareous claystone that overlies ~43 m of glauconitic calcareous sandstone and silty clay interbedded with sandstone and conglomerate (Fig. F4; Table T3). The sedimentary section appears to rest unconformably on igneous basement. We recognize six sedimentary lithologic units (I–VI) in the upper part (0–698 mbsf) of Hole 1138A. The basement volcaniclastic rocks and basalts are designated lithologic Unit VII and are subdivided into basement Units 1–22 (Fig. F4) (see "Physical Volcanology," p. 22, "Igneous Petrology," p. 46, and "Alteration and Weathering," p. 49, for descriptions). Core recovery varied from good to poor throughout the sedimentary sections of Hole 1138A (Fig. F4).

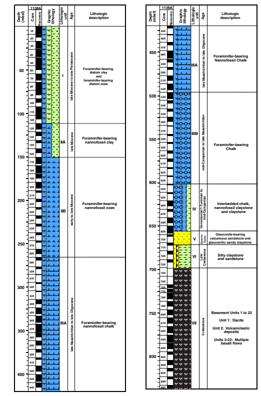

F4. Composite stratigraphic section for Site 1138, p. 69.

T3. Summary of lithologic units, p. 177.

Unit I

Interval: 183-1138A-1R-1, 0 cm, to 12R-CC, 28 cm
Depth: 0–112.00 mbsf
Age: late Pleistocene to late Miocene

Unit I is predominantly foraminifer-bearing diatom clay with interbedded foraminifer-bearing diatom ooze (Fig. F4; Table T3). Much of the sediment in the top three cores is highly deformed and contains soupy intervals because of severe drilling disturbance; thus, we could not determine accurately the true thicknesses and stratigraphic positions of individual ooze and clay beds. Most of the diatom clay ranges in color from light gray to dark gray and dark greenish gray. The interbedded diatom ooze ranges from tan to very light gray. The carbonate content ranges from 4 to 46 wt% $CaCO_3$ with an average of 23 wt%. Organic carbon contents are 0.2% in the upper part and 0.1% in the lower part of the unit (Table T4). X-ray diffraction (XRD) analyses show clay minerals (smectites?) in the diatom clay and amorphous silica in the diatom ooze (Table T4). Alkali-feldspar, quartz, and minor amounts of pyrite and glauconite are found mainly in the diatom clay. Opal-CT and quartz are very rare or absent in the diatom ooze.

T4. XRD results and carbonate contents expressed as $CaCO_3$, p. 178.

Pebbles as long as 6 cm at the tops or in the uppermost intervals of a few cores (e.g., gabbro pebble in interval 183-1138A-4R-1, 0–6 cm) represent ice-rafted debris that has apparently fallen down the hole from higher stratigraphic levels during drilling. A few intervals of Unit I contain volcanic ash. Interval 183-1138A-8R-2, 71–72 cm, contains brown ash, which has been extensively burrowed. A brown ash layer is present in interval 183-1138A-9R-1, 0–8 cm. Brown ash is disseminated through interval 183-1138A-10R-3, 107–127 cm. A pumice fragment is present in interval 183-1138A-10R-2, 46 cm, and a 2-mm-thick lamina of coarse-sand–sized pumice crystals is present in interval 183-1138A-8R-CC, 6–7 cm.

Core 183-1138A-8R contains an interval (183-1138A-8R-3, 0 cm, to 8R-7, 64 cm) with rounded and deformed mud clasts of variegated colors, layers contorted by flowage, and steeply dipping, truncated layers that may represent soft-sediment deformation. The sediment has also suffered from drilling disturbance so the exact interval(s) of primary soft-sediment deformation is uncertain.

The gray color of Unit I reflects a terrigenous component derived from the vicinity of Heard Island (see "Discussion," p. 10). The lower contact with Subunit IIA is transitional.

Unit II

Interval: 183-1138A-13R-1, 0 cm, to 28R-CC, 10 cm
Depth: 112.00–265.90 mbsf
Age: late to early Miocene

Unit II is composed of foraminifer-bearing nannofossil clay underlain by foraminifer-bearing nannofossil ooze. A higher carbonate/silica ratio distinguishes Unit II from Unit I. We divided Unit II into two subunits based on clay content and color (Fig. **F4;** Table **T3**).

Subunit IIA (interval 183-1138A-13R-1, 0 cm, to 16R-CC, 18 cm; 112.00–150.50 mbsf) is light gray foraminifer-bearing nannofossil clay of late Miocene age (Fig. **F4;** Table **T3**). The carbonate content of sediments in Subunit IIA ranges from 24 to 76 wt% $CaCO_3$ and averages 55 wt% (Table **T4**). The XRD analyses show the presence of alkali feldspar, amorphous silica (opal-A), and minor amounts of clay minerals in Cores 183-1138A-13R to 16R. We detected only minor amounts of feldspar in Cores 183-1138A-16R and 17R.

The sediments are homogeneous, but some intervals have fine disseminated black silt- and sand-sized grains of basalt. A sandy layer is present in interval 183-1138A-14R-3, 126–128 cm. A dark gray tephra layer is present in interval 183-1138A-15R-1, 71–73 cm. The predominantly gray color of this subunit may reflect a terrigenous component from the vicinity of Heard Island (see **"Discussion,"** p. 10).

Subunit IIB (interval 183-1138A-17R-1, 0 cm, to 28R-CC, 10 cm; 150.50–265.90 mbsf) is white foraminifer-bearing nannofossil ooze of late to early Miocene age (Fig. **F4;** Table **T3**). The carbonate content of sediments in Subunit IIB ranges from 69 to 95 wt% $CaCO_3$. The average is 90 wt%, which is significantly higher than in Subunit IIA (Table **T4**). XRD analysis shows almost pure calcite. Minor amounts of feldspar are present in interval 183-1138A-17R-1, 90–92 cm, and interval 183-1138A-20R-1, 90–92 cm, has traces of feldspar, clay, and amorphous silica (Table **T4**). The organic carbon content is very low (0.02%). As in Subunit IIA, the sediments of Subunit IIB are essentially homogeneous. Disseminated black silt- and sand-sized grains are common in a few intervals of the upper portion of the subunit. Rare black (basalt?) pebbles are present. Gray volcanic ash is disseminated in interval 183-1138A-19R-1, 110–111 cm. The nannofossil ooze grades to semilithified nannofossil chalk in Core 183-1138A-28R.

Unit III

Interval: 183-1138A-29R-1, 0 cm, to 63R-CC, 18 cm
Depth: 265.90 to 601.80 mbsf
Age: late Oligocene to mid-Campanian

Unit III consists of white to light gray and light greenish gray foraminifer-bearing nannofossil chalk (Fig. **F4;** Table **T3**). We subdivided Unit III into two subunits based on the presence or absence of identifiable nannofossils in smear slides.

Subunit IIIA (interval 183-1138A-29R-1, 0 cm, to 52R-CC, 26 cm; 265.90 to 496.40 mbsf) is white to light gray or light greenish gray foraminifer-bearing nannofossil chalk of late Oligocene to late Maastrichtian age (Fig. **F4;** Table **T3**). Chert nodules are present in Core 183-1138A-41R and below. The carbonate content ranges from 72 to 96 wt% $CaCO_3$ (Table **T4**), with an average of 90 wt%. Organic carbon content is 0.1%. The XRD analysis shows minor amounts of clay and amorphous silica in Cores 183-1138A-33 to 35. We detected traces of clinoptilolite in intervals 183-1138A-37R-2, 64–65 cm, and 49R-1, 90–91 cm (Table **T4**).

Cyclic color variations reflect the abundance (<1%) of disseminated black fine silt-sized particles, which are probably basaltic rock fragments. Gray intervals typically display relatively sharp basal contacts and gradational, bioturbated tops and may reflect a greater abundance of terrigenous material with a source in the vicinity of Heard Island. In Core 183-1138A-36R, the foraminifers in light greenish gray chalk are filled with a green material, presumably glauconite. The sediment is extensively burrowed, and some intervals show multiple generations of burrows.

Core 183-1138A-52R contains the Cretaceous/Tertiary (K/T) boundary (see **"Biostratigraphy,"** p. 10). We did not observe any unusual lithologic changes (e.g., erosional contact in Core 183-1135A-28R) in this core. The sediment shows cyclic color variations from white to greenish gray, and some of these intervals have sharp, well-burrowed bases. Similar color cycles, however, are present in many cores, both above and below this interval.

Subunit IIIB (interval 183-1138A-53R-1, 0 cm, to 63R-CC, 18 cm; 496.40 to 601.80 mbsf) is predominantly white to very light gray foraminifer-bearing chalk of late Maastrichtian to mid-Campanian age. The carbonate content ranges from 92 to 96 wt% $CaCO_3$ (Table **T4**) with an average of 94 wt%. XRD analysis shows pure calcite throughout Subunit IIIB. Organic carbon ranges from 0.02% to 0.2%. Cores 183-1138A-57R through 63R contain two or three chert nodules per core. The contact at the base of Unit III is gradational.

Unit IV

Interval: 183-1138A-64R-1, 0 cm, to 69R-5, 112 cm
Depth: 601.80–655.57 mbsf
Age: mid-Campanian to Turonian

Unit IV consists of cyclic alternations of light gray foraminifer-bearing chalk with gray through greenish gray to black intervals of nannofossil claystone (Figs. **F4, F5;** Table **T4**). The dark gray to black nannofossil claystone beds are increasingly prominent in the lower portion of Core 183-1138A-67R and are increasingly black, clay-rich, and organic carbon–rich toward the base of the unit (Figs. **F5, F6**). In Cores 183-1138A-68R and 69R, these light and dark cycles are ~20–30 cm thick (i.e., ~3/m). The dark gray to black intervals are typically 5 cm thick, with gradational tops and sharp bases, which mark the bases of the cycles (Fig. **F6A, F6B**).

The carbonate content ranges from 93 to 96 wt% $CaCO_3$ near the top, but drops to 1 wt% at the bottom of Unit IV. The light gray chalk has a very low organic carbon content of 0.04% (Table **T4**). The XRD analyses of chalk ($CaCO_3$ contents between 58 and 77 wt%) (Table **T4**), located close to gray chert (porcellanite) nodules, show high amounts of opal-A and a distinct opal-CT peak. A significant amount of quartz is present in only one sample.

Unit IV is extensively burrowed (except for the basal black claystone) (Fig. **F6**). *Chondrites* burrows are below some of the dark intervals. Inoceramid bivalve fragments are present in Cores 183-1138A-65R and 66R.

F5. Schematic diagram showing sediment facies recovered in cores from lithologic Units IV through VI, **p. 70.**

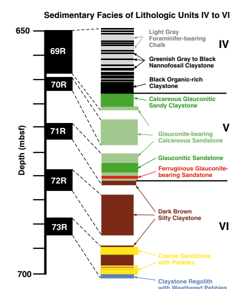

F6. Dark gray to black nannofossil claystone intervals and organically rich claystone interval, **p. 71.**

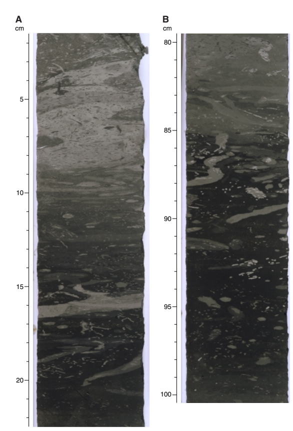

Gray chert nodules are present (two to three per core) in the upper part of the unit.

The deepest dark interval in Unit IV is a bed of black claystone at the base of the unit (interval 183-1138A-69R-5, 21–112 cm) (Figs. F5, F6C). This bed contains two nodules of massive, fine-grained pyrite (intervals 183-1138A-69R-5, 54–56 cm, and 69R-5, 84 cm). Although the top few centimeters of this black interval are moderately burrowed, most of the bed displays undisturbed faint horizontal laminations (Fig. F6C). Sample 183-1138A-69R-5, 89–90 cm, in the lower part of this bed contains only 1 wt% $CaCO_3$, but has a very high organic carbon content of 2.24 wt%. XRD analysis of this layer shows high amounts of clay minerals, clinoptilolite, quartz, and pyrite.

Unit V

Interval: 183-1138A-69R-5, 112 cm, to 71R-2, 138 cm
Depth: 655.57–671.88 mbsf
Age: Santonian to Turonian

Unit V consists predominantly of glauconite-bearing to glauconitic calcareous sandstone (Fig. F4; Table T3). This unit is predominantly reddish to rusty brown but also includes dark green to black (glauconite rich) and light gray to tannish brown (carbonate rich) intervals (Figs. F5, F7, F8). The uppermost interval (interval 183-1138A-69R-5, 112 cm, through 69R-6, 118 cm) is very dark green to black glauconitic sandy claystone. The matrix is light tannish gray; however, fine- to medium-sized glauconite sand grains are so abundant that this light color is obscured. The carbonate content in this dark green sediment is only 7 wt% $CaCO_3$ (Sample 183-1138A-69R-6, 88–89 cm) (Table T4). XRD analysis shows glauconite, calcite, and clay minerals. Light gray to tannish gray glauconite-bearing calcareous sandstone (Sample 183-1138A-69R-6, 118–128 cm) underlies this darker glauconitic unit.

Reddish to orange-brown glauconite-bearing calcareous sandstone constitutes most of the remainder of Unit V (interval 183-1138A-70R-1, 0 cm, to 71R-2, 138 cm) (Figs. F5, F7, F8). The carbonate content is high (55 wt% $CaCO_3$ in Sample 183-1138A-70R-1, 93–96 cm) (Table T4) in the upper part of this interval. The organic carbon content is low (0.1%). XRD analysis shows calcite, opal-CT, opal-A, and clinoptilolite.

The glauconite content increases downward (Fig. F7B) such that interval 183-1138A-71R-1, 100 cm, to 71R-2, 50 cm, consists of glauconitic sandstone with low carbonate content (12 wt% in Sample 183-1138A-71R-2, 15–16 cm) (Table T4). XRD analysis shows the presence of calcite, glauconite, and clinoptilolite.

Abundant white serpulid worm tubes (as much as 0.5 cm in diameter) are present throughout interval 183-1138A-69R-6, 118 cm, to 71R-1, 130 cm (Figs. F7A, F8). Large pectinid bivalve fragments (as much as 2 cm long) are present in interval 183-1138A-71R-2, 27–50 cm. Scattered smaller shell fragments are rare to common throughout the unit. A bioclastic packstone (Sample 183-1138A-70R-2, 46–50 cm) (Table T5) contains 1%–2% glauconite, 1% opaque grains, and 1% brown translucent grains. Bioclasts include bivalves, crinoid columnals, echinoid spines and plate fragments, benthic foraminifers, ostracodes, and bryozoans. Many of the glauconite grains have brown oxidized rims. The echinoderms have syntaxial overgrowths.

F7. Examples of variable lithologies in Unit V, p. 73.

F8. Rusty brown glauconite-bearing calcareous sandstone, p. 75.

T5. Summary of thin sections, p. 180.

Interval 183-1138A-71R-2, 68–91 cm, is light tannish brown because of higher carbonate content. Interval 183-1138A-71R-2, 91–104 cm, is a distinctive orange brown (ferruginous), well-laminated bed of glauconite-bearing fine-grained sandstone (Figs. **F5, F7C**). Some laminae appear to converge slightly and may indicate the presence of subtle cross-stratification. A thin section (Sample 183-1138A-71R-2, 93–95 cm) (Table **T5**) shows abundant brown ferruginous matrix obscuring dominantly nonbiogenic grains. Glauconite is common, and many grains have brown oxidized rims. Brown translucent sand-sized, rounded grains may be oxidized glauconite pellets. Iron ooids are present, including some with magnetite(?) crystal cores. A 1-mm-long iron-coated brown pyroxene(?) crystal and several granule-sized, rounded grains of highly altered plagioclase-phyric lavas are present. The bioclasts include ostracodes, pectinid bivalve shells, benthic foraminifers, echinoderms, and bryozoans. Most bioclasts are reworked, partially rounded, and broken fragments. Echinoderm grains are recrystallized and do not show uniform extinction in polarized light.

Below this bed, the calcareous sandstone is mostly fine grained, but scattered pebbles (as large as 0.5 cm in diameter) are common to the base of the unit (Fig. **F7C, F7D**). Sharp, wavy contacts at the tops of several tannish gray color bands (interval 183-1138A-71R-2, 121–138 cm) may mark diagenetic fronts. We placed the bottom of Unit V at a prominent sharp, undulating contact (possibly caused by loading) between this lithology and underlying dark brown sediments of Unit VI (Fig. **F7D**).

Unit VI

Interval: 183-1138A-71R-2, 138 cm, to 74R-1, 13 cm
Depth: 671.88–698.23 mbsf
Age: Late Cretaceous

Unit VI consists predominantly of dark brown silty claystone with interbedded sandstone and conglomerate (Figs. **F4, F5, F9, F10, F11;** Table **T3**). The carbonate content is uniformly low and ranges from 1 to 14 wt%. The XRD analyses show that all the carbonate is $FeCO_3$; no calcite was detected (Table **T4**). The upper part of Unit VI (interval 183-1138A-71R-2, 138 cm, to 73R-1, 13 cm) is predominantly dark brown silty claystone. The uppermost bed (interval 183-1138A-71R-2, 138–141 cm) is brown, very fine-grained sandstone with some glauconite grains (Fig. **F7D**). The brown sandy claystone (interval 183-1138A-71R-2, 146 cm, to CC, 9 cm) contains scattered small pebbles, shell fragments (as long as 2 mm), and small wood fragments. The sandy clayey siltstone (interval 183-1138A-72R-1, 0–50 cm) contains abundant wood fragments as much as a few millimeters long. A 2-cm-long wood fragment is present at the gradational lower contact of this bed (Fig. **F9A, F9B**). Dark brown silty claystone extends throughout the rest of the upper part of Unit VI to Sample 183-1138A-73R-1, 13 cm (Figs. **F5, F9C, F9D**). Small wood fragments, a few of which are 1–2 cm long, are common throughout most of this claystone. Small white shell fragments and other bioclastic material also are present in this bed. The organic carbon content of Sample 183-1138A-72R-2, 56–60 cm, is 5.6 wt% and reflects the abundant wood fragments in this interval. The XRD analyses show siderite, kaolinite, pyrite, and possibly gibbsite. Pyrite nodules are rare and generally <1 cm in diameter, except for one 5-cm-long nodule or

F9. Examples of sediments in Unit VI, **p. 77.**

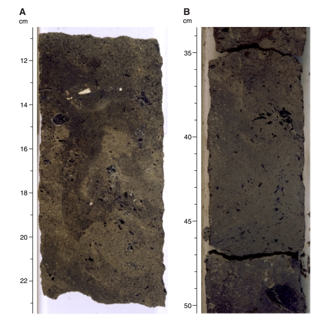

F10. Sandstone beds of variegated color and lithology in Unit VI, **p. 79.**

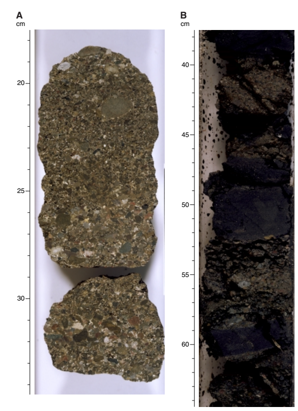

F11. Highly weathered regolith of variegated colors at the base of Unit VI, **p. 80.**

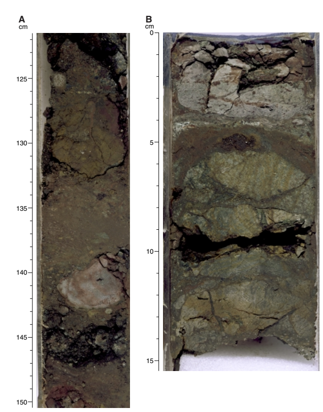

layer (interval 183-1138A-72R-1, 120–122 cm). A 1-cm-thick coarse sandstone bed (interval 183-1138A-72R-3, 6–7 cm) is cemented with pyrite.

Coarse sandstone comprises interval 183-1138A-73R-1, 13–81 cm, and contains abundant granules and pebbles (as much as 1 cm in diameter) that are highly concentrated in several zones (intervals 183-1138A-73R-1, 13–17 cm; 73R-1, 25–28 cm; 73R-1, 31–33 cm; and 73R-1, 43–47 cm) (Figs. **F5, F10A**). The variegated grains and pebbles, dark red and blue through tan, produce an overall brown color. The pebbles and coarse sand grains (Sample 183-1138A-73R-1, 24–28 cm) (Table **T5**) are volcanic and are mostly from lavas with abundant lath-shaped plagioclase microlites. The pebbles are predominantly well rounded, but some of the smaller grains are subangular. This sandstone is moderately well sorted and cemented with carbonate.

Interval 183-1138A-73R-2, 0 cm, to 73R-3, 40 cm, is dark brown silty claystone that contains fine laminated zones. Abundant, very small wood fragments are oriented along many of these laminae and also are found throughout the nonlaminated zones. The carbonate content of this interval is about 14 wt% $FeCO_3$ (Table **T4**). XRD analysis shows siderite, kaolinite, possible gibbsite, and minor pyrite.

Interval 183-1138A-73R-3, 40–126 cm, is mostly brown medium to coarse sandstone with zones of granules and pebbles (Fig. **F10B**). Near the top of this interval, two beds of brown silty clay are interbedded with this sandstone (intervals 183-1138A-73R-3, 47–53 cm, and 73R-3, 59–61 cm). This interval is highly disturbed by drilling so that exact stratigraphic positions and thicknesses of pebble intervals are uncertain. Most pebbles are <0.5 cm and a few are as much as 1 cm in diameter. One horizon shows alignment of pebbles along bedding planes.

The lowermost portion of Unit VI (interval 183-1138A-73R-3, 126 cm, to 73R-CC, 15 cm) is silty claystone of variegated colors including reds, bluish gray, rust, and greenish gray (Fig. **F11**). The carbonate content is very low (<1 wt%) (Table **T4**). XRD analysis shows kaolinite, hematite, quartz, and goethite. Large (2–4 cm) red, rounded pebbles of weathered(?) basalt are present at intervals 183-1138A-73R-3, 138–142 cm; 73R-3, 148–150 cm; and 73R-CC, 0–4 cm. Coarse sand and granules are present in interval 183-1138A-73R-3, 144–146 cm. The material in the core catcher is brecciated and may be weathered basement (i.e., soil) rather than a clastic sedimentary deposit, in which case an unconformity lies somewhere in this interval. We placed the lower contact of Unit VI at the stratigraphically highest occurrence of unambiguous igneous rock in Section 183-1138A-74R-1 at 13 cm. The material in interval 183-1138A-74R-1, 0–13 cm, does not appear to be in the correct stratigraphic position and is probably material that fell downhole during drilling.

Unit VII

Interval: 183-1138A-74R-1, 13 cm, to 89R-3, 73 cm
Depth: 698.23–842.70 mbsf
Age: Late Cretaceous

Lithologic Unit VII consists of basalt flows capped by volcaniclastic rocks with very minor interbedded sedimentary rocks (Fig. **F4;** Table **T3**). Unit VII is subdivided into 22 basement units, which are described in **"Physical Volcanology,"** p. 22, **"Igneous Petrology,"** p. 46, and **"Alteration and Weathering,"** p. 49.

Discussion

The sediments recovered from Site 1138 preserve a nearly complete transgressive sequence from subaerial volcanic deposits (Unit VII) capped by regolith and fluvial deposits (Unit VI) through shallow marine deposits (Unit V) into bathyal pelagic oozes (Units IV–I). Basaltic lava flows appear to have erupted subaerially and weathered by Cenomanian/Turonian time (~99–89 Ma). A thin bed of dark brown claystone and >20 m of felsic volcaniclastic rocks overlie the basalt flows (see **"Physical Volcanology,"** p. 22, and **"Alteration and Weathering,"** p. 49).

At the base of Unit VI, variegated clay with weathered, brecciated volcanic material, which grades upward into sediment with volcanic pebbles, appears to be a regolith. Overlying this regolith, sandstones and interbedded dark brown silty claystones with abundant wood debris were most likely deposited near forested land in a fluvial environment (Fig. **F5**). The sandstones probably represent channels that migrated through flood plain swamps. Fossiliferous glauconitic calcareous sandstones of Unit V (Fig. **F5**) indicate that a shallow neritic environment had developed by Cenomanian/Turonian time (~99–89 Ma).

The transition from neritic to pelagic conditions at Site 1138 is marked by a black pyritic claystone and subsequent cyclic dark/light sediments (Fig. **F5**). At this time, the Kerguelen Plateau was situated in a young, narrow Indian Ocean (Royer and Coffin, 1992), which would have been sensitive to both climatic and paleoceanographic changes. Black pyritic claystone with high organic carbon content at the base of Unit IV implies low oxygen concentrations in waters above the paleoseafloor. The thin dark gray to black nannofossil clay beds interbedded throughout Unit IV most likely represent similar, though increasingly less pronounced, events throughout the Turonian, Coniacian, Santonian, and into the mid-Campanian. The preliminary biostratigraphy permits the possibility of correlating the black pyritic claystone with similar occurrences found worldwide at the Cenomanian/Turonian boundary (Arthur et al., 1987).

Normal bathyal conditions with pelagic deposition of calcareous (Units II and III) and siliceous ooze (Unit I) have existed at Site 1138 since at least mid-Campanian time. Beginning in late Miocene time, these oozes appear to have been diluted by the influx of gray terrigenous clays and sporadic ash derived from a nearby landmass, most likely Heard Island. Seismic data appear to show a large modern submarine canyon with well-developed levees (overbank deposits) located ~45 km to the west-northwest of the drill site. It is possible that the gray terrigenous sediments in Unit I and Subunit IIA represent distal overbank deposits derived from turbidity currents flowing down this canyon since the late Miocene time. The switch from calcareous to siliceous pelagic components, widely observed on the Kerguelen Plateau (Mackensen et al., 1992), reflects movement of the polar front northward through the Site 1138 area during late Miocene time.

BIOSTRATIGRAPHY

Site 1138 was drilled in 1141.4 m of water on the CKP ~150 km north-northwest of Site 747 (Leg 120). Approximately 650 m of Upper Cretaceous through Pleistocene carbonate and biosiliceous pelagic ooze and ~340 m of probable Upper Cretaceous shallow marine and terrestrial sediments overlie volcaniclastic rocks and basaltic lavas.

A relatively complete and expanded section (110 m) of Pliocene and Pleistocene biosiliceous sediments was recovered at this site. A comparable section has not been encountered during previous drilling on the Kerguelen Plateau. Abundant and well-preserved diatoms provide biostratigraphic control in this part of the section. Biogenic carbonate content increases below the upper Neogene, but abundance and preservation of calcareous microfossils fluctuates throughout the succession. The upper Miocene to Upper Cretaceous consists almost entirely of nannofossil ooze and chalk.

The Miocene and Paleogene sections are punctuated by hiatuses, but a complete K/T boundary may be present in Core 183-1193A-52R. Sedimentation rates are very high in the Pliocene and Pleistocene (28.5 m/m.y.) but decrease to between 9 and 13 m/m.y. in the Miocene and upper Paleogene. Sedimentation rates (Fig. **F12**) reach a minimum during the Paleocene (2.8 m/m.y.) and were also low during the Maastrichtian (4.9 m/m.y.). Slightly higher sediment accumulation rates (8.8 m/m.y.) characterize the lower Upper Cretaceous.

F12. Site 1138 age-depth plot, **p. 81.**

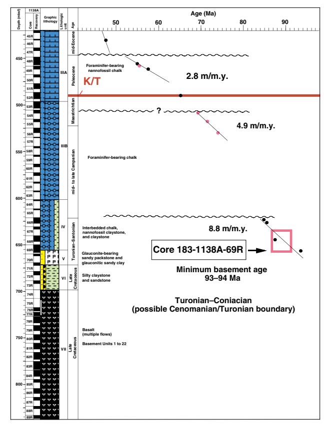

The oldest microfossils encountered are of Late Cretaceous age (early Turonian) and indicate a minimum basement age of ~92–93 Ma. These microfossils are in dark-gray and green horizons within highly bioturbated organic-rich chalks and clays, which are generally too lithified to adequately preserve age-diagnostic microfossils. Immediately beneath this sections is a ~1-m-thick marine black shale unit with 2.2 wt% organic carbon (see **"Organic and Inorganic Geochemistry,"** p. 59). Nannofossils and planktonic foraminifer biostratigraphy suggest that this could represent the Coniacian–Turonian anoxic event (OAE2, the "Bonerelli" horizon; Schlanger and Jenkyns, 1976). The black terrestrial sediments below are rich in fossil plant remains, including common wood fragments, abundant sporangia, and pollen.

Calcareous Nannofossils

Calcareous nannofossils are largely absent in the Pliocene–Pleistocene diatomaceous clays and ooze of lithostratigraphic Unit I, but become common in Sample 183-1138A-12R-CC and abundant below that point until thick black shales are encountered near the bottom of the marine section (Core 183-1138A-69R). Preservation downhole is generally excellent downward to the K/T boundary in Core 183-1138A-52R. Below this boundary, preservation varies between good and moderate in Maastrichtian–Campanian chalks of Subunit IIIB down to Core 183-1138A-60R. From there to the bottom of the marine sedimentary sequence (Core 183-1138A-71R), preservation is good to poor depending on lithology. In general, below Core 183-1138A-61R, preservation deteriorates downhole in the clean, hard chalk until Core 183-1138A-63R, where recovery was also poor. Preservation then improves in the underlying darker greenish and blackish claystone laminae and interbeds that become more common downhole in Unit IV. We dated the lowermost pelagic sediment as early Turonian in age. Indeed, the Cenomanian/Turonian oceanic anoxic event may be represented by the black claystone at the bottom of Core 183-1138A-69R.

Cenozoic

Specimens of *Coccolithus pelagicus* are few in Pleistocene core-catcher Samples 183-1138A-5R-CC and 7R-CC but are common in the mid-Pliocene Sample 183-1138A-9R-CC, where they are accompanied by small (2–5 µm) but very abundant taxa that include various species of *Reticulofenestra*. *Coccolithus pelagicus* are sparse in the upper Miocene Sample 183-1138A-11R-CC, common in Sample 183-1138A-12R-CC, where they are accompanied by *Reticulofenestra perplexa,* and abundant beginning in nannofossil clay of Subunit IIA. From this point down to Sample 183-1138A-20R-CC, we assigned the clay to the long-ranging Zone CN11–5b (for more detailed age determinations, see **"Diatoms,"** p. 21). Dominance of the low-diversity assemblages alternated between *C. pelagicus* and *R. perplexa,* probably depending on paleoclimatic/paleoceanographic factors.

Large *Cyclicargolithus floridanus floridanus,* grading up in size to the larger *Cyclicargolithus floridanus abisectus,* appear in Sample 183-113A-21R-CC, constituting about 10% of the assemblage, but increase downhole to dominant proportions in Sample 183-1138A-24R-CC. In the latter sample, it is accompanied by *Coccolithus miopelagicus,* a few *Calcidiscus leptopora/macintyrei,* and rare *Helicosphaera;* the latter, plus rare *Discoaster deflandrei* in the superjacent core, indicate somewhat warmer surface waters. We assigned cores in this interval to the combined Zones CN5a–CN3. The next interval, from Cores 183-1138A-25R to 28R-CC, is dominated primarily by *C. pelagicus* and belongs to the lower Miocene Zones CN2–CN1, based on the absence of *C. leptoporus/macintyrei*.

Reticulofenestra bisecta, ~10 to 12.5 µm in length, accompanied by *C. floridanus abisectus* of nearly the same length, marks the top of the Oligocene in Sample 183-1138A-29R-CC. *Chiasmolithus altus* dominates the assemblage in Sample 183-1138A-30R-CC, and the mid-Oligocene zone of that name extends down to Sample 183-1138A-35R-CC. The top stratigraphic occurrence of *Zygrabdotus bijugatus* was in Sample 183-113A-33R-CC, along with rare *Sphenolithus moriformis;* dominance alternates strongly among *Cyclicargolithus, Coccolithus, Reticulofenestra,* and *Chiasmolithus* in these cores, probably in response to changing paleoclimatic/paleoceanographic factors.

The co-occurrence of *Reticulofenestra umbilica, Isthmolithus recurvus, Reticulofenestra oamaruensis,* and *Chiasmolithus oamaruensis* in Sample 183-1138A-36R-CC indicates a hiatus between this and the superjacent core catcher. This assemblage belongs to the *R. oamaruensis* Zone, which straddles the Oligocene/Eocene boundary. Certain aspects of the assemblage, however, indicate that we can assign the sediments to the Eocene portion of the zone (Subzone ~CP15b). These include a preponderance of *C. oamaruensis* over its evolutionary descendent, *C. altus,* whereas *Clausicoccus fenestratus* are few in number. The latter bloomed during the earliest Oligocene, but was sparse and sporadic in its distribution during the latest Eocene (compare with the Eocene/Oligocene sequence at Deep Sea Drilling Project Leg 71, Site 511 on the Falkland Plateau and Ocean Drilling Program Leg 119 Hole 737B on the southern Kerguelen Plateau [Wise, 1983, table 1A; Wei and Thierstein, 1991, table 3]).

The next core catcher downhole, Sample 183-1138A-37R-CC, contains a middle Eocene assemblage assigned to Subzone CP14a, which indicates a substantial hiatus between this and the superjacent core catcher. The assemblages contain a few large *Chiasmolithus grandis* and *Coccolithus eopelagicus* (up to 22–24 µm) along with *Chiasmolithus ex-*

pansus, Chiasmolithus solitus, Blackites spinosus, Neococcolithites dubius, Sphenolithus moriformis, and a few six-rayed discoasters, which become common in Sample 183-1138-39R-CC. Specimens of *Discoaster bifax* appear downhole in Sample 183-1138A-41R-CC, but essentially disappear in the subjacent core catcher, although other discoasters increase. We noted *Coronocyclus prinion* in Samples 183-1138A-42R-CC and 44R-CC. Sample 183-1138A-43R-CC contains rare *Nannotetrina cristata,* which increase to few in Sample 183-1138A-44R-CC; this latter core also contains both *Chiasmolithus gigas* and *R. umbilica*. The co-occurrence of these two taxa has also been noted at other mid- to high-latitude sites (e.g., Applegate and Wise, 1987); thus, it is not possible to use the last uphole occurrence of *C. gigas* here as an unequivocal marker to subdivide Subzones CP13b and CP13c. Sample 183-1138A-44R-CC probably lies close to the Zone CP13/14 boundary.

Sample 183-1138A-45R-CC contains no *R. umbilica,* common *C. gigas* ranging in size from 14 to 20 µm, few *N. cristata,* and some discoasters. This sample was assigned to Subzone CP13b. Preservation diminishes downhole from good to moderate in Samples 183-1138A-46R-CC and 47R-CC because of dissolution, fragmentation, and overgrowth. The former sample contained no *Reticulofenestra samodurovii,* rare *Orthostylus tribrachiatus* (reworked?), rare *Discoaster praebifax, Toweius magnicrassus,* common *Discoaster barbadiensis, Coccolithus formosus,* and rare nine-rayed discoasters (*Discoaster binodosus* or *Discoaster nonaradiatus*), and probably lies close to the CP13a/12 zonal boundary, although it may contain some mixed or reworked taxa. Sample 183-1138A-4R-CC contains *Sphenolithus radians, Discoaster lodoensis, Discoaster sublodoensis, Discoaster kuepperi,* and *Toweius magnicrassis* and belongs to Zone CP12, probably the upper part.

A disconformity along which most or all of the lower Eocene is missing is apparently present between Samples 183-1138A-47R-CC and 48R-CC, so we tentatively assign the latter to Zone CP8. It contains *Discoaster multiradiatus, Discoaster mohleri, Prinsius bisulcus, Toweius pertusus, Markalius inversus,* and very abundant, simply constructed, small (3–5 µm) fasciculiths (probably *Fasciculithus tympaniformis* and *Fasciculithus involutus).* Sample 183-1138A-49R-CC contains larger *F. tympaniformis* (up to 8 µm), *F. involutus,* large *Prinsius bisulcus* (up to 11 µm), few *Heliolithus* sp., and abundant *Prinsius martinii*; we assigned the sample to Zone CP5. We assigned Sample 183-1138A-50R-CC to the upper Paleocene, high-latitude Zone NA6 (= ~CP3/CP4). It contains common *Thoracosphaera operculata,* large *Chiasmolithus danicus,* few *C. bidens,* very abundant *Prinsius dimorphosus,* common *P. martinii,* few *Toweius pertusa,* few *Coccolithus subpertusa, Biscutum* sp., *Neochiastozygus concinnus,* and *Placozygus sigmoides*. The subjacent core-catcher sample contains rare fasciculiths (in place?), small *Coccolithus pelagicus* (6 µm), *Chiasmolithus danicus, P. dimorphosus,* but no *Chiasmolithus bidens,* and belongs to Zone NA5.

Cretaceous/Tertiary Boundary

The K/T boundary apparently lies within Core 183-1138A-52R and may be reasonably complete. A reconnaissance study within this core indicated that the boundary probably lies within Section 183-1138A-52R-3 at a color change at 127 cm, where the section passes downhole from a greenish glauconitic chalk to a whitish chalk. The apparent contact has been bioturbated, but the section may have been expanded by the input of fine clastic material derived from volcanic parent material (see **"Lithostratigraphy,"** p. 3). The nannofossils in Section 183-1138A-52R-3 above this contact consist predominantly of Cretaceous taxa. However, we noted a well-preserved specimen of the Tertiary boundary index taxon, *Biantholithus sparsus,* in Sample 183-1138A-52R-3, 60 cm. Two specimens of the Tertiary incoming taxon *Cruciplacolithus tenuis* are also present at 183-1138A-52R-3, 30 cm. *Cruciplacolithus primus* and *C. tenuis* are abundant 3 cm from the top of the section.

Mesozoic

Samples 183-1138A-52R-CC and 53R-CC contain well-preserved *Cribrosphaerella daniae* (centers intact) and abundant *Nephrolithus frequens miniporus,* the respective nominate taxa for the subzone and zone to which we assigned these cores. The next two core-catcher samples downhole (Samples 183-1138A-54R-CC and 55R-CC) exhibit highly variable preservation, with a few well-preserved specimens shown among much micritic carbonate. No *Nephrolithus* are present, perhaps a function of the generally poor preservation. Specimens of *Biscutum coronum* are rare, whereas *Biscutum magnum* and *Reinhardtites levis* are few to common, indicating that these cores belong to the *B. coronum* Zone (assuming that the *B. coronum* are not reworked and the assemblages are not mixed). If this assignment is correct, then a disconformity separates Core 183-1138A-54R from the superjacent Core 53R.

Biscutum coronum was equal in numbers to *B. magnum* in Samples 183-1138A-56R-CC and 57R-CC, which exhibit relatively good preservation and contain common *Neocrepidolithus watkinsii.* The latter is also represented by numerous detached spines in this and the subjacent Sample 183-1138A-58R-CC, where it is accompanied by *Aspidolithus parcus expansus* (indicating the *A. parcus expansus* Subzone of the *B. coronum* Zone [upper Campanian]). Sample 183-1138A-58R-CC also contains extraordinary numbers of *Micula decussata,* a circumstance that cannot be attributed solely to dissolution of other taxa because the preservation of this assemblage is no worse than others in this part of the column.

We also assigned Samples 183-1138A-60R-CC and 61R -CC to the *A. parcus expansus* Subzone based on the presence of the nominate species, *N. watkinsii* and *R. levis*. Preservation, however, deteriorates downsection in the more lithified, poorly recovered sediment; thus, we give no zonal assignment for Sample 183-1138A-62R-CC. The next core downhole contains *Eiffellithus eximius* plus *R. levis;* we assign it to the respective zone and subzone that bear those names (upper Campanian). Sample 183-1138A-64R-CC is too poorly preserved to date; however, Sample 183-1138A-65R-1, 30–32 cm, taken within the core, contains a better preserved assemblage belonging to the *R. levis* Subzone.

As a result of poor preservation in core-catcher samples toward the bottom of the hole, we assigned zones for the rest of the geologic section primarily on samples taken from within the cores. In Cores 183-1168A-66R to 68R, we found the best-preserved nannofossils in the darker colored lithologies, first greenish and then blackish going downhole, in which increased glauconite and clay contents apparently inhibited diagenesis.

Sample 183-1168A-66R-3, 22–24 cm, contains a dissolution-resistant, residual assemblage consisting of *M. decussata,* a single specimen of *Lithastrinus moratus* (= L. *septenarius*), and two specimens of *Marthasterites furcatus,* and we tentatively assigned it to the *Lithastrinus moratus* Subzone of the *Eprolithus floralis* Zone (lower Santonian); however, we noted no *E. floralis*. Nevertheless, a hiatus appears to exist between this and the last datable overlying sample. Sample 183-1138A-66R-4, 66–67 cm, from the next core section downhole, contains several *Thiersteinia ecclesiastica, Micula concava,* common *Helicolithus trabeculatus,* and a single specimen of *Marthasterites furcatus*. We assigned it to the upper portion of the *T. ecclesiastica* Zone (lowermost Santonian). The core-catcher sample from Core 183-1138A-66R lacks *M. concava* but does have *M. decussata,* and we consider it late Coniacian in age.

Sample 183-1138A-67R-2, 34–35 cm, yielded long-rayed *Lithastrinus septenarius* (*L. moratus* according to Varol, 1992) in the absence of *M. decussata,* and we consider it mid-Coniacian in age. Below this level, the rays of the these lithastrinids shorten and straighten as the long-rayed "septenarid" morphotype is traced back to its ancestral "moratid" form, then, ultimately, to the precursor *Eprolithus* lineage. We picked the point at which the latter transition occurred subjectively, using the light microscope on board ship, and the choice depends on the species concepts of the observer. The sole nannofossil paleontologist on this hard-rock leg considered this transition to have occurred at this level in the cored sequence, although some specimens in Section 183-1138A-68R-5 appeared to exhibit some rotation when one focused through them. This transition will have to be examined more closely with the scanning electron microscope onshore. We noted no *Eiffellithus eximius* below Sample 183-1138A-67R-2, 34–35 cm; however, *Eprolithus eptapetalus* and possibly *Eprolithus rarus* are present; thus, we regard the core-catcher sample (183-1138A-67R-CC) as probably mid- to late Turonian in age.

We examined 11 samples from Core 183-1138A-69R to ascertain the locations of the highest concentrations and best-preserved nannofossils. In this core, the highest nannofossil concentrations were in the lighter colored layers and laminae, which diminished in number and thickness downhole, apparently disappearing completely in a ~1-m-thick organic-rich zeolitic claystone at the base of Section 183-1138A-69R-5. Preservation was good in all samples, but best in the darker nannofossil-bearing lithologies.

Sample 183-1138A-69R-1, 25–27 cm, contains common, seven-rayed *E. eptapetalus* and *E. floralis* as well as *Prediscosphaera avita* (about 6 µm in diameter), *Gartnerago obliquum,* and a single specimen of *Stoverius achylosus*. The uppermost range of *S. achylosus* is given as lower Cenomanian by Perch-Nielsen (1985, fig. 70), but it has been recorded as rare in the Turonian of the Naturaliste Plateau Site 258 by both Thierstein (1974) and Watkins et al. (1996). The extinction of *C. achylosus* is considered to be a reliable global biostratigraphic event. It is placed in the lower upper Turonian by J. Bergen (pers. comm., 1999), but somewhat lower (below the lower/middle Turonian boundary) by Burnett (1998, fig. 6.3).

The evolutionary first occurrence datum (base) of the seven-rayed *E. eptapetalus* was noted in Sample 183-1138A-69R-3, 93–95 cm, which we consider no younger than mid-Turonian in age. We recorded the first downhole occurrence (top) of eight-rayed forms attributed to *E. octopetalus* (= *Ephrolithus* sp. 2 of Perch-Nielsen, 1985) in Sample 183-1138A-69R-4, 68–70 cm. Perch-Nielsen (1985, fig. 54) and Varol (1992) suggest a stratigraphic range of Cenomanian to Turonian for this taxon, whereas Burnett (1998, fig. 6.3) restricts it to the lower–middle Turonian. This plus the absence of *E. eptapetalus* confines this sample to the lower Turonian.

Sample 183-1138A-69R-5, 13–15 cm, contains an assemblage dominated by *Watznaueria barnesae, E. floralis* s.l., *Parhabdolithus embergeri,* and an assortment of small zygoliths. Fragments of *Eiffellithus turriseiffelii* were noted, but no *Quadrum gartneri* or any other miculid morphotype. The age of this sample could well be earliest Turonian. Sample 183-1138A-69R-5, 81–83 cm, from a massive black shale at the base of the section, is barren of nannofossils. This black shale has a total organic content of 2.2% (see **"Organic and Inorganic Geochemistry,"** p. 59).

The core catcher from Core 183-1138A-70R is an orange-colored glauconitic, sandy packstone and clay that bears serpulid worm tubes. In a smear-slide preparation, it yielded a large amount of carbonate cement, some zeolite, and no nannofossils. The core catcher from Core 183-1138A-71R is also barren, but a sample from a pectin-bearing, glauconitic sandstone at Section 183-1138A-71R-2, 32 cm, contains a few well-preserved nannofossils somewhat similar to those from Sample 183-1138A-69R-5, 81–83 cm, but also with *Seribiscutum primitivum,* whole *E. touriseiffelii,* and small (5-µm diameter) prediscosphaerids. This sample needs further study before we can determine its age.

Cenomanian/Turonian Anoxic Boundary Event

The ages we determined for Core 183-1138A-69R and the nature of the black shale unit at the bottom of Section 183-1138A-69R-5 (see **"Lithostratigraphy,"** p. 3) suggest that the Cenomanian/Turonian boundary anoxic event (Schlanger and Jenkyns, 1976) may be preserved at the bottom of this core. *Stoverius achylosus*, which ranges from the Cenomanian into the Turonian, is present in Section 183-1138A-69R-5 above the black shale; however, middle Turonian taxa such as *E. eptapetalus,* are absent. Another important index species that is apparently absent is *Q. gartneri* (= *M. decussata* of some authors), which only made its first evolutionary appearance during the early Turonian. This species, however, appears as "few" to "rare" in the early part of its range in this region (Thierstein, 1974; Watkins et al., 1997), and we could have missed it during the shipboard examination of the cores. Thus, such negative evidence only suggests, but does not prove, the existence of a Cenomanian/Turonian boundary black shale at this site. Significantly, however, no characteristic Cenomanian taxa such as *Corolithion kennedyi, Axopodorhabdus albianus,* or *Microstaurius chiasta*, were noted.

On the other hand, the gradual transitional upward in Section 183-1138A-69R-5 from black claystone essentially or totally devoid of nannofossils into laminae and then beds containing progressively more calcareous nannofossils and other calcareous microfossils might be expected during the ventilation of an anoxic deposition environment (e.g., see Frontispiece, *DSDP Initial Reports* Volume 71, Pt. 1; Ludwig, Krasheninnikov, et al., 1983), one which could have existed in the nearshore shelf region during a major transgression. Such a major global transgression has been postulated as the immediate cause of the Cenomanian/Turonian boundary anoxic event and, along with the progressive subsidence of the volcanic platform of the central Kerguelen Plateau, could explain the lithologic succession from nearshore, oxidized sediments to the meter-thick black shale. We will test this hypothesis during the shore-based research on these cores.

Planktonic Foraminifers

Planktonic foraminifers from the Neogene, Paleogene, and Late Cretaceous are comparable to those encountered during previous drilling on the Kerguelen Plateau, in particular the central Kerguelen Plateau Site 747 (Leg 120). We apply the Neogene Kerguelen (NK) zonal system of Berggren (1992) developed specifically for assemblages in this region to the Pleistocene to Miocene sections (see **"Biostratigraphy,"** p. 10, in the "Explanatory Notes" chapter). The Paleogene can be characterized in terms of the Antarctic (AP) zonal scheme of Stott and Kennett (1990; modified by Huber, 1991, and Berggren, 1992). A modified version of the Cita et al. (1997) Southern Ocean Late Cretaceous Scheme is useful for biostratigraphic correlation of the Upper Cretaceous, principally the Maastrichtian and uppermost Campanian sediments. Biostratigraphic control is reduced below this interval because of poor microfossil preservation, hiatuses, and low recovery. Unusually good preservation of planktonic foraminifers in thin clay horizons of Santonian and Turonian age may help to improve existing zonal schemes at these key intervals.

We examined planktonic foraminifers in core-catcher samples from all sediment cores (Cores 183-1138A-1R through 73R), as well as additional samples within cores where necessary, to locate major stratigraphic boundaries. Below the thick Pliocene–Pleistocene siliceous ooze section, in which planktonic foraminifers were generally well preserved, preservation varies considerably downhole. Preservation is reasonable in the Miocene but diminishes in the Paleogene and fluctuates between poor and moderate in the Oligocene, diminishing further in the Eocene and Paleocene as the effects of dissolution increase. Preservation is slightly better in uppermost Cretaceous sediment for several cores but is highly variable and often poor in older material.

The abundance of planktonic foraminifers varies highly in the biosiliceous ooze, ranging from relatively common to virtually absent during the Pliocene and Pleistocene. These fluctuations are reflected in the calcium carbonate profile, which shows large scatter in carbonate values within diatom-rich Unit I (see **"Organic and Inorganic Geochemistry,"** p. 59). Biogenic carbonate content is much higher in the middle Miocene because siliceous microfossils are less abundant. Upper Paleogene sediment contains common to abundant planktonic foraminifers, but abundance falls in the middle Eocene and Paleocene section. Planktonic foraminifers are mostly sparse in the Lower Cretaceous sediment owing to diagenesis and dilution by clay sediments. Examination of additional samples in clay-rich layers within the cores allowed us to determine the age and composition of the sediments in this interval. Quality of preservation and abundance of planktonic foraminifers is very good in these samples. Planktonic foraminifers are essentially absent from the basal Core 183-1138A-69R black shale, as well as from the underlying glauconite sands and wood-bearing claystones and sandstones at the bottom of the sedimentary sequence.

Cenozoic

The top 121.6 m of biosiliceous ooze (Cores 183-1138A-1R through 13R) is characterized by a low-diversity planktonic foraminiferal assemblage dominated by sinistrally coiled *Neogloboquadrina pachyderma* and *Globigerina bulloides*. This assemblage is typical of the subantarctic late Neogene (Pliocene, Pleistocene, and latest Miocene) and falls within

Zone NK7. Less common elements of the fauna are *Globorotalia puncticulata, Turborotalia quinquelobula,* and *Globigerinita ulva*. Diatom biostratigraphy provides greater biostratigraphic control within this interval.

Diversity is also relatively low in the upper Miocene, and foraminifers are often diluted by abundant diatoms, sponge spicules, and variable quantities of fibrous gypsum crystals. Samples 183-1138A-14R-CC through 19R contain common *Globorotalia scitula* and globigerinids, including *G. bulloides* and *Gobigerina woodi*. Based on the absence of *N. pachyderma,* we assigned these samples to the mid- and upper Miocene Zones NK5–NK6. Globigerinids are larger and more abundant in Sample 183-1138A-20R-CC. In this sample *G. bulloides*, *G. woodi,* and *Globigerina falconensis* are accompanied by *Globorotalia praescitula* and *Globorotalia miozea*. A similar range of species is present in the next core downhole, Sample 183-1138A-21R-CC, but forms are generally smaller and globorotalids dominate over globigerinids, perhaps indicating somewhat warmer water. Based on the presence of *G. miozea,* we assign these cores to the lower middle Miocene Zone NK4.

Globorotalia zealandica and *Paragloborotalia incognita* in Samples 183-1138A-21R-CC to 24R-CC indicate an early to middle Miocene age (Zone NK3–NK4). Samples 183-1138A-25R-CC and 26R-CC are characterized by an early Miocene (Zone NK2) fauna composed of catapsydracids, *Paragloborotalia incognita*, and rare *Globigerina brazieri*. *P. incognita* is absent in the core catcher of Core 183-1138A-27R. We assign this and the subjacent sample accordingly to the lower Miocene Zone NK1.

Globigerina euapertura, the nominate taxon of the upper Oligocene Zone AP16, appears in Sample 183-1138A-29R-CC, accompanied by catapsydracids, tenuitellids, *G. brazieri, Globorotaloides suteri*, and various indeterminate globigerinids of late Oligocene affinities. The next two samples downhole contain similar assemblages, and we assign all to combined Zones AP16–AP15. The downhole last appearance datums (LADs) of *Chiloguembelina cubensis* and *Subbotina angiporoides* are in Core 183-1138A-33R. The presence of these taxa in Samples 183-1138A-34R-CC to 36R-CC, and absence of *Globigerinatheka index* and characteristic Eocene *Acarinina* spp. is evidence for a mid- to early Oligocene age.

The next interval, Samples 183-1138A-37R-CC to 43R-CC, is characterized by low dominance–high diversity assemblages of middle Eocene (Zone AP10–AP11) forms including *C. cubensis, Subbotina linaperta, Pseudohastigerina micra, G. index,* and low numbers of small acarininids. This middle Eocene fauna directly underlying cores containing a typical lower Oligocene assemblage indicates a hiatus between Sections 183-1138A-36R-CC and 37R-CC. Sample 183-1138A-38R-CC contains large, abundant, and particularly spherical forms of *G. index* and *Globigerinatheka subconglobata,* commonly possessing numerous bullae and supplementary apertures similar to the New Zealand forms (Jenkins, 1971). At low latitudes the *G. subconglobata–Globigerinatheka beckmanni* group show a similar trend toward development of spherical tests. The two species become very common in a short interval in the middle Eocene (tropical Biozone P13). These comparable evolutionary events may be synchronous and useful for cross-latitude biostratigraphic correlation. Alternatively, increased species diversity and morphological variability in the genus may be related to local climatic variation and warming of surface waters.

Preservation diminishes downhole from moderate to poor in Samples 183-1138A-39R-CC and 46R-CC because of dissolution and fragmentation until planktonic foraminifers are indistinguishable in Sample 183-1138A-47R-CC. Preservation is poor to moderate in Samples 183-1138A-48R-CC and 51R-CC. *Acarinina mckannai, Chiloguembelina* spp., *Globanomalina compressus, Globanomalina australiformis,* and small morozovellids, in the absence of *G. index, P. micra,* and *Acarinina primitva,* indicate an early Eocene–late Paleocene (Zones AP5–AP6) age. Preservation diminishes again in the two subjacent core-catcher samples. We tentatively assign these samples to the upper Paleocene. A poorly preserved, low-diversity assemblage of small globigerinid and biserial forms, including *Eoglobigerina* spp., *Chiloguembelina crinita,* and *Zeuvigerina teuria* are in Sample 183-1138A-51R-CC. Based on the presence of these taxa and the absence of acarininids and well-developed *Globanomalina* spp., we assign this sample to the lower Paleocene Zone AP1b. A possible expanded K/T boundary occurs in Core 183-1138A-52R.

Mesozoic

Cretaceous foraminifers are in Cores 183-1138A-52R-CC through 69R-CC. The Maastrichtian fauna is identical to that at other Kerguelen Plateau and South Atlantic high-latitude sites, although the uppermost Maastrictian *Pseudotextularia elegans* Zone may be missing at Site 1140. Samples 183-1138A-52R-CC and 53R-CC contains moderately well-preserved *Globigerinelloides subcarinatus, Globigerinelloides multispina, Heterohelix globulosa, Heterohelix planata, Hedgerbella sliteri, Globotruncanella petaloidea, Abathmophallus mayeroensis,* and *Archeoglobigerina australis,* an assemblage characteristic of Huber's (1992) *G. subcarinatus* Subzone. The downhole first appearance datum of *G. subcarinatus* is in Core 183-1138A-54R. Therefore, we assign the next sample downhole, Sample 183-1138A-54R-CC, to the lower Maastrichtian *G. petaloidea* Subzone. *Abathmophalus,* the nominate genus for the middle and upper Maastrichtian, is absent from core catchers, except Sample 183-1138A-53R-CC, in which *A. mayaroensis* is present.

Samples 183-1138A-54R-CC and 55R-CC contain a slightly different assemblage consisting of *Archeoglobigerina australis*, *Rugoglobotruncana circumnodifer, Globotruncana arca, G. petaloidea,* and rare *Abathmophalus intermedius.* This fauna appears to be older than that found in the overlying sample. Nannofossil studies indicate a possible hiatus between Samples 183-1138A-53R-CC and 54R-CC.

Planktonic foraminifers are highly fragmented and dissolved in Sample 183-1138A-56R-CC, but preservation improves slightly downhole so that we were able to identify key zonal markers. In Samples 183-1138A-57R-CC and 58R-CC we recognize *Globigerinelloides impensus,* the nominate taxon for the upper Campanian zone bearing this name. Also present is *H. globulosa, A. australis,* and a small planispiral form resembling *G. impensus,* comparable to *Globigerinelloides* sp. recorded by Huber (1990, pl. 1, figs. 8, 9) and Quilty (1992, pl. 1, figs 22, 23). Inoceramid prisms are found in these sample in varying quantities.

The *G. impensus* Total Range Zone is a useful and consistently recognizable biozone in Upper Cretaceous sediments on the Kerguelen Plateau. The position of the upper boundary of this zone, however, is ambiguous. In Leg 183 cores, we observe the LAD of *G. impensus* above rather than below the *Aspidiolithus parcus expansus* nannofossil datum (74.6 Ma) within magnetic Chron C33n and have modified the Upper

Cretaceous *G. impensus* Zone accordingly (see Fig. **F6D,** p. 61, in the "Explanatory Notes," chapter).

Preservation varies considerably downhole in Unit IV (Cores 183-1138A-59R through 69R) as diagenesis increases. Low recovery and poor microfossil preservation in Cores 183-1138A-59R through 65R prevented us from assigning zones. Recovery was greater in Cores 183-1138A-66R through 69R; we interpreted ages where we could examine samples from carefully selected clay-rich horizons within the chalks and nannofossil claystones. We recovered relatively well-preserved assemblages of mid-Cretaceous planktonic foraminifers from these clay-rich intervals. The fauna is more diverse and richer in keeled forms than other mid- to lower Late Cretaceous faunas described from the South Atlantic (Huber, 1990; Sliter, 1977; Krasheninikov and Basov, 1983). The assemblage is comparable to Upper Cretaceous Austral realm faunas (Huber, 1992), but we also recognize affinities with more temperate Cretaceous faunas such as those from the Exmouth Plateau (Wonders, 1992). Paleogeographic reconstructions suggest that the Exmouth Plateau, which at present lies at about 17°S, was more than 10° south of this position during the Late Cretaceous.

Planktonic foraminifers are abundant, but only moderately to poorly preserved in Sample 1138A-66R-4, 99–102 cm. In addition to abundant *Hedbergella planispira* and *Heterohelix* spp., relatively rare but large double-keeled forms are present which, although difficult to identify because of adhering carbonate obscuring surface details, probably belong to the genera *Dicarinella* and *Globotruncana*. Based on the presence of the *Whitinella baltica* and the absence of *Archeoglobigerina cretacea,* we assign this sample to the Coniacian–Turonian *W. baltica* Zone.

We also assign the next interval of samples downhole to the *W. baltica* Zone, but the planktonic foraminiferal assemblage shows some differences in faunal composition. Sample 183-1138A-67R-4, 68–71 cm, contains *Heterohelix* spp., *W. baltica, Whitinella archeocretacea, Whiteinella paradubia,* and common double-keeled forms comparable to *Dicarinella imbricata* and *Globutruncana* spp. Samples 1138A-68R-1, 102–104 cm, and 68R-4, 5–7 cm, contain *H. planispira, W. baltica*, and less rare keeled forms. The double-keeled forms are rarely intact, commonly occurring as detached umbilical and spiral halves. Also common in these samples are small, compressed forms with probable hedbergellid or praeglobotruncanid affinities.

Sample 183-1138A-69R-1, 25–27 cm, contains abundant inoceramid prisms and a rather poorly preserved fauna that includes *Whitinella* spp., *H. planispira,* and probable *Praeglobotruncana stephanii.* We tentatively assign these samples to the upper part of the *Praeglobotruncana* spp. Zone (early Turonian). Forms with widely spaced double keels are missing from the last two samples above the essentially microfossil-barren black shale (Samples 183-1138A-69R-5, 14–16 cm, and 69R-5, 81–83 cm). Sample 183-1138A-69R-5, 14–16 cm, is the better preserved of the two and contains a diverse assemblage of planktonic foraminifers that includes *Dicarinella imbracata, Praeglobotruncana* sp.*, W. baltica*, and rare *Shackoina cenomana.* We also assign these samples to the upper *Praeglobotruncana* spp. Zone because of the absence of characteristic Cenomanian forms. The presence of this lower Turonian assemblage directly above the black shale in Section 183-1138A-69R-5 suggests this horizon may represent the Cenomanian–Turonian oceanic anoxic event.

Sediments that compose Units V and VI (Cores 183-1138A-70R through 72R) do not contain planktonic foraminifers. Sample 183-1138A-70R-CC is composed of abundant carbonate grains and zeolite crystals and is barren of fossils except for a few small calcite tubes that are considered to be the mineralized linings of serpulid worm burrows. The rusty brown glauconite sand in the subjacent core (Sample 183-1138A-70R-2, 12–18 cm) contains pectin shells and rare benthic foraminifers, registering the earliest marine sediments above a thin layer of terrestrial sediments and igneous basement.

Diatoms

We looked for Neogene diatoms in the smear slides that were prepared from core-catcher samples for calcareous nannofossil studies. In some cases, diatom preservation was good and biostratigraphic control by coccoliths was poor because of low-diversity, high-latitude assemblages. We did not attempt to prepare proper samples for diatom studies, and our preliminary results could be greatly improved by shore-based study by a diatom specialist.

Cores 183-1138A-1R and 2R contained abundant *Thalassiosira lentiginosa* but no *Actinocyclus ingens,* and we assigned them to the upper Quaternary *Thalassiosira lentiginosa* Zone. *A. ingens* is quite abundant in Sample 183-1138A-3R-CC; we assign this sample and the next four cores downhole to the zone of that name. *Fragilariopsis barronii* is abundant in Samples 183-1138A-5R-CC through 7R-CC (perhaps as high as 4R-CC), which indicates the lower portion of the *A. ingens* Zone (= the *Nitzschia kerguelensis* Zone of Harwood and Maruyama, 1992).

A disconformity apparently lies above the next core catcher because Sample 183-1138A-8R-CC contains abundant *Thalassiosira insigna* and belongs to the upper Pliocene *T. insigna–Thalassiosira vulnifica* Zone. Sample 183-1138A-9R-CC yielded *Nitzschia clementii, Thalassiosira inura, Nitzschia reinholdii, T. oestrupii, N. barronii,* and *Fragilariopsis interfrigidaria*. We assigned it and the next two cores downhole to the mid-Pliocene *F. interfrigidaria* Zone.

Another disconformity probably lies between Samples 183-1138A-11R-CC and 12R-CC. We assign the latter sample as well as Sample 183-1138A-13R-CC to the *N. reinholdii* Zone. Besides the nominate species, Sample 183-1138A-13R-CC contains *Nitzschia aurica, Rhizosolenia hebetata* group, *Simonseniella barboi, Hemidiscus ovalis,* and *Thalassiosira oliverana*. Sample 183-1138A-14R-CC contains *Denticulopsis hustedtii,* whereas Sample 183-1138A-15R-CC yielded that taxon plus rare *Nitzschia donahuensis* and few *A. kennettii*. Sample 183-1138A-15R-CC, therefore, belongs to the *Asteromphalus kennettii* Zone, as do probably the next two core-catcher samples downhole, although we did not discern the nominate species in the smear slides. In this region, however, the occurrence of *A. kennettii* can be rare and sporadic except in the uppermost part of its range (Harwood and Maruyama, 1992, table 14).

Sample 183-1138A-18R-CC contains common *Denticulopsis dimorpha,* indicating that we reached the top of the zone of that name. The next core-catcher sample downhole yielded *Denticulopsis lauta, Denticulopsis hustedtii,* common *Nitzschia dentiduloides,* and abundant *Denticulopsis dimorpha,* and we assigned it to the middle Miocene *Denticulopsis praedimorpha–N. denticuloides* Zone. Sample 183-1138A-20R-CC probably belongs to this zone or lower in the biostratigraphic column; *D. hustedtii* and *N. denticuloides* are present but *D. dimorpha* is absent in this core. Below this point in the hole, pennate diatoms become rare in the smear slides; *Denticulopsis maccollumii* is present in Samples 183-1138A-22R-CC and 23R-CC, but we could not assign zones confidently because of the lack of diatoms in the smear slides; at this point in the hole they are strongly diluted by calcareous nannofossils.

Plant Fossils at Site 1138

Preparation for analyzing plant fossils included four-fraction wet sieving with 750-, 250-, 125-, and 45-µm sieves, followed by air drying for 16 days. We then picked individual pieces from dry-sieved fractions under the binocular microscope.

The pieces range in size from a few millimeters to 3 cm. The state of fossilization/permineralization ranges up to coal. Most pieces are covered with a light brown glaze of iron-bearing, low-temperature altered material and are very well rounded. Preservation ranges from good to poor, down to nearly amorphous black remains.

We found parts of fern axes that probably belong to different species, within particularly well-preserved vessels. We also noted leaves of different sizes. Rarely, leaves were even preserved with sporangia, and in one example we found the top part of a young, enrolled frond. Fronds are unique features of ferns.

The material also contains gymnosperm remains, probably of more than one species. These include wood fragments, parts of seeds, and cone scales. We could not classify other pieces found, such as epiderms or spines, at sea. The material is promising for other kinds of shore-based analyses, such as various sectioning techniques, cuticular analysis, and electron microscope observations.

With proper specimen preparation onshore, the material should also be useful for palynomorphological biostratigraphy. The core-catcher material of Core 183-1138A-69R-CC seems to contain a rich flora of spores; we also observed some in the core catcher of Core 183-1138A-71R.

PHYSICAL VOLCANOLOGY

Introduction

The basement volcanic units encountered in Hole 1138A comprise aphyric, flow-banded, dacitic cobbles (basement Unit 1), a succession of pumice lithic breccias (pyroclastic flow deposits) and intercalated volcanic ashes (Unit 2), and 20 lava units that show a range of emplacement styles (Units 3–22) (see Fig. **F4**, p. 69). The distribution of volcaniclastic deposits and components at Site 1138 is summarized in Table **T6**, and the lava flow units and the interpreted flow types are listed in Table **T7**. The boundaries between different lava structures, which correlate with changes in physical properties and other measurements, are listed in Table **T8**. The criteria for dividing these units and interpretations regarding the mode of emplacement are discussed after the descriptions of the recovered rocks. For some readers, it may be helpful to first read the interpretive section and refer to the unit descriptions in conjunction with the core photographs for the observations leading us to these conclusions. The interpreted lava flow features within each lava unit are summarized in Table **T9**.

Volcanic intervals within the sedimentary sequence overlying basement in Hole 1138A include disseminated volcanic glass shards, small pumice, volcanic lithics, feldspar in foraminifer-bearing diatom clay and ooze (lithologic Unit I), and discrete pyroclastic fall tephras in the

T6. Summary of volcaniclastic components, **p. 181.**

T7. Lava units, **p. 182.**

T8. Summary of curated positions of contacts and internal boundaries for lava units, **p. 183.**

T9. Summary of internal textures of lava units, **p. 184.**

upper part of the sedimentary section (Unit I through Subunit IIIA) (Table T6).

Unit Summaries

Lithologic Units

Unit I: Foraminifer-Bearing diatom ooze

Cores 183-1138A-1R, 2R, and 5R to 7R contain variable amounts (<2%) of disseminated silt- to sand-sized feldspar crystals, rare lithic clasts, and scattered pumice fragments. Felsic glass is always present as clear glass shards. Disseminated brown glass shards are found in Cores 183-1138A-8R to 10R (see **"Lithostratigraphy,"** p. 3), and discrete tephra layers are present in the succession from Core 183-1138A-12R to 36R (Table **T10**).

T10. Distribution of volcanic components in Units I, II, and III, **p. 185.**

Units I and II and Subunit IIIA: Pyroclastic Fall Deposits

The uppermost part of the sedimentary sequence (Sections 183-1138A-1R to 3R) was variably disturbed (contorted bedding to soupy) because of the rotary drilling technique used. For this reason, the volcanic components in Cores 183-1138A-1R through 3R have been homogenized. Elsewhere, tephra fall deposits (Table **T10**) are preserved as variably burrowed disseminated intervals of volcanic glass shards with scattered lithic fragments and pumice clasts of <2 mm (see **"Lithostratigraphy,"** p. 3). A pattern was observed in the abundance of volcanic ash material in washed coarse fractions from core-catcher samples (Table **T10**) in Unit I to Subunit IIIA, and 10 discrete tephra intervals were identified (Table **T11**).

T11. Pyroclastic ash-fall deposits identified, **p. 186.**

The distribution of volcanic components can be broadly bracketed into (1) disseminated mostly felsic (trachytic?) glass and pumice in sediments with ages <~6.4 Ma, a felsic (trachytic?) event represented by tephra distributed in Section 183-1138A-11R-CC (~3.8–3.2 Ma), (2) including a suite of mixed tephras that have bimodal compositions (basalt+trachyte?) at ~10.6–8.9 Ma, and (3) a thick succession of basalt tephra present in core-catcher concentrates for Cores 183-1138A-30R through 34R (31–26.5 Ma) (Table **T10**). Ages are calculated based on biostratigraphic distribution of diatoms, foraminifers, and nannofossils (see **"Biostratigraphy,"** p. 10).

Basement Units

Unit 1: Aphyric Flow-Banded Dacite Cobbles

Basement Unit 1 consists of rounded dacite cobbles. The dacites are aphyric, sparsely vesicular, pale pinkish brown to grayish green in color, and have very light brown to pale green spherulitic bands in a dark green mesostasis (see **"Igneous Petrology,"** p. 46). Flow banding is poorly developed in Section 183-1138A-74R-1 (Pieces 1 through 5, 7, and 8), but wider bands with clear spherulitic texture are preserved in Pieces 6, 9, and 10. Two cobbles at the top of Unit 1 in interval 183-1138A-74R-1, 0–13 cm, are fine-grained, massive dark gray rocks that are similar to material in Core 183-1138A-73R and may have fallen downhole. A black and red cobble (silicified?) in Section 183-1138A-75R-CC may have the same origin (see **"Alteration and Weathering,"** p. 49).

Unit 2: Bedded Pumice Lithic Breccia, Lithic Breccia, Ash-Fall Deposits, and Volcanic Clay

Basement Unit 2 is a 20-m-thick complex succession of volcaniclastic rocks (Fig. **F13**) subdivided into 15 subunits (2A–2O). Unit 2 is volumetrically dominated by five variably oxidized and altered pumice lithic breccias (Subunits 2D, 2G, 2H, 2I, and 2K) (Fig. **F14**) and one lithic breccia with pumice as clasts and in the matrix (Subunit 2E) (Fig. **F15**). Despite appearing relatively poorly sorted, all of these intervals have ungraded to normally graded lithic clasts and reverse graded pumice lapilli.

Pumice is the dominant component in all pumice-lithic breccias, with clasts up to 3 cm but more commonly in the range 0.5 to 2 cm (Fig. **F16**). Although there is some subhorizontal alignment of elongate pumiceous clasts, and variable flattening of pumice depending on the degree of alteration, there is no evidence of welding in these intervals. The lithic clasts commonly show a more limited range in grain size, 0.2 to 1.5 cm, with a maximum clast size of 2 cm. There is one large (mafic volcanic?) cobble in interval 183-1138A-77R-2, 30–35 cm. Lithic clasts are principally felsic volcanic rocks (trachyte and rhyolite?) that have been subjected to a broad range of oxidation and alteration processes. They show a range of colors (commonly dark green or red) and textures, which partially obscure primary mineralogy. In Subunit 2E, lithic clasts are more abundant than pumice clasts, but pumice is the principal matrix component (Fig. **F17**). The matrix in Subunits 2D, 2E, 2G, 2H, 2I, and 2K is dominated by medium to very coarse sand-sized fragmented pumice with evenly distributed lithic clasts in a similar size fraction.

Subunit 2A is dark gray to black, variably indurated clay, with some red (oxidized?) bands. This material may have fallen downhole as it is similar to material in Unit 1 (interval 183-1138A-74R-1, 0–13 cm, Section 183-1138A-75R-CC). Similar out-of-place cobbles are at the top of interval 183-1138A-78R-1, 0–15 cm (Subunit 2G).

Subunit 2B is bedded on a centimeter scale with variable concentrations of pumice and lithic clasts and a variety of grain sizes, grading, and sorting (Figs. **F18, F19**). Alteration is generally high, and many intervals are altered almost completely to clay minerals. Several red (oxidized?) intervals may reflect former subaerial exposure.

Two intensely altered clay-rich intervals (Subunits 2C and 2N), 1 to 1.4 m thick, preserve the outline of pumice lapilli (Fig. **F20**). Both units are pale green with red (oxidized) domains nearer the top of the section and some red subhorizontal banding (Fig. **F21**). Clay pseudomorphs of pumice lapilli (1.5 to 3 cm) are only preserved in the pale green parts of the interval.

A 35-cm-thick reverse-graded lithic gravel (Subunit 2K) is dominated by variably altered lithic fragments up to small pebble size (<1.2 cm). This interval is darker colored (dark green and red clasts) and less altered than adjacent, more pumice-rich breccias (e.g., Subunit 2J). It is not clear if this interval forms the lower part of the overlying pumice lithic breccia (Subunit 2J) or is an individual depositional unit.

Two 10- to 12-cm-thick normally graded primary pyroclastic ash-fall deposits (Subunits 2F, 2L) contain accretionary lapilli <1 cm in diameter. The accretionary lapilli are concentrated near the top of these units, and some lapilli are partially flattened (Figs. **F22, F23, F24**). The grain size of the ash ranges from medium sand to fine sand with more dense lithic grains concentrated near the base of the intervals. In both cases,

F13. Stratigraphic section of the volcaniclastic succession in basement Unit 2, **p. 82.**

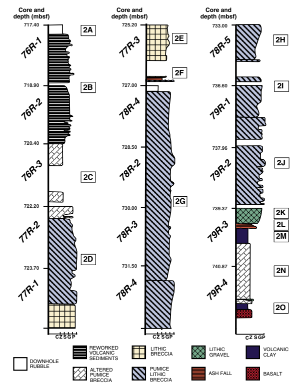

F14. Close-up photograph of interval 183-1138A-78R-4, 69–81 cm, **p. 83.**

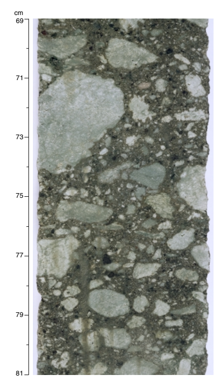

F15. Close-up photograph of interval 183-1138A-77R-2, 136–146 cm, **p. 84.**

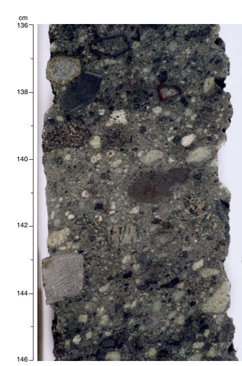

the lower contact of the ash mantles the underlying unit (Subunits 2G and 2M, respectively).

Two massive, very fine grained volcanic clay intervals (Subunits 2M and 2O) are highly altered and retain little evidence of their primary origin (Fig. F25). They contain scattered (<2%) angular lithic clasts (<0.4 cm). Subunit 2M is grayish brown, and Subunit 2O is dark brown.

Unit 3

Unit 3 is the uppermost lava flow in Hole 1138A and consists entirely of massive, moderately plagioclase-phyric basalt. The contact between Unit 2 and 3 was not recovered. The top of the lava is neither oxidized nor strongly altered. The first three pieces of lava are vesicular with 7%–15% equant and rounded, generally 1- to 2-mm-diameter vesicles that are randomly distributed. The remainder of Unit 3 (interval 183-1138A-80R-1, 94 cm, through 79R-5, 0 cm) consists of (1%–10% vesicularity) lava with larger (generally 1–5 mm) diameter vesicles. The vesicles become less round and spherical with depth. Megavesicles 2–3 cm in diameter are prominent in the upper 30 cm of Section 183-1138A-80R-1, and vesicle size gradually decreases with depth. Vesicles are elongated in the horizontal direction and subangular in shape within this dense part of Unit 3. In Section 183-1138A-80R-1 at 94 cm, vesicularity increases sharply to 25%–30% and vesicles are small and irregular in shape. The lowermost piece of Unit 3 (Section 183-1138A-80R-1 [Piece 16]) is a breccia with rectangular angular clasts 2–3 cm in size. These clasts contain ~30% vesicles that are mostly <1 mm in diameter. The bulk of the lava is mildly altered to a greenish gray (10BG 5/1) color, but this last piece is slightly oxidized.

Unit 4

Unit 4 is an aphyric basalt topped by a thin altered breccia. This breccia is marked by a highly altered, black (N1), clay-rich material with relict breccia clasts, but the actual contact between Units 3 and 4 is not recovered. The intense alteration of the top of the flow makes identification of flow features difficult. Relict clasts may have highly irregular, gnarled aa-like shapes. However, the alteration preferentially attacks the most angular protrusions, producing more rounded clasts with a halo of finer grained angular fragments. Although vesicle distributions are still easily identified as voids, clast boundaries are not readily discerned. We find ~10% angular, irregular small vesicles in this black material. We note that in this (and subsequent breccias), the alteration veins commonly follow concentrations of vesicles, obliterating the vesicles in the process. This process can lead to significant underestimation of the original vesicularity of altered breccia clasts. The last loose piece of recovered basalt in Section 183-1138A-81R-2 at 33 cm appears more coherent and has larger, elongate vesicles. Below this, the coherent lava is altered only to a bluish gray (10B 6/1). The vesicularity is 15%–20% with irregular vesicle shapes and generally 1- to 5-mm diameters (Fig. F26). Megavesicles (1–3 cm) are present in interval 183-1138A-80R-2 (Pieces 10–12, 87–117 cm). Highly vesicular clots (1–2 cm) are present in Section 183-1138A-80R-2 at 114 cm and Section 183-1138A-80R-3 at 6 cm, 12 cm, and 23 cm (Fig. F27). A >8-cm-diameter spheroidal vesicular zone intersects the core at Core 183-1138A-80R-2, 131–140 cm. From Section 183-1138A-80R-3 (Pieces 3–5, 29–46 cm), vesicularity gradually increases (from 10% to 25%) and vesicle size decreases (average size changes from 1.2 to 0.6 mm). The lowermost 2 cm of Unit 4 is

F16. Close-up photograph of interval 183-1138A-78R-4, 145–151 cm, p. 85.

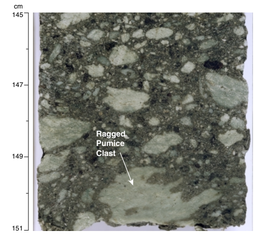

F17. Photomicrographs showing the nature of the pumiceous matrix in the pumice-lithic breccia and lithic breccia units, p. 86.

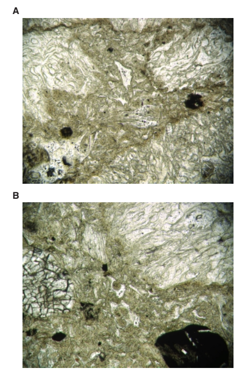

F18. Close-up photograph of interval 183-1138A-76R-2, 88–106 cm, p. 89.

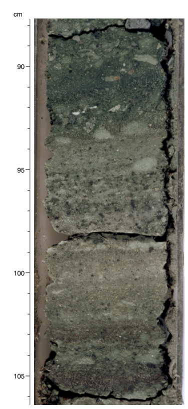

denser, with large numbers (~100/cm²) of small (<0.5 mm) diameter vesicles.

Unit 5

Unit 5 is a sparsely plagioclase-phyric basalt with an altered breccia top. This breccia is altered to grayish black (N2) with 20% irregular angular vesicles generally >1 mm in diameter. In Section 183-1138A-80R-3 at 60 cm, the lava becomes coherent and medium gray (N6) without any recovered transition. Vesicle size in the upper part of the recovered coherent lava fines upward. Average vesicle diameter increases from ~0.5 to 7 mm over interval 183-1138A-80R-3, 60–109 cm. This sequence is punctuated by several 1- to 5-cm vesicular clots. The coherent lava remains variably vesicular (5%–25%) on a 2- to 3-cm scale. One zone of equant and rounded bubbles is present in interval 183-1138A-80R-4, 75–83 cm, with a distinct fining-upward sequence. Otherwise, vesicles are irregular and angular in shape. Irregular megavesicles (2–5 cm) form a horizon at interval 183-1138A-80R-4, 120–135 cm. Mesostasis blebs appear in the 10 cm above these megavesicles. The last small loose pieces of lava recovered from Unit 5 are quite dense (3% vesicularity) and contain a relatively large number (25/cm²) of small vesicles. A sliver of the same material is found welded to the top of Unit 6 (Fig. F28).

Unit 6

Unit 6 is an aphyric basalt with a coherent vesicular top and a massive interior. The top of Unit 6 is an oxidized, slightly brecciated, vesicular, smooth pahoehoe surface (Fig. F28). A patchy alteration pattern following fractures creates the brecciated appearance, but the vesicle patterns indicate minimal clast rotation with mostly in situ fracturing, oxidation, and alteration. Within the upper vesicular crust, vesicularity gradually decreases from 20% to 12%, whereas average vesicle size increases from 1 to 6 mm in the interval 183-1138A-81R-1, 6–99 cm. Vesicularity increases once (with large vesicles) before fining down into the massive portion. By Section 183-1138A-81R-1, 119 cm, the lava contains only 5% vesicles. The vesicles become distinctly more spherical in this fining-downward zone. The lava becomes completely massive at the top of Section 183-1138A-81R-2 with <0.5% vesicles. Vesicularity increases again near the base of Unit 6, starting in Section 183-1138A-81R-2 at 50 cm. A gradual increase in both vesicle number density and vesicle size follows this increase in vesicularity. Vesicularity peaks at 30% with elongated 0.2- to 7-mm-diameter vesicles with a density of 15/cm² immediately above a very fine grained smooth pahoehoe base. This basal zone crosses the core at an angle, cutting from ~12 to 17 cm depth (Fig. F29). There is a hint of another fine-grained zone at the break between Sections 183-1138A-81R-2 and 81R-3, but the recovery is inadequate to be certain. The very base of Unit 6 is also moderately fractured and more highly altered than the rest of the unit.

Unit 7

Unit 7 consists of a sparsely plagioclase-phyric basalt breccia with an underlying coherent flow interior. At the top of Unit 7, in interval 183-1138A-81R-3, 10–27 cm, the breccia consists of 0.2–2.5 cm of poorly sorted rounded to subangular clasts with smaller fragments filling the spaces between the larger clasts (Fig. F29). The clasts are not jigsaw fit, nor are the round shapes defined by spheroidal alteration. Clast size increases down to Section 183-1138A-81R-3 at 106 cm, where the clasts

F19. Close-up photograph of interval 183-1138A-76R-2, 65–83 cm, p. 90.

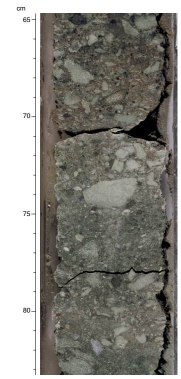

F20. Close-up photograph of interval 183-1138A-77R-1, 10–25 cm, p. 91.

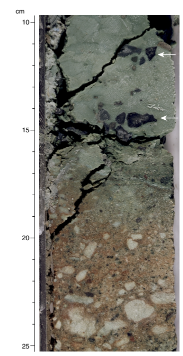

F21. Close-up photograph of interval 183-1138A-79R-4, 37–48 cm, p. 92.

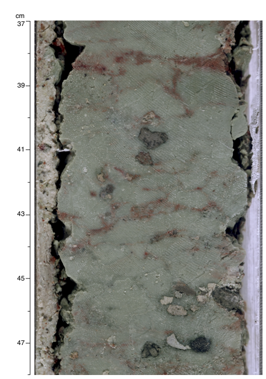

are >10 cm in size. At interval 183-1138A-81R-3, 60–67 cm, a well-defined round basaltic cobble with oxidized rims is present. The open void space comprises 5–10 vol% of the upper part of the breccia while clays make up ≤5%. The character of the breccia below Section 183-1138A-81R-3 at 106 cm is very different. The clasts are smaller (0.2–5 cm) and more angular, and the breccia has no open void space. Instead, a silty-clay fills interstices down to Section 183-1138A-81R-4 at 68 cm, locally making up as much as 60% of the breccia. The infiltrating sediment (brown clay) is altered to clay minerals and quartz, appears massive in core, and no longer preserves primary textures. In interval 183-1138A-81R-4, 42–52 cm, the clasts appear to be suspended in the sediment matrix with little clast-to-clast contact. Some of the larger clasts are jigsaw fit (Fig. F30) or are locally rotated (Fig. F31). For the entire breccia, the vesicles within the clasts are generally small (<0.5 mm) and angular in shape. In the larger clasts, vesicle number densities exceed 100/cm^2, and vesicularity commonly increases toward the inside of clasts. The lava becomes relatively coherent in Section 183-1138A-81R-4 at ~53 cm, though irregular patches of vesicles and sediment-filled cavities extend down to Section 183-1138A-81R-4, 68 cm. The coherent lava contains 7%–15% irregular, angular vesicles, generally 1–2 mm in size, distributed in irregular patches. The last two pieces of Unit 7 that were recovered are somewhat denser (3%–10% vesicularity) and contain wispy mesostasis blebs, some of which are associated with trains of vesicles.

Unit 8

Unit 8 is another sparsely plagioclase-phyric basalt with a breccia top. This breccia shares many features with the one on Unit 7. The upper part consists of oxidized, subrounded clasts. The entire recovered breccia is filled with clay-rich sediments, which make up 1–15 vol% of the breccia, with increasing abundance toward the top. Open voids make up ≤1% of the breccia. Clasts range in size from 7 cm down to sand-sized fragments. Many of the larger clasts have jigsaw-fit margins, usually with alteration minerals in the space between the main clast and the smaller fragments. In other areas, the smaller fragments come from clasts with a range of oxidation and vesicularity. The lava transitions to a coherent structure over interval 183-1138A-82R-1, 67–84 cm. However, in interval 183-1138A-82R-1, 71–92 cm, an elongate zone of brecciated material is filled with sand- to centimeter-sized angular fragments. Both the clasts and the massive interior of Unit 8 generally contain only 1–2 vol% vesicles that are <1 mm in diameter and irregular and angular in shape, but alteration and brecciation may be lowering the visible vesicularity of the clasts. The interior of the flow becomes slightly more vesicular (2%–7%) below Section 183-1138A-82R-1 at 140 cm. In Section 183-1138A-82R-2, from 59 cm downward, the vesicles are found in 1.5- to 3-cm-diameter clumps, which have as much as 20% vesicles (Fig. F32). The base of Unit 8 is slightly oxidized, highly altered, and brecciated.

Unit 9

Unit 9 is another sparsely plagioclase-phyric basalt flow with a breccia top over a coherent interior. Although there are similarities to the breccias on Units 7 and 8, some features are much clearer in Unit 9 and some differences are also noted. The clasts are mostly 1- to 10-cm angular to subangular pieces that are locally fragmented into 2- to 5-mm angular shards. Sediments fill the entire breccia, but some open void

F22. Close-up photograph of interval 183-1138A-77R-CC, 0–8 cm, p. 93.

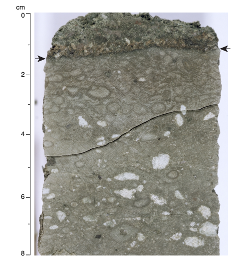

F23. Close-up photograph of interval 183-1138A-79R-3, 34–40 cm, p. 94.

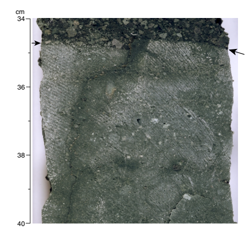

F24. Close-up photograph of interval 183-1138A-79R-3, 26–47 cm, p. 95.

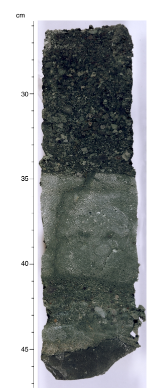

F25. Close-up photograph of interval 183-1138A-79R-4, 74–94 cm, p. 96.

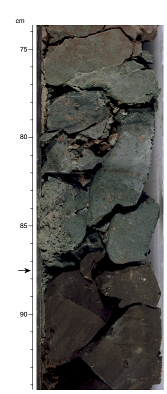

spaces remain, especially along the lower surface of larger clasts. The largest clast is a >15-cm-long folded slab of ropy pahoehoe in Section 183-1138A-82R-2 (Piece 10, 100–114 cm) (Fig. **F33**). The slab has a dark (altered) glassy chill on the ropy side, and the groundmass coarsens away from this side. The other margins are also very fine grained but were not quenched to glass. Other smaller clasts with pahoehoe surfaces along a single margin are scattered throughout the breccia. Another fascinating feature of this breccia is a zone in Section 183-1138A-83R-3 (Pieces 3, 4), which locally appears to have clasts suspended in sediments with very loose grain-to-grain contact (Figs. **F34, F35**). Within this interval, the clasts coarsen upward in Section 183-1138A-83R-3 from 0.1–1 cm at 61 cm to 1–5 cm at 28 cm. The sediments make up 10%–40% of this interval, being more abundant toward the top. Clasts are slightly more altered (darker) at their margins. There is no consistent evidence of finer grained groundmass toward the clast margins. Although the clasts are angular and largely appear to have similar lithology, they are not jigsaw fit. Overall, the clasts in this breccia are quite vesicular (7%–25%), but vesicle shapes remain irregular, even within the slab pahoehoe. The third striking feature of Unit 9 is the interface between the coherent and brecciated parts in interval 183-1138A-82R-3, 89–118 cm, Piece 8 (Fig. **F36**). The lava on one side of the core (left in the archive half) is dense but gradationally becomes disaggregated and oxidized toward the other side of the core. Alteration veins pick out discontinuous 0.1-mm-wide, 1- to 2-cm-long, en echelon cavities that parallel the disaggregating margin of the dense lava. Below this point, the lava is coherent. Irregular angular vesicles dominate until Section 183-1138A-82R-4 at 138 cm. Vesicularity within this region is highly variable (2%–15%), but, in general, vesicularity and vesicle size decrease with depth. Interval 183-1138A-82R-4, 138–147 cm, contains a remarkable set of anastomosing vesicular sheet-like bodies with a matrix that has a distinctly lighter appearance from the surrounding lava (Fig. **F37**). Below this feature, vesicularity remains variable but lower (1%–10%), and the vesicles become spherical. Vesicularity remains low until the last few rock fragments brought up in Section 183-1138A-82R-6, which have 20% round vesicles. Several loose pebbles of vesicular basalt found at the very top of Core 183-1138A-83R are included with Unit 9.

Unit 10

Unit 10 is a breccia-topped aphyric basalt flow, similar in most respects to Units 7–9. Flow top oxidation is minimal with only a <1-mm-thick discontinuous coating on the uppermost clasts. The upper part of the breccia has a large amount of open void space, with sand- and silt-sized sediments filling the interclast spaces only in Section 183-1138A-83R-1 from 85 cm downward. However, interclast space generally decreases with depth with smaller clasts filling the interstices. A few open spaces remain in the lower part of the breccia but are mainly within clasts. Three laminations, each ~1 cm thick, are present in the sediments at interval 183-1138A-83R-1, 89–92 cm. Most clasts are equant, 2–4 cm in size and subangular to subrounded in shape. One >15-cm clast is present at interval 183-1138A-83R-1, 5–18 cm. The pieces <0.5 cm in size appear to be jigsaw fit to larger clasts with alteration minerals filling the gaps. Several of the larger clasts have smooth chill margins on one side and fracture surfaces on the others. About 10% of the clasts have large stretched elliptical vesicles. The remainder have smaller, more irregular vesicles. A zone of dense lava near the base of the breccia

F26. Close-up photograph of interval 183-1138A-80R-3 (Piece 11, 96–116 cm), **p. 97.**

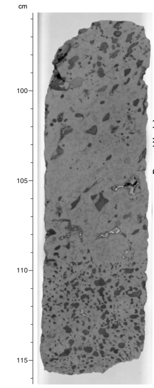

F27. Close-up photograph of interval 183-1138A-80R-3 (Piece 2, 18–28 cm), **p. 98.**

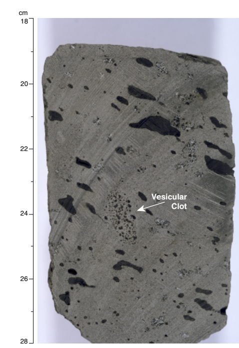

F28. Close-up photograph of interval 183-1138A-81R-1 (Piece 2, 5–15 cm) showing contact between basement Units 5 and 6, **p. 99.**

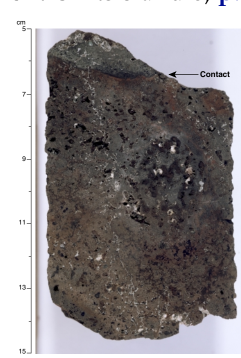

at interval 183-1138A-83R-1, 129–135 cm, has a disaggregated margin. There is a distinct contact between the breccia and the underlying coherent lava. The coherent lava at this contact has a fine-grained groundmass and smaller vesicles. The lava is coherent below Section 183-1138A-83R-1, 137 cm, with one 1.2 cm × 1.2 cm vesicular clast found at interval 183-1138A-83R-1, 148–149 cm. The interior contains a wide variety of vesicles, alternating between zones of round and irregular shapes over 10- to 20-cm-length scales. Although vesicle sizes and shapes are highly variable, vesicularity remains 7%–20%. Megavesicles (1–3 cm) appear in the interval 183-1138A-83R-3, 34–55 cm. One has a long "tail" extending downward that is filled with glassy mesostasis. Wispy mesostasis blebs appear in this same interval and persist through the rest of Unit 10, becoming most prominent in the least vesicular areas. The vesicularity below the megavesicle horizon falls to 0.5%–7%, and vesicles are more spherical. An irregular horizontally elongated vesicular zone with glassy mesostasis is present at interval 183-1138A-83R-4, 19–21 cm. Vesicularity increases again starting at Section 183-1138A-83R-4, 69 cm, reaching 30% at the base of the Unit 10. From interval 183-1138A-83R-4, 91 cm, to the base of the unit, the vesicles are arranged in 3- to >5-cm sized irregular but horizontally elongated domains surrounded by denser boundaries (Fig. **F38**). The contact between Units 10 and 11 is indicated in Figure **F39**.

Unit 11

Unit 11 is an oxidized, coherent, vesicular aphyric basalt flow. However, the uppermost 2 cm of rock included with Unit 11 is a black, fine-grained lobe base, welded to and flowing into two small, angular pieces of oxidized vesicular lava (Fig. **F39**). The most striking feature of Unit 11 is the large vertically elongated vesicles in the upper part (Fig. **F40**). Although the flow never becomes truly vesicle poor, at Section 183-1138A-83R-5, 60 cm, vesicularity drops from 20%–30% to 10%–25%. Vesicle sizes increase downward from the top of the flow until this same point, grading from 2–10 mm to 5–30 mm. The vesicles in this upper part have elongated, well-rounded elliptical shapes. The direction of elongation swirls about on a 10- to 20-cm scale but is near vertical for the largest and most prominent vesicles. This upper part of the lava is also oxidized to a dark reddish gray (10R 4/1). Within the lower vesicularity part of the flow, most vesicles are consistently ~1–5 mm, and vesicle shapes become much more irregular. In the interval 183-1138A-83R-5, 112 cm to 83R-6, 25 cm, the vesicles have unusual angular shapes similar to a granophyre texture. In interval 183-1138A-83R-6, 40–53 cm, the vesicles start to become rounder and elongated in a subhorizontal direction. This same region has scattered 1- to 3-cm-diameter indistinct clots with ~25 vol% small (<0.3 mm) vesicles. Below this, the remainder of Unit 11 contains 25% vesicles arranged in irregular 1- to 3-cm domains with 1- to 2-cm dense (1.5% vesicle) rinds (Fig. **F41**). These dense rinds have large numbers (~100/cm²) of <0.5-mm vesicles, whereas the inner parts of the vesicular clots generally have 1- to 4-mm round vesicles (30/cm²).

Unit 12

Unit 12 consists of coherent vesicular aphyric basalt except for the uppermost pieces, which are the breccia at the base of Section 183-1138A-83R-6 (Fig. **F41**). This breccia has 3- to 5-cm equant rounded to subangular clasts with some evidence of welding. The spaces between the clasts are mostly filled with angular fragments of the larger clasts.

F29. Close-up photograph of Sample 183-1138A-81R-3 (Piece 1, 0–25 cm) showing contact between basement Units 6 and 7, **p. 100.**

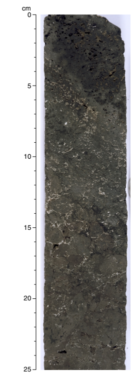

F30. Photomicrograph showing in situ brecciation textures at the margin of a chilled clast, **p. 100.**

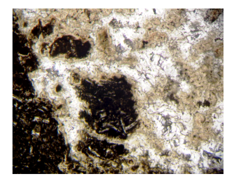

F31. Photomicrograph showing the accumulation of basaltic fragments behind a protrusion in a chilled basaltic clast, **p. 102.**

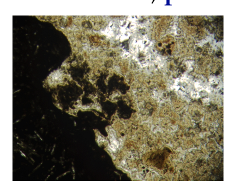

F32. Close-up photograph of Sample 183-1138A-82R-2 (Pieces 7–9, 63–79 cm), **p. 103.**

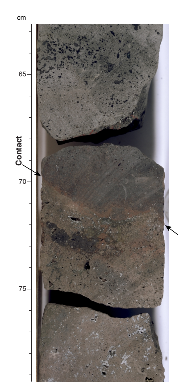

The remainder of Unit 12 is a coherent lava with 20–25 discrete vesicular domains with 5- to 20-cm diameters separated by low vesicularity rinds. Vesicularity varies from domain to domain, ranging from 5% to 40%. Many domains appear "spongy" with small (<<0.5 mm) irregular vesicles (100–180/cm^2). The domains with lower vesicularity have considerably fewer, and somewhat larger (1–0.5 mm) vesicles. Only three domains have vesicles in the 1- to 5-mm size range, but these domains have 10%–25% vesicularity, so vesicle size and vesicularity do not correlate inversely. Macroscopically the rinds between domains appear dense (1%–3% vesicles), but under the binocular microscope we find that this lava contains 30 vol% microscopic (<0.1 mm) vesicles at a density of 750/cm^2. The bottom of Unit 12 is such a (visually) dense rind welded to the oxidized breccia of Unit 13 (Fig. **F42**).

Unit 13

Unit 13 is a breccia-topped sparsely plagioclase-phyric basalt flow. Two irregular pieces of oxidized breccia mark the top of Unit 13. Immediately below this, in the interval 183-1138A-84R-2, 0–26 cm, three oxidized vesicular domains with smooth curved margins are delineated by ~1-cm-wide dark zones with smaller vesicles (Fig. **F43**). These domains contain ~15% very small (≤0.1 mm) round vesicles at a density of ~300/cm^2. A breccia extends from below these domains to Section 183-1138A-84R-3, 137 cm, with the portion of Section 183-1138A-84R-3 below 39 cm filled with fine-grained sediments. The clasts are a mix of ≤40% irregular gnarled aa clasts and ≥60% clasts with a single side with a smooth pahoehoe surface on one margin and fracture surfaces on the other margins. Clast size grades from 2 to 10 cm near the top to 1 to 4 cm from Section 183-1138A-84R-2, 90 cm, downward, and the clasts are generally angular throughout. Clast vesicularity varies from 5% to 15% with most vesicles being ~1 mm in diameter. The pattern of fracturing within some clasts suggest that they were crushed by the overlying clasts. Other clasts show jigsaw-fit margins with alteration minerals filling the gaps. In the upper part of the breccia, open void space makes up ~15% of the recovered core. Interval 183-1138A-84R-3, 24–39 cm, was only recovered as a handful of angular clasts. Within the sediments the clasts appear rounder with a halo of small fragments and alteration minerals. An arm of dense lava (0.5%–3% vesicularity) with small irregular vesicles is present in interval 183-1138A-84R-3, 124 cm, through 84R-4, 18 cm. The recovered margin of this dense lava is disaggregating in the same manner as the dense arm in Unit 9. The vesicles form small discontinuous sheets elongate in the direction parallel to the margin of the arm. The coherent lava in interval 183-1138A-84R-4, 20–30 cm, contains vesicles in which the direction of elongation changes from subhorizontal below to subvertical in the arm. The coherent lava remains somewhat vesicular (2%–15%) until Section 183-1138A-84R-5 at 26 cm. The vesicles have irregular, angular shapes and are distributed in irregular 5- to 20-cm domains. The lava is massive with only 1% vesicularity in interval 183-1138A-84R-4, 26–110 cm, but irregular 3- to 5-cm vesicular pods persist. Below this interval, the lava increases to 2%–5% vesicularity with mesostasis blebs visible in interval 183-1138A-84R-6, 0–11 cm. Vesicularity reaches 10%–20% near the bottom of Unit 13 at interval 183-1138A-84R-6, 12–29 cm. In this interval the vesicles are distributed in 2- to 7-cm-scale domains that become more distinct with depth. Vesicle sizes within these small domains are typically <0.5 mm.

F33. Close-up photograph of Sample 183-1138A-82R-2 (Piece 11, 98–114 cm), **p. 104.**

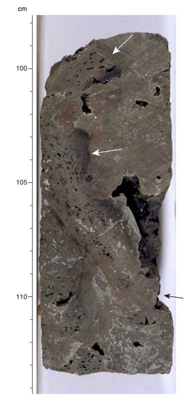

F34. Close-up photograph of Sample 183-1138A-82R-3 (Piece 4, 27–45 cm), **p. 105.**

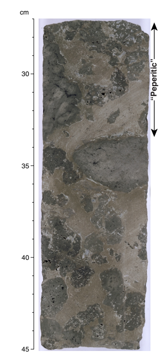

F35. Close-up photograph of Sample 183-1138A-82R-3 (Piece 5, 46–63 cm), **p. 106.**

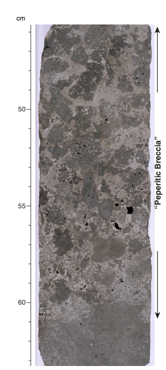

Unit 14

Unit 14 is another breccia-topped aphyric basalt flow. The breccia is heavily altered with rounded clasts and little open void space. Alteration masks many features, but the clasts appear to be 0.3–13 cm in size and subangular to subrounded in shape. The largest piece has a cauliflower-like appearance. From Section 183-1138A-85R-1, 15 cm, downward, the lava is coherent and massive. Vesicles are distributed in 10-cm-scale zones with a few 1- to 2-cm vesicular clots near the top of the massive section. Vesicles are angular in the upper portion and rounder below Section 183-1138A-85R-1 at 121 cm. Thin vesicle trains also appear at this point. These rounder vesicles gradationally develop into discrete 1- to 3-cm vesicular domains with distinct margins visible from about the top of Section 183-1138A-85R-2 (Fig. **F44**).

Unit 15

Unit 15 consists of various pieces of aphyric basalt. The top of Unit 15 consists of various loose pieces of unwelded breccia (Fig. **F44**). These range from 1- to 5-cm angular fragments cemented by alteration minerals to a single 3 cm × 5 cm rounded clast with a fine-grained zone on one side. Coherent lava was recovered from Section 183-1138A-85R-2 at 75 cm, downward. In the upper part of the coherent lava, clots with small vesicles are surrounded by a matrix of lava with larger vesicles. Both populations of vesicles are angular. Below Section 183-1138A-85R-2 at 96 cm, the vesicles become rounder and vesicularity varies on a 10-cm scale. Beneath the coherent lava, Unit 15 consists of a mixture of various lithologies with no clear relationships. Section 183-1138A-85R-3 (Pieces 1–3) appears to be breccia, but is heavily altered, obscuring the original clast morphology. Pieces 4 and 5 from the same section contain an oxidized breccia with a mix of 0.1- to 4-cm angular clasts. Pieces 6 and 8 are an unoxidized coherent lava with 20% moderately spherical 1- to 10-mm-diameter vesicles. Piece 7 consists of a handful of loose 1- to 2.5-cm pebble-sized fragments of mildly oxidized vesicular lava with <1-mm vesicles.

Unit 16

Unit 16 contains the lower part of an aphyric basalt flow. The top of Unit 16 begins with fractured but coherent lava. The first piece contains a 3- to 4-mm-wide vein with clast-rotated pieces in loose grain-to-grain contact. Moving the pieces back together, it is apparent that all the fragments moved downward. The uppermost lava contains 15% round vesicles with 2- to 7-mm diameters with size increasing downward. Below interval 183-1138A-86R-1, 15–51 cm, the vesicularity drops to 2%–3% with angular shapes and 0.1- to 10-mm diameters with vesicles generally elongated in the horizontal direction. Fine sets of fractures filled with alteration minerals give the appearance of discrete 1- to 3-cm clasts, but the lava is coherent. Vesicle patterns pass through these fractures, and there is no evidence for clast rotation. Both alteration and vesicularity increase from Section 183-1138A-86R-1, 52 cm, to the base of Unit 16 (Fig. **F45**). This area may be brecciated, but the alteration is too severe to be sure.

Unit 17

Unit 17 is a breccia-topped aphyric basalt flow. The breccia has angular fragments and 10%–15% open void space (Fig. **F45**). The clasts within the breccia preserve some features that probably exist in the flow-top breccias on other units, but were not as evident. In particular,

F36. Close-up photograph of Sample 183-1138A-82R-3 (Piece 8, 88–116 cm), **p. 107.**

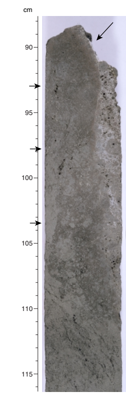

F37. Close-up photograph of Sample 183-1138A-82R-4 (Piece 5B, 137–147 cm), **p. 108.**

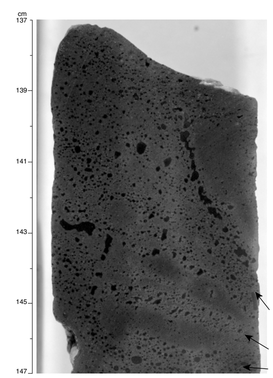

F38. Close-up photograph of Sample 183-1138A-83R-4 (Pieces 6–8, 85–105 cm), **p. 109.**

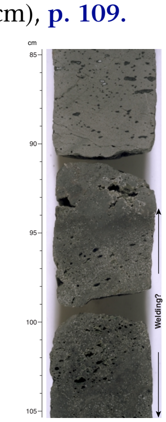

several 1- to 5-cm clasts preserve ropy textures and fine-grained glassy surfaces on one margin of the clast. These glassy surfaces have a 0.5-mm-thick oxidized rim, but the other margins of the clast show no evidence for either chilling or oxidation. A 2 cm × 5 cm clast at interval 183-1138A-86R-1, 86–87 cm, has vesicles elongated parallel to the fold axis of the ropes. The breccia contains a wide variety of lava clasts including those full of small vesicles and very dense lava with only a few large vesicles. However, no evidence was found for aa clasts with their characteristic gnarled shapes. The larger rotated clasts show that more coherent clasts were being pushed into other more fragmented clasts. Clast size generally decreases downward, changing from 1 to 5 cm at interval 183-1138A-86R-1, 10–30 cm, to 1–2 cm at interval 183-1138A-86R-1, 80–90 cm. At about interval 183-1138A-86R-1, 45 cm, the interclast voids are largely filled with 0.1- to 5-mm angular fragments. In the lower part, the breccia has more of this finer material than the larger clasts. The lava abruptly becomes coherent at interval 183-1138A-86R-1, 93 cm, at the top of Piece 13. Down to interval 183-1138A-86R-1, 134 cm, the lava contains 5% irregular angular vesicles 0.1–10 mm in diameter that are elongated in swirling and patchy patterns ~5 cm across. Below this, the vesicularity increases slightly (7%–10%), the vesicles become rounded, and their diameters increase to 0.2–15 mm. Section 183-1138A-86R-2 at 6 cm, the lava becomes more dense with a vesicularity of just 1%–3%. The vesicles remain quite round but are slightly elongated at an inclined direction. Vesicularity slightly increases when the coherent lava and Unit 17 abruptly ends.

Unit 18

Unit 18 is yet another breccia-topped aphyric basalt flow. The breccia is highly altered but appears to have a similar character to that of Unit 17: 1- to 3-cm angular clasts of highly vesicular and dense lava with voids between clasts filled with smaller angular fragments. In Section 183-1138A-86R-3 at 145 cm, massive lava with small (<1 mm) vesicle trains begins. This massive interior is recovered in a number of small pieces, making it difficult to discern larger scale patterns. Vesicularity is irregular on a 1- to 5-cm scale and is generally 3%–7%, but the last three pieces (Section 183-1138A-86R-4 [Pieces 7–9]) are dense, containing <1% vesicles and faint mesostasis blebs.

Unit 19

Unit 19 is a sparsely plagioclase-phyric flow with a breccia top that extends down to Section 183-1138A-87R-1, 138 cm. Although there are many similarities between this breccia and those on Units 17 and 18, there are some interesting differences and some additional features are visible that may be critical in deciphering these breccias. The clasts are all fragments of pahoehoe with no evidence for aa clasts. Clasts are largest at the top (including >10 cm at interval 183-1138A-87R-1, 13–17 cm, with a well-preserved pahoehoe top) but 3- to 4-cm size clasts persist throughout. There is a paucity of the 0.1- to 5-mm smaller angular fragments. Consequently, there is more open void space deep in this breccia. The dense clasts also make up a greater proportion of this breccia (15%–25% vs. ~5% for both Units 17 and 18). Again the dense clasts contain a few large elongated vesicles. However, one of the dense clasts at Section 183-1138A-87R-1 at 93 cm is welded to a vesicular clast (Fig. F46). Other dense clasts have dark clay rims. A small amount of fine-grained green laminated material is found coating the tops of larger clasts. The top of the coherent lava at interval 183-1138A-87R-1, 138

F39. Close-up photograph of Sample 183-1138A-83R-4 (Pieces 8–10, 105–125 cm), p. 110.

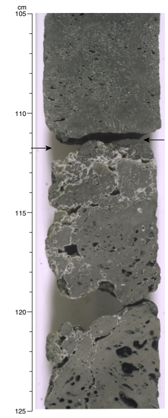

F40. Close-up photograph of Core 183-1138A-83R, p. 111.

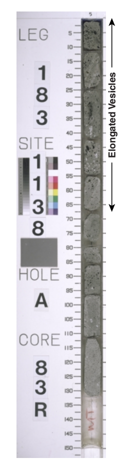

F41. Close-up photograph of Sample 183-1138A-83R-6 (Pieces 6 and 7, 70–90 cm), p. 112.

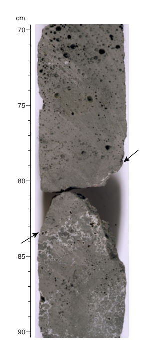

cm, is perfectly recovered and the contact with the breccia can be examined. The top of the coherent lava has 3- to 6-mm-deep open vertical gashes and 0.5- to 1.5-cm-long, 1- to 2-mm amplitude folds. Under the binocular microscope, we see that these folds contain vesicles that have been sheared into <0.1-mm-wide, >1-cm-long tears. The vesicle shapes grade from these extremely elongated shapes to more elliptical shapes over a distance of about 1–2 cm. The top of the coherent lava has a ~0.5-mm dark clay rim. The immediately underlying lava has 1.5% elliptical elongate vesicles 0.1–6 mm in diameter. The following pieces (Section 183-1138A-87R-2 [Pieces 1–7]) contain ~5% elongate vesicles ~1 cm in length with a second population of 0.1- to 2-mm round bubbles. Core 183-1138A-87R-2 (Piece 8) is a breccia with imbricated 3- to 5-cm-long angular clasts (Fig. **F47**). The geometry of the imbrication does not allow for lateral motion of the clasts, and the clasts contain up to 1.5-cm-long elongate vesicles. In the interval below (interval 183-1138A-87R-2, 54–130 cm), the vesicles are round and gradually decrease in size and number downward. At Section 183-1138A-87R-2 at 83 cm the vesicularity is 15%, and the vesicles are 0.3–6 mm in diameter. At Section 183-1138A-87R-2 at 107 cm the vesicularity has dropped to 3%, and vesicles are 0.5–1.5 mm in diameter. Vesicularity increases in Section 183-1138A-87R-2 (Piece 17, 130–134 cm) to 5%, and the vesicles become subangular and larger (1–4 mm). The piece is fractured, but the pieces can be reassembled into a single coherent piece. Section 183-1138A-87R-3 (Piece 1, 0–15 cm) contains coherent lava with 25 vol% elongate subangular vesicles 3–15 mm in diameter. The vesicles are generally elongated in the horizontal direction, but there are some swirling patterns as well. Section 183-1138A-87R-2 (Piece 2) is a handful of loose fragments of vesicular lava. The following piece is clearly a breccia with the black clay rind on two clasts spalling off at the point of contact between the two. The base of Unit 19 is Section 183-1138A-87R-2 (Piece 4), which contains a fine-grained margin fragmenting into a thin veneer of sediments.

Unit 20

Unit 20 is an aphyric basalt flow with several very unusual features. The top of Unit 20 is a coherent vesicular lava with 20 vol% large (~1 cm) irregularly shaped coalescing subangular vesicles. A large fracture running diagonally through interval 183-1138A-88R-1, 48–74 cm, divides lavas of two distinctly different vesicle morphologies (Fig. **F48**). The lava on the footwall of the fracture has a vesicularity of ~5% with generally round vesicles in a bimodal size distribution (≥1 cm and ≤3 mm). Small wispy mesostasis blebs are also visible, paralleling the fracture. The fracture itself has matching undulating surfaces that preclude any significant vertical motion, but examination of the core was not able to rule out purely horizontal motion. Anastomosing dipping sheets of vesicular material are evident in interval 183-1138A-88R-1, 80–90 cm. In interval 183-1138A-88R-1, 90–124 cm, 2- to 7-cm-long and 0.5- to 1-cm-wide curved vesicular domains with a fine-grained groundmass appear (Fig. **F49**). These domains have 20%–40% vesicularity and vesicle sizes are generally <0.5 mm. However, some 3- to 4-cm-long coalescing vesicles mark the margins of the domains. Below this, a handful of lava fragments are present before reaching the coherent and exquisitely preserved base of Unit 20. These fragments are extremely vesicular with >35%–40% highly irregular 0.5- to 5-mm-sized vesicles. The base of Unit 20 contains a bulbous cavity with many curious features (see Fig.

F42. Close-up photograph of Sample 183-1138A-84R-1 (Pieces 6 and 7, 120–135 cm), **p. 113.**

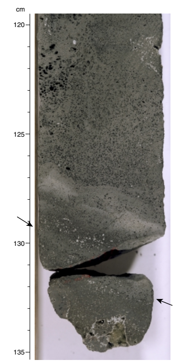

F43. Close-up photograph of Sample 183-1138A-84R-2 (Piece 1, 0–20 cm), **p. 114.**

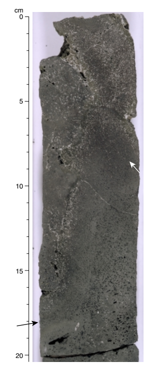

F44. Close-up photograph of Sample 183-1138A-85R-2 (Pieces 1–3, 25–45 cm), **p. 115.**

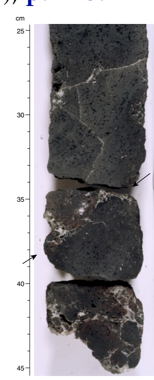

F50). In three dimensions, it is clear that this bulbous cavity is marginal to a much larger cavity.

Unit 21

Unit 21 is a breccia-topped aphyric basalt flow. The uppermost few centimeters of Unit 21 are a smooth pahoehoe surface that has been highly fractured. This is followed by a breccia exhibiting a wide range of curious features. In interval 183-1138A-88R-2, 0–30 cm, the breccia is composed of at least seven originally >5-cm clasts that have been broken into 1- to 3-cm angular fragments that can be fit to reconstruct the original clasts. One of these clasts is recognizable as a >8-cm-diameter pahoehoe lobe with a 3-mm-thick glassy rind. The lobe has 20%–30% vesicularity, with slightly elongated <0.5-mm-diameter vesicles. The vesicle sizes become slightly smaller toward the margins. In interval 183-1138A-88R-2, 33–45 cm, a >12-cm dense (7% vesicularity) lobe with 0.5- to 1.5-cm elongate angular vesicles is present (Fig. F51). The top of this lobe has an irregular fluidal arm that the elongated vesicles fan into. There is no evidence of baking or welding of this clast to the surrounding clasts. However, a clast at interval 183-1138A-88R-2, 50–60 cm, does have a welded margin on one side (Fig. F52). Another margin of this same clast is glassy and fragmented, and a third margin has a fluidal shape with small angular fragments filling the void underneath. We find a clast at interval 183-1138A-88R-2, 74–75 cm, that is molded around another clast and has formed a welded and chilled margin. In general, fragmentation decreases with depth in this breccia. However, recovery of the breccia is poor at the base of Core 183-1138A-88R with several ≤10-cm pieces alternating between small fragments and coherent vesicular lava. The breccia continues in the top of Core 183-1138A-89R, but with a large zone of dense lava running up one side of the core (right side of the archive half) from interval 183-1138A-89R-1, 9–53 cm. This dense lava has a set of dipping joints that open in a fanning fashion on the opposite side of the core. This lava contains 3% irregular vesicles <1 mm in diameter. Between 53 and 58 cm, Section 183-1138A-89R-1 has only breccia, mostly composed of fragments of the dense lava. In interval 183-1138A-89R-1, 58–62 cm, the dense lava returns and has a square 3 cm × 4 cm vesicular clast in the center with a chill margin surrounding it. The pieces below this appear to be 5- to 10-cm clumps with 15%–20% vesicularity with ≤1-mm spherical vesicles surrounded by a matrix of lava with 10%–15% vesicularity with 0.5- to 5-mm round vesicles. From here, recovery drops and isolated pieces were recovered. Section 183-1138A-89R-1 (Piece 5) has 15% irregular, >1-cm angular vesicles. Piece 6 from the same section has 5% angular, <1-mm vesicles. Piece 7 is the bottom of Unit 21 and consists of a handful of highly vesicular pebble-sized fragments with 20%–30% round, ~1-mm vesicles.

Unit 22

Unit 22 is the final flow drilled at Site 1138 and is another breccia-topped aphyric basalt flow with some unique features. Parts of the breccia are composed of ~3-cm clasts surrounded by smaller angular fragments, much like the other breccias, but large portions are composed of intact pahoehoe lobes. In interval 183-1138A-89R-2, 0–19 cm, a lobe with 15% irregular but rounded 1- to 10-mm vesicles has partially enveloped and chilled against another lobe with ~40% small (<1 mm) vesicles. Interval 183-1138A-88R-2, 26–40 cm, contains the edge of a lobe with a near-circular cross section. This lobe is fractured in both radial

F45. Close-up photograph of Sample 183-1138A-86R-1 (Pieces 3 and 4, 60–80 cm), p. 116.

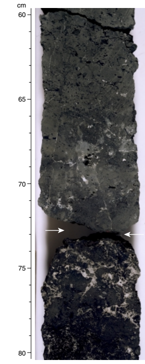

F46. Close-up photograph of Sample 183-1138A-87R-1 (Piece 11, 89–98 cm), p. 117.

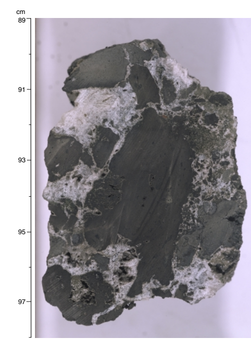

F47. Close-up photograph of Sample 183-1138A-87R-2 (Pieces 7–9, 40–57 cm), p. 118.

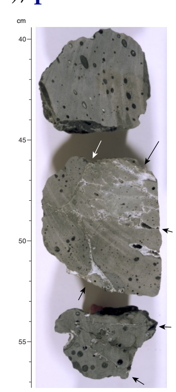

and concentric directions and contains 25% round, ~1-mm vesicles. Interval 183-1138A-88R-2, 43–53 cm, contains a single coherent lobe with a fragmented upper margin. Section 183-1138A-88R-2 (Piece 4, 53–80 cm) has a lobe that partially enveloped and is quenched against another lobe. Below, the lava appears to be coherent with 10% rounded, occasionally elongated, 2- to 3-mm vesicles. A 3-cm clast with the surrounding lava chilled against it is present in Section 183-1138A-88R-2 at 100 cm. Below this, the lava contains 2%–5%, subrounded, 0.5- to 3-cm vesicles elongated in a generally horizontal direction.

Interpretation

Lithologic Units

Unit I: Foraminifer-Bearing Diatom Ooze

The unconsolidated upper part of this interval was disturbed during coring. The sediments are variable mixtures of clay and pelagic material. The disseminated volcaniclastic components indicate contributions from primary felsic and mafic pyroclastic fall deposits as well as a reworked lithic fraction (Table **T10**).

Units I, II and III: Pyroclastic Fall Deposits

Intervals with a concentration of volcanic ash material (Tables **T10, T11**) have been divided into (1) disseminated felsic glass and pumice in Cores 183-1138A-1R to 10R (<3.8 Ma), (2) felsic (trachytic?) tephra material in Core 183-1138A-11R (~3.8–3.2 Ma), (3) a suite of mixed (basalt + trachyte?) tephras in Cores 183-1138A-14R to 17R (10.6–8.9 Ma), and (4) a concentration of basaltic ash in Cores 183-1136A-30R to 34R (~31–26.5 Ma).

Previous work on Legs 119 and 120 (Bitschene et al., 1992) identified tephra layers preserved in similar age intervals to those at Site 1138 (Tables **T10, T11**). In Hole 120-736A, volcanic components with ages of 0.4, 0.7, and 0.8 Ma were recognized. Ash of these ages fall within the zone of disturbance during coring at Site 1138 (see [1] above), so correlation is not possible. However, at Site 736, a 2.8-Ma trachytic debris flow was identified. This age may correspond with feldspar-bearing pumiceous ash found in Core 183-1138A-8R.

Site 120-747 lies 150 km south-southeast of, and is the closest hole to, Site 1138 (Fig. **F1**), so ash horizons may be correlated with some confidence. Felsic ash with ages of 3.7, 3.8, and 4.3 Ma was recovered at Site 119-737, which indicates considerable activity in the region at the time that the ~3.8- to 3.2-Ma basaltic to bimodal ash (see [2] above) (Core 183-1138A-11R) was deposited. Volcanic material described as mixed basaltic and trachytic ash in Hole 119-737B does not have an equivalent at Site 1138, but we observe ~6.4–5.6 Ma trachytic ash in Core 183-1138A-12R and a ~10.6–8.9 Ma basaltic to bimodal interval in Cores 183-1138A-14R and 15R (see [3] above). These ages bracket the Hole 120-737B 7.8-Ma age and may or may not be related. Site 737 is north of Heard Island and close to the Kerguelen Archipelago, so it may be more strongly influenced by proximal volcanism. An older series of mafic volcanic events (28.3 Ma, 31.4 Ma, and 32 Ma) at Site 737 has the same age range (31–26.5 Ma) as basaltic ash in Core 183-1138A-30R to 34R (see [4] above). Two trachytic ash layers (2.2 Ma and 4.3 Ma) in Hole 120-745B on the Southern Kerguelen Plateau do not have equivalents at Site 1138.

Late Pliocene (3.7 Ma and 3.8 Ma) trachytic ashes and early Oligocene (30 Ma) basaltic ashes in Hole 120-747A correlate well with sim-

F48. Close-up photograph of interval 183-1138A-88R-1, 0–100 cm, **p. 119.**

F49. Close-up photograph of Sample 183-1138A-88R-1 (Piece 7, 91–102 cm), **p. 120.**

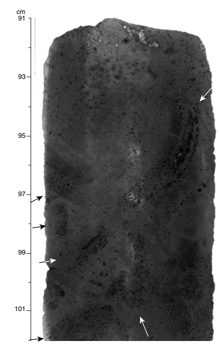

F50. Close-up photograph of Sample 183-1138A-88R-1 (Piece 10, 130–141 cm), **p. 121.**

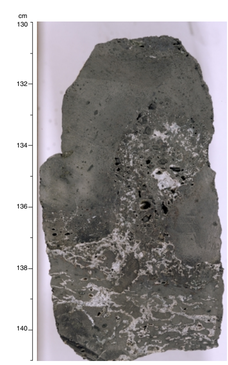

F51. Close-up photograph of Sample 183-1138A-88R-2 (Piece 2, 30–40 cm), **p. 122.**

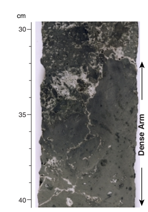

ilar age intervals at Site 1138 (see [2] and [4] above). However, Cretaceous to Paleocene volcanic material observed in Hole 120-747A was not found at Site 1138.

Basement Units

Unit 1: Aphyric Flow-Banded Dacite Cobbles

Unit 1 consists almost entirely of rounded, aphyric, flow banded dacite (see **"Igneous Petrology,"** p. 46). These cobbles represent a layer of dacitic rubble at the top of basement. Flow banding and the fine-grained internal texture suggest that they are eroded from a lava or a densely welded tuff. Dacitic lava is not preserved elsewhere in the basement succession cored at Site 1138.

Unit 2: Bedded Pumice Lithic Breccia, Lithic Breccia, Ash-Fall Deposits, and Volcanic Clay

Unit 2 is dominated by pumice lithic breccias together with reworked volcaniclastic sediments and altered pyroclastic fall deposits. Subunit 2A is an interval of dark gray massive clay and lithified fine-grained altered rock that does not appear to be related to the underlying volcaniclastic succession and may be rubble that has fallen downhole.

Subunit 2B is a reworked succession of alternating pumiceous and lithic-rich beds, each a few centimeters thick, which show a variety of grainsizes, sorting, and grading features (Figs. **F18, F19**). These intervals are interpreted as water-settled deposits and low-angle, clast- to matrix-supported flow deposits. The reworked materials have identical textures, range of clast types, and alteration features to the underlying pumice and lithic breccia deposits. They have probably been reworked in a low- to moderate-energy shallow-water environment. The degree of alteration of different sedimentary packages in the succession varies considerably, which relates to the porosity and permeability of the intervals. Generally, more pumiceous intervals are pale green and clay-rich, reflecting more intense alteration.

Overall, Unit 2 is dominated by pumice-lithic breccias (Subunits 2D, 2G, 2H, 2I, and 2J) (Fig. **F14**) and a lithic breccia (Subunit 2E) (Fig. **F15**). These breccias exhibit good hydraulic sorting and could be primary subaerial pyroclastic flow deposits. One of the breccias (Subunit 2E) is considerably more lithic rich than the others and is interpreted to either be the basal part of a thick flow, or may be more proximal to the source. Internally, the flow units show limited stratification, and contacts with overlying flow units are usually sharp. Subhorizontal alignment of elongate pumice clasts may be related to flow alignment during emplacement or load alignment after emplacement, but there is no evidence of welding. Clasts are variably altered, but generally the pumice is pale green and soft, indicating partial replacement by clay minerals (Fig. **F16**). In more indurated parts of the profile, relatively fresh pumice can be observed in thin section. Commonly, lithic fragments are less altered than pumice clasts. The matrix in all flow units is dominated by medium to very coarse sand–sized fragmented pumice material (Fig. **F17**).

The Subunit 2K lithic breccia is reverse graded and has clasts that are similar to the lithic component in the pumice lithic breccias. This interval may be the basal layer of the overlying pyroclastic flow (Subunit 2J) and shows reverse grading because of tractional processes at the base of the flow.

F52. Close-up photograph of Sample 183-1138A-88R-2 (Piece 4, 53–73 cm), **p. 123.**

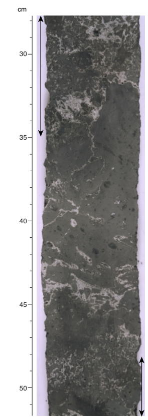

Two intensely weathered intervals (Subunits 2C and 2N) (Figs. F20, F21) retain little evidence of primary features. These may have been zones of enhanced fluid percolation, or were exposed at the land surface for some time to become so intensely altered. Both have evidence of clay pseudomorphs after pumice. One interpretation is that these are pumice fall deposits.

Accretionary lapilli were found in two places in the stratigraphy (Subunits 2F and 2L) within normally graded medium to fine ash deposits (Figs. F22, F23, F24). These are pyroclastic fall deposits, and the presence of accretionary lapilli indicates interaction with water in the eruption cloud. Two other highly altered volcanic clay intervals (Subunits 2M and 2O) (Fig. F25) may also be fine-grained volcanic ash deposits, but the presence of scattered lithic fragments in these deposits suggests they have been reworked.

Unit 2/Unit 3 Boundary

The appearance of basalt marks the boundary between Units 2 and 3. However, it is unusual to find relatively unaltered, unoxidized lava at the top of the lava sequence. This suggests an erosional unconformity or that we did not recover any altered material from the top of the lava pile.

Unit 3: Transitional (Slab-Pahoehoe?) Lava Flow

The first rocks from Unit 3 that we recovered have vesicularity consistent with being the lowermost part of the vesicular upper crust. The bulk of Unit 3 that was recovered is from the massive interior of a flow. Although the round vesicles in the upper part of the flow are consistent with pahoehoe, the elongated subangular shapes further down are unusual and suggest motion and shearing of a highly viscous, partly crystallized lava. The formation of megavesicles, but no sheets of segregated material, also suggests a lack of complete stagnation before crystallization. A large number of small vesicles in the lower chill zone suggests a near-vent location. With time and distance from the vent, bubbles will coalesce, forming larger vesicles. The angular breccia at the base of the flow suggests that Unit 3 might have been emplaced as a slab pahoehoe flow.

Slab pahoehoe flows are usually characterized by relatively rapid motion of relatively fluid lava. They are particularly common in steeper areas (3°–10° slopes) or where the lava has surged, breaking up the earlier more coherent top. In Hawaii, they are commonly emplaced as 10- to 100-m-wide sheets but can also form along the sides of channeled flows.

Unit 3/Unit 4 Boundary

A highly altered breccia makes a visually clear break between Units 3 and 4. However, there really is no definitive evidence that this altered material is not a basal breccia for Unit 3. The high alteration probably results from the extreme permeability of the breccia, but it is surprising that there is no obvious gradation from the more fresh rock into this clay-rich zone. We suspect that the partially altered, but less clay-cemented rocks were not recovered. Also, the high degree of alteration might suggest a significant time break between Units 3 and 4, but it is likely that much (if not all) of the alteration followed emplacement of Unit 3. It is therefore possible that Units 3 and 4 are simply different flows from the same eruption.

Unit 4: Aa Flow

On the basis of vesicle shapes (Fig. F26) and the suggestion of irregular clasts within the clay-rich material, it is likely that Unit 4 is a typical aa flow. The various vesicular clots and patchy zones are interpreted to be entrained clasts (Fig. F27), diagnostic of a disrupted flow top, but not necessarily an aa flow. The apparently higher vesicularity of the flow interior as compared to the upper and lowermost parts suggests that the vesiculation during crystallization was trapped in place. Also, lack of complete degassing of an aa flow suggests that the lava was not transported a great distance. The lack of vesicle sheets and similar features indicates that major segregation of late-stage vesicle-rich material did not happen, though a few 1- to 3-cm megavesicles were able to coalesce. The lowermost vesicular zone is interpreted to be a lower vesicular crust. In a typical aa flow, we would expect a substantial basal breccia below the massive interior, but no basal breccia was recovered with Unit 4.

Aa flows are most common where relatively viscous lava is subjected to high-strain rates. This can result from high eruption rates, steeper slopes, or topographic channeling. The longest aa flow known is the ~50-km-long 1859 Mauna Loa flow, so it is unlikely that this aa flow traveled more than a few tens of kilometers from its vent.

Unit 4/Unit 5 Boundary

The dark gray altered breccia underneath a coherent lava makes another visually obvious boundary. However, it is possible that this breccia is the basal portion of Unit 4. The most likely scenario is that Unit 4 had a basal breccia and Unit 5 had a brecciated top. However, given that no pieces showing the relationship between the altered breccia and the coherent lavas above and below were recovered, it was deemed simplest to place the unit boundary at the visually obvious location. Given the equivocal nature of this boundary, we are not confident in interpreting a major time break at this location.

Unit 5: Aa(?) Flow

The vesicular clots within the interior of Unit 5 indicate that it was entraining vesicular material, presumably from a disrupted brecciated flow top. The fining-upward sequence in vesicle size within the coherent lava can be explained by a reduction in the rate of crust growth with time, allowing vesicles to coalesce to a greater degree as they were trapped at the base of the upper crust. The elongated, irregular vesicle shapes are consistent with these vesicles forming in a shearing mush zone at the base of a crust while vigorous active flow persisted underneath. The sudden transition to rounder bubbles could indicate stagnation of the flow. The formation of mesostasis blebs and a megavesicle horizon are also consistent with the deeper interior of the flow crystallizing under more stagnant conditions. The loose pieces at the base of the flow could be from a basal chill zone. Given that it is not clear that the breccia at the top of Unit 5 belongs to the coherent lava from Unit 5 and the evidence for relatively fluid stagnant lava in the interior of the flow, we cannot confidently conclude that this is an aa flow. A slab pahoehoe or other type of transitional flow would also be consistent with the observations.

Irrespective of whether the flow is aa or a transitional lava flow, the observed morphology is strongly indicative of relatively fluid lava subjected to high strain rates. High flow rates through a confined area or higher slopes are the most common cause for high strain rates in a lava flow.

Unit 5/Unit 6 Boundary

The oxidized and slightly brecciated pahoehoe top is a clear visual break and is the first reasonably strong evidence for a significant hiatus in lava flow emplacement at Site 1138 (Fig. **F28**). However, the oxidized zone is quite thin and the flow top is not highly modified, suggesting a short time interval between the emplacement of Unit 6 and the arrival of Unit 5.

Unit 6: Inflated Pahoehoe Flow

Unit 6 has the features of an inflated pahoehoe flow. The top and bottom have smooth, undisrupted pahoehoe surfaces and fine-grained chills. The vesicle distribution changes from a vesicular flow top to a dense interior and back to a vesicular base, exactly as in the idealized models (see Fig. **F9,** p. 70, in the "Explanatory Notes" chapter). The lack of evidence for extensive pooling of segregated material at the base of the upper crust suggests that this was a relatively thin inflated flow, probably of typical Hawaiian dimensions (3–5 m thick). The steep angle of the basal chill of Unit 6 indicates that the flow moved over local topography on the order of tens of centimeters. The possible internal chill zone at the section break could indicate that this pahoehoe flow was compound, with smaller lobes at the base overrun by the lobe that was able to inflate to a few meters thickness. In Hawaii, these relatively thin inflated pahoehoe flows are commonly found on slopes of 0.5°–4°.

Unit 6/Unit 7 Boundary

The contact between the relatively unoxidized pahoehoe lobe and the more oxidized underlying breccia is evident (Fig. **F29**) and indicates both a significant time break and a change in the style of eruptive activity. Also, fragmentation at the base of Unit 6 might suggest some quenching against a small amount of water. Alternatively, it could result from concentrated alteration from the fluids passing through the permeable breccia underneath. The rounding of the upper clasts in the breccia suggests some reworking by perhaps fluvial processes, again implying an extended time break between Units 6 and 7.

Unit 7: Aa(?) Flow

Isolated domains in the breccia at the top of Unit 7 show chill features and in situ brecciation textures (Fig. **F30**) that might be consistent with quenching of magma in water-saturated sediment (peperite). However, the upper part of the breccia with rounded clasts, many with only partially preserved chill margins, looks more like a volcaniclastic conglomerate. It is likely that the locally peperitic textures are an artifact of the reworking and partial sediment infilling of this flow-top breccia.

The shapes of the vesicles in the clasts and the coherent interior suggests that this flow was originally an aa flow. Angular protrusions on the aa clasts are readily broken by erosion and reworking processes. There is evidence of localized transport of glassy material within the sediment (Fig. **F31**), and rounding of clasts in the upper part of the profile implies more intense reworking near the top of the interval. The remainder of the structures within the coherent lava are consistent with a relatively thick aa flow that entrained clasts during emplacement and whose deep interior was able to undergo a small amount of segregation of late-stage liquids. This segregation might also suggest that the lava was more fluid than typical aa and that the flow was more similar to slab pahoehoe than aa.

Unit 7/Unit 8 Boundary

The contact between Units 7 and 8 was not recovered. The last recovered pieces in Core 183-1138A-81R appear to be from deep in the interior of Unit 7. The first recovered rocks in Core 183-1138A-82R are highly altered breccia that grades into coherent lava. Given the rounded clasts, slight oxidation, and sediment fill in the top of Unit 8, it is likely that Units 7 and 8 are distinct lava flows and that some time passed between their emplacement.

Unit 8: Aa(?) Flow

The similarities between Units 7 and 8 are rather striking and it is likely that they formed in similar manners. Thus, the relatively well-recovered base of Unit 8 might also provide information about the unrecovered basal portion of Unit 7. The patches of vesicular material at the base of Unit 8 are probably welded clasts of a basal breccia. Such a basal breccia would be rapidly covered by the bulk of the flow and would not be able to cool effectively. Although the weight of the overlying lava would help to meld the individual clasts into a coherent mass, the basal breccias of aa flows are commonly not welded. This suggests that Unit 8 (and presumably Unit 7) might have been more akin to slab pahoehoe where the disrupted clast is more fluid and plastic than typical aa clinker. It is also possible that the breccia clasts are actually spatter and were recovered extremely close to the vent. The presence of welding is strong evidence that the base of Unit 8 did not significantly interact with water or wet sediments.

Unit 8/Unit 9 Boundary

The change from the highly altered and welded breccia at the base of Unit 8 to the unwelded, moderately oxidized breccia of Unit 9 is a clear boundary (Fig. F32). The breccia on top of Unit 9 is only partially filled with sediments and is not highly oxidized, eroded, or weathered. This suggests that the time break between Units 8 and 9 was not very large.

Unit 9

The slabs of ropy pahoehoe (Fig. F33) and other pahoehoe fragments leave no question that flow was primarily emplaced as a slab pahoehoe. The prominent slab and many other pieces show one strongly quenched margin that cooled at the surface of the flow while the other sides cooled more slowly within the breccia. This is consistent with the clasts being slab pahoehoe that was actively disrupted from within by the flowing lava. The zone that has a mix of sediment and loose pieces of lava has the appearance of a peperite (Figs. F34, F35), but the absence of chill margins surrounding the clasts suggests that the sediments may have been deposited well after the lava flow had been emplaced. The material could be a slurry of fine-grained sediments (perhaps dominated by silt-sand sized glass shards from the flow breccia itself) and 1- to 2-cm vesicular lava clasts that flowed into a large open cavity in the breccia. The shapes of the voids at the bases of larger clasts also suggest that the sediments flowed in as a viscous slurry. However, these cavities might also have formed by trapped steam from water being driven off of the wet sediments by hot lava. Despite the appearance of this small portion of the breccia, the evidence for interaction between wet sediments and hot lava is equivocal, at best. The disaggregating dense zone (Fig. F36) has the appearance of a dense arm of aa-like lava pushing up into a breccia. This kind of disaggregation is identical in degree and morphology to that caused by subaerial chilling of microlite-rich lava in aa flows (see **"Interpretation,"** p. 19, in the "Explanatory Notes" chapter). The transition from irregular vesicle shapes to more spherical ones suggests a sudden cessation of shearing while the interior of the lava was still relatively fluid. This is supported by the presence of what appears to be a complicated set of sheets of segregated material at this boundary (Fig. **F37**). The increase in vesicularity at the base of the flow suggests that the last recovered rocks were from near the base of the flow, although a basal breccia might also have existed.

Unit 9/Unit 10 Boundary

The pebbles found at the top of Core 183-1138A-83R have been placed in Unit 9 but are likely to have fallen into the hole from anywhere above Unit 10. No contact between Units 9 and 10 was retrieved, but the change from the coherent lava interior of Unit 9 to the breccia of Unit 10 is a clear boundary. What is not as clear is whether any of the Unit 10 breccia might be part of a basal breccia for Unit 9. The minimal oxidation, only partial infilling of Unit 10 breccia with sediments, and limited erosion and weathering of the Unit 10 breccia suggest that a relatively short time passed between the emplacement of Units 10 and 9.

Unit 10: Transitional Flow

In many respects, the interpretation of Unit 10 is similar to that of Units 7–9. Whereas the breccia originally formed during emplacement of the flow, it was probably modified to some extent by sedimentary processes, including the deposition of sediments that filled the lower part of the breccia. The chill at the top of the coherent lava and the disaggregating dense arm both suggest that the flow top-breccia was quite cold near the end of the emplacement of Unit 10. The entrained clast within the top of the coherent lava indicates active mixing between the disrupted crust and coherent interior of the flow during emplacement. The irregular vesicles in the upper part of the flow indicate substantial shearing of a relatively viscous lava early in the emplacement history. The rounder vesicles below a megavesicle horizon and the formation of a sheet of segregated material and a dense interior suggest a more quiescent emplacement of relatively fluid lava before the flow stagnated. The irregular vesicular pods at the base of Unit 10 (Fig. **F38**) are partially welded clasts of a basal breccia. The subhorizontal shape of many of these suggests some flattening by the weight of the overlying lava. This suggests that the leading elements of Unit 10 were hot and plastic and not a cold aa-like breccia, implying that Unit 10 was again more similar to a slab-pahoehoe flow than an aa flow. Alternatively, the welded basal breccia could be welded spatter from a nearby vent.

Unit 10/Unit 11 Boundary

The change from a welded breccia to an oxidized coherent vesicular flow forms a clear boundary (Fig. **F39**). The contact between the two units may be the glassy chill pressed into the top of the 2 cm of vesicular breccia at the top of Unit 11. These two angular fragments could easily be the loose top of a slightly weathered pahoehoe flow top. Such surfaces are very common on Hawaiian pahoehoe flows that are several decades to a few hundred years old. This and the oxidation of Unit 11 suggest a significant time break between Units 10 and 11.

Unit 11: Transitional Flow

The large elongate vesicles in the top and bottom of Unit 11 seem to require that the lava was viscous enough to keep nonspherical shapes while being fluid enough to flow in a very laminar and plastic fashion. This is not typical of either pahoehoe or aa flows, but smaller elongate bubbles are common in pahoehoe flows. The irregularly shaped vesicles in the interior of the flow are somewhat similar to vesicles found in aa flows. The 1- to 3-cm vesicular clots could be welded breccia clasts or spatter. The high density of small vesicles strongly suggests a near-vent facies, making it likely that the clasts were originally pieces of spatter, not breccia. This requires proximity of the fountain or fissure vent, probably within a few tens to hundreds of meters.

Unit 11/Unit 12 Boundary

The break between Units 11 and 12 is defined by a single piece of slightly welded breccia (Fig. **F41**). However, the change from a relatively thick coherent flow with large vesicles to a mass of small lobes is visually obvious and a volcanologically important distinction.

Unit 12: Compound Pahoehoe Flow

The vesicular domains in Unit 12 are interpreted to be spongy pahoehoe lobes (S-type pahoehoe of Walker, 1989) that were welded together to produce a coherent rock. This level of welding requires very rapid accumulation and is most common very close to a lava source. Although the source of lava might be the eruptive vent, it can also be an overflowing skylight (also known as ephemeral vents or boccas) or an open lava channel. However, the very high density of extremely small vesicles trapped in the margins of the lobes strongly suggests that we are close to the primary vent. Based on examples in Hawaii, the eruptive vent is unlikely to be more than a few kilometers from Hole 1138A.

Unit 12/Unit 13 Boundary

The change from a welded stack of spongy pahoehoe lobes to an oxidized breccia is a clear break (Fig. **F42**). Whereas oxidation can form very quickly in a near-vent environment, the partial sediment infilling of the Unit 13 breccia suggests that this boundary reflects a significant time break. However, the angular clasts at the top of the breccia (which the Unit 12 lobes flowed onto) suggest quite minimal erosion and weathering.

Unit 13: Transitional (Aa?) Flow

The mix of aa and pahoehoe clasts suggests that this flow was sampled at a point shortly after it had made the transition from pahoehoe to aa. The vesicular domains at the top of Core 183-1138A-84R-2 (Fig. **F43**) are interpreted to be large folded pieces of pahoehoe, of the sort that typically forms on open lava channels where the lava is subjected to high shear but is too fluid to form aa or even slab pahoehoe. Pieces of such pahoehoe can be rafted many kilometers on the top of an aa flow. The pahoehoe pieces that have been dragged into the deeper parts of the breccia are rapidly broken into the smaller angular clasts such as those observed in the Unit 13 breccia. It is interesting that alteration-driven rounding of the clasts is more prevalent in the sediment-filled part of the breccia. Also, the loose pieces of recovered breccia suggest that zones with large void spaces can be found deep within this kind of breccia. The dense arm of lava pushing into the breccia from the flow interior is strong evidence of aa-like emplacement. The base of the flow appears to have incorporated and welded clasts (or possibly spatter), with the degree of welding decreasing downward. If the clasts are indeed spatter, they imply proximity to the vent.

Unit 13/Unit 14 Boundary

The highly altered breccia beneath the relatively unaltered welded breccia of Unit 13 is a clear visual marker. However, it is not clear if this alteration indicates a significant time break.

Unit 14: Transitional(?) Lava Flow

Given the alteration and relatively poor recovery of Unit 14, detailed interpretations are difficult. However, it appears generally similar to the other units with brecciated flow tops and is likely to be an aa or slab pahoehoe flow.

Unit 14/Unit 15 Boundary

The change from the welded base of Unit 14 to the oxidized, unwelded breccia at the top of Unit 15 is a clear change (Fig. **F44**) and is likely to signify some time break. However, given the poor recovery of Unit 15, it is not possible to rule out the possibility that some of Unit 15 might be unwelded basal breccia from the flow comprising Unit 14.

Unit 15: Transitional(?) Lava Flow(s)

The few pieces of breccia at the top of Unit 15 appear generally similar to the breccias found farther up the hole. The lone clast with a chilled margin might be from the top of a pahoehoe lobe or just be a clast within the breccia. Although it is clear that Unit 15 contains a change from breccia to coherent vesicular lava, what happens below the coherent lava is unclear. The loose pieces are too large to have been brought out of the hole in the wrong order, so it is likely that there are several dense and brecciated horizons within the lower part of what we have called Unit 15. These might be pieces of breccia from the base of the Unit 15 lava flow, parts of an entirely different lava flow, or some pieces from the top of the breccia on Unit 16.

Unit 15/Unit 16 Boundary

This boundary is completely arbitrary and reflects the return to better recovery where we can actually distinguish some internal features of the lava flows.

Unit 16: Lava Flow (Type Unknown)

The recovered rocks from Unit 16 are from the interior of a lava flow. It is reasonable to suppose that some of Unit 15 represents material from the top of Unit 16. Given the limited amount of lava recovered and the high degree of alteration and fracturing, it is hard to make any interpretation of this flow. It is possible that the poor recovery and the high alteration of this unit are related to the highly fractured nature of the lava.

Unit 16/Unit 17 Boundary

The change from the interior of a lava flow to a breccia is a clear boundary (Fig. **F45**). However, given the alteration and poor recovery, it is not possible to determine if this boundary indicates a significant time break.

Unit 17: Transitional Lava Flow (Unnamed Type)

Although the breccia on Unit 17 shares many features common to breccias higher up in Hole 1138A, two characteristics stand out. First is the lack of any evidence of aa-like irregular shaped clasts. Second is the appearance of 1- to 5-cm angular clasts of dense lava. Previously, the dense lava has been in the form of large coherent arms reaching into the breccia. The clasts within the breccia of Unit 17 seem to be derived from both the upper and the central parts of the pahoehoe flows. The simplest explanation is that this breccia is a redeposited eroded pahoehoe flow, but it is difficult to reconcile this with the lack of evidence for significant weathering, rounding, or sorting of the clasts. Our favored, but speculative, interpretation is that this is a pahoehoe flow brecciated by remobilization (see **"Physical Volcanology,"** p. 16, in the "Explanatory Notes" chapter).

Unit 17/Unit 18 Boundary

The change from the interior of a flow to a breccia is a clear boundary. However, the contact was not retrieved and the breccia at the top of Unit 18 is heavily altered, so it is not possible to determine any relationship between the two flows. If the breccias result from erosion and redeposition, this implies a major time break. However, if the breccias are primary, there is no reason to suppose that these two units were not closely spaced in time and could possibly be from the same eruption.

Unit 18: Transitional(?) Lava Flow

Given the poor recovery and altered state of Unit 18, we can only suggest that it is similar to Unit 17. Mesostasis blebs suggest only limited segregation of late-stage liquids inside these flows.

Unit 18/Unit 19 Boundary

The change from the coherent interior of Unit 18 to the breccia of Unit 19 is a clear boundary. However, no contact was recovered, making it difficult to interpret this change. The boundary separates two packages of lava that may be separate flows or two lobes of a single compound flow.

Unit 19: Transitional Lava Flow (Unnamed Type)

The excellent recovery of key parts of Unit 19 sheds light on the formation of the breccias on Units 17, 18, and 19. Of greatest importance is the observation that the dense lava is (in at least one case) welded to vesicular pieces (Fig. **F46**). This requires hot lava from the interior of a flow to have mingled with a solidified vesicular pahoehoe crust. The dark clay rims (which we interpret to have been glassy chill margins) on the other dense clasts supports this idea and indicates that at least part of the solid crust was cold relative to the solidus of the lava. The tearing and intense stretching of the top of the coherent lava is the final proof that the liquid interior of the flow was moving against the breccia. This allows us to rule out resedimentation for the primary mechanism for the formation of the breccia on at least Unit 19. Both the reactivated pahoehoe and hyaloclastite models are viable, but there are no observations diagnostic of water quenching. The various loose pieces in Section 183-1138A-87R-3 are difficult to place, much less interpret. It does appear that the coherent part of Unit 19 has elongated vesicles at its top and bottom and more rounded vesicles in the center. Also, somewhere between the coherent interiors of Units 19 and 20 there is a breccia where some clasts interacted with at least a thin (≤1 cm) layer of sediments.

Unit 19/Unit 20 Boundary

The location of the boundary between Units 19 and 20 is arbitrary and primarily reflects the return to more complete recovery. As noted above, a number of enigmatic pieces are placed at the base of Unit 19, including a breccia and some altered glass that could be related to nearby explosive activity.

Unit 20: Spiracle(?)

The unusual features within Unit 20 are not consistent with aa, pahoehoe, or transitional lava flows. The only scenario we have been able to construct that is consistent with all the observations is that we have recovered the side of a spiracle, a feature formed by the escape of steam from beneath a lava flow. The formation of spiracles and rootless cones requires at least groundwater or very wet sediments. The flow would also have to be emplaced rapidly in order to cover the wet ground before the steam could escape along the margins of the flow. The lack of sediments at the base of Unit 20 requires the underlying flow to have been water saturated.

Unit 20/Unit 21 Boundary

The chill margin between Units 20 and 21 and the change from coherent lava to a breccia make a clear boundary. If Unit 20 does include a spiracle, then time was sufficient between the emplacement of the two units for Unit 21 to cool and become saturated with water. The smooth pahoehoe surface immediately below Unit 20 is likely to be the surface of a pahoehoe lobe in the breccia of Unit 21.

Unit 21: Transitional Lava Flow (Unnamed Type)

While the breccia of Unit 21 has similarities to those in the overlying flows (e.g., Units 17–19), there are some interesting differences. The pahoehoe lobes at the top are relatively intact, whereas farther down there is evidence for the lobes fragmenting while their interiors were still hot enough to weld to adjacent lobes (Fig. **F52**). The dense arm (Fig. **F51**) that pushes into this breccia has the small angular vesicles more typical of aa flow, rather than the long elongate vesicles in the dense material intruding Units 17, 18, and 19. The fanning joints in the dense arm in Unit 21 are common where hot, viscous lava forms an overhanging margin and gravity attempts to pull the lava apart. Such features are quite commonly seen on the dense arms of aa flows. The incorporated vesicular clast with chill margin is proof that this dense arm actively pushed into the bottom of this breccia. The sporadic recovery of the coherent interior of Unit 21 makes interpretation difficult, but the observations suggest multiple domains with a variety of vesicle morphologies, as has been seen in most of the overlying units. The high degree of fracturing and poor recovery of the interior and base of Unit 21 might be consistent with quenching by water in the later part of its cooling history.

Unit 21/Unit 22 Boundary

There must be a boundary between the coherent interior of Unit 21 and the breccia on the top of Unit 22. However, the position we have selected is arbitrary and marks the first appearance of well-recovered breccia from Unit 22. It is likely that some of the pieces included in Unit 21 are actually from the top of Unit 22. Given that we did not recover a contact, we cannot interpret the relationship or time gap between Units 21 and 22.

Unit 22: Transitional Lava Flow (Unnamed Type)

The intact pahoehoe lobes mixed with fragmented pahoehoe lobes in the breccia on Unit 22 suggest that it formed by the repeated intrusion of vesicular pahoehoe lobes into the breccia. This process is identical to that envisioned for the formation of the breccia on Unit 2 at Site 1137 (see **"Physical Volcanology,"** p. 13, in the "Site 1137" chapter). The intense fracturing of some of the lobes may suggest the presence of water during a brief part of the formation of the breccia. The vesicles from the interior of Unit 22 suggest shearing of a lava that was too viscous to allow the bubbles to return to a spherical shape before freezing.

Summary of Lava Flow Observations and Interpretations

The internal characteristics of lava flows in the basement of Hole 1138A are diverse. However, all the flows are consistent with subaerial emplacement on slopes of 1°–4°. Much greater flow thicknesses are required to achieve the stresses (i.e., velocities) needed to brecciate the top of a basaltic flow on slopes <1°. Inflated pahoehoe flows such as Unit 12 have not been seen to have formed on slopes >4°. The repeated circumstantial evidence for running water suggests intermittent small rivers or lakes. The preponderance of various brecciated flow tops suggests that the eruptions had moderate eruption rates. Also, these types of flows are unlikely to have traveled more than tens of kilometers from the vent. The large proportion of very small vesicles and possible welded spatter suggest that Hole 1138A was probably no more than a few kilometers from the vents for at least a few of the flows.

IGNEOUS PETROLOGY

Lithology

In this section we describe the primary texture, mineralogy, and geochemistry of the igneous basement units at Site 1138 (Fig. **F53;** Table **T12**). Volcanic structures and secondary mineralogy are described briefly here and in greater detail in **"Physical Volcanology,"** p. 22, and **"Alteration and Weathering,"** p. 49.

We recognize 22 units within the recovered portion (48%) of the 145.2 m of igneous basement drilled at Site 1138. Unit 1 occupies the uppermost 19.5 m and is composed of rounded cobbles of aphyric to sparsely feldspar-phyric dacite (Fig. **F54**). Unit 2 is a 24.3-m succession of interbedded pumice-lithic breccias and clays that contain clasts of highly plagioclase-clinopyroxene-phyric basalt. A rather uniform sequence of thin basaltic lava flows, ranging in curated thickness from 0.7 to 9.6 m, comprises Units 3 to 22 and forms the bulk of the drilled basement section. We interpret these units to represent a series of subaerial eruptions. The presence or absence of oxidized flow tops, rounded clasts, and sediments filling pore space in breccias indicate variable time intervals between flows (see **"Physical Volcanology,"** p. 22). Most flows exhibit both brecciated and massive portions, with wide variation in vesicularity. Alteration ranges from high to complete in brecciated zones and slight to locally high in massive intervals. Figure **F53** illustrates the recovered section, the positions of unit boundaries, flow type, and mineralogy together with a schematic representation of flow structure.

F53. Interpretative summary of the lithology, morphology, and mineralogy of basaltic lava flows, **p. 124.**

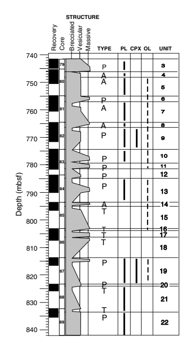

T12. Petrographic summary of Site 1138 igneous units with mineralogies, **p. 187.**

F54. Alkali feldspar-bearing dacite cobble from Unit 1, **p. 125.**

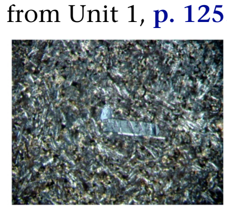

We distinguish the individual basement units on the basis of volcanological features, principally on significant downward changes in flow structure from brecciated or highly vesicular flow tops to massive interiors in the case of lava flows and degree of welding and types of clasts within the (possibly reworked) pyroclastic flows. As at Sites 1136 and 1137, the tops of several flows are marked by a notable zone of oxidation, suggesting subaerial weathering between some eruptions. Marked changes in vesicularity, vesicle shape, and distribution are also evident within units. We have noted features characteristic of pahoehoe, aa, and transitional flows (Fig. F53; see "Physical Volcanology," p. 22). The sequence of relatively thin flows at Site 1138 shows similarities to Hawaiian lava sequences (see "Physical Volcanology," p. 22) and contrasts with the generally thicker flows drilled at Sites 1136 and 1137.

Petrography and Primary Mineralogy

Overall, Site 1138 basalts are moderately to highly vesicular and aphyric to sparsely plagioclase-phyric. Groundmass textures are generally intersertal to intergranular, although occasionally subtrachytic (Fig. F55). The massive interiors of several flows exhibit subhorizontal glassy mesostasis segregations up to 1 mm wide, at approximately centimeter-scale spacing (Fig. F56). The relatively fast cooling of these units is highlighted by the skeletal dendritic forms of the titanomagnetites (Figs. F57, F58). Green and brown clay has replaced large portions of the glassy mesostasis and groundmass clinopyroxene. Vesicles and veins are generally completely filled, with clay at the margins and with zeolite in the interiors.

Discrete clinopyroxene phenocrysts are present only in Units 9 and 19. Glomerocrysts in Units 3 and 4 consist of monomineralic aggregates of plagioclase. In Unit 9, glomerocrysts contain both clinopyroxene and plagioclase (Fig. F59). The percentage of phenocrysts and glomerocrysts correlates weakly with flow thickness. Plagioclase phenocryst compositions are An_{60-65}, whereas microphenocrysts are ~An_{55}. In many of the more altered flow margins, rounded plagioclase phenocrysts have been replaced by low-relief, weakly birefringent zeolites that have grown parallel to the feldspar cleavage and preserved its Carlsbad twinning.

A notable aspect of Units 5–16 and 19 is the presence of 1%–5% olivine microphenocrysts, now completely replaced by clay although original morphologies are still preserved (Fig. F60). The olivines are generally euhedral to subhedral and are slightly larger than the groundmass plagioclase, clinopyroxene, and titanomagnetite. Extensive maghemite has formed, apparently via exsolution from the titanomagnetite (or by alteration along crystallographic planes) in Units 4, 5, and 20, but it is rare in other units. Sulfides are generally absent, with the exception of trace amounts of chalcopyrite, pyrite, and/or pentlandite, which are associated with groundmass alteration and as inclusions in primary phases in Units 6, 15, 17, and 21.

Major and Trace Element Compositions

We list XRF analyses of major and trace elements for 20 basalts and three felsic rocks in Table T13. Basalt compositions are tholeiitic to transitional (Fig. F61) and are slightly olivine to quartz normative. With the exception of one sample from Unit 18, which has anomalously high Na_2O, the low alkali contents ($Na_2O + K_2O$ = 2.5 to 3.5 wt%) and

F55. Typical intergranular to intersertal, subtrachytic texture of Site 1138 basalts, p. 126.

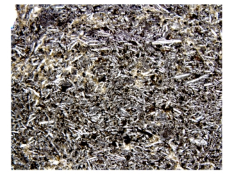

F56. Segregation of glassy mesostasis, p. 127.

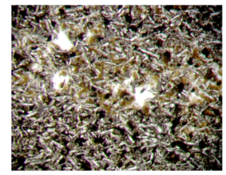

F57. Close-up photograph of skeletal, dendritic titanomagnetite groundmass crystals in flow margin, p. 128.

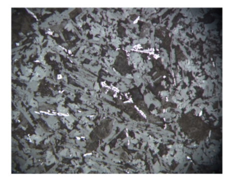

F58. Close-up photograph of skeletal, dendritic titanomagnetite groundmass crystals in the flow margin, p. 129.

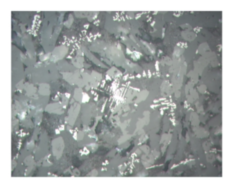

F59. Glomerocryst of plagioclase and smaller clinopyroxene, p. 130.

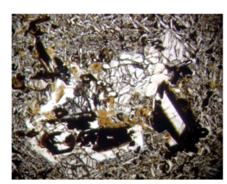

F60. Olivine microphenocrysts in Unit 8, p. 131.

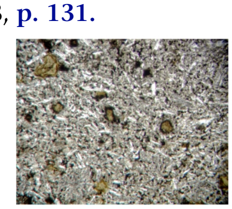

LOI (0.5 to 2.0 wt%) indicate that the massive portions of these units are relatively unaltered. Major element abundances are relatively uniform, with narrow ranges in MgO (4.5 to 7.0 wt%) and SiO_2 (47.0 to 49.9 wt%) (Fig. **F62**). In detail, however, there are systematic changes downcore in major and minor element abundances (Fig. **F62**) and in variation of abundance with Mg# (Mg# = Mg/[Mg + Fe^{2+}] with Fe^{2+} estimated as 80% of total iron) (Fig. **F63**; Table **T13**). For Site 1138 basalt compositions, we found that smoother trends developed in plotting elemental abundance variations against Mg# rather than MgO. Overall, these downcore changes are rather continuous, but there appears to be a notable break halfway through the sequence, seen particularly in TiO_2 and P_2O_5 and in a change from irregular to smooth variation in Mg# (Fig. **F62**). The boundary between the upper series (Units 3–13) and the lower series (Units 14–22) is marked by an oxidized breccia with rounded clasts, which is one of several possible time breaks within this eruptive sequence (see **"Physical Volcanology,"** p. 22).

MgO decreases downcore, whereas Fe_2O_3* (total Fe expressed as Fe_2O_3) increases, resulting in a trend toward lower Mg# (i.e., more evolved compositions with depth) (Fig. **F62**). Al_2O_3 is distinctly lower in the lower series (12.9 to 13.8 wt%) than in the upper series (13.9 to 16.8 wt%). As noted above, TiO_2 and P_2O_5 contents are greater in the lower series (2.6 to 3.2 wt% and 0.30 to 0.38 wt%, respectively) than in the upper series (1.9 to 2.3 wt% and 0.19 to 0.26 wt%, respectively). Compositional variability within the entire sequence of lava flows is consistent with shallow-level fractionation of the phases observed in thin section (i.e., olivine, clinopyroxene, and plagioclase). Interestingly, however, the compositions reflect a magmatic system that moved toward more primitive melts, rather than evolved liquids, with decreasing age. The lower Al_2O_3 abundances in Units 14–22 (Fig. **F63**) suggest that plagioclase fractionation was important.

The major element trends are mirrored by variations in trace element abundances. Incompatible elements, such as Zr and Y, decrease upsection, whereas compatible elements, such as Ni and Cr, increase, reflecting diminishing extents of crystal fractionation with time (Fig. **F64**). Incompatible trace element ratios Zr/Ti and Zr/Y decrease very slightly upcore, in keeping with the slightly more incompatible behavior of Zr compared with Ti and Y (Fig. **F64**). Patterns of incompatible trace elements, normalized to primitive mantle values in Figure **F65**, are intermediate, relative to those from other CKP sites. The important role of plagioclase fractionation inferred from Al_2O_3 content and Al_2O_3/TiO_2 ratio (Fig. **F63**) is corroborated by a depletion in Sr relative to Zr, especially in the lower series basalts (Figs. **F64, F65**).

Two cobbles from Unit 1 have very similar dacitic compositions, whereas a pumice lithic breccia sample from Unit 2 plots in the trachyte field (Fig. **F61**). These highly silicic compositions are consistent with formation during explosive subaerial volcanism at the waning stage of magmatic activity, inferred from the pyroclastic deposits in Unit 2 (see **"Physical Volcanology,"** p. 22).

Comparison with Other Sites

The enrichment in TiO_2 (up to 3.2 wt%), and especially Fe_2O_3* (up to 19.2 wt%) distinguishes the lower group of Site 1138 basalts from those of other sites on the plateau (Fig. **F66**). Such trends are similar to those for Fe-Ti–rich basalts from other large igneous provinces that are in-

T13. XRF analyses of major and trace elements for Site 1138 igneous units, **p. 188.**

F61. Rock compositions, **p. 132.**

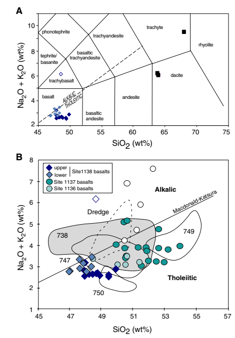

F62. Downhole variations in major element compositions, **p. 133.**

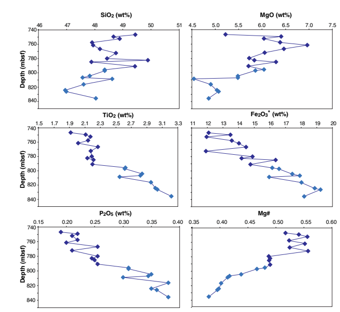

F63. Major element compositional variations plotted against Mg# for Site 1138 basalts, **p. 134.**

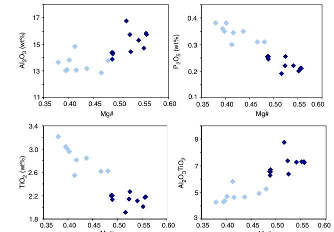

F64. Downhole variations in trace element abundances and primitive mantle–normalized ratios for Site 1138 basalts, **p. 135.**

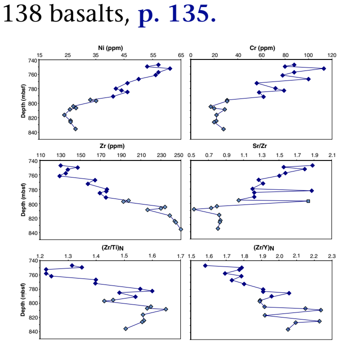

ferred to have evolved at low pressures from tholeiitic magmas (e.g., Imnaha basalts and Columbia River flood basalt province, Hooper, 1997; Mananjary basalts and Cretaceous Madagascar province, Storey et al., 1997; East Greenland ferrobasalts, Brooks et al., 1991). Another notable feature of Site 1138 basalts relative to basalts from Sites 1136 and 1137 is their low Al_2O_3/CaO (Fig. **F66**) and strong Sr depletions (Fig. **F65**), reflecting large amounts of plagioclase fractionation.

Trace element discriminants such as $(Zr/Ti)_N$ vs. Zr reveal that the Site 1138 basalts fall within the range of other central and southern Kerguelen Plateau basalts (Fig. **F67**). The $(Zr/Ti)_N$ values, in fact, are most similar to those for Site 747 basalts and fall between those of Site 1136 and 1137 basalts. This kinship is also shown in Figure **F65**, where the incompatible trace element patterns for Site 1138 basalts fall between the flatter Site 1136 patterns and the more elevated patterns from Site 1137 and most closely match the Site 747 patterns. With regard to Nb/Y vs. Zr/Y, we see that the Site 1138 basalts are again most similar to the Site 747 basalts (Fig. **F68**). The Site 1138 basalts plot mainly within the field defined by basalts derived from the Iceland mantle plume thought to be uncontaminated by continental crustal material or depleted asthenosphere (Fitton et al., 1997, 1998). This field also contains the Sun and McDonough (1989) estimate for the composition of primitive mantle, as well as compositions of basalts from the Kerguelen Plateau that do not show other evidence of continental crustal assimilation (Fig. **F68**). The most evolved basalt compositions from Site 1138 (lower series) trend from the plume field toward the Site 1137 basalts. Given that higher Zr/Ti and lower Nb/Y values may derive from contamination of melts with continental crust (see **"Igneous Petrology,"** p. 28, in the "Site 1137" chapter), one interpretation of this trend is that Site 1138 magmas have assimilated small amounts of continental material. However, removal of clinopyroxene, which has a significant partition coefficient for Y (Pearce and Norry, 1979), from more evolved tholeiitic magmas will drive the residual liquid away from the array at a shallow angle (constant Nb/Zr), in precisely the direction observed for the most evolved Site 1138 basalts. We conclude, then, that there is no strong evidence from shipboard analyses that Site 1138 magmas assimilated any continental crustal material, and we await further shore-based studies to resolve this issue.

ALTERATION AND WEATHERING

Twenty-two basement units have been defined in Hole 1138A, including cobbles of dacite (Unit 1), 20 igneous units (Units 3 through 22) interpreted to be various subaerial basaltic lava flows (see **"Physical Volcanology,"** p. 22, and **"Igneous Petrology,"** p. 46), and Unit 2 of volcaniclastic origin (see **"Lithostratigraphy,"** p. 3, and **"Physical Volcanology,"** p. 22). Fluid/rock interaction has variably altered all basement units after emplacement, as indicated by secondary minerals that partly replace primary minerals, partly to completely replace mesostasis, and partly to completely fill veins, vesicles, and open spaces between clasts within breccias. We recorded the distribution of secondary minerals in the alteration and vein/structure logs (see the **"Supplementary Materials"** contents list) for Hole 1138A (Fig. **F69**). In addition, we performed XRD analyses to identify secondary minerals (Table **T14**).

F65. Trace element patterns for Site 1138 and other Kerguelen Plateau basalts, **p. 136.**

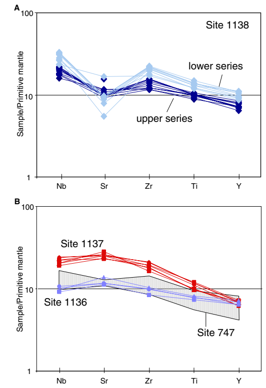

F66. Major element compositional variations for Site 1138 compared with other Kerguelen Plateau sites, **p. 137.**

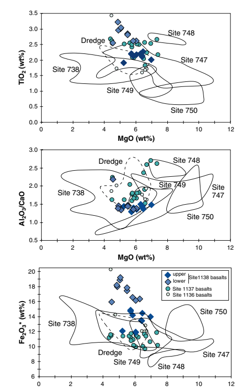

F67. Primitive mantle–normalized Zr/Ti vs. Zr for Site 1138 basalts, **p. 138.**

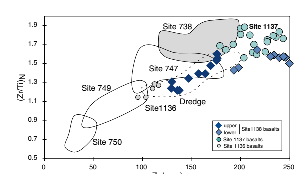

F68. Discriminant for contamination of mantle plume–derived melts, **p. 139.**

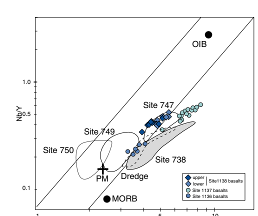

Unit 1

Basement Unit 1 is comprised of rounded isolated cobbles of pale pinkish brown to grayish green aphyric to sparsely sanidine phyric dacite. These rocks have a prominent flow banding, delineated by common streaks of groundmass altered to green clay (e.g., Sample 183-1138A-74R-1 [Piece 10, 50–56 cm]). The pieces that are uppermost in this unit, which directly underlie the dark brown clays and a thin layer of well-rounded, coarse sandstone to conglomerate (grain size ≤5 mm; lithostratigraphic Unit III), are completely altered to red-brown to gray to green clays. A relict igneous texture is present in some pieces (e.g., interval 183-1138A-73R-CC, 0–15 cm), however. In less-altered dacite pieces, late-stage oxidation halos (~5 mm) are common along fractures. Sparse veins, <0.5 mm wide, are filled with dark green and blue-green clay and rare calcite. Core 183-1138A-75R recovered only a single piece of hard, black aphyric cryptocrystalline igneous rock, with minor, wispy, red oxidation streaks. Its relationship to the pinkish dacite is unknown, but soft material that looks morphologically identical but is completely altered to black clay in the upper 20 cm of Section 183-1138A-76R-1 directly overlies Unit 2.

Unit 2

Unit 2 is a heterogeneous sequence of volcaniclastic deposits that contains multiple beds of laminated sediments with variable concentrations of pumice, lithic clasts, and ash. The grain size of the clasts and matrix varies widely, as do the degrees of grading and sorting. The rocks are generally highly altered with some glass-rich intervals, including altered ash layers and the matrix of poorly sorted sediments, completely altered to green clay. Commonly, however, the groundmass of clast-rich intervals remains gritty, indicating only the partial replacement of the finer grained fragments by clay minerals. Lithic and pumice clasts are also altered to clay, but the intensity of replacement is more variable; many pumice clasts are quite fresh and retain primary igneous textures. Also, numerous intervals have been oxidized to red-brown clay. In some cases, this oxidation occurs only in the matrix between volcanic clasts, which are altered to green clay (e.g., Sample 183-1138A-76R-1 [Piece 1, 35–45 cm]).

Units 3–22

The alteration of the subaerial basalt flows in Hole 1138A (Units 3–22) is relatively uniform. Secondary mineralogy varies little downhole (Fig. **F69**), and alteration is dominated by clay and zeolite that partly to completely fill vesicles and the interclast open spaces in the volcanic breccias that dominate the recovered rock. Highly vesicular flow tops and bottoms and areas with higher vein and fracture density generally exhibit moderate degrees of alteration, whereas the least-altered rocks are the minor, massive flow interiors. Within each basement unit, secondary mineral assemblages do not vary with alteration intensity (Fig. **F69**). One noteworthy characteristic of the alteration within these subaerial basalt flows is the complete absence of carbonate minerals in groundmass, vesicles, and veins except for Unit 3 (Fig. **F69**). In Unit 3, calcite locally replaces the groundmass and plagioclase phenocrysts (e.g., Sample 183-1138A-79R-4 [Piece 2, 108–115 cm]). Calcite veins as much as 5 mm wide are common and in some cases connect large cal-

F69. Distribution and abundance of secondary minerals as well as other alteration features, **p. 140.**

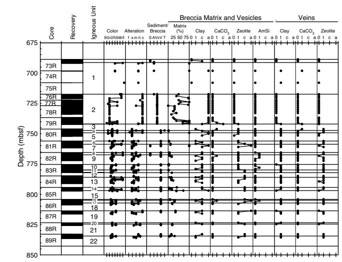

T14. Alteration minerals within basement units, **p. 190.**

cite-filled vesicles. Calcite composes ~3% of the unit, and this alteration gives the rock a distinctive light gray hue. The complete absence of carbonate alteration in the rest of the basement in Hole 1138A contrasts with basement recovered from other Leg 183 holes where calcite is a common secondary mineral.

Seventeen brecciated intervals have been defined within basement Units 3–22, representing both flow tops and flow bottoms (see **"Physical Volcanology,"** p. 22). All of these intervals are highly to completely altered and vary from gray (e.g., Sample 183-1138A-87R-1 [Piece 1, 0–12 cm]) to dark red (e.g., Sample 183-1138A-82R-1 [Piece 1, 0–15 cm]), suggesting different degrees of oxidation at the top and bottom of each unit.

Most breccias consist of ~30% matrix and ~70% volcanic clasts, although locally the percentage of matrix can be as high as 75% (see Fig. **F69**). The clasts are variably altered to green and red-brown clay, and vesicles within clasts are filled with similar clay in addition to clinoptilolite (Fig. **F29**). Secondary minerals within the matrix of all breccias include clinoptilolite and smectite (Fig. **F46**), with amorphous silica and quartz occurring in trace amounts (<1%). The relative proportion of zeolite and clay in the matrix varies among different breccias, from ~20% to ~80% clay. Spectacular zeolite crystals, exhibiting different colors and habits, are common in large open cavities within the matrix of many breccias, although XRD analyses confirm that clinoptilolite is the only zeolite present (Table **T14**). Well-indurated silts fill the matrix within some brecciated intervals (e.g., Sections 183-1138A-81R-4 and 82R-2; Fig. **F34**). These sediments are most likely clastic debris washed into open spaces between volcanic clasts in the subaerial environment (see **"Physical Volcanology,"** p. 22). An XRD analysis indicates that these silts are quartz rich (Table **T14**), suggesting that the induration may be a result of silicification, although some of the quartz may also be clastic. We also identified small amounts of clay and amorphous silica (~5%) in the sediments in thin section.

Twenty highly vesicular intervals have been defined within basalt Units 3–22 in Hole 1138A (see **"Physical Volcanology,"** p. 22). Vesicles compose ~30% of the rock in the most vesicle-rich intervals; these intervals are typically moderately altered and variably oxidized. Vesicles are 50%–100% filled with zeolites, smectite, and, more rarely, quartz, although calcite-filled vesicles are present in Unit 3 (Table **T14**). Smectite lines most zeolite-filled vesicles, indicating clay formation before zeolite. Some vesicles also have green to blue-green alteration halos <1 cm wide. Similar to our observations from brecciated intervals, larger vesicles commonly contain zeolites with different colors and crystal forms. The XRD analyses indicate that clinoptilolite is the only zeolite present, although we identified analcime in the center of one vesicle lined with clinoptilolite (Table **T14**). Geopetal structures are rare and are characterized by zeolite and smectite divided by a subhorizontal boundary that bisects the vesicle. These structures do not have a consistent form, however, and we observed zeolite above the boundary in some vesicles and below the boundary in others.

Vein and fracture density does not exhibit large downhole variations within the more massive and vesicular portions of Units 3–22 (Fig. **F69**), although generally veins are less common in these cores compared to other Leg 183 sites (see **"Structural Geology,"** p. 52). Moreover, with the exception of calcite-filled veins in Unit 3, the only vein minerals present are green and blue-green smectite and zeolite. Veins are <2 mm wide and are typically lined with smectite and filled with zeolite. Some veins have narrow (<5 mm) green alteration halos. Although zeolites of different color and morphology are present in some veins, by analogy with our XRD results from vesicles it is likely that clinoptilolite is the only zeolite present. In rare circumstances, vein mineralogy changes abruptly from zeolite to smectite where the vein crosses a color change in the wall rock from light gray to dark gray (e.g., Sample 183-1138A-85R-1 [Piece 6, 57–63 cm]). Also, some veins form fine networks in which the included small (<1 cm) wall rock fragments are completely changed to clay (e.g., Sample 183-1138A-81R-1 [Piece 14, 125–136 cm]).

In summary, the typical basalt flow in the basement of Hole 1138A exhibits a brecciated or vesicular flow top that has been moderately to completely altered to clay and zeolite, with a gradual progression to only slightly altered rock in the relatively thin massive flow interiors. Alteration of vesicular or brecciated flow bases is most commonly similar to the underlying flow top, although oxidation differs slightly across some flow contacts. In addition, smectite and zeolite fill vesicles and veins in Units 4–22. This alteration is most likely the product of both weathering and low-temperature fluid-rock reaction. The most notable difference in alteration within the basement of Hole 1138A (below Unit 3) compared to other Leg 183 holes is that zeolite is an abundant secondary mineral whereas calcite is absent. Such a difference in secondary mineralogy may be related to the relative importance of alteration in the submarine vs. subaerial environment and will be a focus of shore-based studies.

STRUCTURAL GEOLOGY

The basement rocks recovered from Hole 1138A displayed relatively few structural features. The lava flows that comprise Units 3–22 have brecciated flow tops and thin massive interiors. Veins are the most common structure, and they are dominantly in the more highly fractured massive portions of basement Units 3–22 (see **"Igneous Petrology,"** p. 46). The true dip, vein abundance, and fracture density of oriented features from the basement of Hole 1138A (Fig. **F70**) are recorded in the vein-structure log for this Site (see the **"Core Descriptions"** contents list).

F70. Diagrams showing the dip and fracture distribution, **p. 141.**

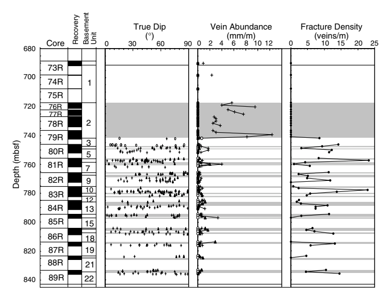

The uppermost portions of Unit 1 include intensely weathered igneous rocks, completely altered to brown to gray to green clays, but rare pieces retain a relict igneous texture. We could not establish the orientation of either veins or the prominent flow-banding because loose felsic pebbles and other altered lava types from beneath the altered top of Unit 1 do not include any oriented pieces.

Unit 2 contains multiple beds or regular layers of highly altered volcaniclastic material with variable concentrations of pumice, lithic clasts, and ash (see **"Physical Volcanology,"** p. 22). Bedding is not strongly developed in most of this unit, but diffuse laminations, flattened clasts, and rare scoured bases of the debris and/or pyroclastic flows indicate a subhorizontal orientation for the sediments. The ashes and other clay-rich horizons fracture along subconchoidal partings.

The structure in the subaerial basaltic lavas in Hole 1138A (Units 3–22) is monotonous and follows a regular pattern of brecciated flow tops, which overlie minor, more massive interiors hosting numerous veins (clay > zeolite > calcite). Few structures provide evidence for significant tectonic disturbance, and slickensides are rare on either vein surfaces or on the rims of breccia clasts. A minor interval of tectonic breccia, comprising fractured altered glass within a zeolite-clay matrix, is present at the contact between Units 3 and 4 (Interval 183-1138A-80R-1 [Pieces 16–19, 118–154 cm]) (Fig. F70). Three other subplanar contacts between basement units or subunits were recovered intact, and these structures all have moderate dips (Table T15).

T15. True dips of intact basement unit boundaries, p. 191.

We recorded the orientation of >350 veins and their mineral fillings from the basaltic lava flows (Fig. F70) (see also "Alteration and Weathering," p. 49). Vein abundance and fracture density generally decrease with depth (Fig. F70). Clay minerals fill two-thirds of the veins, whereas minor (4%) calcite veins are present at the top of the basaltic section (Unit 3) (Sections 183-1138A-80R-1 to 80R-3) and zeolite-filled veins (~30%) are in most of the underlying lava units. The clay veins do not dip at any preferred angle throughout the section, but the carbonate veins most commonly dip gently. Zeolite veins dip moderately to steeply (Figs. F70, F71).

F71. Histogram showing the distribution of vein dips subdivided according to mineral filling, p. 142.

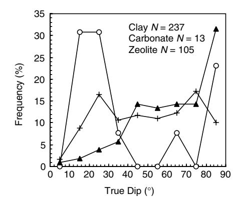

Geopetal structures are rare (*N* = 6) in Hole 1138A, and the boundaries between the different mineral fillings (clays, calcite, and zeolite) in these features are subhorizontal (<10° dip), although a consistent mineral paragenesis is not present. Fine wisps of mesostasis altered to clay minerals, and veins formed by the linking of vesicle trails subparallel to the mesostasis fabric, dip gently to moderately (average dip = 33°, *N* = 33).

PALEOMAGNETISM

We measured the natural remanent magnetization (NRM) of most archive halves from Hole 1138A with the pass-through cryogenic magnetometer using measurement intervals of 5 and 2.5 cm for sediment and basement rocks, respectively. Subsequently, sediment and basement core sections were demagnetized with peak alternating fields (AF) of 20 and 50 mT, respectively. Discrete sediment samples were stepwise AF demagnetized up to 60 mT. Discrete basement samples were stepwise AF demagnetized in a peak field of up to 60 mT or thermally demagnetized in temperatures of up to 620°C. We determined the anisotropy of magnetic susceptibility (AMS) of discrete basement samples to obtain information about the magnetic fabric.

We obtained stable and reliable paleomagnetic directions from the sediments of Hole 1138A. Correlation of biostratigraphic data and polarity reversals suggests that the reversed and normal chrons are Pliocene to Late Cretaceous in age. We compared magnetic properties with lithologic and basement units. The basement rocks yielded reliable paleomagnetic directions and a normal polarity. We found a difference of approximately 8° between the paleolatitude (46°S) and the present latitude (54°S) of Site 1138.

Sediments

We measured the remanent magnetization of all archive halves from Hole 1138A, except for highly disturbed sections. One archive section for each core was stepwise AF demagnetized up to 30 mT. We took two discrete samples per section, and 42 samples were stepwise AF demagnetized up to 60 mT to confirm the reliability of whole-core measurements. We obtained reliable results in undisturbed cores, and correlated normal and reversed segments with biostratigraphic zones (see “**Biostratigraphy,**” p. 10). The sediments of Hole 1138A generally have stable magnetization, which was obtained after AF demagnetization at 10 mT. Most discrete samples have a high median destructive field (MDF), and the remanent direction is stable in demagnetization steps between 10 and 30 mT (Fig. **F72**). We, therefore, used the remanent magnetization after AF demagnetization at 20 mT to correlate the paleomagnetic record with geomagnetic chrons. Furthermore, we used the data selection criteria described in “**Paleomagnetism,**” p. 27, in the “Explanatory Notes” chapter for magnetostratigraphic studies of Hole 1138A (Fig. **F73**). The selection criteria were that (1) the intensity of remanent magnetization after AF demagnetization at 20 mT was >2 × 10^{-4} A/m, (2) the inclination was >±30°, (3) at least two consecutive values (which corresponds to a 10-cm length of split core) had the same polarity, and (4) there was no significant core disturbance. Characteristic inclinations from discrete samples generally agree well with selected inclinations from whole-core measurements (Fig. **F73**).

Correlation of biostratigraphic data and polarity reversals (Fig. **F73**) suggests that the reversed and normal chrons in Hole 1138A are Pliocene to Late Cretaceous in age (see “**Biostratigraphy,**” p. 10). We obtained a relatively continuous paleomagnetic record from high-recovery core except in the upper part of Unit I (see “**Lithostratigraphy,**” p. 3). Between 75 and 190 mbsf, 315 and 370 mbsf, 450 and 510 mbsf, and 620 and 665 mbsf, the paleomagnetic record appears continuous. We propose the following correlations with paleontological data from the core catcher of each core (see “**Biostratigraphy,**” p. 10). We correlate the normal and reversed segment between 70 and ~120 mbsf to Pliocene Chrons C2r to C3n. The underlying normal and reversed segment between ~120 and 135 mbsf corresponds to late Miocene chrons between C3r and C4. We correlate the normal segment between 140 and 153 mbsf and the reversed segment between 153 and 175 mbsf with Chrons C5n and C5r, respectively. Dispersed normal and reversed segments between 180 and 330 mbsf correlate with Chrons C5An (middle Miocene) to C11r (early Oligocene). We correlate normal and reversed polarities between 343 and 442 mbsf, and between 448 and 470 mbsf to middle Eocene Chrons C17–C21 and early Eocene Chron C24 to late Paleocene Chron C26, respectively. We obtained a polarity record from early Paleocene Chron C27 to Late Cretaceous Chron C32 between 475 and 575 mbsf. The normal sequences at ~613 mbsf and between 620 and 692 mbsf may correlate with Campanian Chron C33n and Cretaceous long normal Chron C34n, respectively.

We obtained reliable paleomagnetic data from most of the sediments in Hole 1138A. The record is less reliable, however, between 0 and 70 mbsf and between 540 and 605 mbsf. We observed high susceptibilities (whole-core MST measurements, see “**Physical Properties,**” p. 56) and strong NRM intensities, but scattered inclinations in the upper part of Unit I (diatom clay and ooze, see “**Lithostratigraphy,**” p. 3) (Fig. **F73**). Scattered directions are probably caused by core disturbance. Among the sediment units of Hole 1138A, we observed the lowest susceptibilities and weakest NRM intensities in Unit III (white chalk) (Fig. **F74**). The lower part of Unit IIIB is characterized by negative susceptibilities and weak remanent magnetization, and the paleomagnetic results are unreliable. We observed high susceptibilities and strong NRM intensities in neritic sediments (Units V and VI, see “**Lithostratigraphy,**” p. 3) (Fig. **F74**).

F72. AF demagnetization of a discrete sediment sample, **p. 143.**

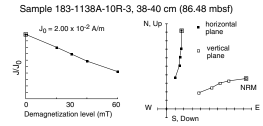

F73. Inclination, intensity, and susceptibility of sediments, **p. 144.**

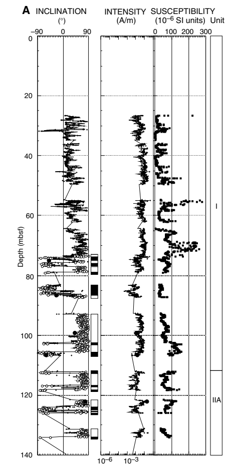

F74. Average intensity and susceptibility of all units, **p. 149.**

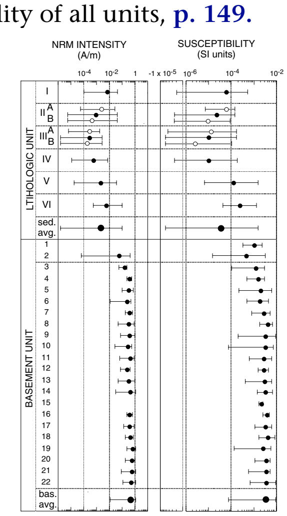

Basement Rocks

We determined the magnetic properties of each basement unit (see **"Physical Volcanology,"** p. 22, and **"Igneous Petrology,"** p. 46) and the variation of magnetic properties within each unit (Fig. **F75**). Three independent types of susceptibility measurements, MST, AMST, and discrete samples generally show consistent results. We observed no significant differences in average susceptibility and NRM intensity among lava flows (basement Units 3–22) (Figs. **F74, F75**) and no significant variations within the units. In several parts of the lava flows, we observed scattered inclinations of whole-core measurements after AF demagnetization at 40 mT. However, we chose the data points obtained from core pieces that fit together and are longer than the effective sensitivity of the pass-through magnetometer (~15 cm) to obtain reliable inclinations without drilling disturbance. Scattered inclinations from the upper part of basement Units 9, 10, and 13 correspond to brecciated parts. Inclinations are also scattered in the lower parts of basement Units 9, 10, 11, 13, and 14. These rocks were probably rotated after acquisition of thermal remanent magnetization (<~600°C). Basement Unit 2 (volcaniclastic sediments, see **"Physical Volcanology,"** p. 22) has lower susceptibilities and lower NRM intensities than the lava flows (Fig. **F74**). Susceptibilities and NRM intensities are lower in the uppermost 3 m (reworked volcanic sediments) and in the lowermost 2 m (altered pumice flow) of basement Unit 2 than in the middle part (mostly pumice lithic breccia or lithic breccia) (Fig. **F75**). Inclinations are scattered in the lowest 2 m.

F75. Inclination, intensity, and susceptibility of basement rocks, **p. 150.**

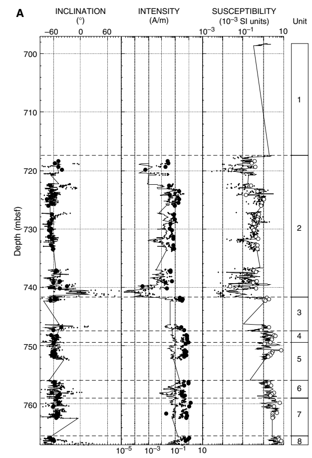

From 30 discrete samples of basement Units 6, 7, 8, 12, and 13, we measured magnetic susceptibility in 15 different directions to determine the AMS and the magnetic fabric. The degree of anisotropy (ratio between maximum and minimum axes) was generally low and its magnitude ranged from 1.01 (basement Unit 6) to 1.05 (basement Unit 13). We found better developed shapes of magnetic fabric with increasing degree of anisotropy. All samples have negative shape parameters or shape parameters close to zero; hence, prolate (rod) shapes predominate. In basement Unit 13, which is described as channelized shelly/slab pahoehoe lava (see **"Physical Volcanology,"** p. 22), we found a relatively high degree of anisotropy and a grouping of the minimum axes along the vertical axis (Fig. **F76A**). However, in the other basement units of different origins (e.g., basement Unit 6, inflated pahoehoe), we found lower degrees of anisotropy and we could not determine groupings of any (minimum and/or maximum) axes (Fig. **F76B**).

F76. Directional anisotropy data from Units 13 and 6, **p. 152.**

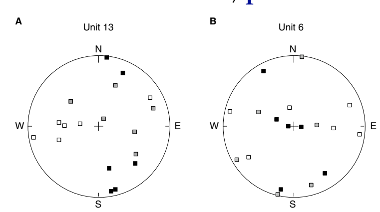

Five discrete samples from basement Units 3, 7, 9, 13, and 20 were stepwise thermally demagnetized up to 620°C, and two samples from Units 10 and 20 were progressively AF demagnetized up to 60 mT. We measured the susceptibility of the samples after each heating step to detect changes in their magnetic minerals. The two AF demagnetized samples have stable, single-component remanent magnetization (Fig. **F77**), and their MDFs were ~20 mT. We found two magnetic phases during stepwise thermal demagnetization. The high-temperature phase is characterized by an unblocking temperature of ~580°C (Fig. **F78A**) and the low-temperature phase by an unblocking temperature of ~300°C (Fig. **F78B**). The high-temperature phase probably corresponds to magnetite or titanium-poor titanomagnetite, and the low-temperature phase to (titano)maghemite as previous rock magnetism studies of the southern Kerguelen Plateau basalts have shown (Heider et al., 1992) (see **"Paleomagnetism,"** p. 23, in the "Site 1136" chapter). Most samples exhibit

F77. AF demagnetization of a discrete basement sample, **p. 153.**

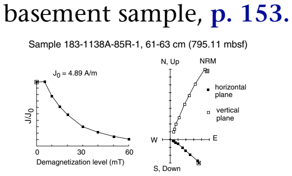

F78. Thermal demagnetization of discrete basement samples, **p. 154.**

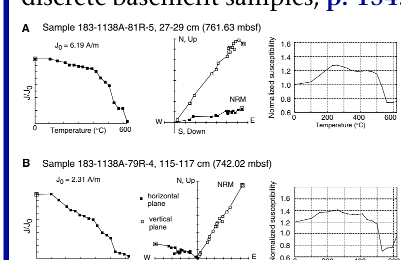

two magnetic phases and stable, single components of remanent magnetization.

We calculated the characteristic inclinations of discrete samples using component analysis (Table **T16**). Inclinations are negative, indicating normal polarity, and range from –53° to –80°. Variation of inclinations among samples is probably caused by secular variation. We calculated a mean inclination of –65°, which corresponds to a paleolatitude of 46°S assuming a geocentric dipole field. The difference between the present latitude of 54°S of Site 1138 and its paleolatitude during the Cretaceous (see **"Biostratigraphy,"** p. 10) is 8°, suggesting that either the central Kerguelen Plateau has moved south or basement has been tilted since Cretaceous time. Interpreted igneous basement contains some internal reflections with a slight apparent dip to the southwest. The top of basaltic basement, however, is flat lying (see **"Background and Objectives,"** p. 1). We conclude that the central Kerguelen Plateau has moved ~8° southward since Cretaceous time, which is consistent with the contemporaneous southward movement of the southern Kerguelen Plateau (Inokuchi and Heider, 1992) and Elan Bank (see **"Paleomagnetism,"** p. 45, in the "Site 1137" chapter). Limited measurements, however, preclude definitive paleolatitude estimates at this time. We will investigate this problem further with shore-based studies.

T16. Characteristic inclinations and NRM intensities of discrete basalts, **p. 192.**

T17. Index properties data, **p. 193.**

PHYSICAL PROPERTIES

Introduction

Measurements of whole sections of core taken at Site 1138 included magnetic susceptibility, gamma ray attenuation porosity evaluator (GRAPE) bulk density, and natural gamma radiation (NGR). We also determined the following physical properties data: (1) index properties data (bulk density, grain density, porosity, and water content) in discrete samples, (2) wet bulk density in discrete samples, (3) compressional wave velocities (V_p) through the working half of the core and in discrete samples, (4) magnitude of velocity anisotropy, and (5) thermal conductivity for sediments and basement rocks.

F79. Downhole index properties and velocities, **p. 155.**

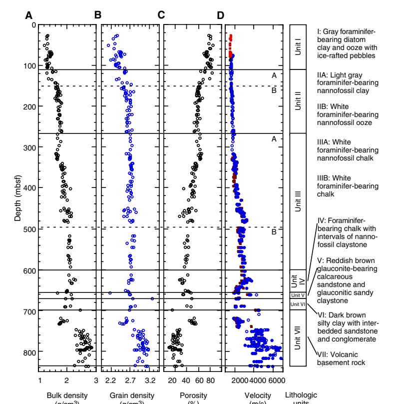

Index Properties

We obtained index properties data (bulk density, grain density, porosity, and water content) using gravimetric methods on discrete samples from Site 1138 (Table **T17**). Overall downhole trends in index properties show great variability at Site 1138 (Fig. **F79** and enlarged subset in Fig. **F80**). From the seafloor to ~112 mbsf in Unit I (foraminifer-bearing diatom clay and ooze with scattered ice-rafted pebbles) (see **"Lithostratigraphy,"** p. 3), wet bulk density is low (<1.5 g/cm³), porosity is high (>70%), and average grain density is 2.4 g/cm³.

F80. Summary of physical properties measurements in basaltic basement, **p. 156.**

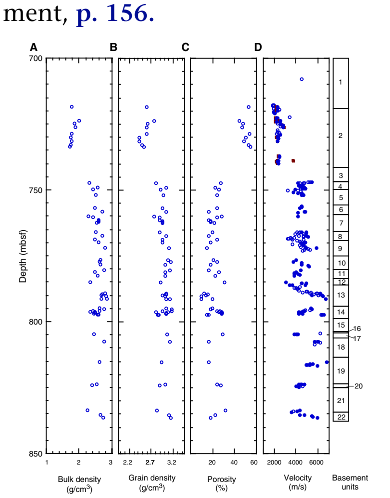

Between ~112 and ~155 mbsf, within Unit II, index properties change significantly. Grain density increases from 2.3 to 2.8 g/cm³, porosity decreases from ~80% to ~50%, and bulk density ranges from 1.2 to 1.8 g/cm³. These changes reflect lithologic changes from foraminifer-bearing nannofossil clay to white foraminifer-bearing nannofossil ooze. The carbonate content of these sediments also changes abruptly, from ~30% at a depth of ~112 mbsf to over 85% near a depth of ~155 mbsf (see **"Lithostratigraphy,"** p. 3). Within the first two units (Units I and II), the porosity-depth trend changes at the boundary of Subunit IIA and IIB. Unit I and Subunit IIA sediments consist of gray foraminifer-bearing diatom clay and light gray foraminifer-bearing nannofossil clay respectively, and here the porosity changes more with depth than in the foraminifer-bearing nannofossil ooze of Subunit IIA.

From just below a depth of ~150 mbsf, below the contact between Subunits IIA and IIB, to a depth of ~310 mbsf, bulk density, grain density, and porosity change little, except for some variation in grain density in the upper 30 m of Subunit IIB.

Between ~320 and ~640 mbsf, bulk density decreases from 1.66 g/cm³ at ~320 mbsf to 2.00 g/cm³ at ~640 mbsf, and porosity decreases from an average value of 62% at the top to 37% at the bottom. Grain density maintains a nearly constant value of ~2.6 g/cm³. In this zone, the dominant lithologies are foraminifer-bearing and nannofossil chalks with intervals of nannofossil claystone, and carbonate contents are uniformly high.

In the lower part of Unit IV through Unit VI, index properties values are scattered and relatively sparse. Nevertheless, the slope of all index properties data changes noticeably at the boundary between Units V and VI (~670 mbsf), corresponding to a change in lithology from glauconitic calcareous sandstone to silty claystone.

At the boundary between Unit VI and basement (~698 mbsf), index properties change abruptly (Figs. **F79, F80**). Between ~718.4 and 733.3 mbsf, bulk density for basement Units 1 and 2 (flow-banded dacite, and pumice breccia and clay, respectively) ranges from 1.71 to 2.00 g/cm³, grain density changes between 2.44 to 2.75 g/cm³, and porosity varies from 44% to 55%. All index properties change markedly again near 747 mbsf of the transition to the basaltic basement units. Bulk density and grain density increase downhole with mean values of 2.56 and 2.96 g/cm³, respectively, and porosity decreases to a mean value of 21% (Fig. **F80**).

MST Measurements

GRAPE Density

Bulk densities were also estimated from whole-core GRAPE measurements taken in sections recovered from Hole 1138A (Fig. **F81A**), which provide a semicontinuous record. The GRAPE data show fairly constant bulk densities with depth to ~320 mbsf. Deeper data exhibit trends similar to those seen in the index properties (see previous paragraphs). Maximum GRAPE densities (right side of the bulk density profile) (Fig. **F81A**) correlate best with bulk densities obtained from discrete samples (solid line in Fig. **F81A**). Discrete sample data for the basement units consistently show higher values than the GRAPE density data. As noted previously in the other Leg 183 site chapters, the larger scatter in the GRAPE bulk density data for the basement units results from the fractured nature and narrow diameters of the cores, which do not fill the core liner (see **"Physical Properties,"** p. 31, in the "Explanatory Notes" chapter).

F81. Downhole profiles of whole-core measurements, **p. 157.**

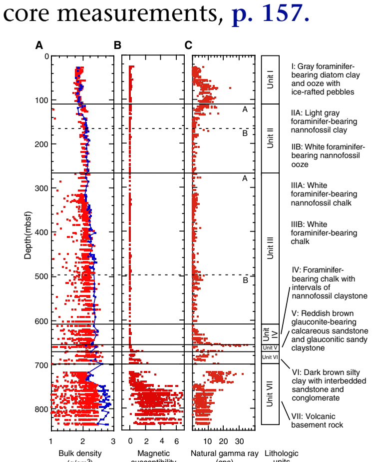

Natural Gamma Radiation

NGR measurements in the sedimentary sections of Hole 1138A show positive peaks of >10 counts per s (cps) at depth ranges centered around

~100, ~660, and ~700 mbsf (Fig. F81). These intervals correspond to the foraminifer-bearing diatom clay in Unit I, the glauconite-bearing calcareous claystone and sandstone in Units IV and V, and the dark brown siltstone in Unit VI, respectively. In the rest of the Site 1138 section, NGR values vary little, except for a relatively significant increase (>5 cps) at ~490 mbsf, probably reflecting the K/T boundary (Core 183-1138A-52R). In basement Units 1 and 2 (718.4–833.3 mbsf), NGR values fluctuate between 8 and 32 cps with a mean value of 17 cps. NGR values for other basement units average 7 cps (Fig. F81C).

Magnetic Susceptibility

We determined magnetic susceptibility on all cores from Site 1138, with whole-core sections measured at 4-cm intervals by the Bartington meter, and split-half sections at 2-cm intervals by the point-susceptibility meter. The characteristic susceptibility peaks and troughs correlate with flow boundaries. Detailed results are discussed in "Paleomagnetism," p. 53, in conjunction with the NRM pass-through and discrete sample measurements.

Compressional Wave Velocity

Variations in compressional wave velocity downhole commonly correlate with changes in lithology. At Site 1138 we calculated compressional wave velocity from discrete samples in split-core sections or cut samples (Fig. F79D). Measurements were generally made into the core (x direction), although we also measured some discrete samples in the other two directions to investigate velocity anisotropy (Table T18).

T18. V_p in discrete samples, p. 197.

The compressional wave velocity data for sedimentary Units I and II show very little scatter ranging from 1514 to 1865 m/s (Table T18; Fig. F79D). Velocities in Unit III increase with depth, ranging between 1700 and 3190 m/s. A slight change in the velocity trend just above the boundary of Subunit IIIB may correspond to a diagenetic change in the sediment (see "Lithostratigraphy," p. 3). Velocities for Units IV through VI are more scattered with a mean around 2500 m/s.

Velocities for the basement units vary more (Fig. F80), from 1884 to >6000 m/s, with a mean value of 4014 m/s. The highest velocities of >6000 m/s correspond to lava flows forming basement Units 13 through 19 with significant changes in flow morphology (see "Physical Volcanology," p. 22). In particular, velocities in basement Unit 13 increase dramatically downhole, from ~3000 m/s at the top to >6000 m/s at the bottom of the unit. This increase in velocity appears to correspond to the vesicular basalt grading into massive basalt. Velocities >6000 m/s could be a consequence of measurements on cut samples with a relatively small length that often gives larger uncertainties, combined with the calibration method (see "Physical Properties," p. 31, in the "Explanatory Notes" chapter).

Velocity anisotropy at Site 1138 is generally low (<15%). However, velocity anisotropy is found in the chalks of Subunit IIIB and Unit IV. As shown in Figure F79D, measurements made in the x and y directions (parallel to layers) yielded relative larger velocities than measurements done in the z direction (perpendicular to the layers). This velocity anisotropy in sediments with laminations may arise because the densest layer and less stress release provides a better route for wave propagation, whereas the perpendicular wave must propagate through all layers.

Thermal Conductivity

We determined thermal conductivity on selected lithified sediments and basaltic rock samples from Site 1138 (Fig. F82, Table T19). In the sedimentary section, thermal conductivity values for Unit I average 0.7 W/(m·K). Between ~115 and ~300 mbsf (Unit II and part of Unit III), thermal conductivity averages 1.1 W/(m·K). The volcanic basement units exhibit higher thermal conductivity values ranging between 0.6 and 2.2 W/(m·K), with a mean value of 1.3 W/(m·K) (Table T19).

F82. Downhole profiles of thermal conductivity for soft sediments and basement rocks, p. 158.

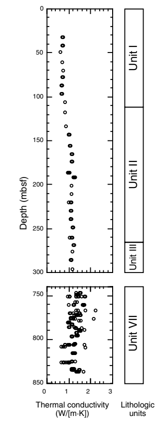

Concluding Discussion

The physical properties data obtained at Site 1138 vary greatly downhole. Offsets and changes in slope can be correlated with distinct changes in lithology. Changes from siliceous to calcareous-dominated lithologies are evident in fluctuations in index properties and sonic velocities. The variations in index properties and velocities within the basement units reflect the effect of alteration and brecciation on the physical properties of basalt at this site.

ORGANIC AND INORGANIC GEOCHEMISTRY

We measured concentrations of carbonate in sediments from Hole 1138A on ~1 sample per core (Table T20). In addition, we analyzed 26 of the sediment samples for organic carbon, total nitrogen, sulfur, and hydrogen. The results of the analyses are discussed in "Lithostratigraphy," p. 3.

For volcanic and volcaniclastic rocks that were analyzed by XRF, we measured total carbon, total nitrogen, sulfur, and hydrogen using the NCS analyzer (Table T21). These data are useful for assessing the degree of alteration in the basalts (e.g., total carbon and hydrogen can be converted to CO_2 and H_2O, respectively, and compared with loss on ignition values).

T19. Thermal conductivity values, p. 203.

T20. Carbon, nitrogen, sulfur, and hydrogen analyses of sediments, p. 204.

T21. Carbon, nitrogen, sulfur, and hydrogen analyses of volcanic and volcaniclastic rocks, p. 205.

SEISMIC STRATIGRAPHY

Data

We used densities and compressional wave velocity from index properties and MST measurements (Fig. F83) to synthesize seismograms at Site 1138, as no downhole logs were collected. A detailed comparison of velocities from samples and logs is given in "Downhole Measurements," p. 54, in the "Site 1137" chapter. Based on the coherence analysis of velocity data from Site 1137 (Fig. F86, p. 155, in the "Site 1137" chapter), we filtered the sample velocities from Site 1138 using a filter width of 5 m. The data were resampled simultaneously with filtering at an increment of 2.5 m. A more closely spaced sampling rate results in the inclusion of noise in the filtered profiles. We used a robust mode filter (i.e., a maximum likelihood probability estimator) that calculates the mode within the given data window. In addition, the median of the filtered data set was computed during filtering, and outliers, whose values exceed 2.5 times the L1 scale, were replaced with the median, as described in "Downhole Measurements," p. 54, in the "Site 1137" chapter.

F83. Comparison of densities determined from core samples, GRAPE, MST, and V_p from downhole logs and core samples, p. 159.

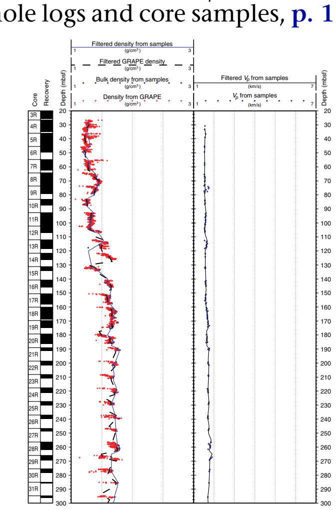

Velocity data show little scatter within nannofossil ooze in Units I and II (Fig. **F83**). Velocities in the underlying sedimentary units show much larger variations, including a well-resolved inversion from 475–505 mbsf, corresponding to the lower part of Subunit IIIA (i.e., foraminifer-bearing nannofossil chalk) and its transition to Subunit IIIB (foraminifer-bearing chalk) (Fig. **F83**). Six other velocity inversions are present at 625–660, 665–670, 710–720, 780–785, 792.5–795, and 810–835 mbsf (Fig. **F83**), all of which result in reflections that can be linked to the MCS reflection data (Figs. **F84, F85**).

GRAPE and discrete sample densities agree well at depths above ~290 mbsf, except for one instance at 118 mbsf where GRAPE densities are substantially higher than a calculated sample density (see **"Physical Properties,"** p. 56). At greater depths, all GRAPE density measurements are lower than those from discrete samples. All major velocity anomalies are reflected in density anomalies based on discrete samples, illustrating a good agreement between the two profiles.

Synthetic Seismogram

We synthesized seismograms for Site 1138 (see **"Seismic Stratigraphy,"** p. 47, in the "Explanatory Notes" chapter). We resampled both densities and velocities every 0.5 ms as a function of two-way traveltime (TWT), and we created profiles for impedance, reflection coefficients, and a seismic trace. The seismic trace is based on convolution with a Ricker wavelet with a peak frequency of 40 Hz. Reflection coefficients with and without multiples and transmission losses show distinct differences at this site. The upper Miocene–Pliocene section shows three interbed multiple reflections (MUL1–MUL3) based on reflection coefficients including multiples (red trace) (Fig. **F84F**). In the lower part of the section, amplitudes are reduced by up to a factor of 2 (red trace) (Fig. **F84F**), if transmission losses within the basement are accounted for, compared with the synthetic seismogram excluding multiples and transmission losses (black trace) (Fig. **F84F**).

Seismic Stratigraphy

We find substantial differences between the two synthetic seismograms shown in Figure **F84F** (Figs. **F84F, F85A, F85B**). Both synthetic traces match the MCS data, except for those reflections resulting from multiples. The MCS data show three reflections in the upper Miocene to upper Pleistocene part of the section, which are not present on the synthetic trace (Fig. **F85A**); however, these emerge as prominent reflections if we include interbed multiples (MUL1–MUL3) (Fig. **F85B**). This leaves little doubt that the three corresponding MCS reflections are products of positive interference of interbed multiples.

The Miocene section shows five distinct reflections labeled M1–M5. M1, M2, M4, and M5 are distinct reflections in both synthetic seismograms (Figs. **F84, F85A, F85B**). However, M3, the most prominent Miocene reflection in the MCS data, correlates with a broad low-amplitude reflection in the synthetic seismogram excluding multiples, whereas the alternative synthetic trace, including multiples, shows a distinct short-wavelength, high-amplitude reflection (Fig. **F85B**). This demonstrates the potential importance of identifying and including multiples when trying to determine the origin of MCS reflections. Reflections M4 and M2 correspond roughly to the boundaries between Unit I and Sub-

F84. Composite of core recovery, depth, lithostratigraphy, age, density and velocity, **p. 162.**

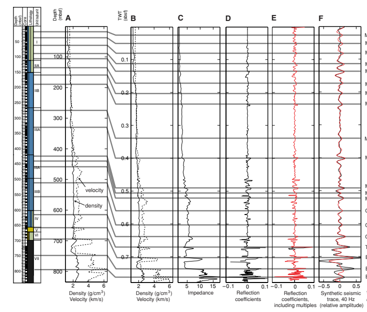

F85. Seismic reflection data and a synthetic seismic trace, **p. 164.**

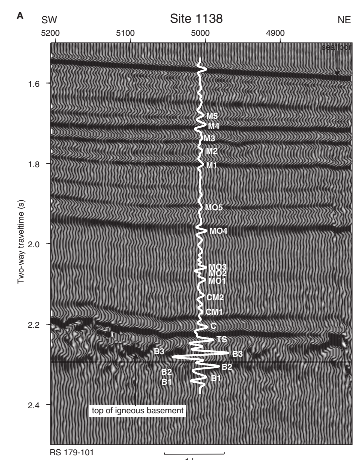

unit IIA, and Subunits IIA and IIB, respectively. M5 is a product of density variations within Unit I (Fig. **F84**).

Five late Maastrichtian to late Oligocene reflections (labeled MO1–MO5) result largely from velocity variations within Subunit IIIA of nannofossil chalk. The largest amplitude reflection in this section, both in the synthetic seismograms and in the MCS data, is MO4. It is associated with an increase in both velocity and density within Subunit IIIA (Figs. **F83, F84**). MO4 shows no obvious link with a change in lithology and, thus, may represent a diagenetic effect. MO3 cannot be linked to any MCS reflection, and both MO1 and MO2 correspond to a broad MCS reflection at 2.05 s TWT (Fig. **F85A, F85B**).

Two reflections labeled CM1 and CM2 from the mid-Campanian–upper Maastrichtian section (Subunit IIIB) in the synthetic seismogram may correspond to low-amplitude MCS reflections between 2.1 and 2.15 s TWT. We correlate the prominent MCS reflection labeled C to the upper part of the Cenomanian–Turonian–mid-Campanian Unit IV (Fig. **F84**). Reflection C is caused by the velocity increase from foraminifer-bearing chalk (Subunit IIIB) to chalk interbedded with claystone in Unit IV. Synthetic reflection C is deeper than the equivalent MCS reflection (Fig. **F85**), indicating cumulative errors in transit time summation based on incomplete core data. Reflection TS (Turonian–Santonian) marks the boundary between Units IV and V, accompanied by a marked increase in velocity from chalk/claystone to glauconite-bearing sandstone/claystone. Similar lithologic units, found at other sites overlying acoustic basement (e.g., 1135 and 1137), typically result in large-amplitude reflections.

The basement reflection B3 constitutes the most prominent reflection of the entire section on the synthetic and can be tied to the MCS data unambiguously (Fig. **F85A, F85B**). However, its relative amplitude in the synthetic trace scales more realistically if transmission losses are considered (Fig. **F85B**). The large negative peak underlying the positive basement reflection is caused by a major velocity inversion at 720–740 mbsf (Fig. **F83**). Reflection B2 is associated with the top of relatively unweathered basalt flows, and B1 is caused by a velocity inversion resulting from the transition from pahoehoe basalt flows to underlying aa flows and transitional/rubbly units at ~795 mbsf (see **"Igneous Petrology,"** p. 46). Reflections B1 and B2 interfere in the MCS data to form a broad reflection that cannot be clearly separated into two distinct reflections at Site 1138 (Fig. **F85B**). However, the distance between these two reflections increases southeast of Site 1138, where they diverge to form two separate MCS reflections. The basement units in the vicinity of Site 1138 show an apparent dip to the southwest on the MCS data. The MCS data indicate no faults; thus, this dip appears to represent the geometry of local basalt-flow emplacement.

REFERENCES

Applegate, J.L., and Wise, S.W., Jr., 1987. Eocene calcareous nannofossils, Deep Sea Drilling Project Site 605, upper continental rise off New Jersey U.S.A. *In* van Hinte, J.E., Wise, S.W., Jr., et al., *Init. Repts. DSDP,* 93: Washington (U.S. Govt. Printing Office), 685–698.

Arthur, M.A., Schlanger, S.O., and Jenkyns, H.C., 1987. The Cenomanian-Turonian oceanic anoxic event, II. Palaeoceanographic controls on organic-matter production and preservation. *In* Brooks, J., and Fleet, A.J. (Eds.), *Marine Petroleum Source Rocks*. Geol. Soc. Spec. Publ. London, 26:401–420.

Barling, J., 1990. Heard and McDonald Islands. *In* LeMasurier, W.E., and Thomson, J.W. (Eds.), *Volcanoes of the Antarctic Plate and Southern Ocean*. Am. Geophys. Union, Antarct. Res. Ser., 48:435–441.

Berggren, W.A., 1992. Neogene planktonic foraminifer magnetobiostratigraphy of the southern Kerguelen Plateau (Sites 747, 748, and 751). *In* Wise, S.W., Jr., Schlich, R., et al., *Proc. ODP, Sci. Results,* 120 (Pt. 2): College Station, TX (Ocean Drilling Program), 631–647.

Bitschene, P.R., Mehl, K.W., and Schmincke, H.-U., 1992. Composition and origin of marine ash layers and epiclastic rocks from the Kerguelen Plateau, southern Indian Ocean (Legs 119 and 120). *In* Wise, S.W., Jr., Schlich, R., et al., *Proc. ODP, Sci. Results,* 120: College Station, TX (Ocean Drilling Program), 135–149.

Brooks, C.K., Larsen, L.M., and Nielsen, T.F.D., 1991. Importance of iron-rich tholeiitic magmas at divergent plate margins: a reappraisal. *Geology,* 19:269–272.

Burnett, J.A., 1998. Upper Cretaceous. *In* Bown, P.R. (Ed.), *Calcareous Nannofossil Biostratigraphy:* London (Chapman & Hall), 132–199.

Cita, M.B., Coccioni, R., Edwards, A.R., Monechi, S., Morgans, H.E.G., Strong, C.P., Watkins, D.K., and Webb, P.-N., 1997. Nannofossils and foraminifera. *In* Hannah, M.J., and Raine, J.I. (Eds.), *Southern Ocean Late Cretaceous/Early Cenozoic Biostratigraphic Datums*. Inst. Geol. Nucl. Sci., Sci. Rep., 97/4:5–10.

Davies, H.L., Sun, S.-S., Frey, F.A., Gautier, I., McCulloch, M.T., Price, R.C., Bassias, Y., Klootwijk, C.T., and Leclaire, L., 1989. Basalt basement from the Kerguelen Plateau and the trail of the DUPAL plume. *Contrib. Mineral. Petrol.,* 103:457–469.

Dickin, A.P., 1981. Isotope geochemistry of Tertiary igneous rocks from the Isle of Skye, N. W. Scotland. *J. Petrol.,* 22:155–189.

Fisher, R.L., 1997. Bathymetry of the Southern Indian Ocean. *General Bathymetric Chart of the Oceans*. GEBCO, Sheet 97.1.

Fitton, J.G., Saunders, A.D., Larsen, L.M., Hardarson, B.S., and Norry, M.J., 1998. Volcanic rocks from the southeast Greenland Margin at 63°N: composition, petrogenesis, and mantle sources. *In* Saunders, A.D., Larsen, H.C., and Wise, S.W., Jr. (Eds.), *Proc. ODP, Sci. Results,* 152: College Station, TX (Ocean Drilling Program), 331–350.

Fitton, J.G., Saunders, A.D. Norry, M.J., Hardarson, B.S., and Taylor, R., 1997. Thermal and chemical structure of the Iceland plume. *Earth Planet. Sci. Lett.,* 153:97–208.

Harwood, D.M., and Maruyama, T., 1992. Middle Eocene to Pleistocene diatom biostratigraphy of Southern Ocean sediments from the Kerguelen Plateau, Leg 120. *In* Wise, S.W., Jr., Schlich, R., et al., *Proc. ODP, Sci. Results,* 120: College Station, TX (Ocean Drilling Program), 683–733.

Heider, F., Geiss, C., Dunlop, D.J., and Inokuchi, H., 1992. Rock-magnetic investigation of basalts from the southern Kerguelen Plateau (Leg 120). *In* Wise, S.W., Jr., Schlich, R., et al., *Proc. ODP, Sci. Results,* 120: College Station, TX (Ocean Drilling Program), 79–87.

Hooper, P.R., 1997. The Columbia River flood basalt province: current status. *In* Mahoney, J.J., and Coffin, M.F. (Eds.), *Large Igneous Provinces: Continental, Oceanic and Planetary Flood Volcanism.*Geophys. Monogr., Am. Geophys. Union, 100:1–28.

Huber, B.T., 1990. Maestrichtian planktonic foraminifer biostratigraphy of the Maud Rise (Weddell Sea, Antarctica): ODP Leg 113 Holes 689B and 690C. *In* Barker, P.F., Kennett, J.P., et al., *Proc. ODP, Sci. Results,* 113: College Station, TX (Ocean Drilling Program), 489–513.

————, 1991. Paleogene and early Neogene planktonic foraminifer biostratigraphy of Sites 738 and 744, Kerguelen Plateau (southern Indian Ocean). *In* Barron, J., Larsen, B., et al., *Proc. ODP, Sci. Results,* 119: College Station, TX (Ocean Drilling Program), 427–449.

————, 1992. Upper Cretaceous planktic foraminiferal biozonation for the Austral Realm. *Mar. Micropaleontol.,* 20:107–128.

Inokuchi, H., and Heider, F., 1992. Paleolatitude of the southern Kerguelen Plateau inferred from the paleomagnetic study of Upper Cretaceous basalts. *In* Wise, S.W., Jr., Schlich, R., et al., *Proc. ODP, Sci. Results,* 120: College Station, TX (Ocean Drilling Program), 89–96.

Jenkins, D.G., 1971. New Zealand Cenozoic planktonic foraminifera. *N.Z. Geol. Surv. Paleontol. Bull.,* 42:1–278.

Krasheninnikov, V.A., and Basov, I.A., 1983. Stratigraphy of Cretaceous sediments of the Falkland Plateau based on planktonic foraminifers, Deep Sea Drilling Project, Leg 71. *In* Ludwig, W.J., Krasheninnikov, V.A., et al., *Init. Repts. DSDP,* 71: Washington (U.S. Govt. Printing Office), 789–820.

Ludwig, W.J., Krasheninnikov, V.A., et al., 1983. *Init. Repts. DSDP,* 71: Washington (U.S. Govt. Printing Office).

Macdonald, G.A., and Katsura, T., 1964. Chemical composition of Hawaiian lavas. *J. Petrol.,* 5:82–133.

Mackensen, A., Barrera, E., and Hubberten, H.-W., 1992. Neogene circulation in the southern Indian Ocean: evidence from benthic foraminifers, carbonate data, and stable isotope analyses (Site 751). *In* Wise, S.W., Jr., Schlich, R., et al., *Proc. ODP, Sci. Results,* 120: College Station, TX (Ocean Drilling Program), 867–878.

Pearce, J.A., and Norry, M.J., 1979. Petrogenetic implications of Ti, Zr, Y and Nb variations in volcanic rocks. *Contrib. Mineral. Petrol.,* 69:33–47.

Perch-Nielsen, K., 1985. Mesozoic calcareous nannofossils. *In* Bolli, H.M., Saunders, J.B., and Perch-Nielsen, K. (Eds.), *Plankton Stratigraphy:* Cambridge (Cambridge Univ. Press), 329–426.

Pringle, M.S., Storey, M., and Wijbrans, J., 1994. $^{40}Ar/^{39}Ar$ geochronology of mid-Cretaceous Indian ocean basalts: constraints on the origin of large flood basalt. *Eos,* 75:728.

Quilty, P.G., 1992. Upper Cretaceous planktonic foraminifers and biostratigraphy, Leg 120, southern Kerguelen Plateau. *In* Wise, S.W., Jr., Schlich, R., et al., *Proc. ODP, Sci. Results,* 120: College Station, TX (Ocean Drilling Program), 371–392.

Royer, J.-Y., and Coffin, M.F., 1992. Jurassic to Eocene plate tectonic reconstructions in the Kerguelen Plateau region. *In* Wise, S.W., Jr., Schlich, R., et al., *Proc. ODP, Sci. Results,* 120: College Station, TX (Ocean Drilling Program), 917–928.

Sandwell, D.T., and Smith, W.H.F., 1997. Marine gravity anomaly from Geosat and ERS-1 satellite altimetry. *J. Geophys. Res.,* 102:10039–10054.

Schlanger, S.O., and Jenkyns, H.C., 1976. Cretaceous oceanic anoxic events: causes and consequences. *Geol. Mijnbouw,* 55:179–184.

Sliter, W.V., 1977. Cretaceous foraminifers from the southwestern Atlantic Ocean, Leg 36, Deep Sea Drilling Project. *In* Barker, P.F., Dalziel, I.W.D., et al., *Init. Repts. DSDP,* 36: Washington (U.S. Govt. Printing office), 519–573.

Storey, M., Mahoney, J.J., and Saunders, A.D., 1997. Cretaceous basalts in Madagascar and the transition between plumes and continental lithosphere mantle sources. *In* Mahoney, J.J., and Coffin, M.F. (Eds.), *Large Igneous Provinces: Continental, Oceanic and Planetary Flood Volcanism.* Am. Geophys. Union, Geophys. Mon., 100:96–122.

Storey, M., Pringle, M.S., Coffin, M.F., and Wijbrans, J., 1996. Geochemistry and geochronology of Kerguelen Plateau basalts: results from ODP Legs 119 and 120. *Eos,* 76:123.

Stott, L.D., and Kennett, J.P., 1990. Antarctic Paleogene planktonic foraminifer biostratigraphy: ODP Leg 113, Sites 689 and 690. *In* Barker, P.F., Kennett, J.P., et al., *Proc. ODP, Sci. Results,* 113: College Station, TX (Ocean Drilling Program), 549–569.

Sun, S.-S., and McDonough, W.F., 1989. Chemical and isotopic systematics of oceanic basalts: implications for mantle composition and processes. *In* Saunders, A.D., and Norry, M.J. (Eds.), *Magmatism in the Ocean Basins*. Geol. Soc. Spec. Publ. London, 42:313–345.

Thierstein, H.R., 1974. Calcareous nannoplankton, Leg 26, Deep Sea Drilling Project. *In* Davies, T.A., Luyendyk, B.P., et al., *Init. Repts. DSDP,* 26: Washington (U.S. Govt. Printing Office), 619–667.

Varol, O., 1992. Polycyclolithaceae. *Newsl. Stratigr.,* 27:93–128.

Walker, G.P.L., 1989. Spongy pahoehoe in Hawai'i: a study of vesicle-distribution patterns in basalt and their significance. *Bull. Volcanol.,* 51:199–209.

Watkins, D.K., 1992. Upper Cretaceous nannofossils from Leg 120, Kerguelen Plateau, Southern Ocean. *In* Wise, S.W., Jr., Schlich, R., et al., *Proc. ODP, Sci. Results,* 120: College Station, TX (Ocean Drilling Program), 343–370.

Watkins, D.K., Wise, S.W., Jr., Pospichal, J.J., and Crux, J., 1996. Upper Cretaceous calcareous nannofossil biostratigraphy and paleoceanography of the Southern Ocean. *In* Moguilevsky, A., and Whatley, R. (Eds.), *Microfossils and Oceanic Environments:* Univ. of Wales (Aberystwyth Press), 355–381.

Weaver, B., and Tarney, J., 1984. Empirical approach to estimating the composition of the continental crust. *Nature,* 310:575–577.

Wei, W., and Thierstein, H.R., 1991. Upper Cretaceous and Cenozoic calcareous nannofossils of the Kerguelen Plateau (southern Indian Ocean) and Prydz Bay (East Antarctica). *In* Barron, J., Larsen, B., et al., *Proc. ODP, Sci. Results,* 119: College Station, TX (Ocean Drilling Program), 467–494.

Weis, D., Bassias, Y., Gautier, I., and Mennesier, J.-P., 1989. DUPAL anomaly in existence 115 Ma ago: evidence from isotopic study of the Kerguelen Plateau (South Indian Ocean). *Geochim. Cosmochim. Acta,* 53:2125–2131.

Wise, S.W., Jr., 1983. Mesozoic and Cenozoic calcareous nannofossils recovered by Deep Sea Drilling Project Leg 71 in the Falkland Plateau region, Southwest Atlantic Ocean. *In* Ludwig, W.J., Krasheninnikov, V.A., et al., *Init. Repts. DSDP,* 71 (Pt. 2): Washington (U.S. Govt. Printing Office), 481–550.

Wonders, A.A.H., 1992. Cretaceous planktonic foraminiferal biostratigraphy, Leg 122, Exmouth Plateau, Australia. *In* von Rad, U., Haq, B.U., et al., *Proc. ODP, Sci. Results,* 122: College Station, TX (Ocean Drilling Program), 587–599.

Figure F1. Satellite-derived free-air gravity map of the Kerguelen Plateau (after Sandwell and Smith, 1997). The five plateau province sectors are northern, central, southern, Elan Bank, and Labuan Basin (outlined in white). Leg 183 and previous (Legs 119 and 120) ODP sites are indicated by stars and circles, respectively (black = basement sites; white = sediment sites). Squares indicate dredge and piston core sites where igneous rock (black) and sediment (white) were recovered. (**Figure shown on next page.**)

Figure F1. (Caption on previous page.)

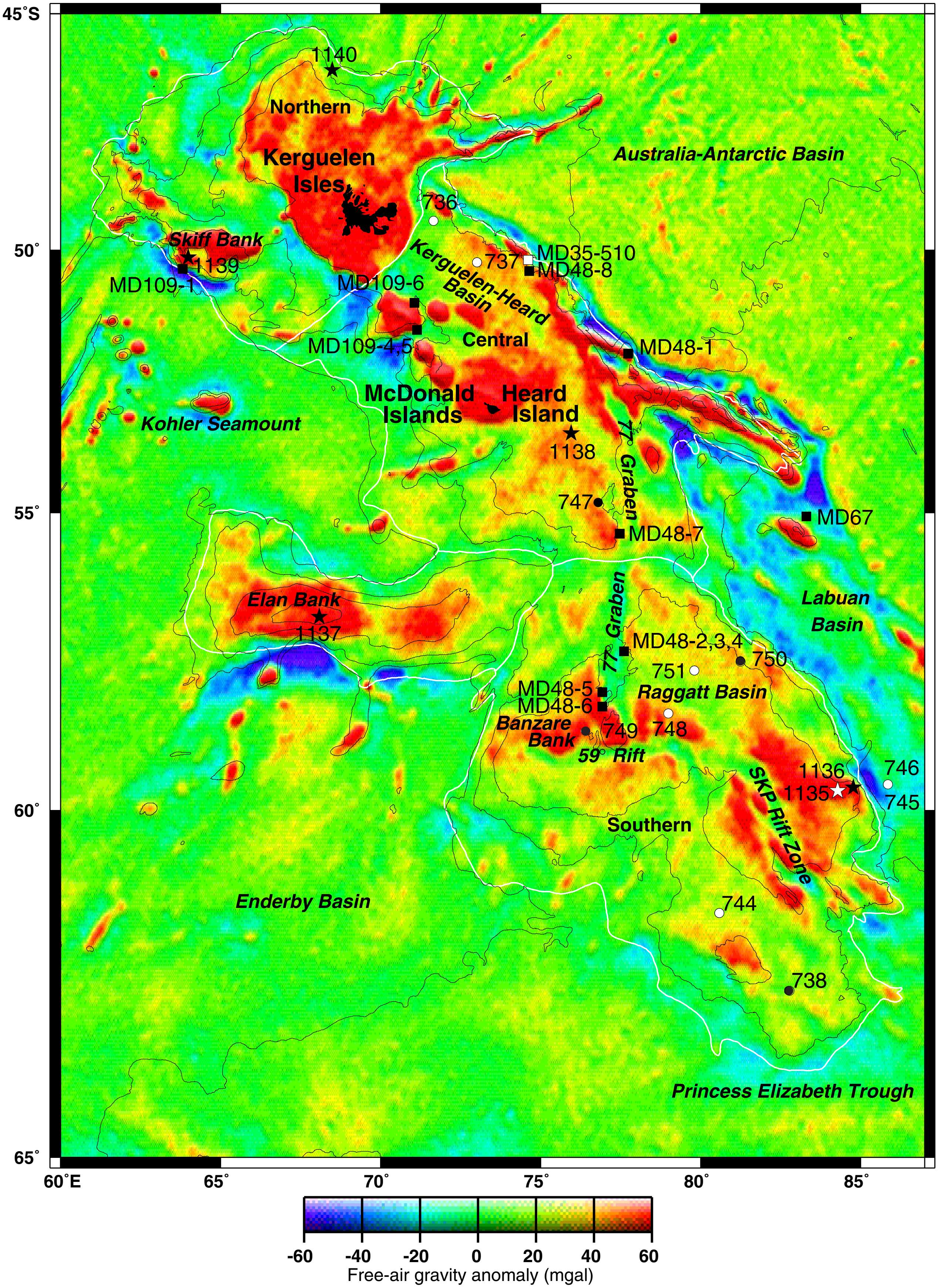

Figure F2. Location of Site 1138 and site-survey data. Navigation for *Rig Seismic* survey 179, line 101 (RS179/101), data is shown in Julian day:time. Bathymetric contour interval = 500 m (Fisher, 1997).

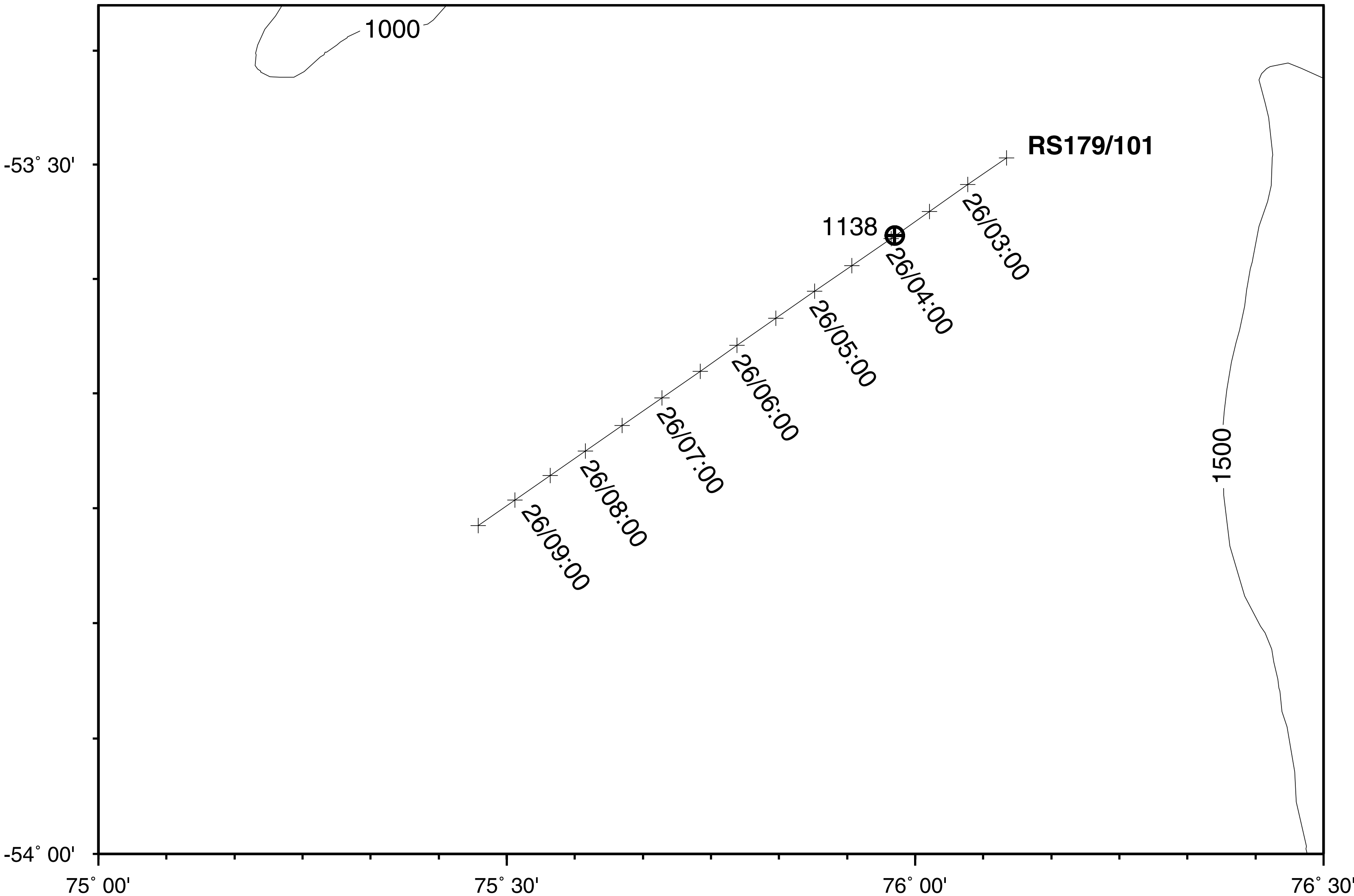

Figure F3. *Rig Seismic* RS179/101 multichannel seismic profile across Site 1138. Vertical exaggeration = ~16 at the seafloor.

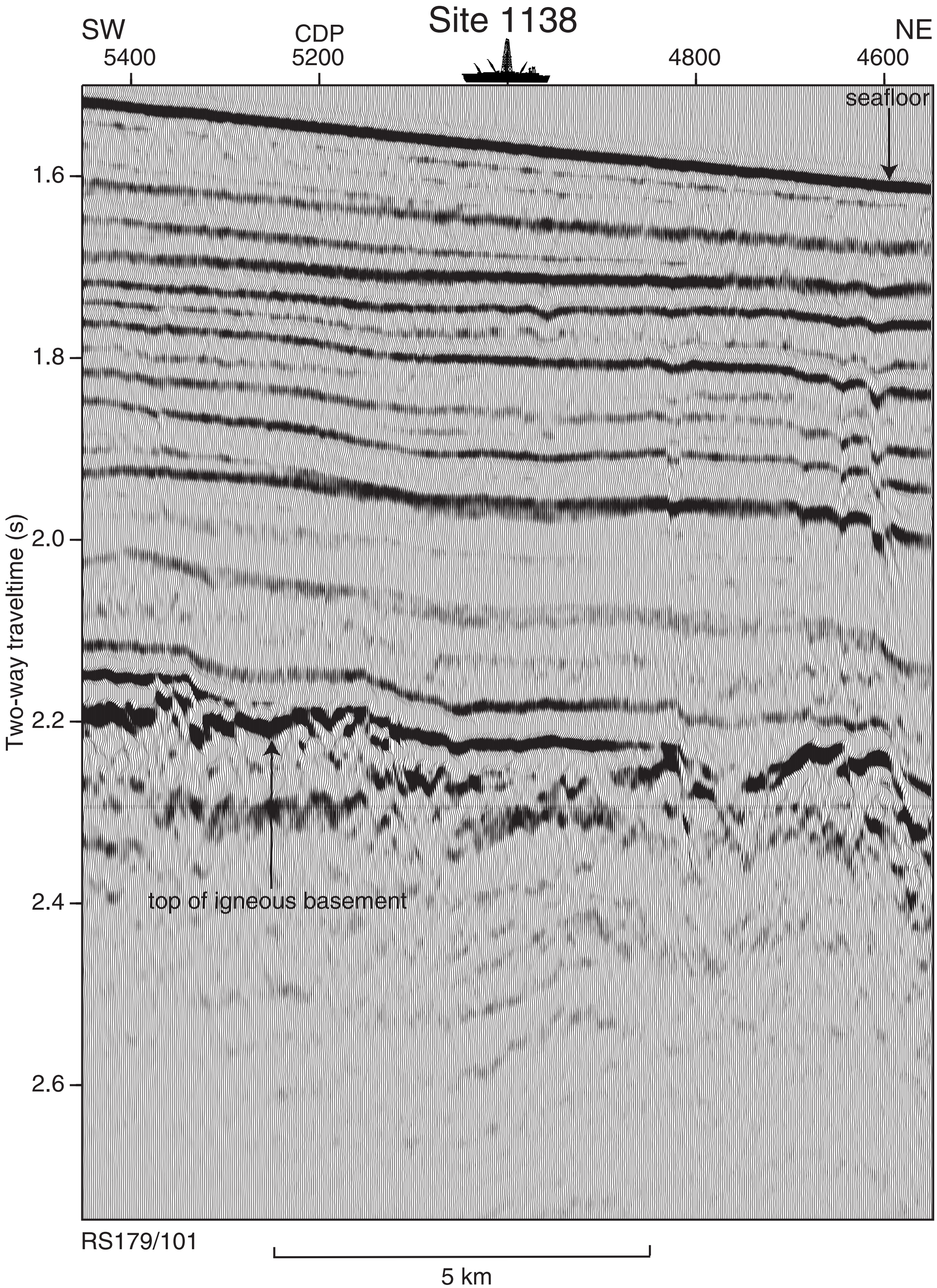

Figure F4. Composite stratigraphic section for Site 1138 showing core recovery, a simplified summary of lithology, lithologic unit boundaries, ages of units, and names of lithologies. The lithologic symbols are explained in Figure F3, p. 57, in the "Explanatory Notes" chapter.

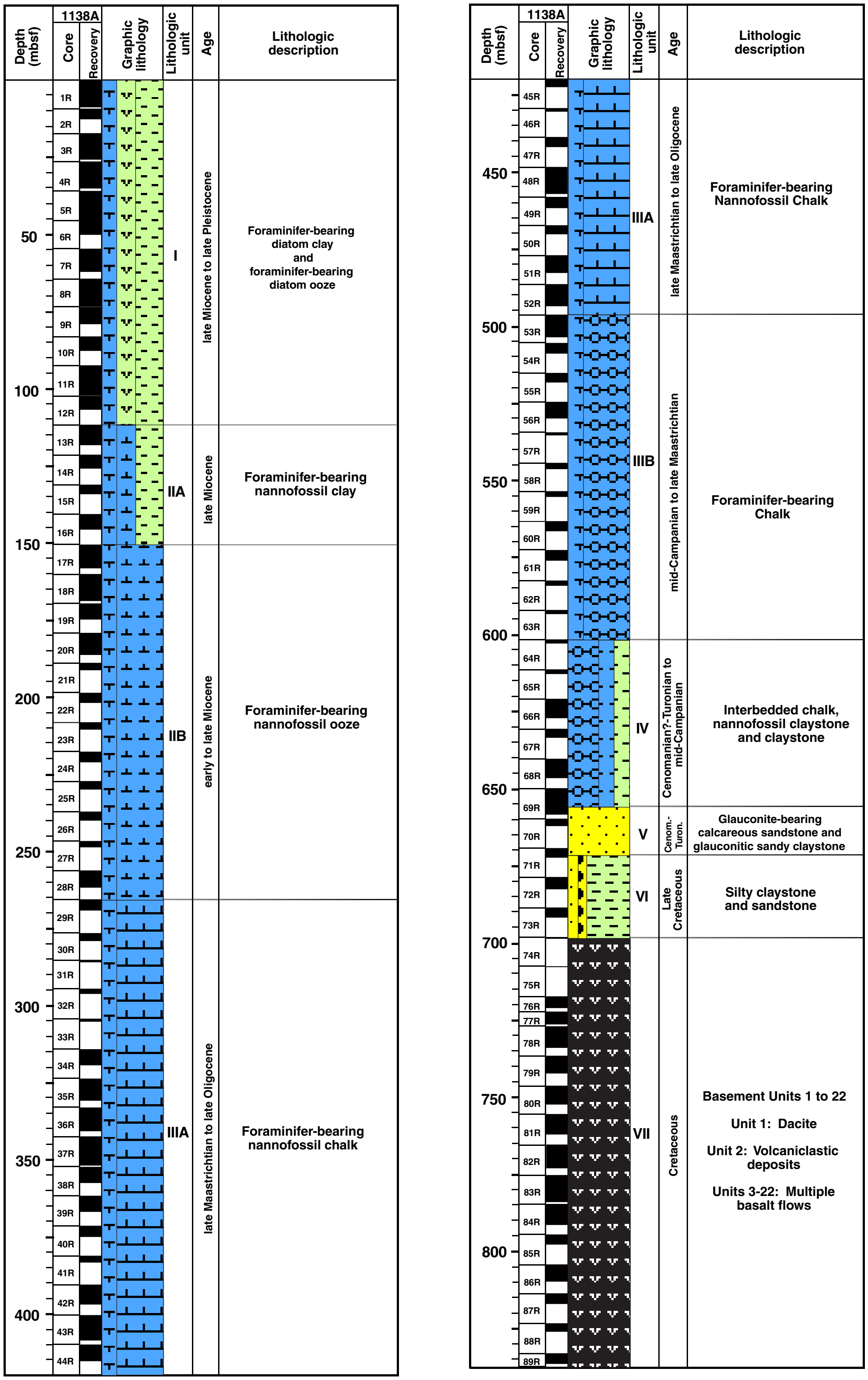

Figure F5. Schematic diagram showing sediment facies recovered in cores from lithologic Units IV through VI.

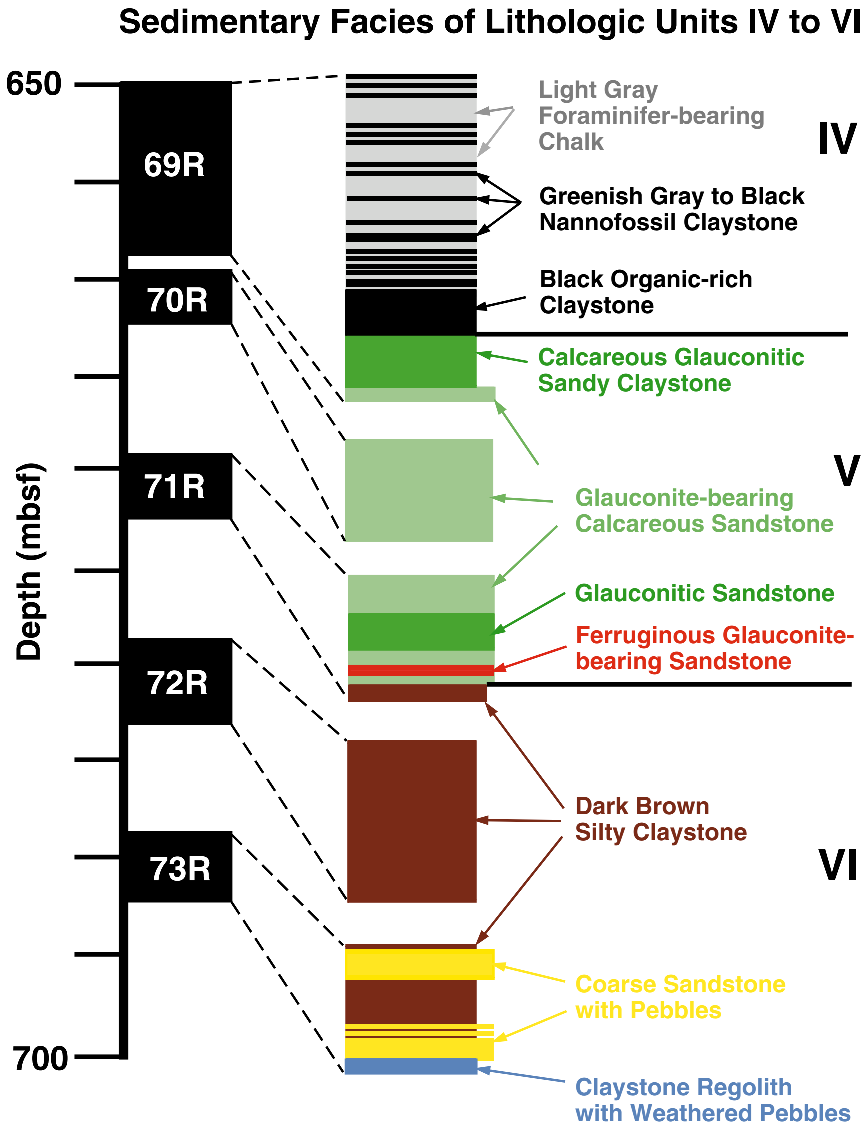

Figure F6. Dark gray to black nannofossil claystone intervals in Unit IV from intervals (**A**) 183-1138A-69R-3, 2–22 cm, and (**B**) 183-1138A-69R-3, 80–100 cm. (Continued on next page.)

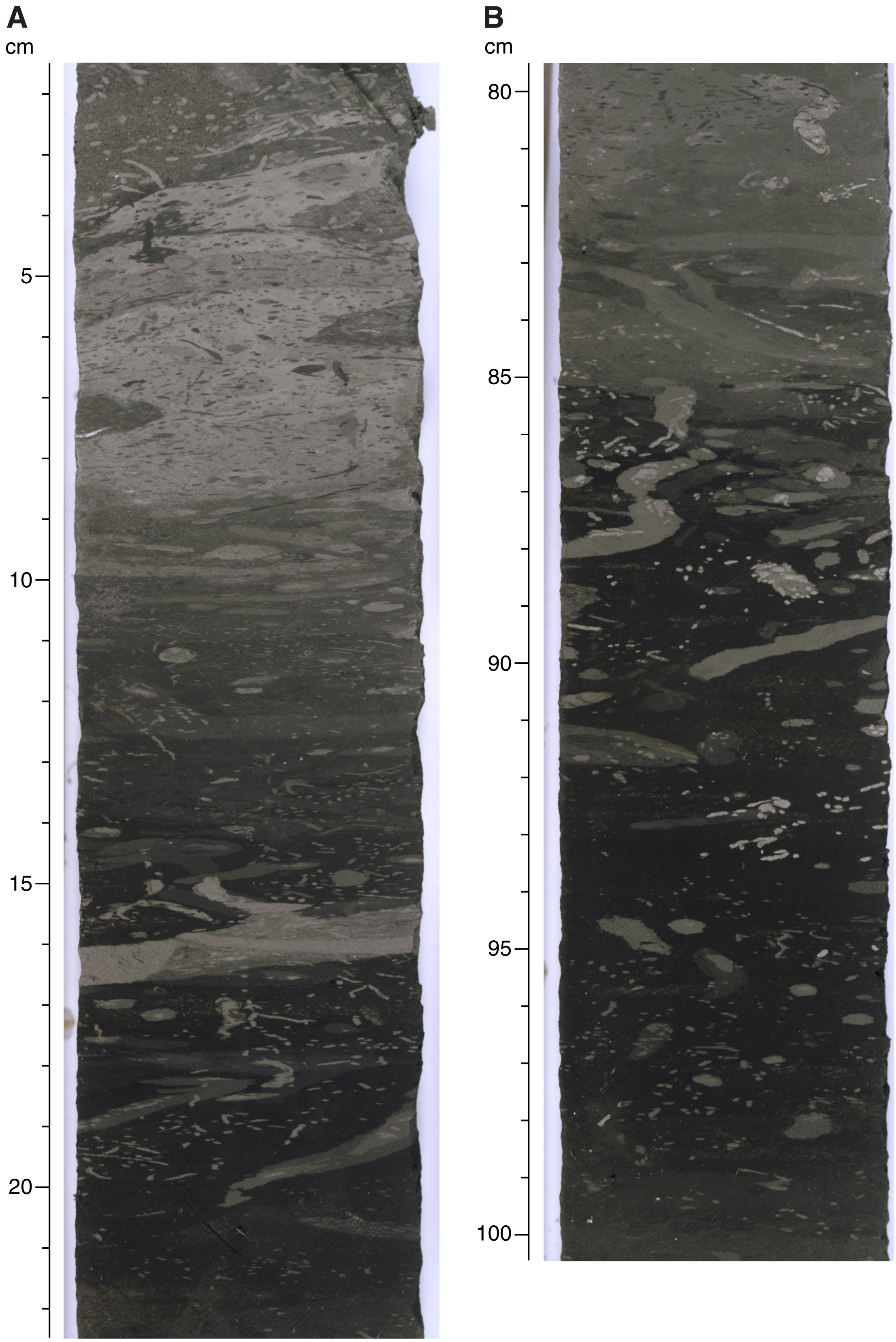

Figure F6 (continued). Top of black organically rich claystone at base of Unit IV from (**C**) interval 183-1138A-69R-5, 14–35 cm.

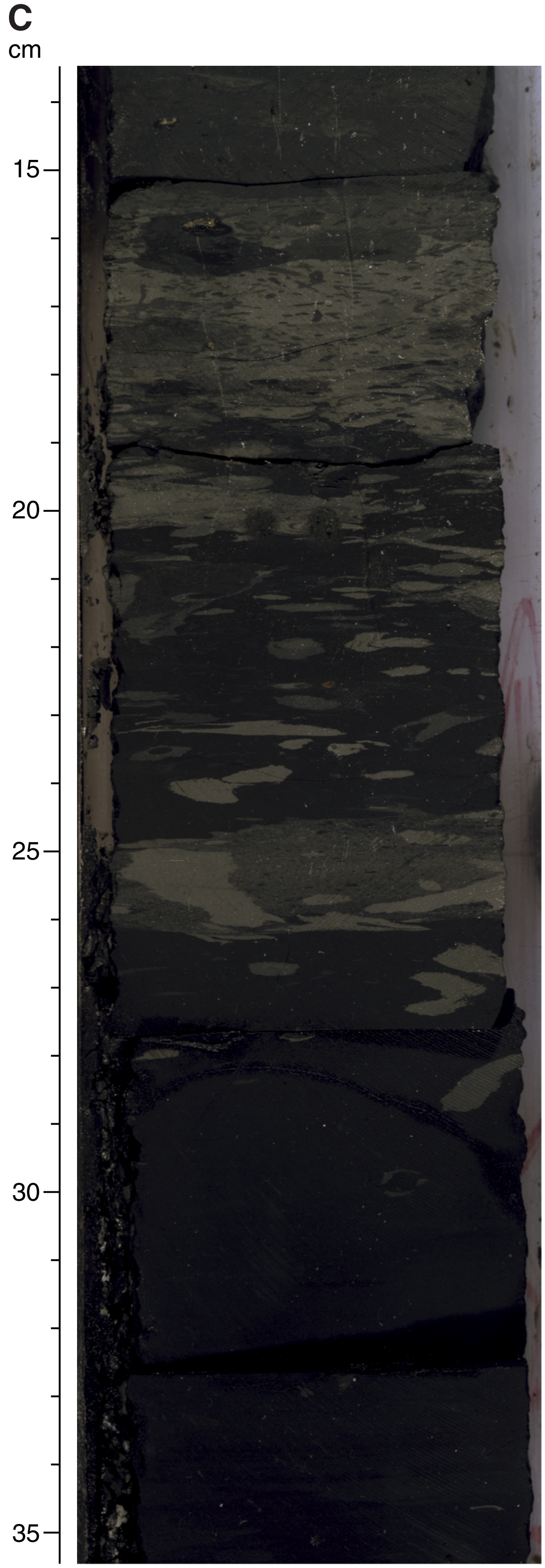

Figure F7. Examples of variable lithologies in Unit V. **A.** Rusty brown glauconite-bearing calcareous sandstone with white serpulid worm tubes (interval 183-1138A-70R-1, 128–144 cm). **B.** Darker colored glauconitic sandstone (interval 183-1138A-71R-1, 85–105 cm). (Continued on next page.)

Figure F7 (continued). **C.** Orange or rusty brown well-laminated, glauconite-bearing silty fine sandstone over glauconite-bearing calcareous sandstone with scattered pebbles (interval 183-1138A-71R-2, 92–115 cm). **D.** Glauconite-bearing calcareous sandstone at the base of Unit V. The wavy contact at ~137–138 cm is the boundary between units V and VI (interval 183-1138A-71R-2, 130–150 cm).

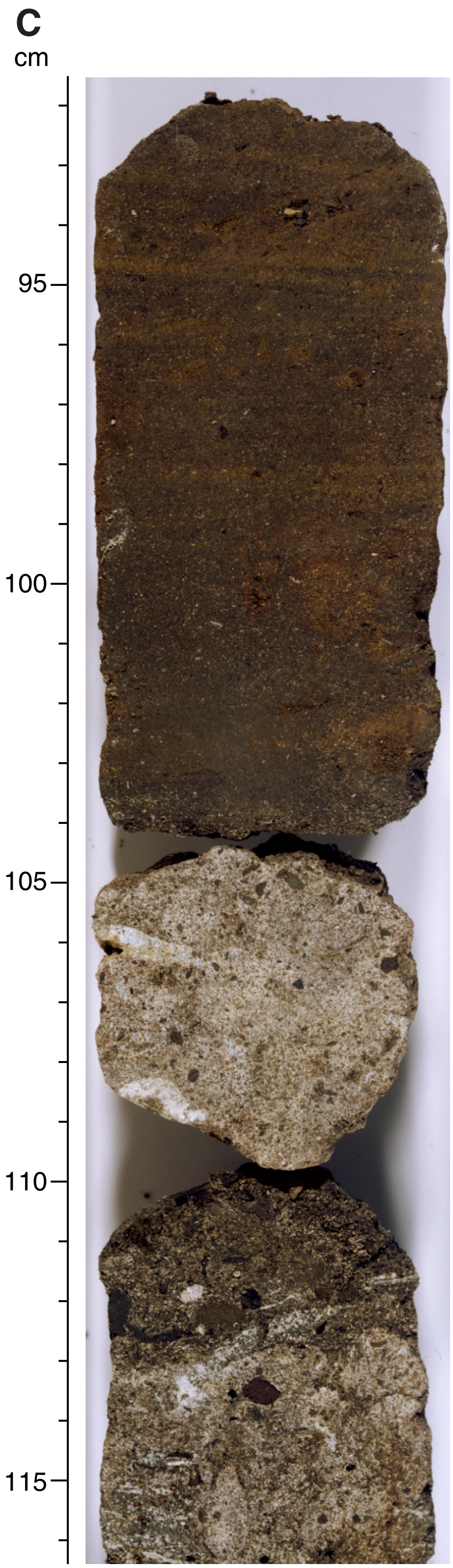

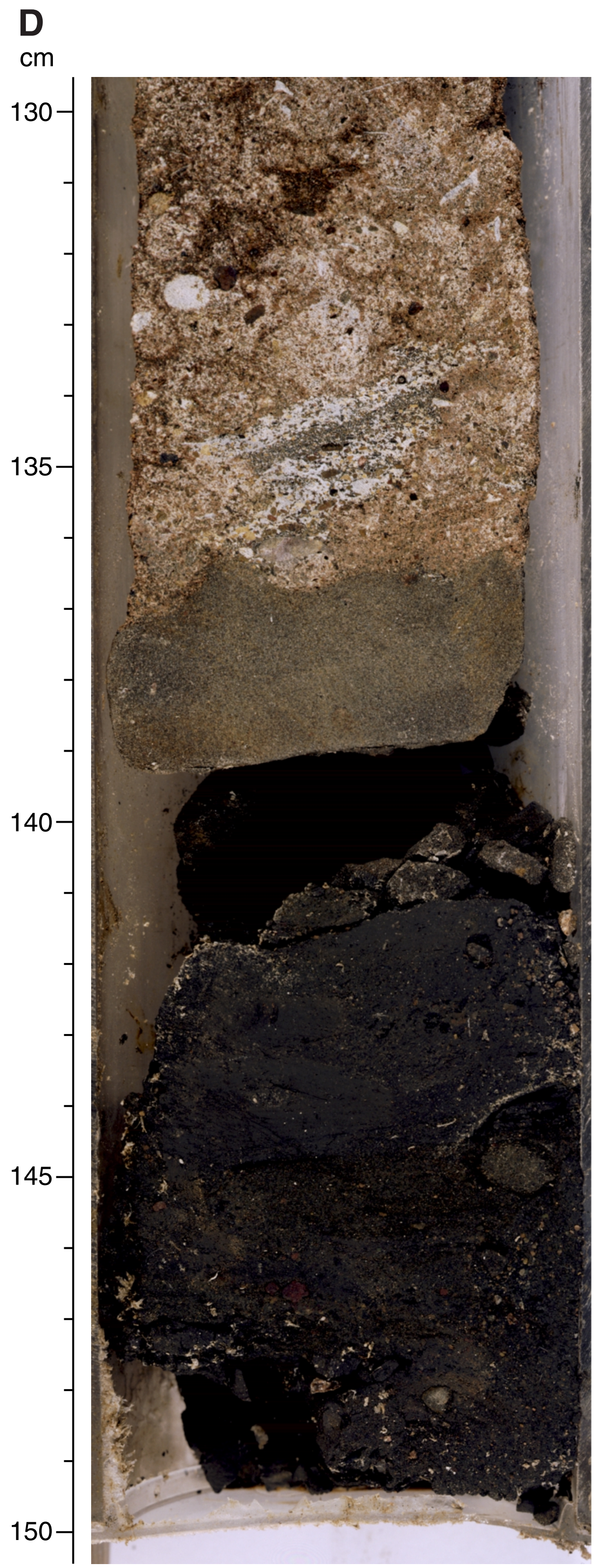

Figure F8. Rusty brown glauconite-bearing calcareous sandstone of Unit V showing abundant white serpulid worm tubes. **A.** Interval 183-1138A-70R-1, 112–122 cm. (Continued on next page.)

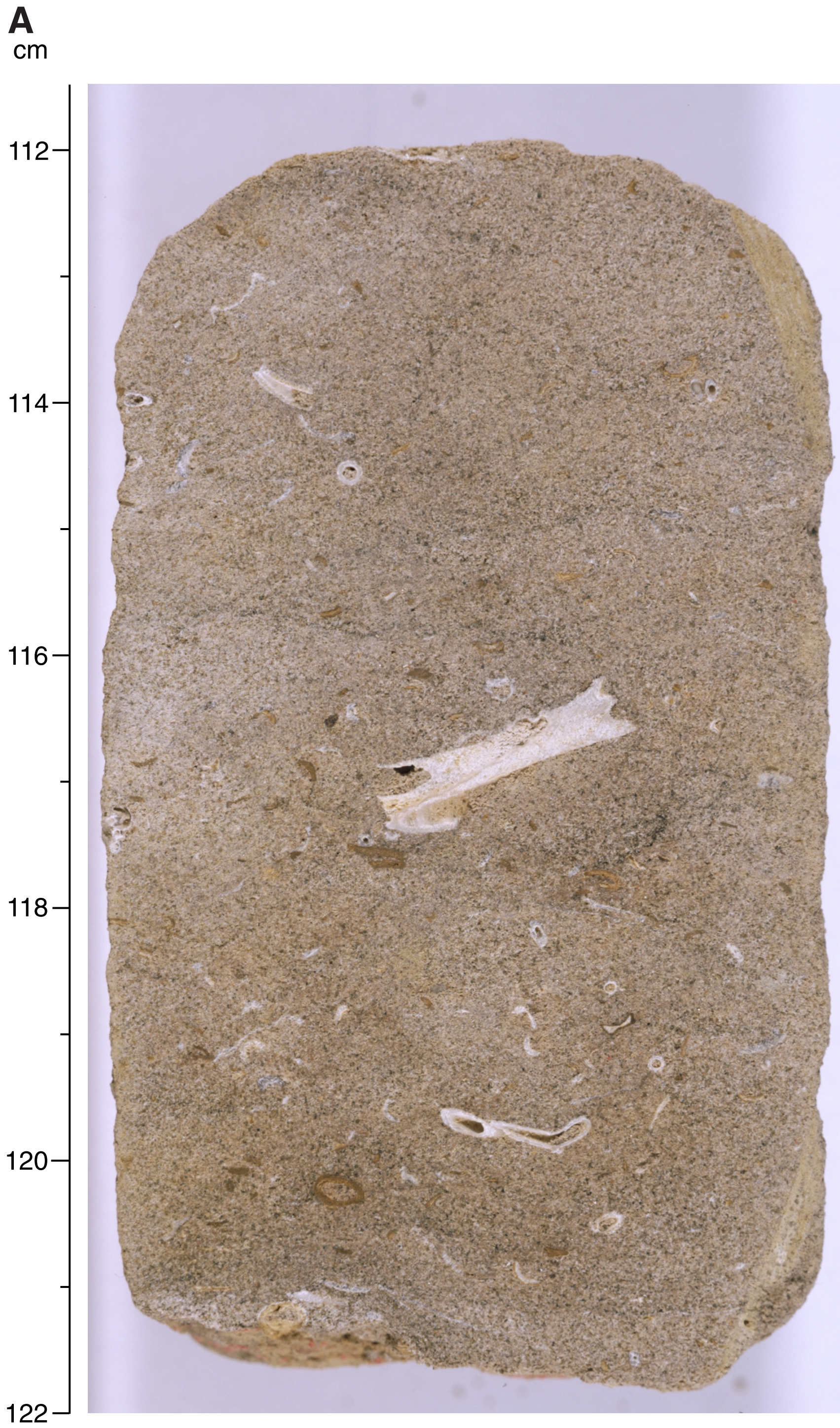

Figure F8 (continued). B. Interval 183-1138A-70R-2, 23–38.

Figure F9. Examples of sediments in Unit VI. Brown sandy clayey siltstone containing abundant wood fragments and common shell fragments from intervals (**A**) 183-1138A-72R-1, 11–23 cm, and (**B**) 183-1138A-72R-1, 34–50 cm. Note large (2 cm) wood fragment in (B) at 50 cm. (Continued on next page.)

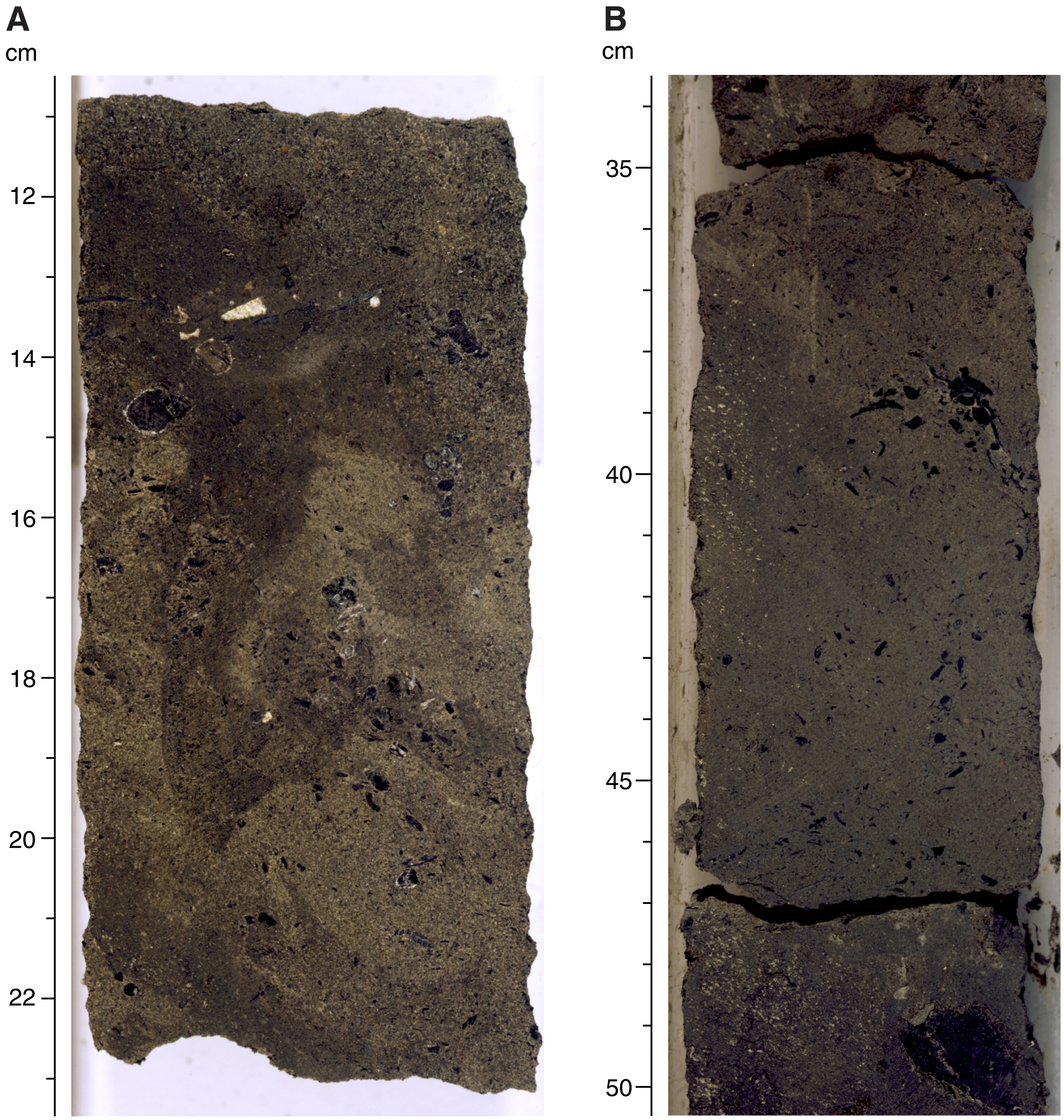

Figure F9 (continued). Dark brown silty claystone with wood fragments from intervals (**C**) 183-1138A-72R-3, 8–20 cm, and (**D**) 183-1138A-72R-3, 20–32 cm.

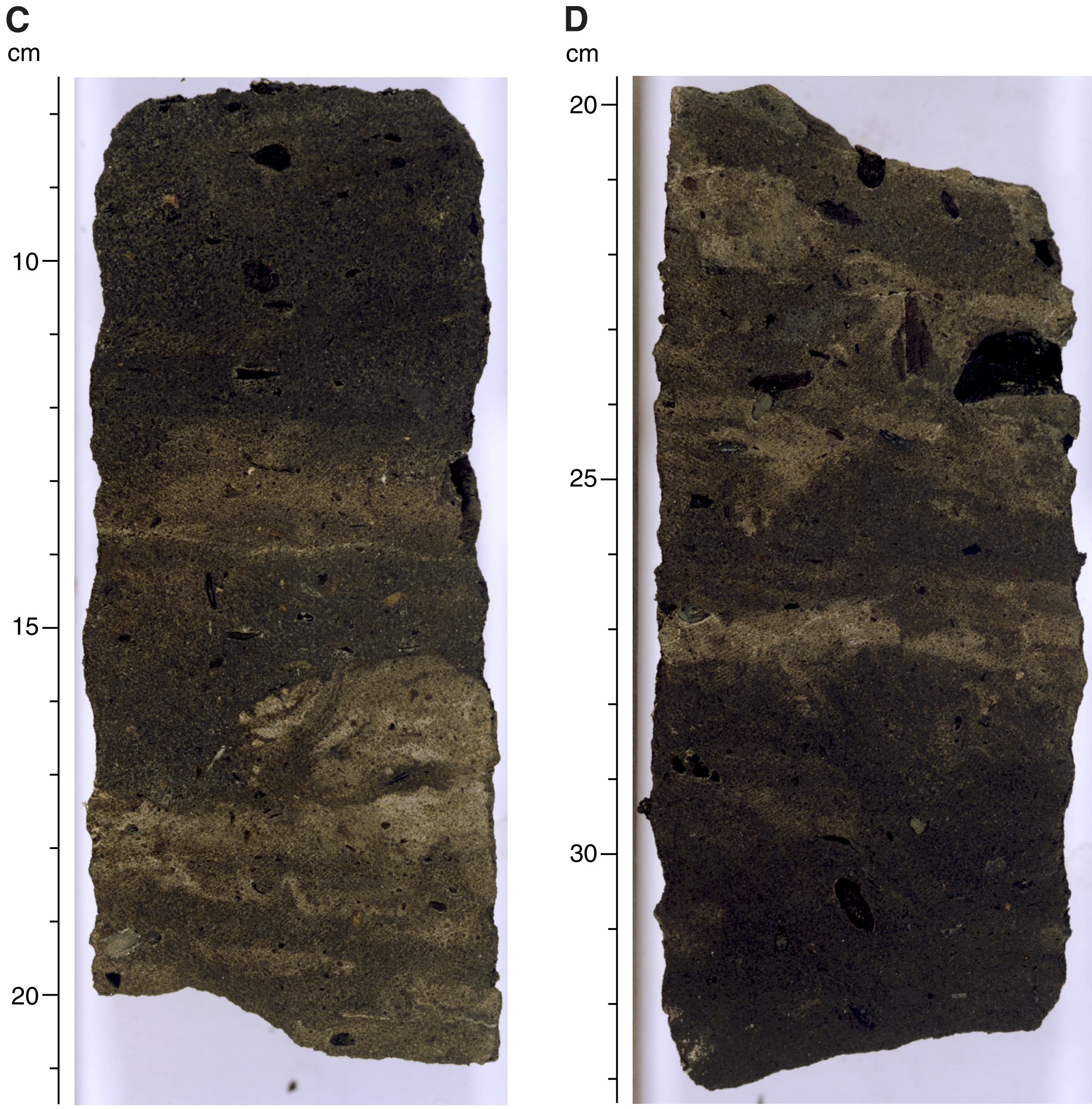

Figure F10. Sandstone beds of variegated color and lithology in Unit VI. **A.** Coarse sandstone with abundant granules and pebbles (interval 183-1138A-73R-1, 18–34 cm). **B.** Drilling disturbed medium to coarse sandstone with pebbles and two brown silty clay beds (interval 183-1138A-73R-3, 38–64 cm).

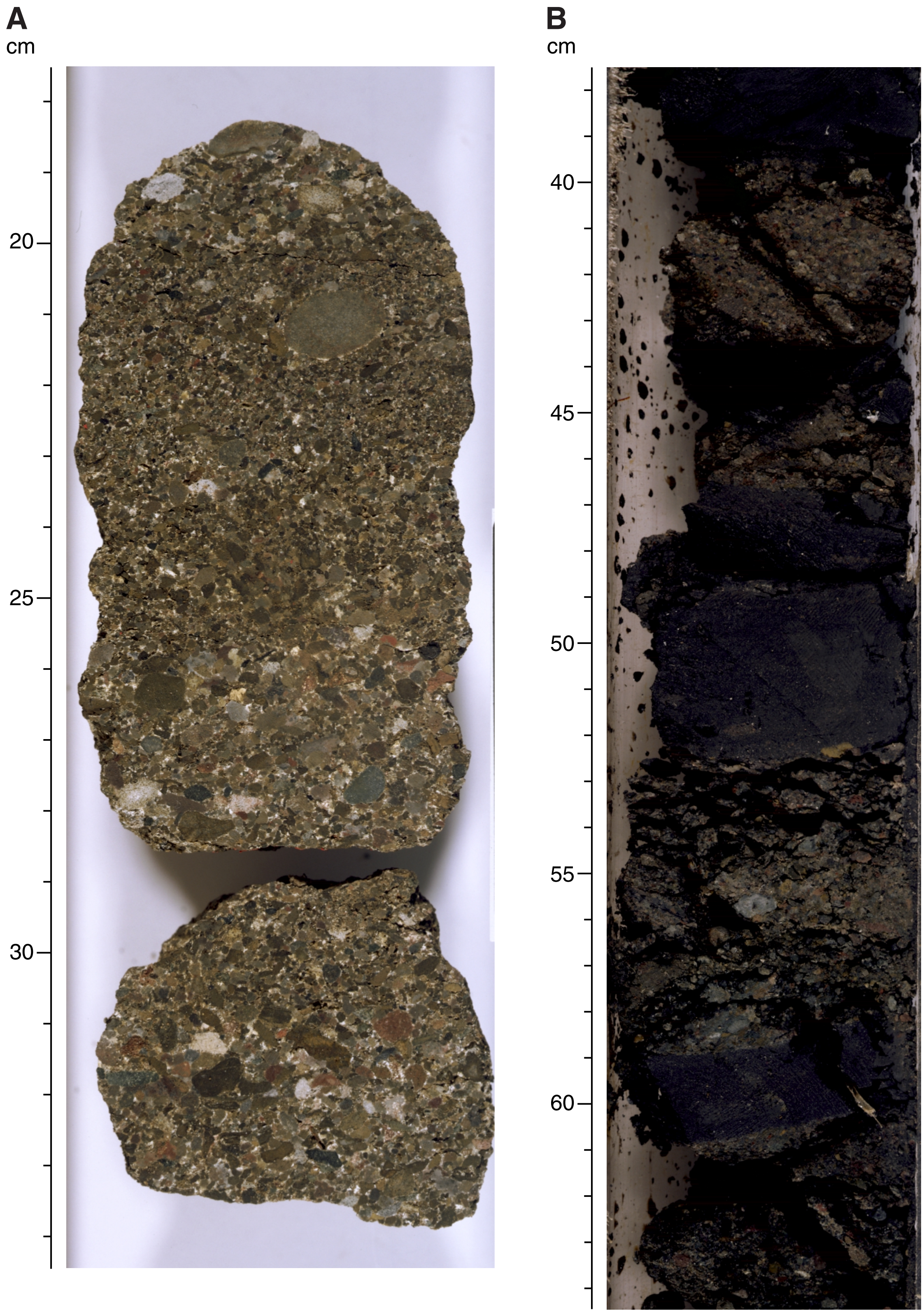

Figure F11. Highly weathered regolith of variegated colors at the base of Unit VI, which overlies the top of volcanic basement. **A.** Claystone containing large red-colored pebbles of weathered basalt plus coarse sand and granules (interval 183-1138A-73R-3, 122–150 cm). **B.** Brecciated material in regolith (interval 183-1138A-73R-CC, 0–15 cm).

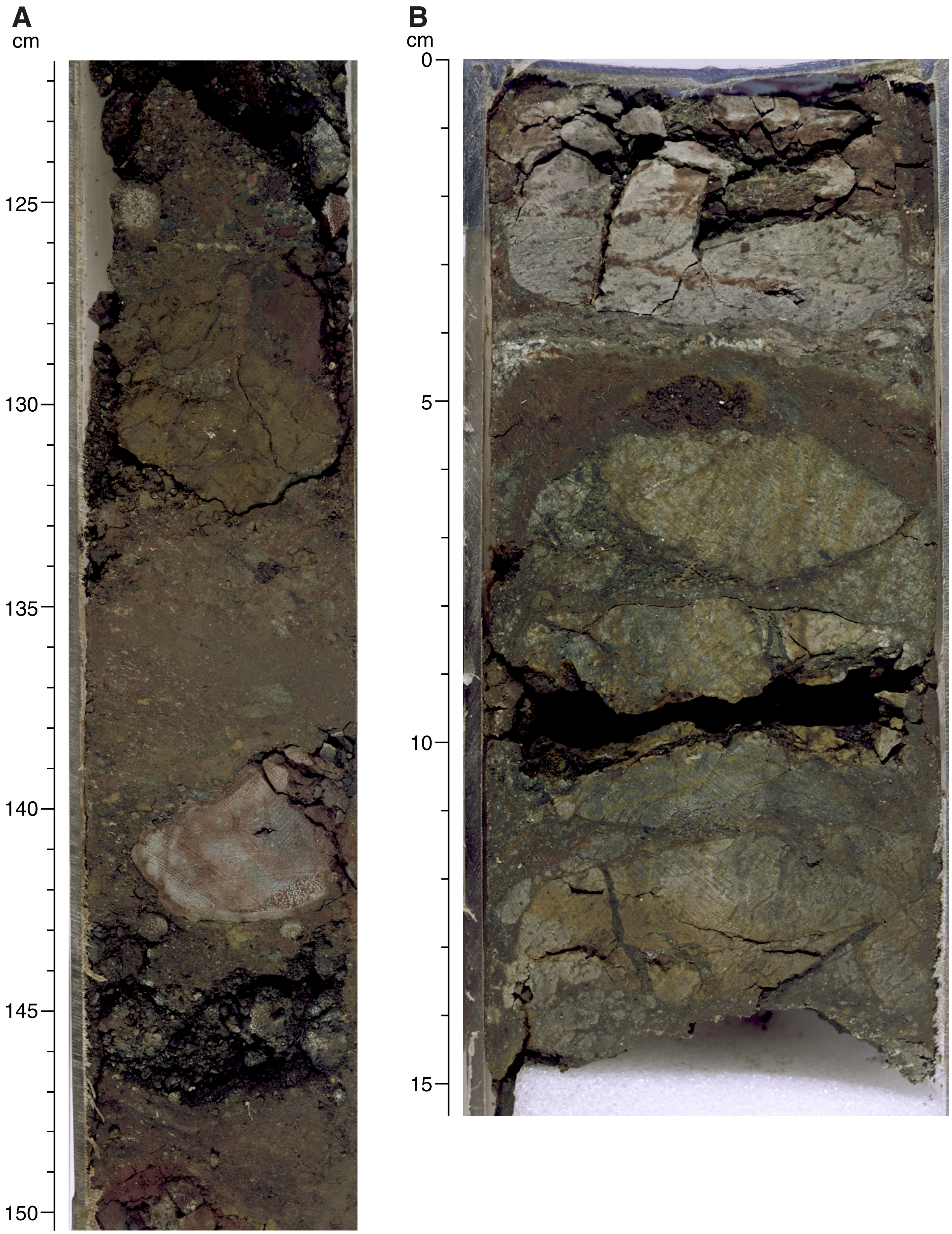

Figure F12. Site 1138 age-depth plot.

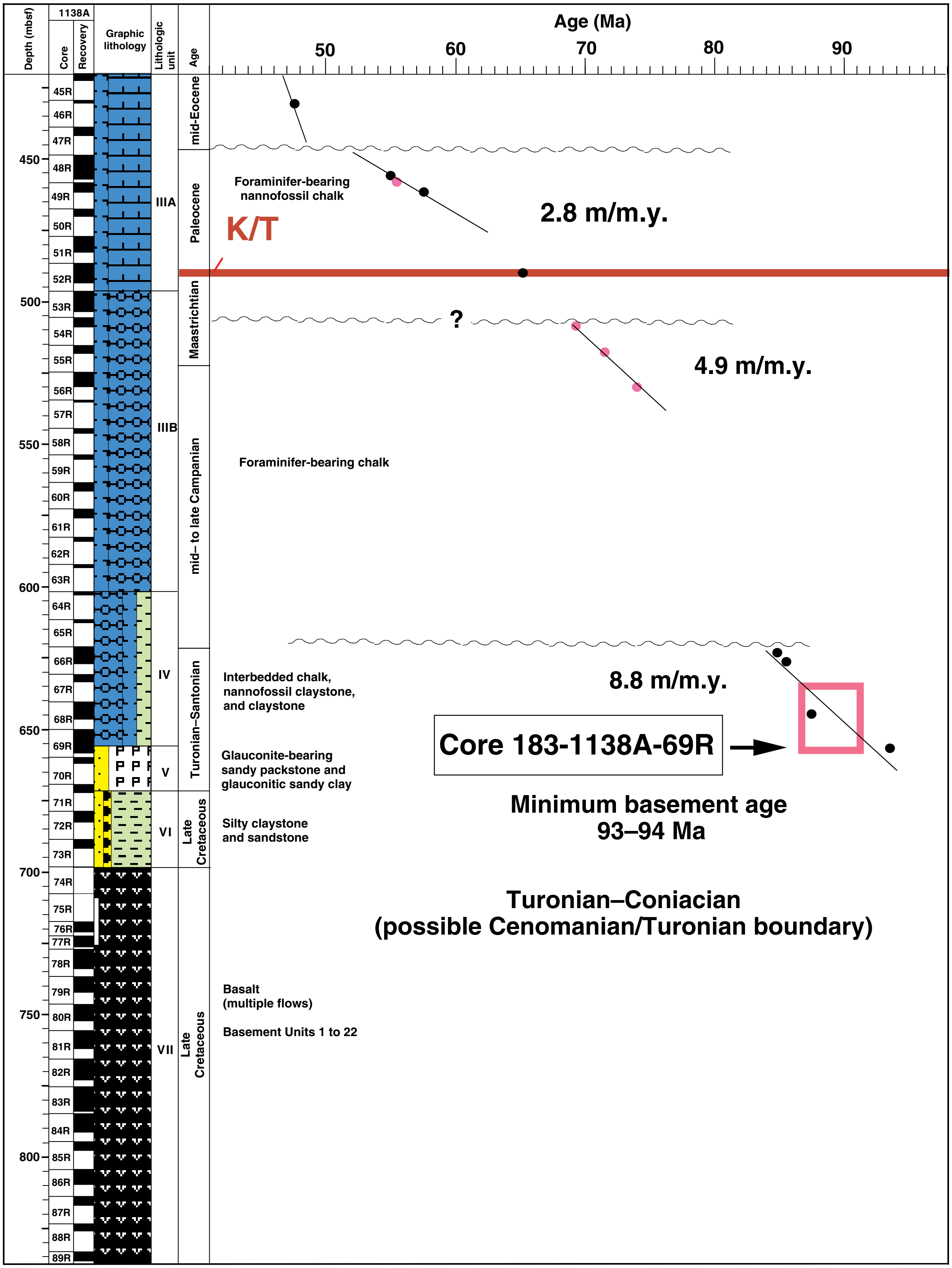

Figure F13. Stratigraphic section of the volcaniclastic succession in basement Unit 2 (Hole 1138A). Grain-size distribution is indicated by the width of the column, with clay (C), silt (Z), sand (S), granule (G), and pebble (P) fields represented. Core and section information is shown in italics. Depth in mbsf is noted for the top of each section. Lava-flow unit numbers (Subunit 2A through Subunit 2O) are shown in boxes. Lava-flow Subunit 2B shows a poorly sorted interval in reworked sediments. Note that the range of pumice clast sizes (designated by altered pumice breccia pattern) is much greater than the range of lithic clast sizes.

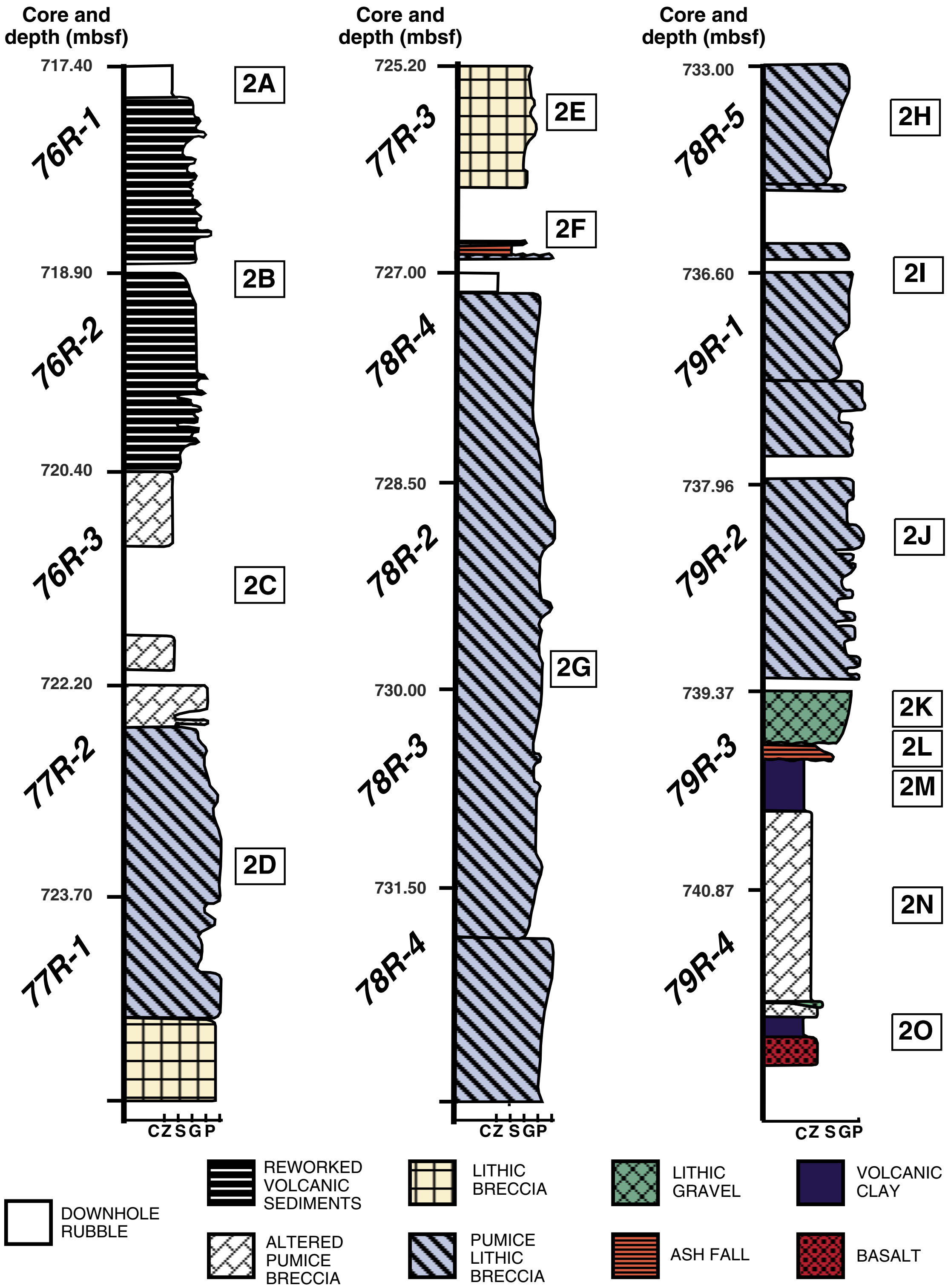

Figure F14. Close-up photograph of interval 183-1138A-78R-4, 69–81 cm, showing a typical clast distribution in the more pumice-rich parts of the pumice lithic breccia units (basement Subunits 2D, 2G, 2H, 2I, and 2J). Pumice clasts are rounded to subangular, and lithic clasts are abundant in the matrix.

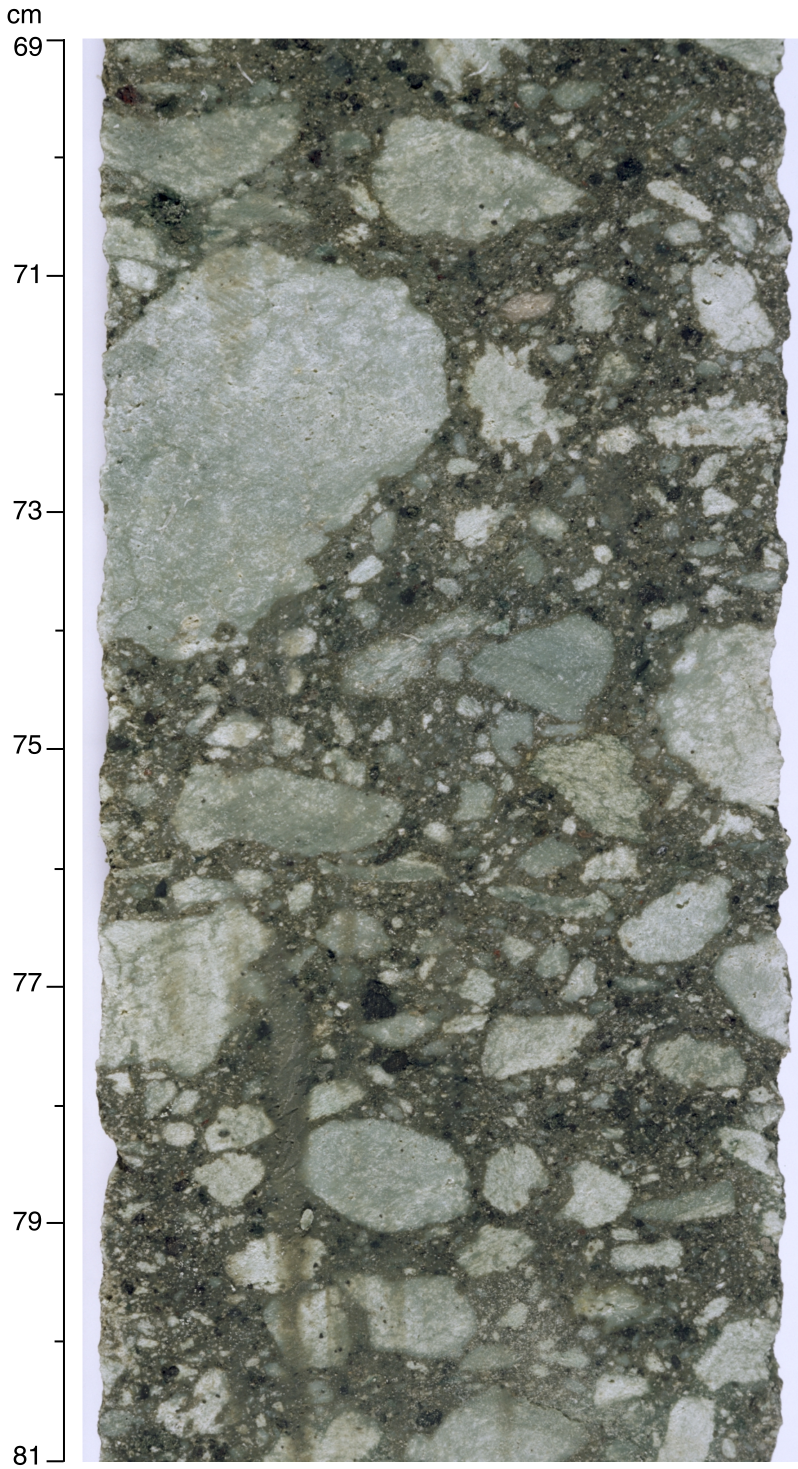

Figure F15. Close-up photograph of interval 183-1138A-77R-2, 136–146 cm, showing a typical clast distribution in the lithic breccia (basement Subunit 2E). Lithic fragments are dominantly trachytic and basaltic and show a range of alteration states. In this interval, lithic clasts are more abundant than pumice clasts.

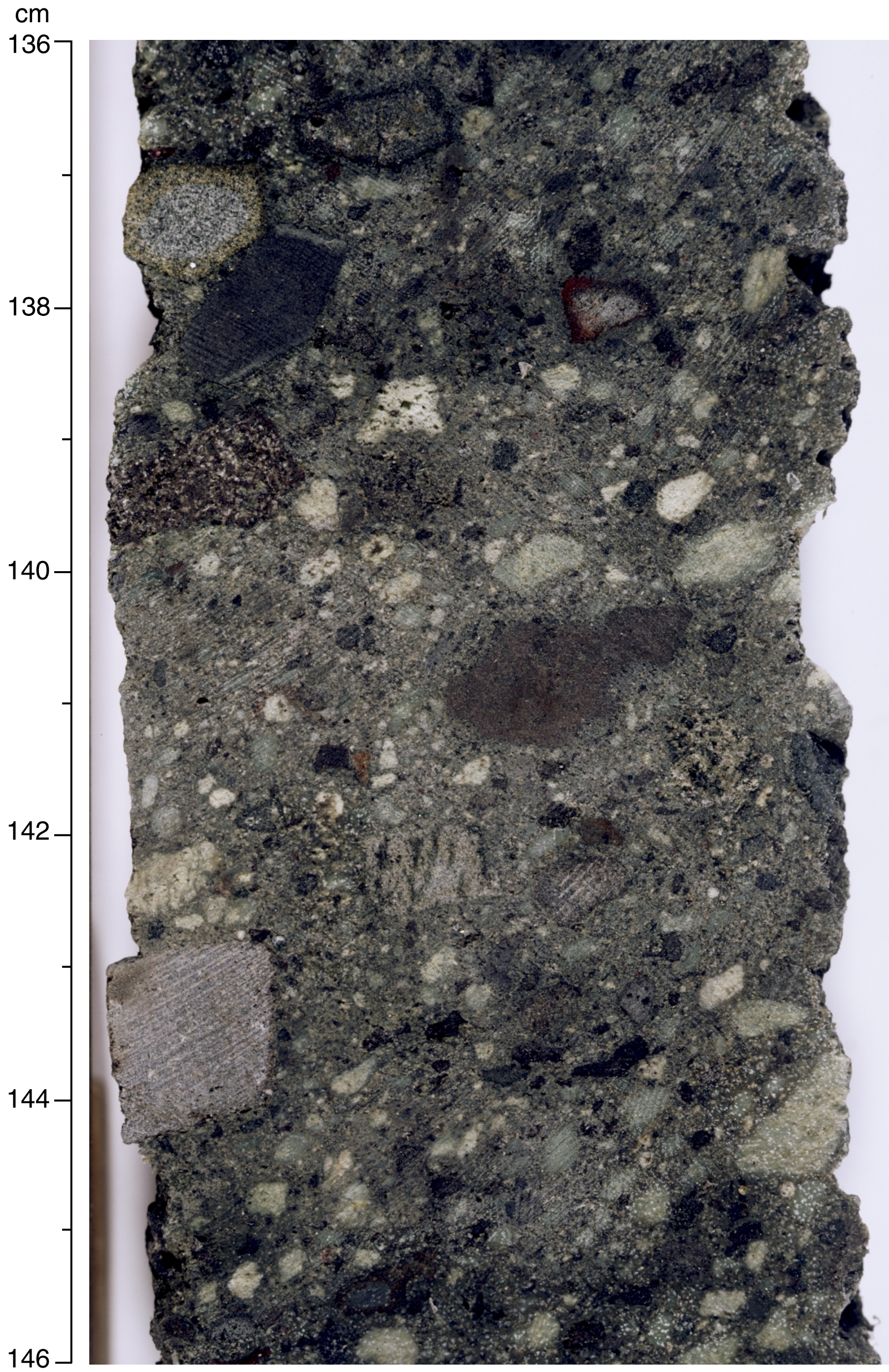

Figure F16. Close-up photograph of interval 183-1138A-78R-4, 145–151 cm, showing a large ragged pumice clast in a pumice lithic breccia (basement Subunit 2H). Pumice clasts are up to 3 cm diameter but more commonly range from 0.5 cm to 2 cm in size. Almost all pumice clasts show alteration to pale green clay minerals.

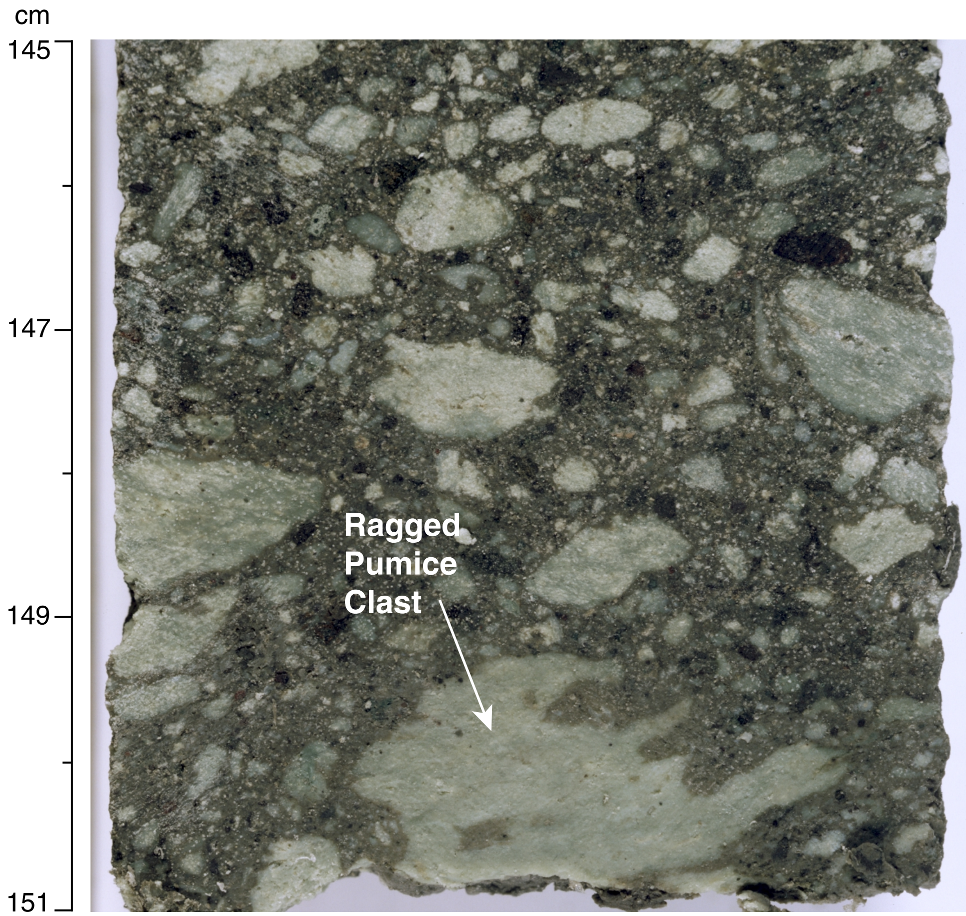

Figure F17. Photomicrographs showing the nature of the pumiceous matrix in the pumice-lithic breccia and lithic breccia units. **A.** Pumice-rich matrix in the pumice lithic breccia, pumice clasts, and a few small lithic clasts. **B.** Pumice-rich matrix, a shattered K-feldspar crystal (left center), pumice clasts, and a basaltic lithic clast (lower right). (Continued on next two pages.)

A

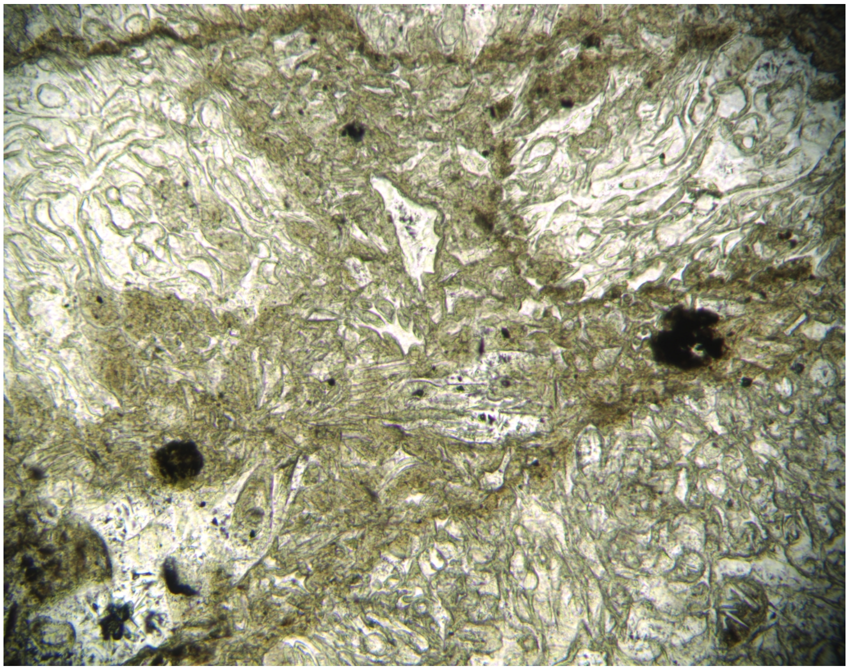

B

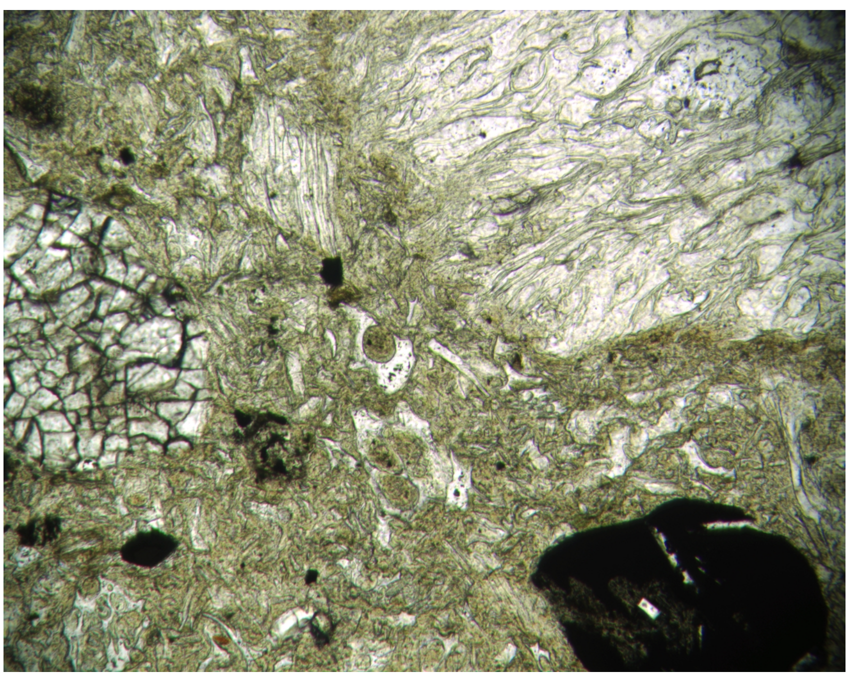

Figure F17 (continued). **C.** Internal texture in a pumice clast showing sections through tube vesicles and incipient alteration to pale green clay minerals. **D.** Pumice-rich matrix and lithic (basalt) and pumice fragments in a pumice lithic breccia. (Continued on next page.)

C

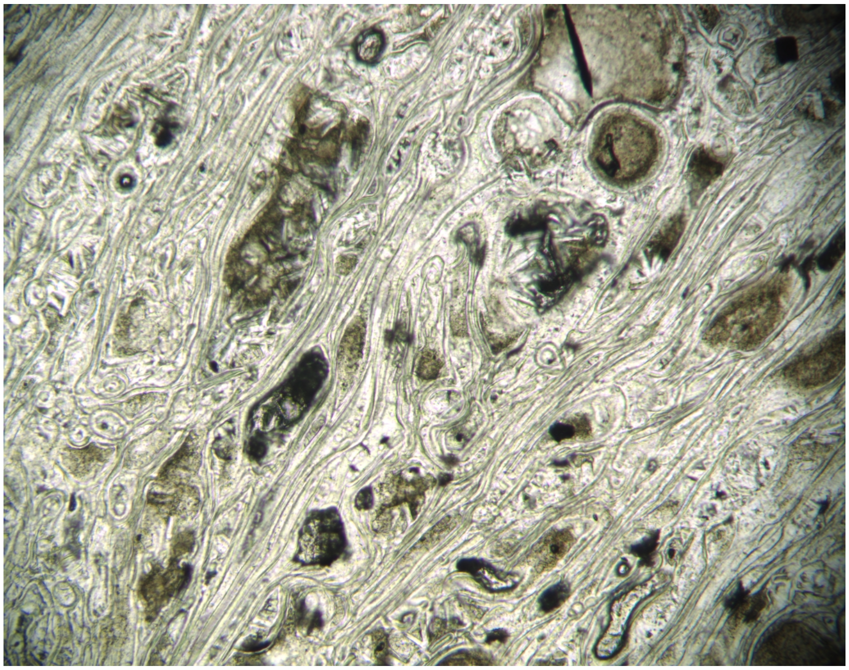

D

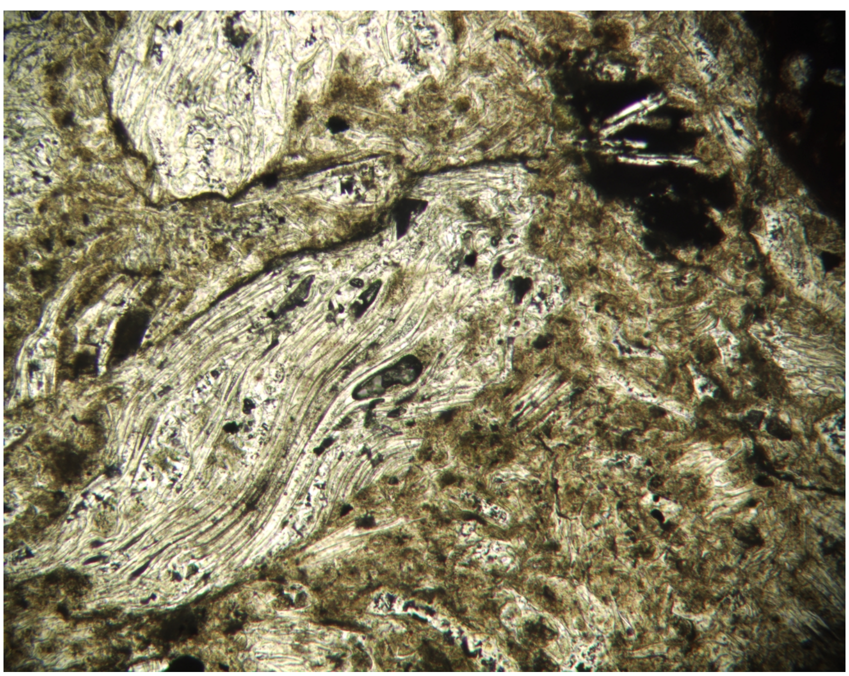

Figure F17 (continued). **E.** Fragmentation of a larger pumice clast to generate smaller pumice fragments in the matrix. **F.** Internal texture in a pumice clast showing changes in orientation of tube vesicles and incipient alteration to pale green clay minerals. Photomicrographs A–C are from Sample 183-1138A-78R-4, 23–26 cm (in plane-polarized light; field of view = 1.4 mm). Photomicrographs D–F are from Sample 183-1138A-78R-3, 50–54 cm (in plane-polarized light; field of view = 1.4 mm).

E

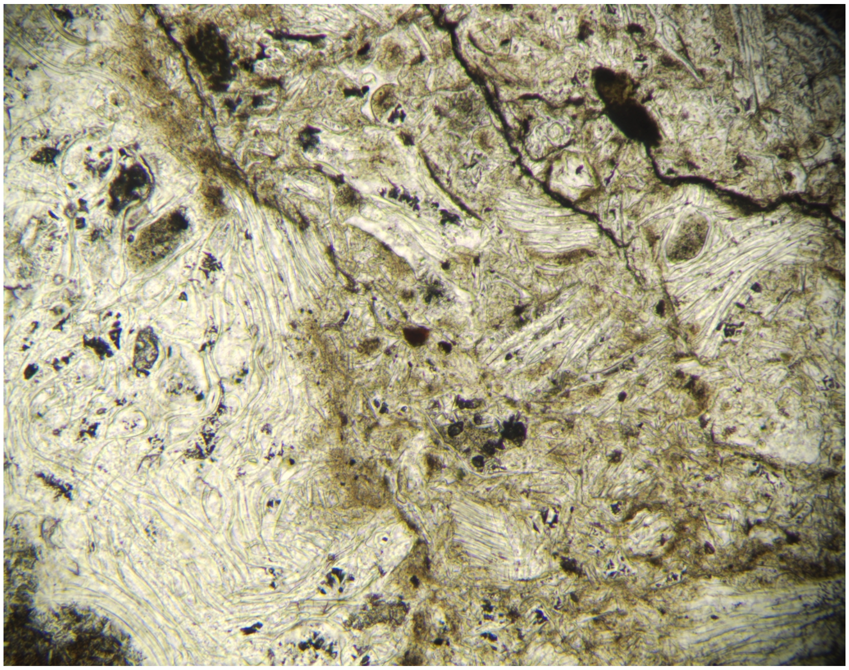

F

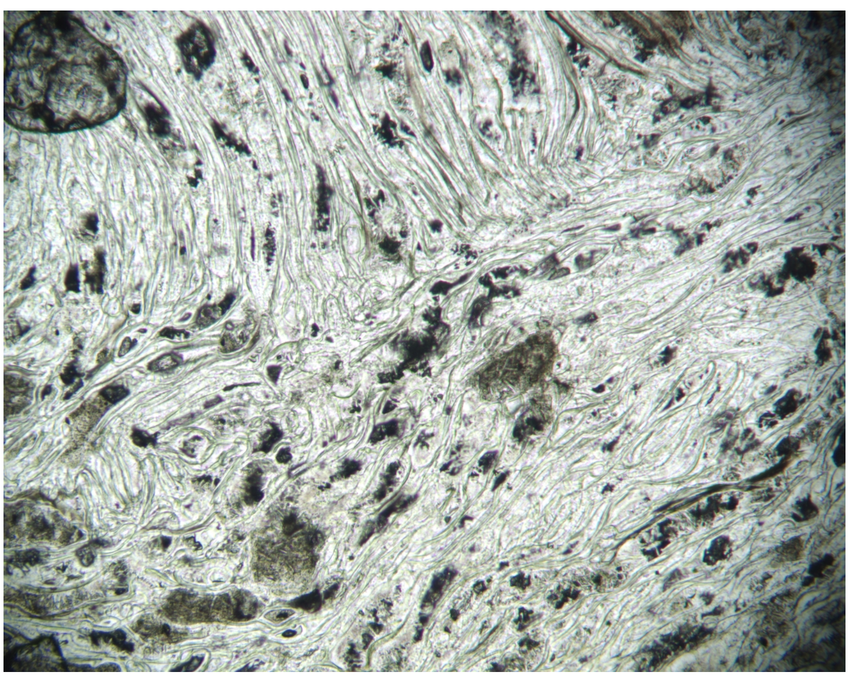

Figure F18. Close-up photograph of interval 183-1138A-76R-2, 88–106 cm, showing regularly bedded intervals in basement Subunit 2B. Note the variable sorting and concentration of pumice (pale green) and lithic fragments.

Figure F19. Close-up photograph of interval 183-1138A-76R-2, 65–83 cm, showing a poorly sorted interval in reworked sediments in basement Subunit 2B. Note that the range of pumice (pale green) clast sizes is much greater than the range of lithic clast sizes.

Figure F20. Close-up photograph of interval 183-1138A-77R-1, 10–25 cm, showing the lower part of the massive, green, clay-rich, altered pumice breccia (basement Subunit 2C) and upper orange part of pumice lithic breccia (basement Subunit 2D). Note the clay pseudomorphs (arrows) of pumice in the pale green, altered pumice breccia interval.

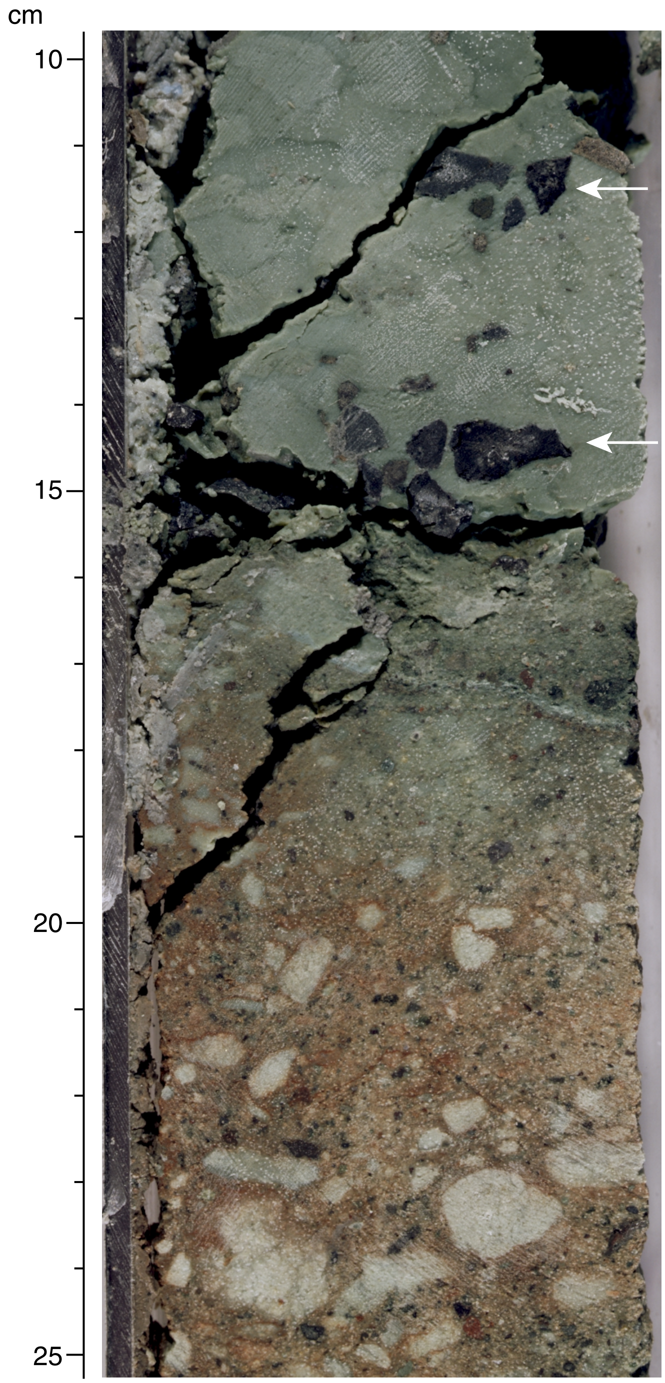

Figure F21. Close-up photograph of interval 183-1138A-79R-4, 37–48 cm, showing pale green clay (pumice breccia) with scattered angular lithic fragments and red bands (oxidation) through formerly pumiceous material, now highly altered (basement Subunit 2N).

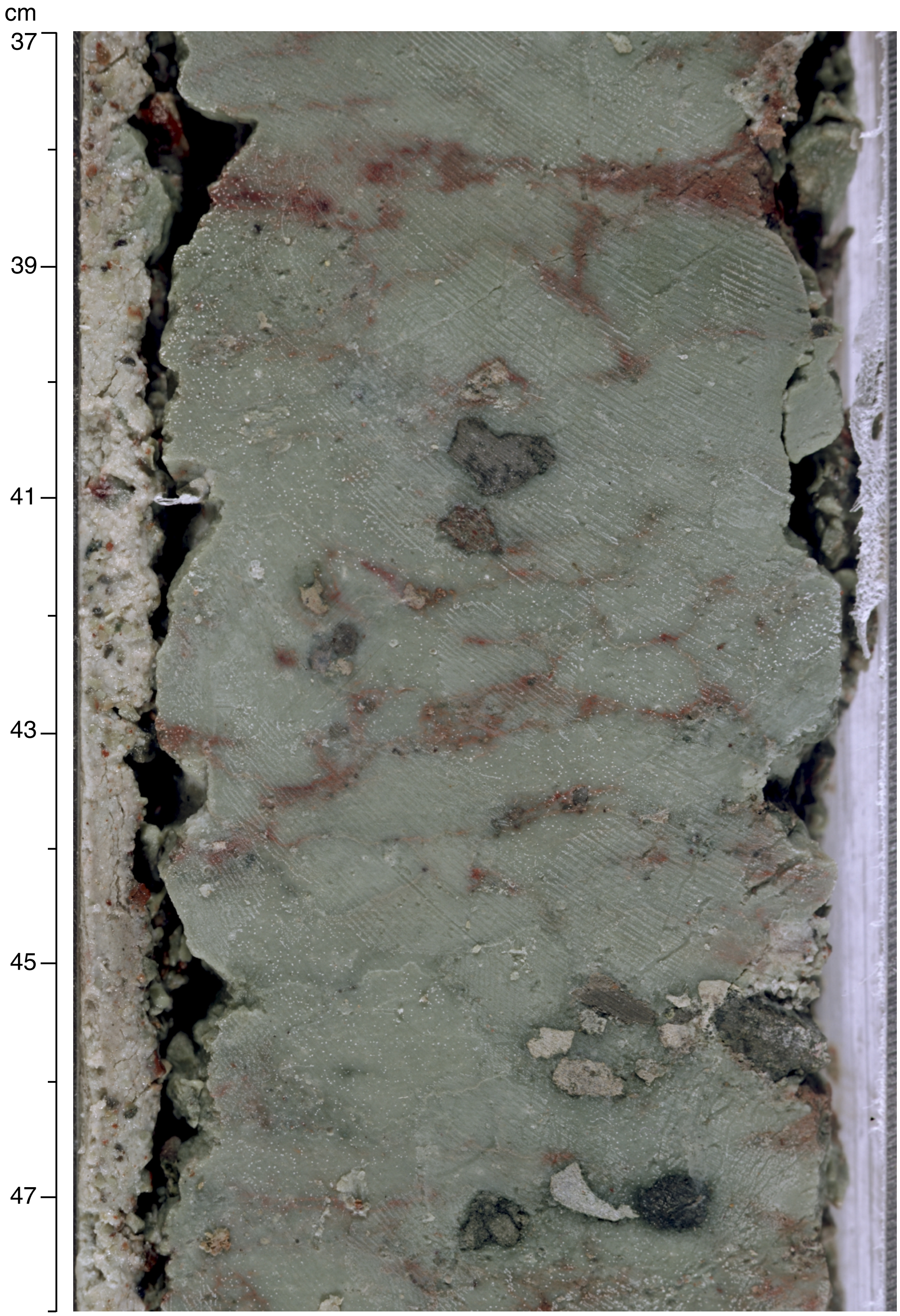

Figure F22. Close-up photograph of interval 183-1138A-77R-CC, 0–8 cm, showing sharp (scoured) upper contact at the granular base of the lithic breccia (basement Subunit 2E) over a normally graded accretionary lapilli-bearing pyroclastic ash-fall deposit (basement Subunit 2F). Note that this interval mantles large pumice clasts at the top of the underlying pumice lithic breccia (basement Subunit 2G).

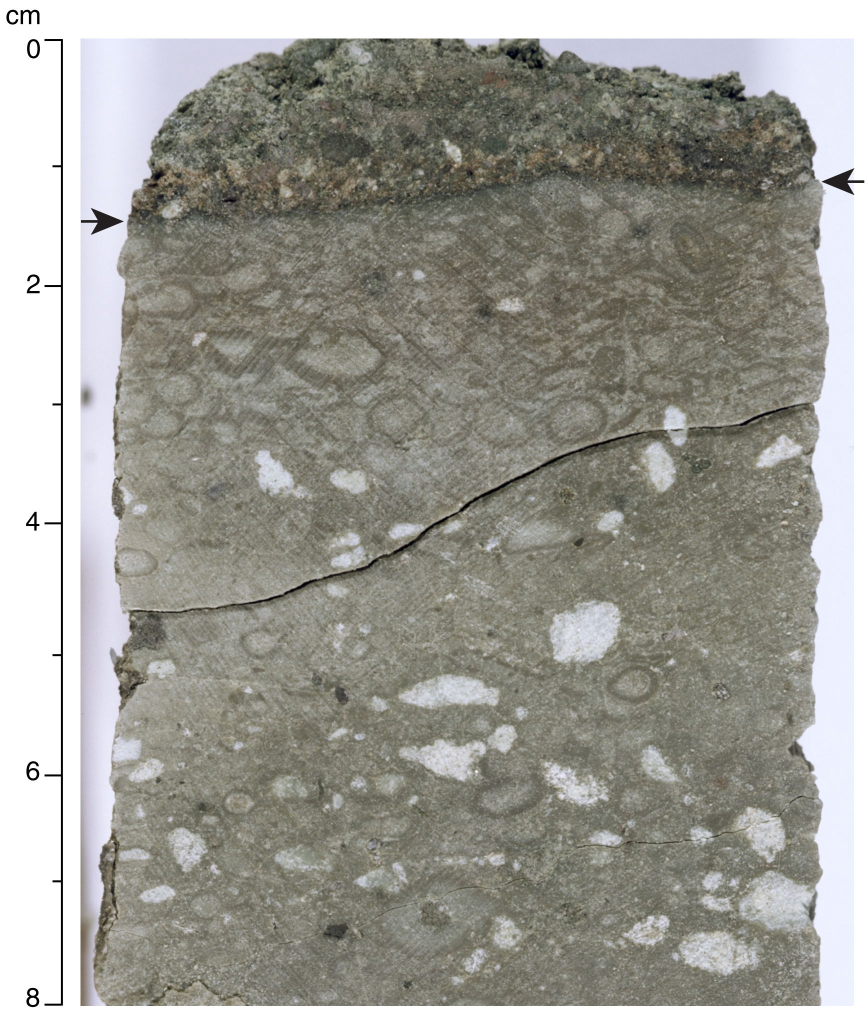

Figure F23. Close-up photograph of interval 183-1138A-79R-3, 34–40 cm, showing intergraded accretionary lapilli-bearing pyroclastic ash-fall material (basement Subunit 2L) and the granular base of the overlying reversely graded lithic breccia (basement Subunit 2K).

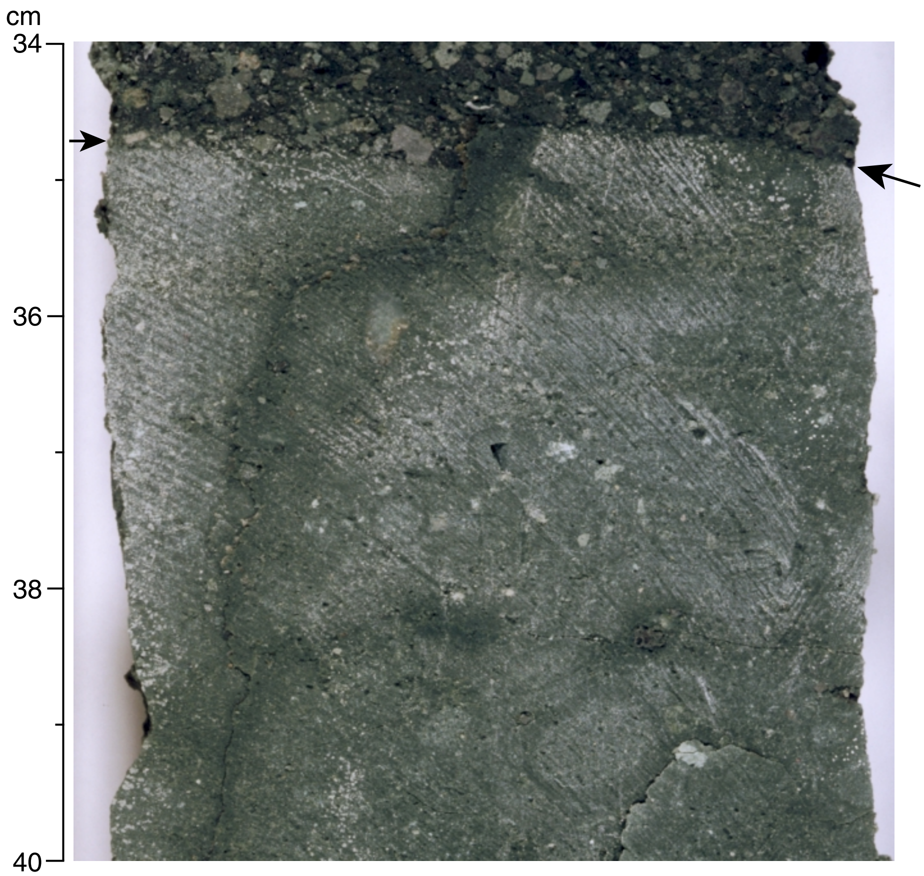

Figure F24. Close-up photograph of interval 183-1138A-79R-3, 26–47 cm, showing sharp upper erosional (scoured) contact of normally graded accretionary lapilli-bearing pyroclastic ash-fall material (basement Subunit 2L) and the granular base of the overlying reversely graded lithic breccia (basement Subunit 2K). Accretionary lapilli are visible only in the dry archive-half image (see Fig. **F23**, p. 94).

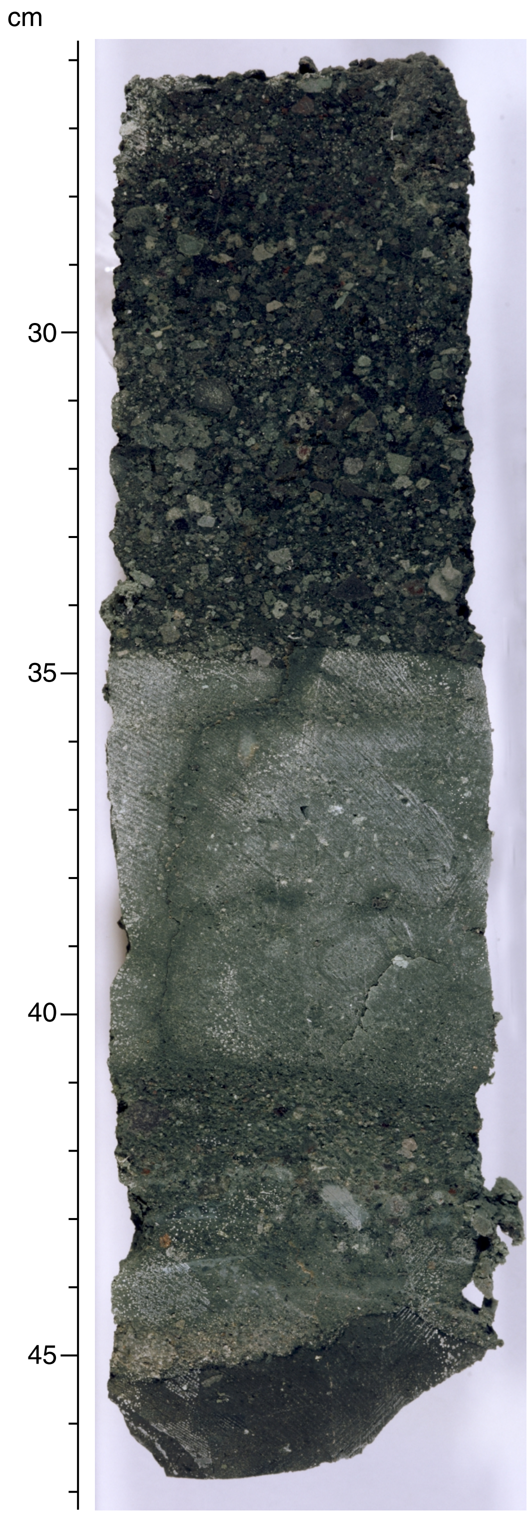

Figure F25. Close-up photograph of interval 183-1138A-79R-4, 74–94 cm, showing a normally graded base of green clay-rich altered pumiceous breccia and the underlying massive, highly altered volcanic clay.

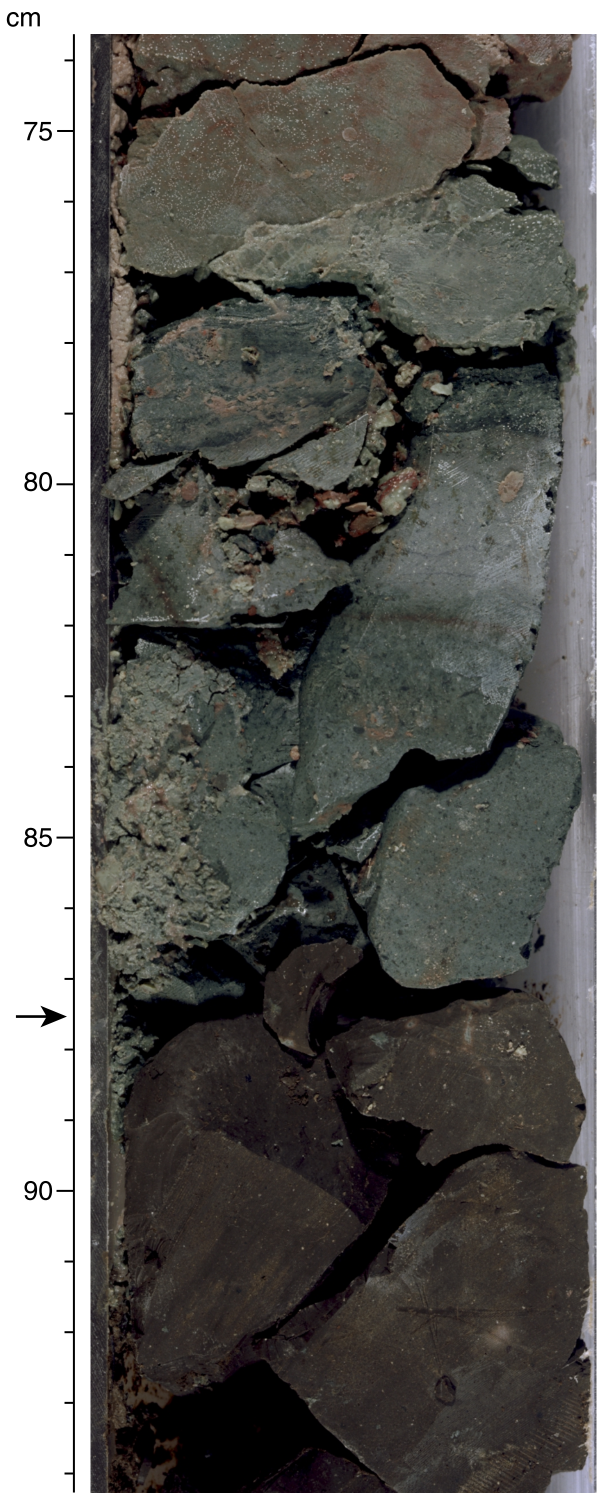

Figure F26. Close-up photograph of interval 183-1138A-80R-3 (Piece 11, 96–116 cm) showing irregular, "ragged" vesicles in basement Unit 4. This vesicle shape is typical of aa flows.

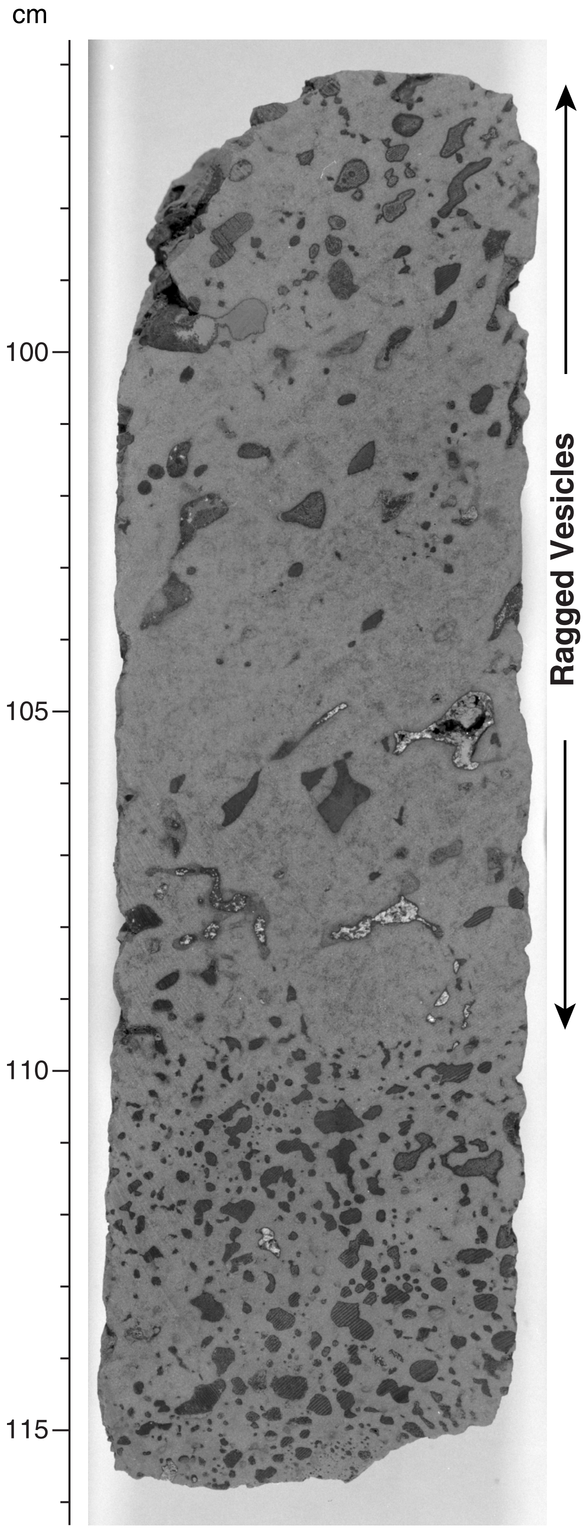

Figure F27. Close-up photograph of interval 183-1138A-80R-3 (Piece 2, 18–28 cm) showing small vesicular clot in coherent lava of basement Unit 4. These clots are interpreted to be entrained and remelting vesicular clasts from the flow-top breccia.

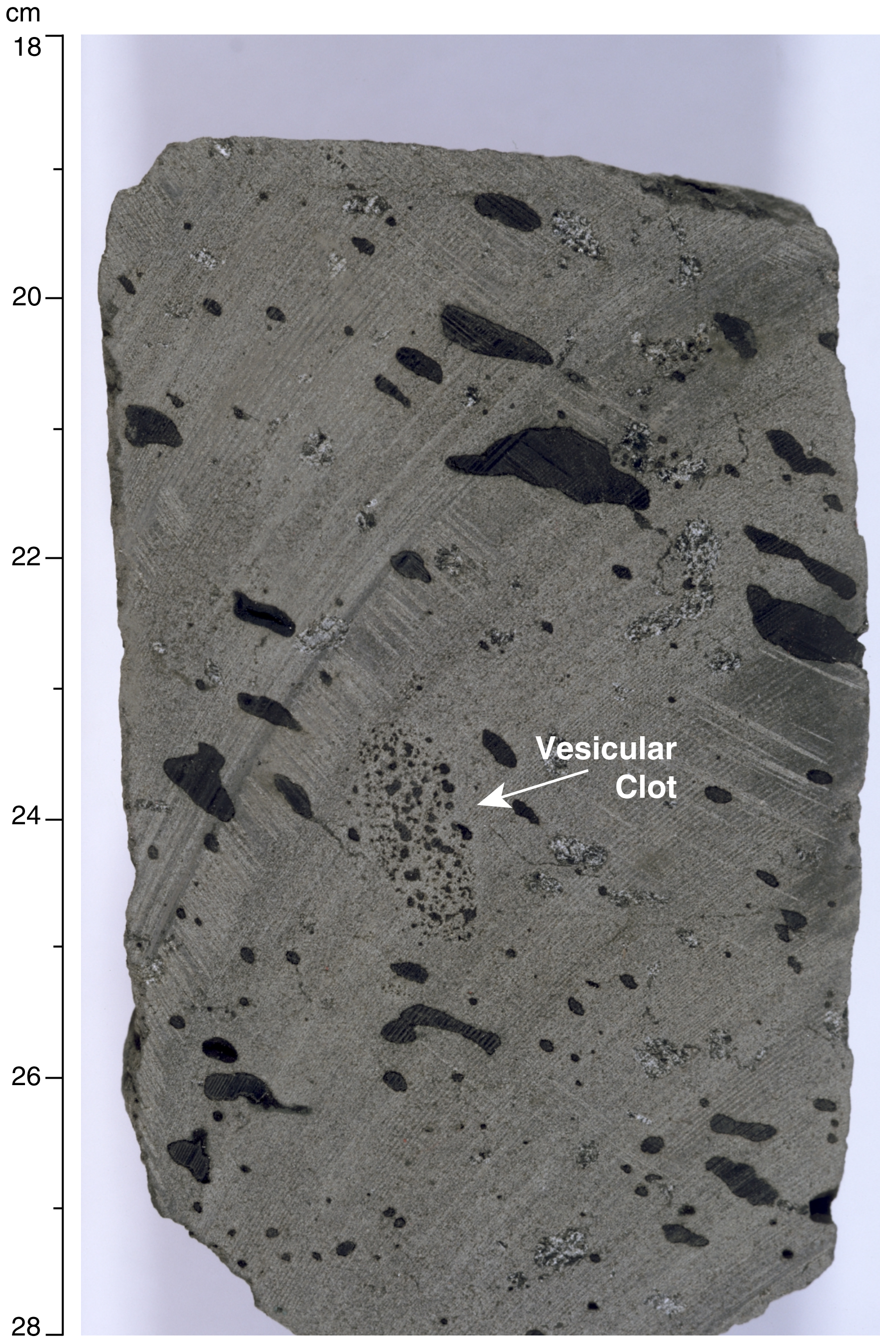

Figure F28. Close-up photograph of interval 183-1138A-81R-1 (Piece 2, 5–15 cm) showing contact between basement Units 5 and 6.

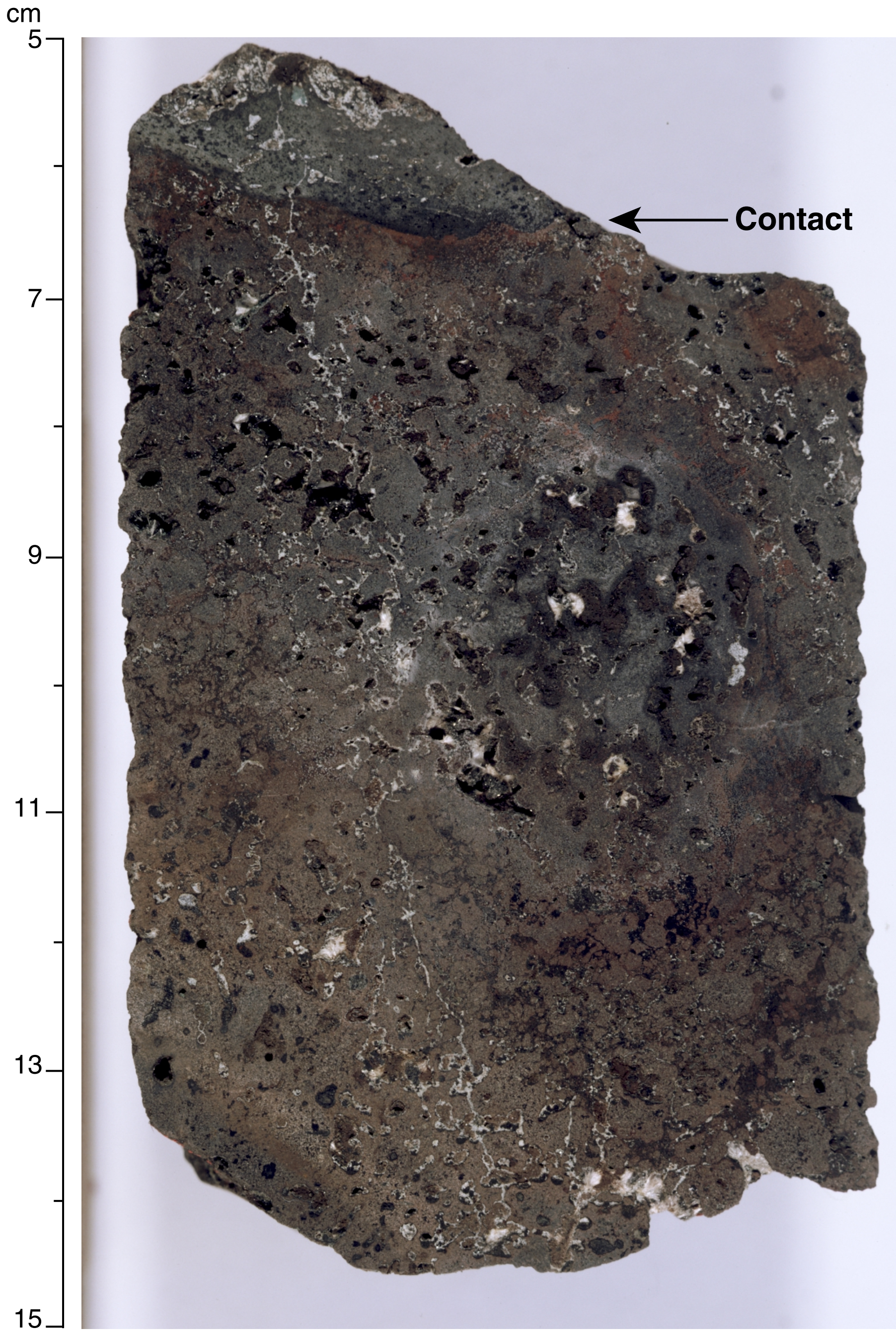

Figure F29. Color close-up photograph of Sample 183-1138A-81R-3 (Piece 1, 0–25 cm). The contact between Units 6 and 7 in Hole 1138A is marked by a change in color from gray to pink gray at 10–17 cm. The flow bottom to Unit 6 is moderately altered with irregularly shaped vesicles filled with clinoptilolite. The top of Unit 7 is brecciated and weakly oxidized with clinoptilolite and clay-cementing volcanic clasts that are variably altered to smectite.

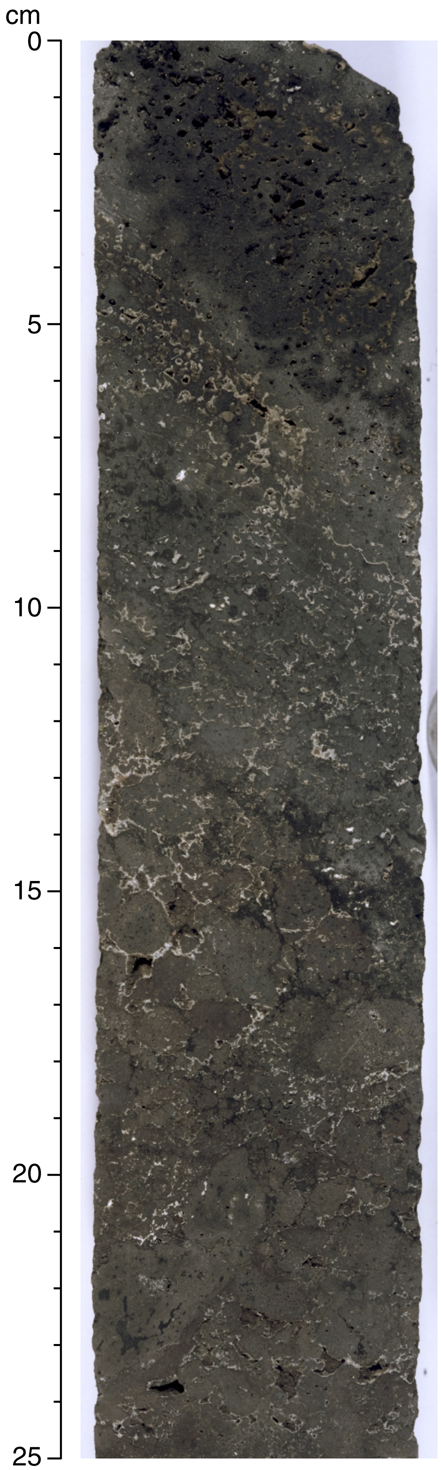

Figure F30. Photomicrograph of Sample 183-1138A-82R-3, 49–51 cm, showing in situ brecciation textures at the margin of a chilled clast. The sediment enclosing this clast has been altered and silicified to clay minerals and quartz, and primary textures have been obliterated. Field of view = 1.4 mm (plane-polarized light).

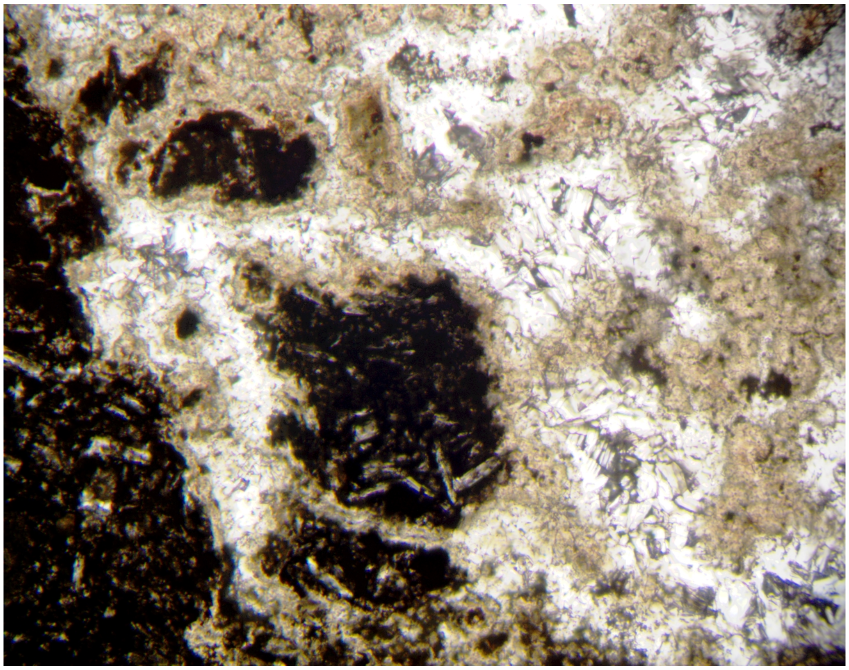

Figure F31. Photomicrograph of Sample 183-1138A-82R-3, 49–51 cm, showing the accumulation of basaltic fragments behind a protrusion of infiltrated sediment in a chilled basaltic clast, indicating localized transport of brecciated material along clast surfaces. The way up is to the left of this image. Field of view = 1.4 mm (plane-polarized light).

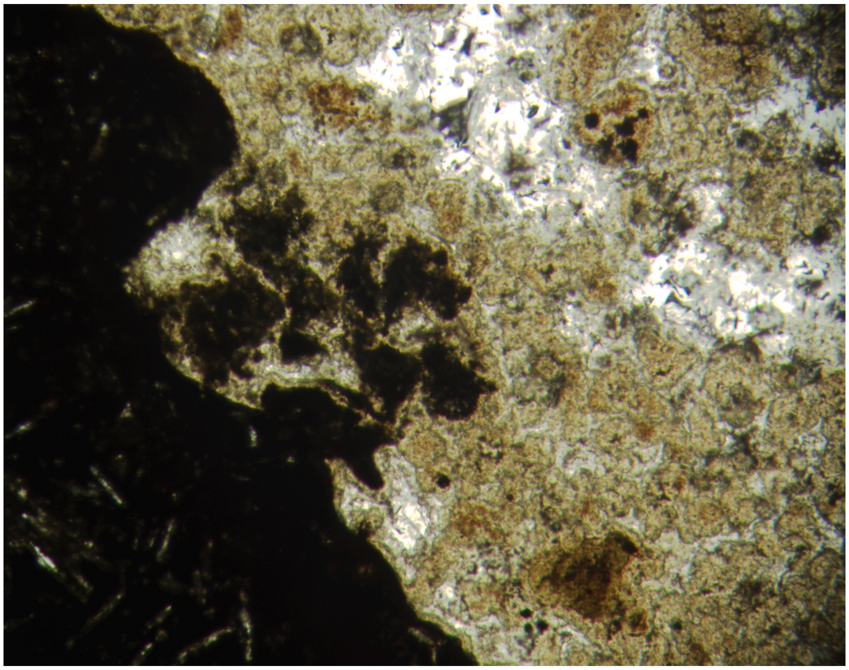

Figure F32. Close-up photograph of Sample 183-1138A-82R-2 (Pieces 7–9, 63–79 cm) showing contact between basement Units 8 and 9.

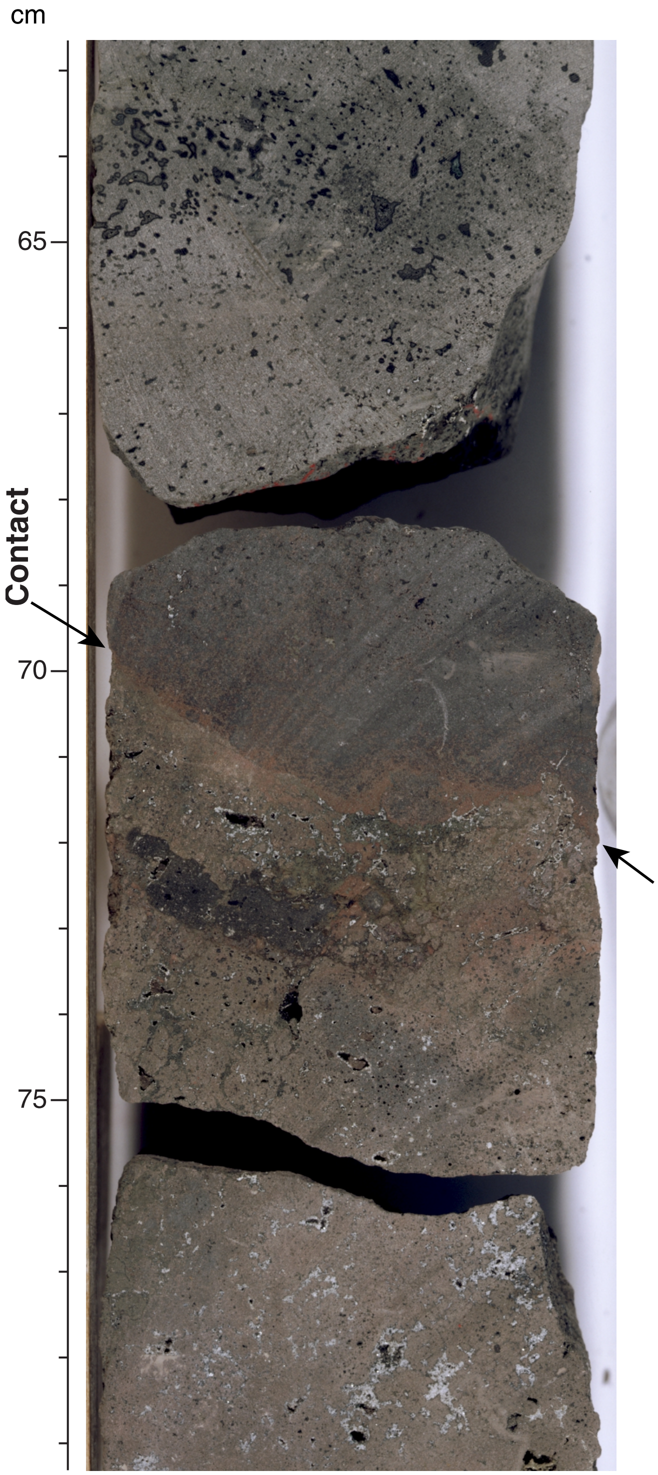

Figure F33. Close-up photograph of Sample 183-1138A-82R-2 (Piece 11, 98–114 cm) showing slab pahoehoe with ropy surface in flow-top breccia of basement Unit 9.

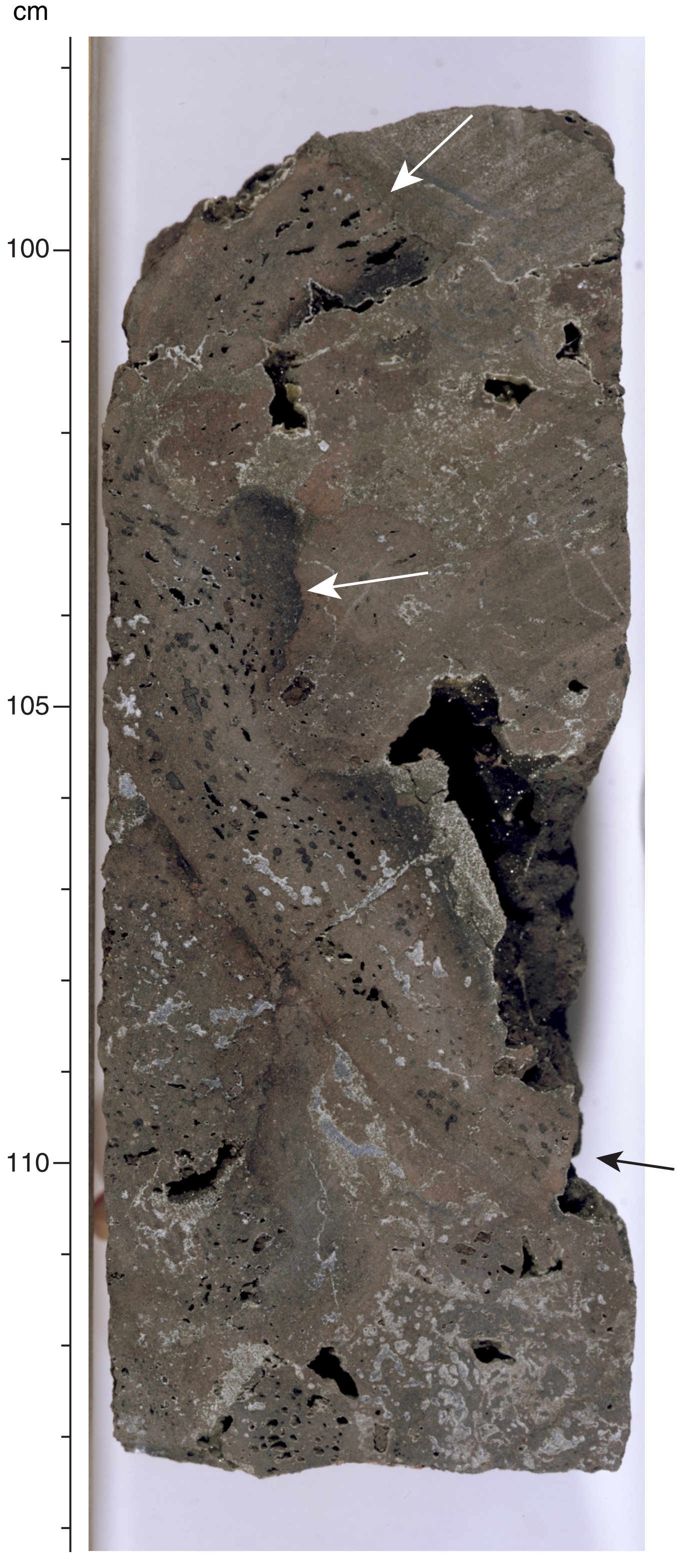

Figure F34. Close-up photograph of Sample 183-1138A-82R-3 (Piece 4, 27–45 cm) showing upper part of the zone with peperitic textures in the flow-top breccia of basement Unit 9. An XRD analysis indicates that quartz is the dominant phase present in the sediment, with only trace amounts of clay and amorphous silica. Clinoptilolite fills vesicles within clasts and very small stringers crosscutting the sediment.

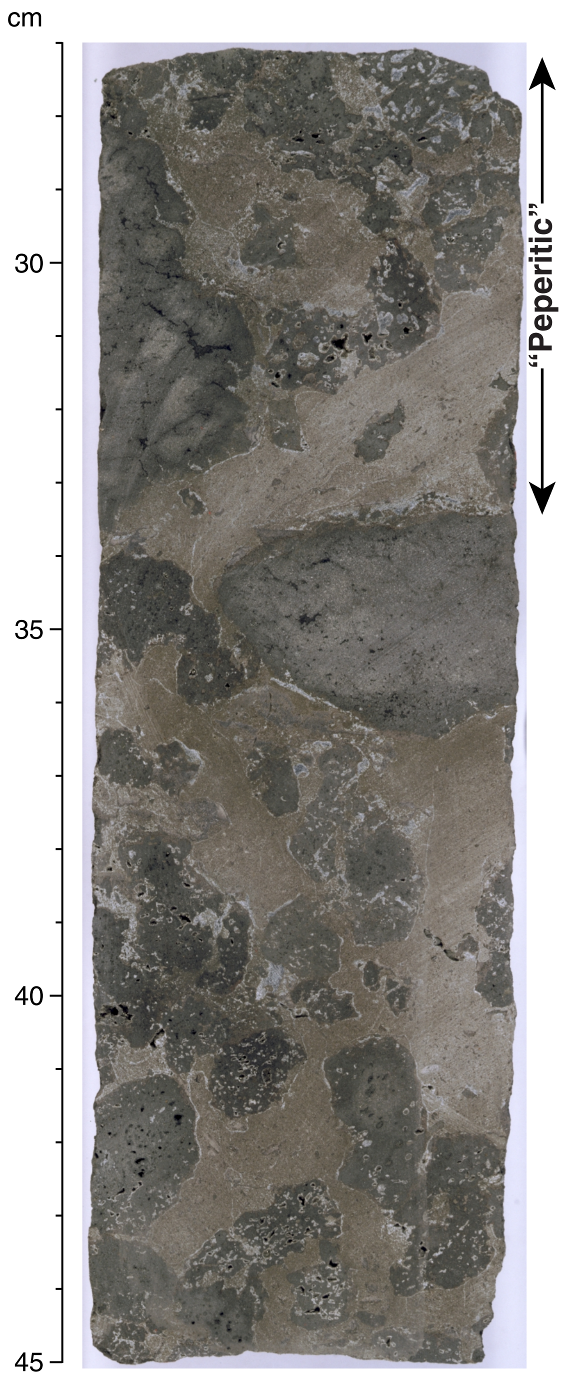

Figure F35. Close-up photograph of Sample 183-1138A-82R-3 (Piece 5, 46–63 cm) showing lower part of the zone with peperitic textures in the flow-top breccia of basement Unit 9.

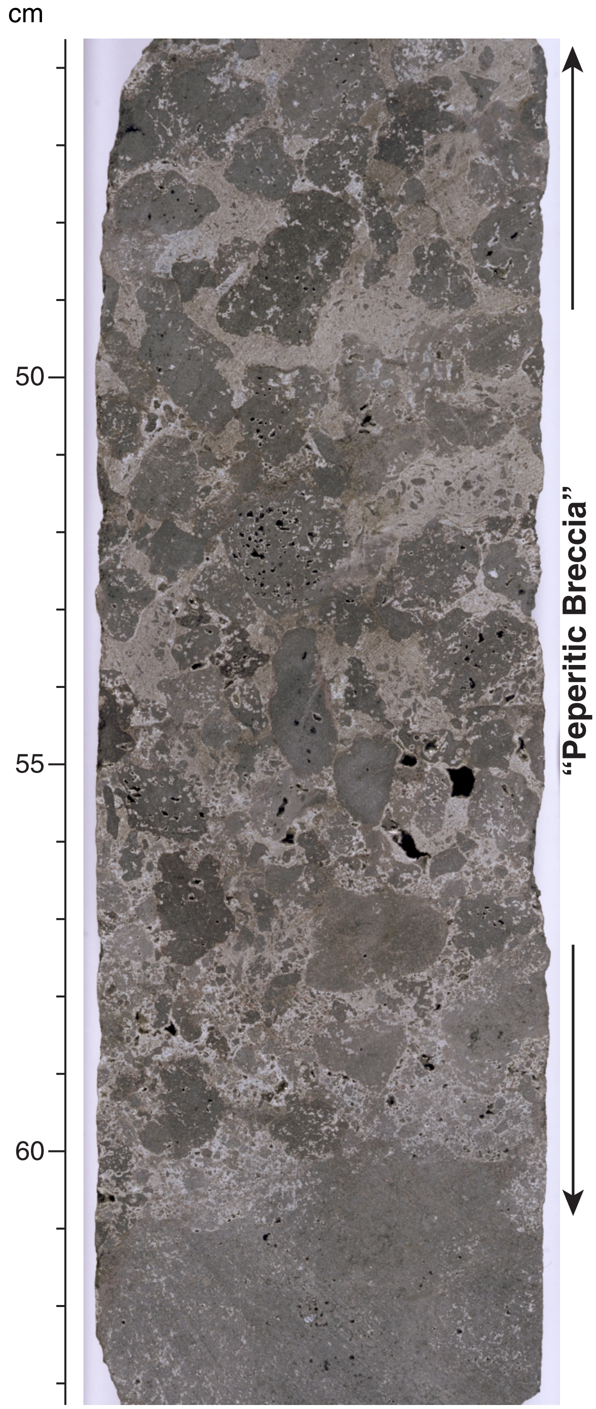

Figure F36. Close-up photograph of Sample 183-1138A-82R-3 (Piece 8, 88–116 cm) showing a dense lava arm intruding into the base of the flow-top breccia of basement Unit 9.

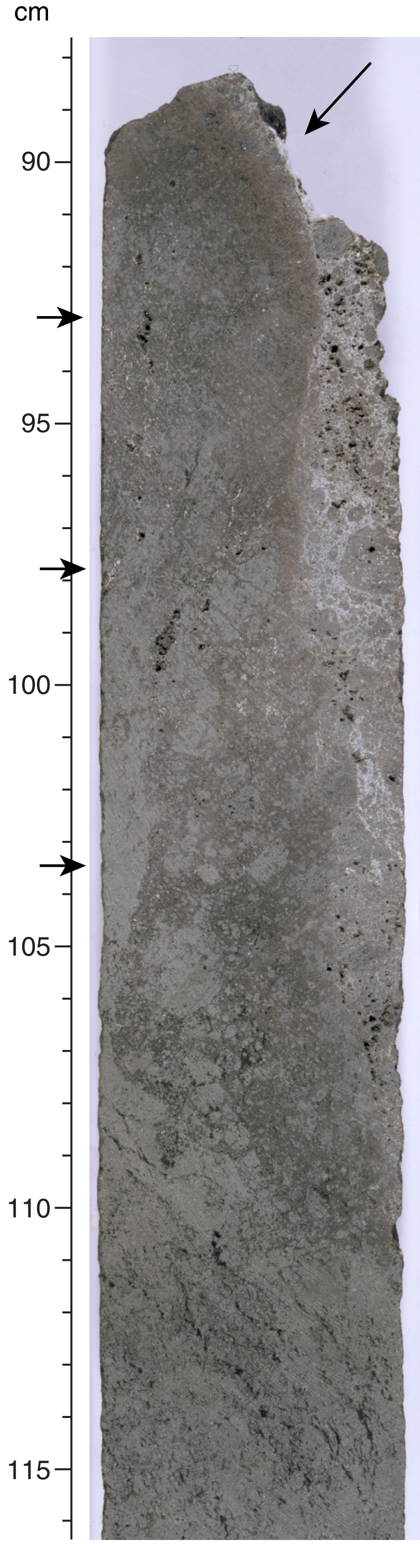

Figure F37. Close-up photograph of Sample 183-1138A-82R-4 (Piece 5B, 137–147 cm) showing unusual vesicular sheet-like bodies within the massive interior of basement Unit 9.

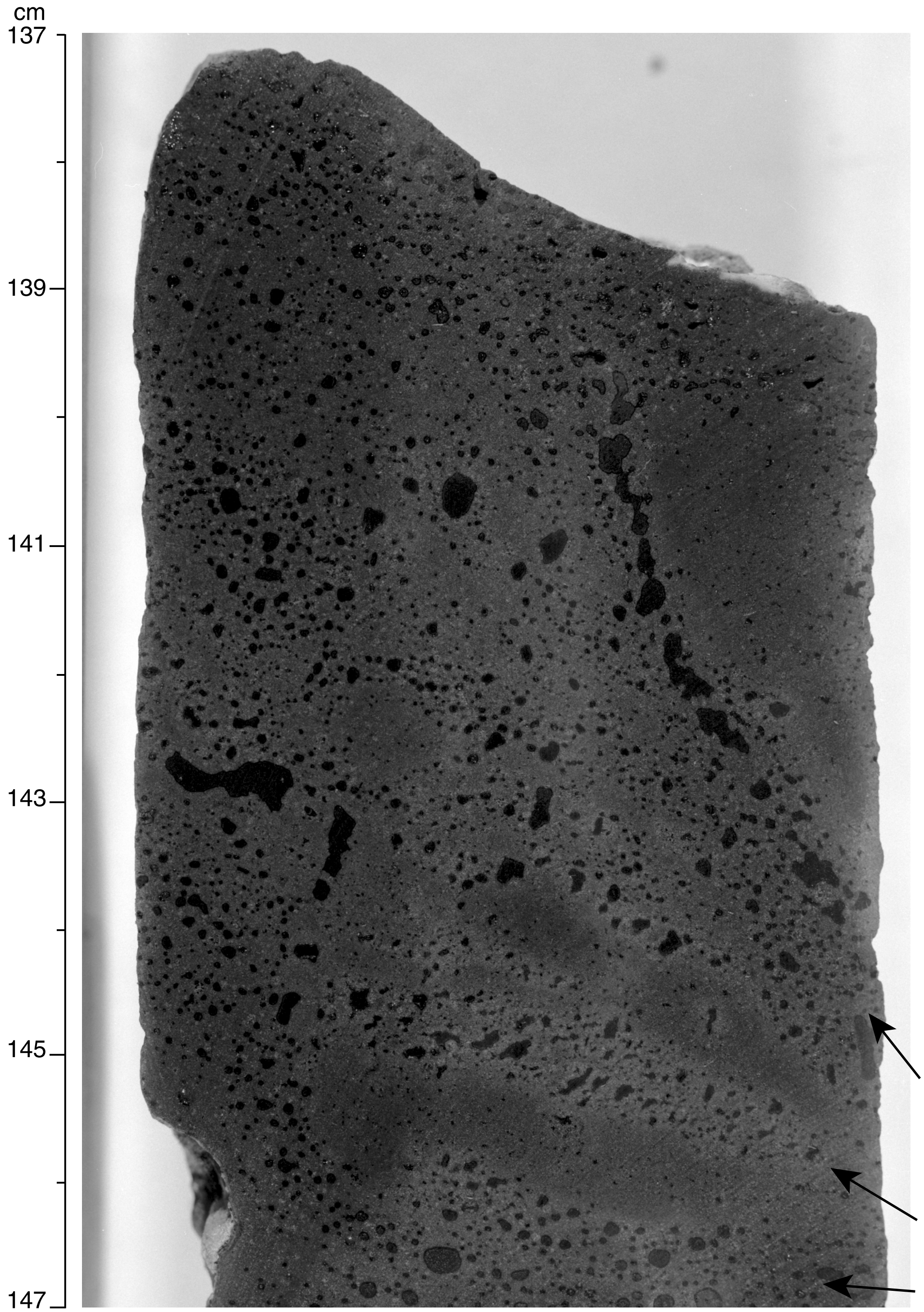

Figure F38. Close-up photograph of Sample 183-1138A-83R-4 (Pieces 6–8, 85–105 cm) showing welded lobes or spatter with horizontally elongated vesicle-like domains at the base of basement Unit 10.

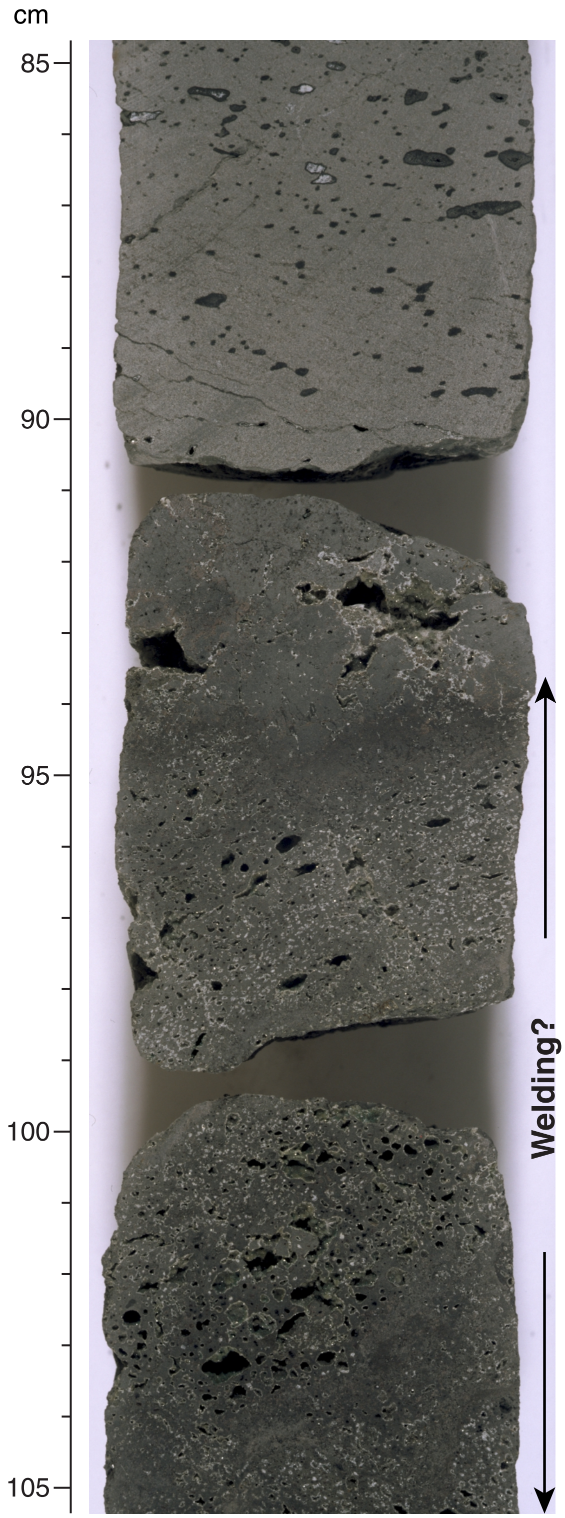

Figure F39. Close-up photograph of Sample 183-1138A-83R-4 (Pieces 8–10, 105–125 cm) showing contact between basement Units 10 and 11.

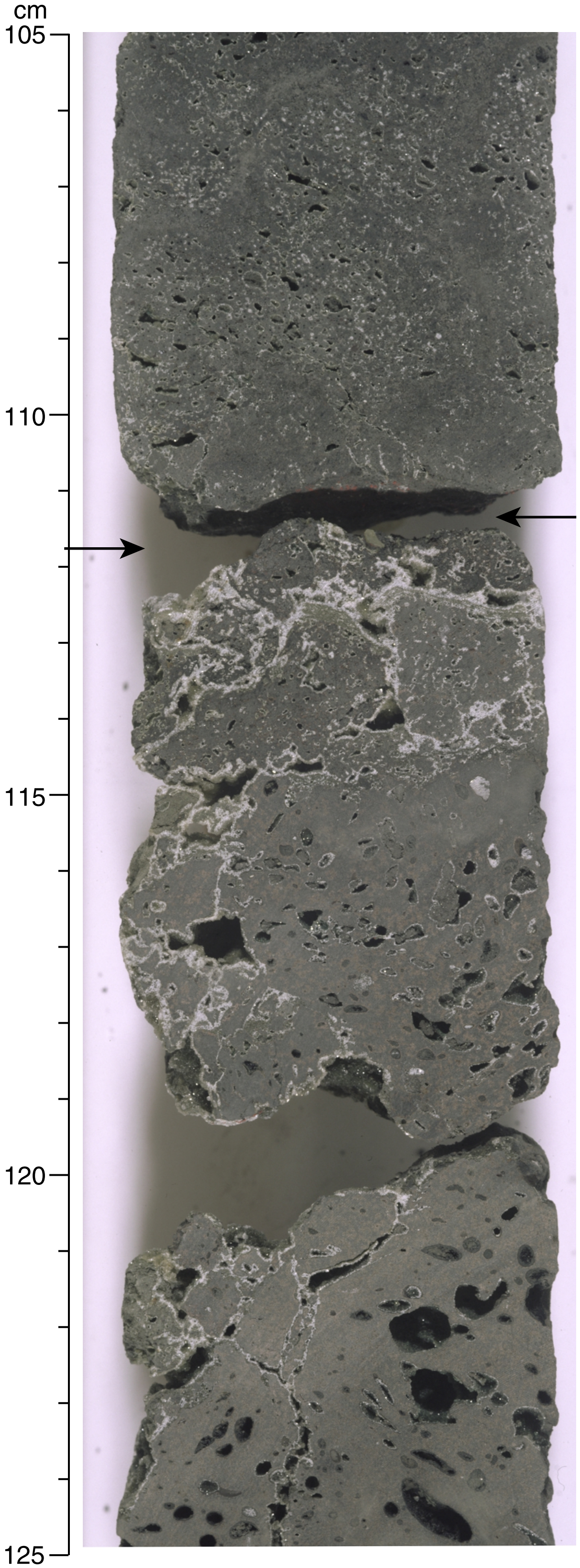

Figure F40. Photograph of Section 183-1138A-83R-5 showing vertically elongated vesicles in the upper part of basement Unit 11.

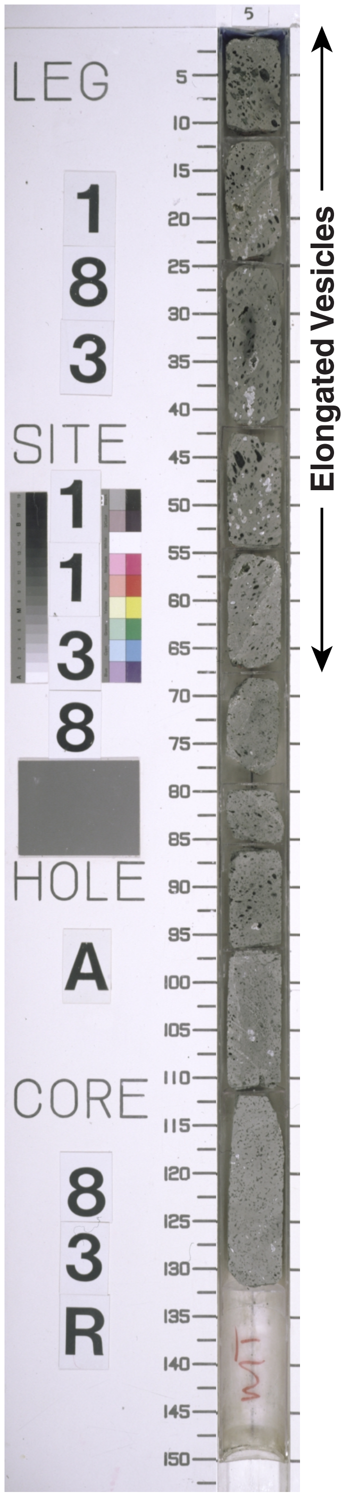

Figure F41. Close-up photograph of Sample 183-1138A-83R-6 (Pieces 6 and 7, 70–90 cm) showing contact between basement Units 11 and 12.

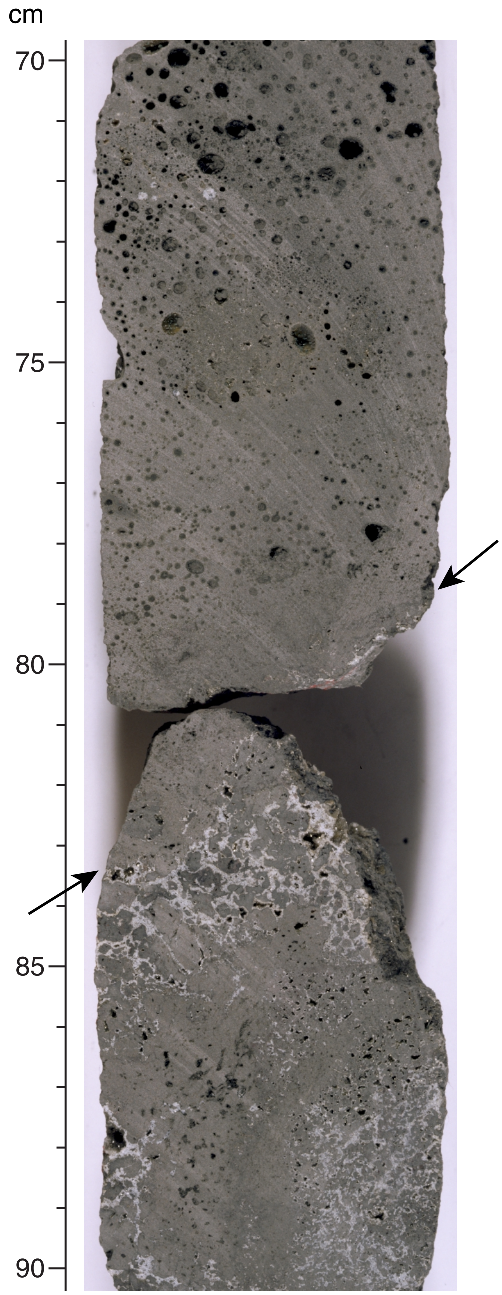

Figure F42. Close-up photograph of Sample 183-1138A-84R-1 (Pieces 6 and 7, 120–135 cm) showing contact between basement Units 12 and 13.

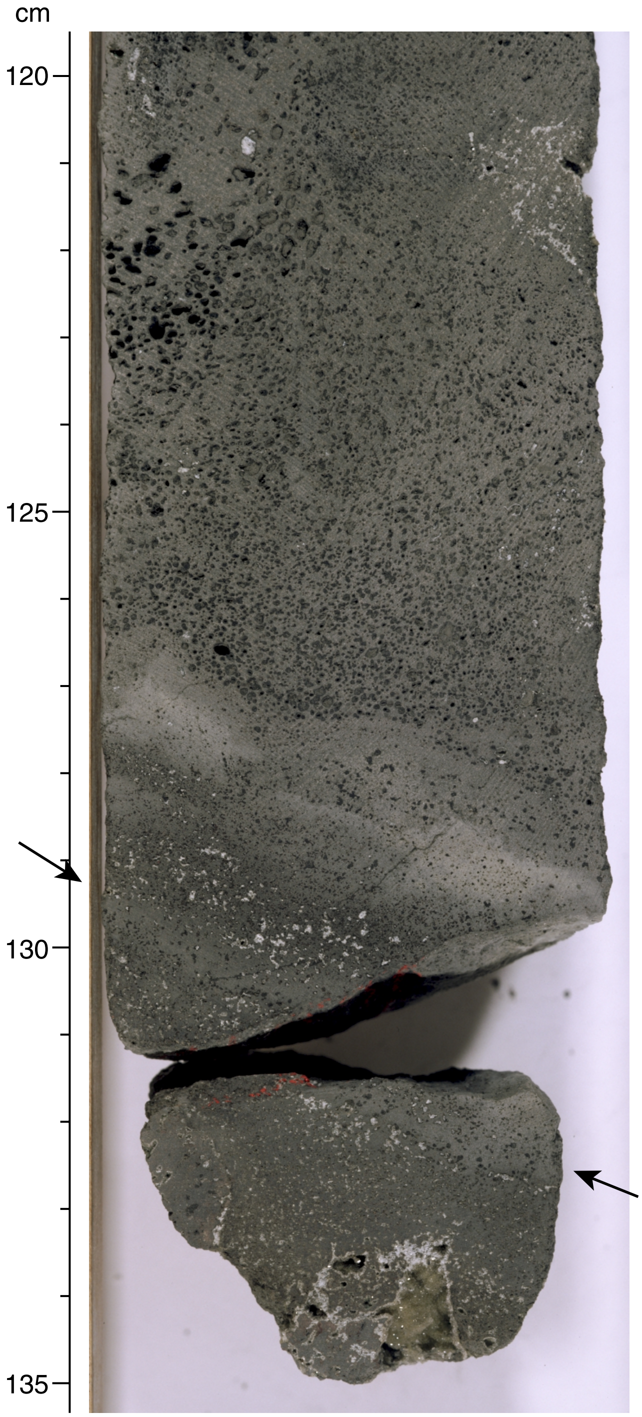

Figure F43. Close-up photograph of Sample 183-1138A-84R-2 (Piece 1, 0–20 cm) showing folded pahoehoe crust on top of the basement Unit 13 flow-top breccia, typical of crust on channelized pahoehoe.

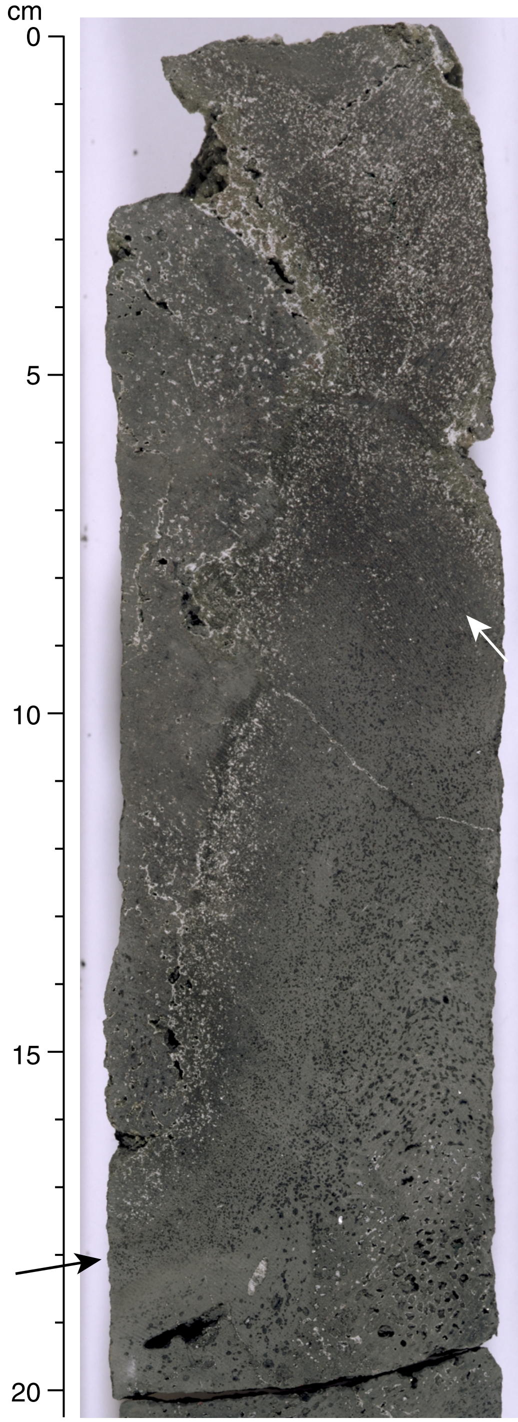

Figure F44. Close-up photograph of Sample 183-1138A-85R-2 (Pieces 1–3, 25–45 cm) showing contact between basement Units 14 and 15.

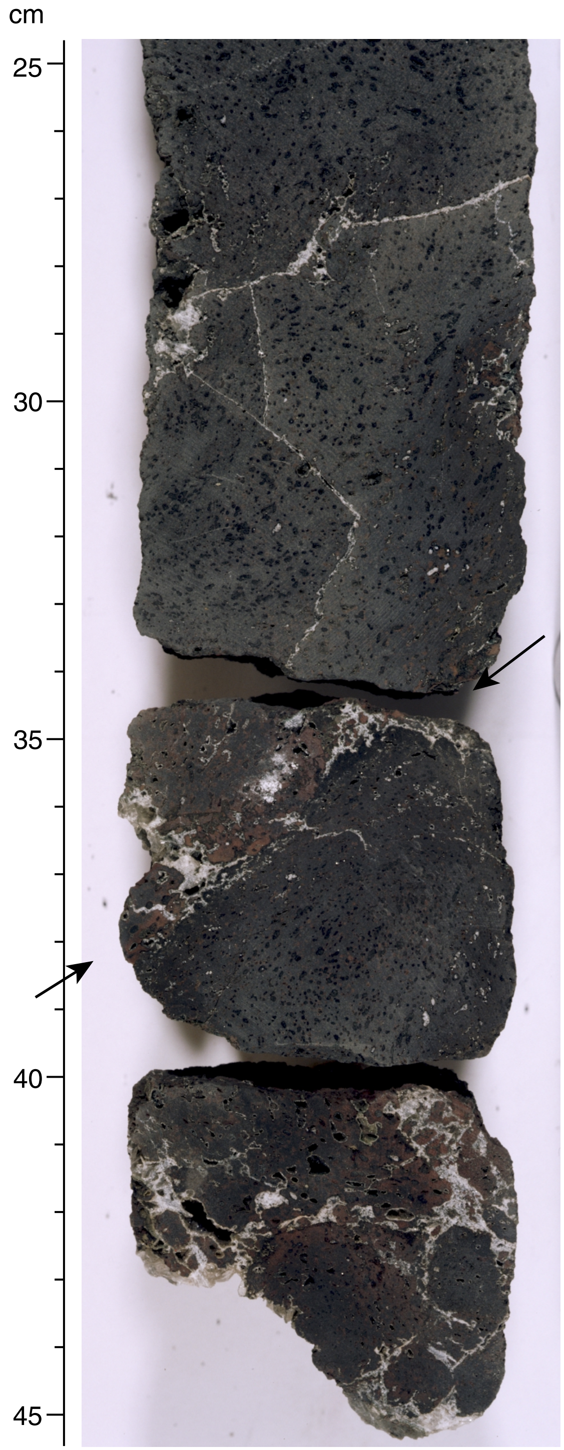

Figure F45. Close-up photograph of Sample 183-1138A-86R-1 (Pieces 3 and 4, 60–80 cm) showing contact between basement Units 16 and 17.

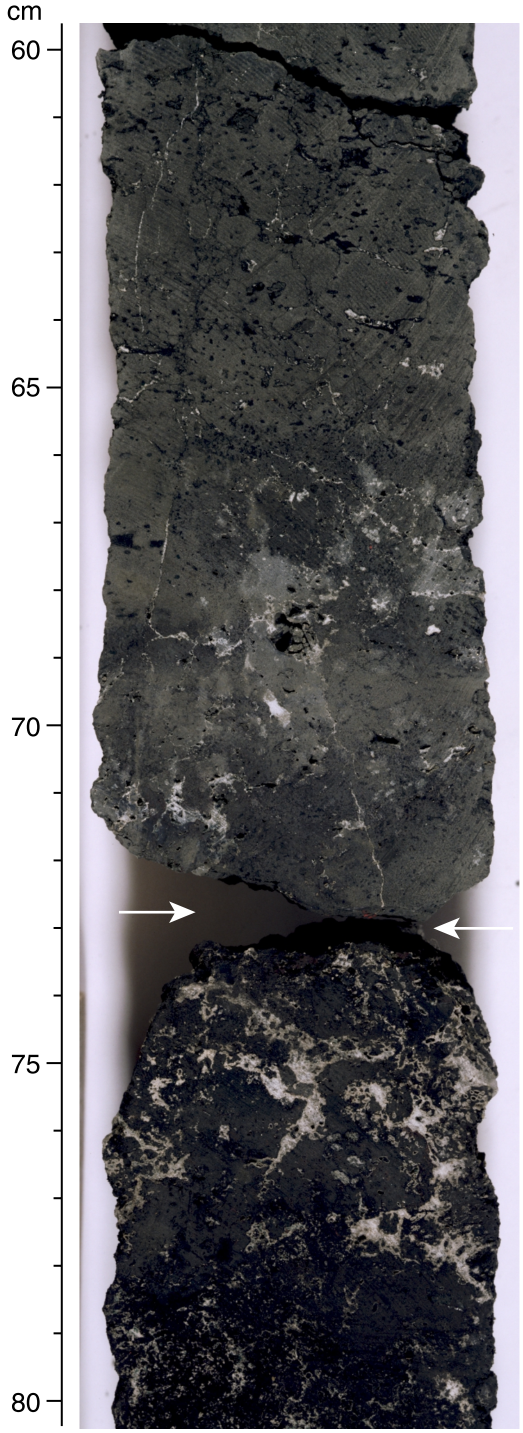

Figure F46. Color close-up photograph of Sample 183-1138A-87R-1 (Piece 11, 89–97 cm) showing welding of clasts in the flow-top breccia of basement Unit 19. Clasts are highly to completely altered to dark green and brown clay. Vesicles within clasts and large cavities between clasts are partly filled with clay and clinoptilolite.

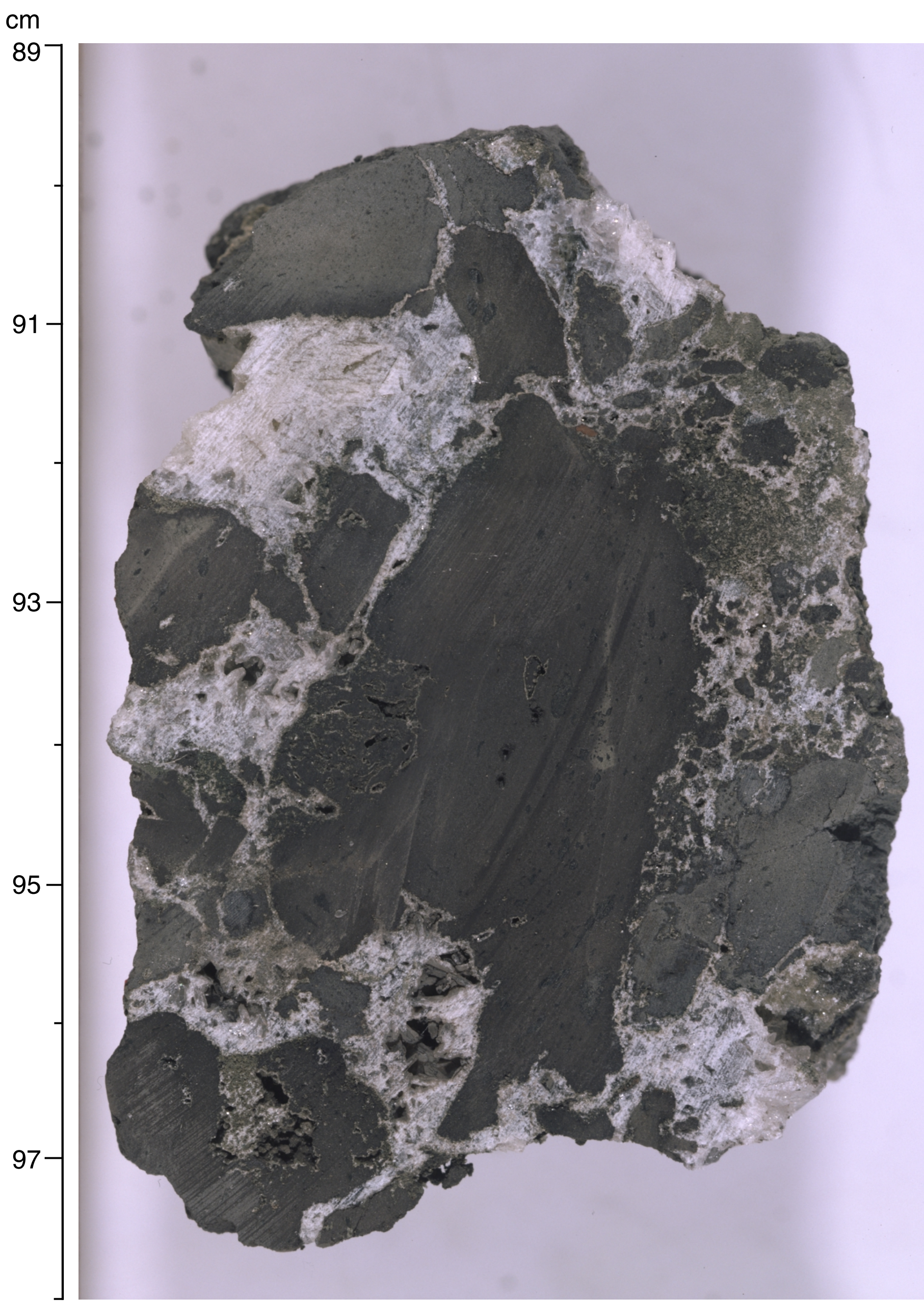

Figure F47. Close-up photograph of Sample 183-1138A-87R-2 (Pieces 7–9, 40–57 cm) showing brecciation within the coherent crust of basement Unit 19. This is interpreted to be unrelated to the emplacement of the lava flow.

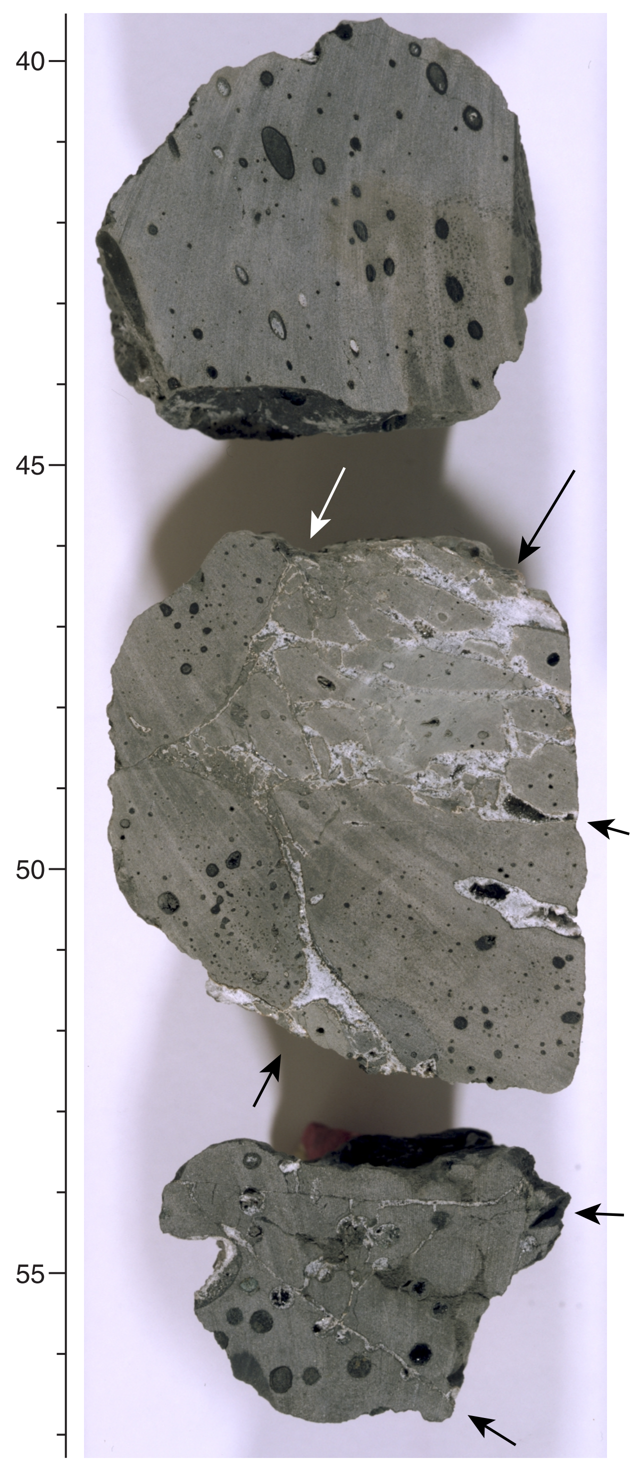

Figure F48. Photograph of interval 183-1138A-88R-1, 0–100 cm, showing fracture and vesicle patterns in basement Unit 20 interpreted to be the upper part of a spiracle where groundwater that had turned to steam escaped by blasting through the lava flow.

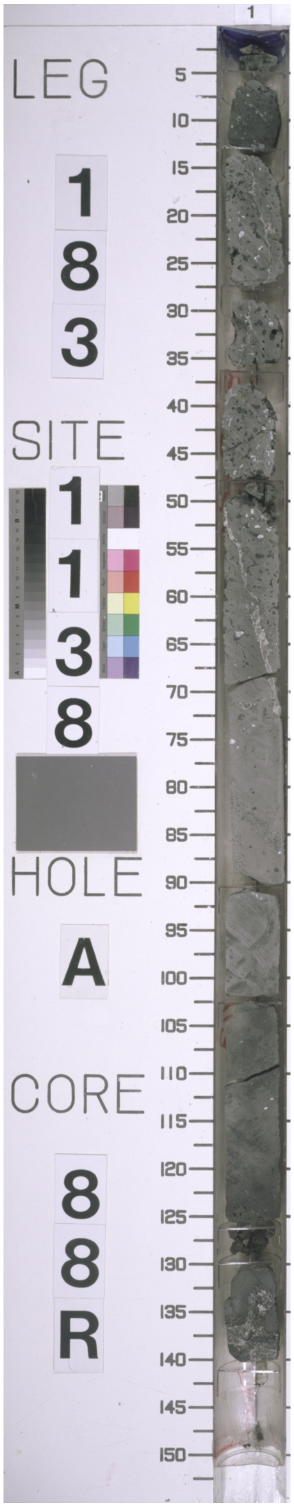

Figure F49. Close-up photograph of Sample 183-1138A-88R-1 (Piece 7, 91–102 cm) showing glassy rip-ups inside basement Unit 20. Interpreted to be parts of the flow margin blasted into the liquid lava by the formation of the spiracle.

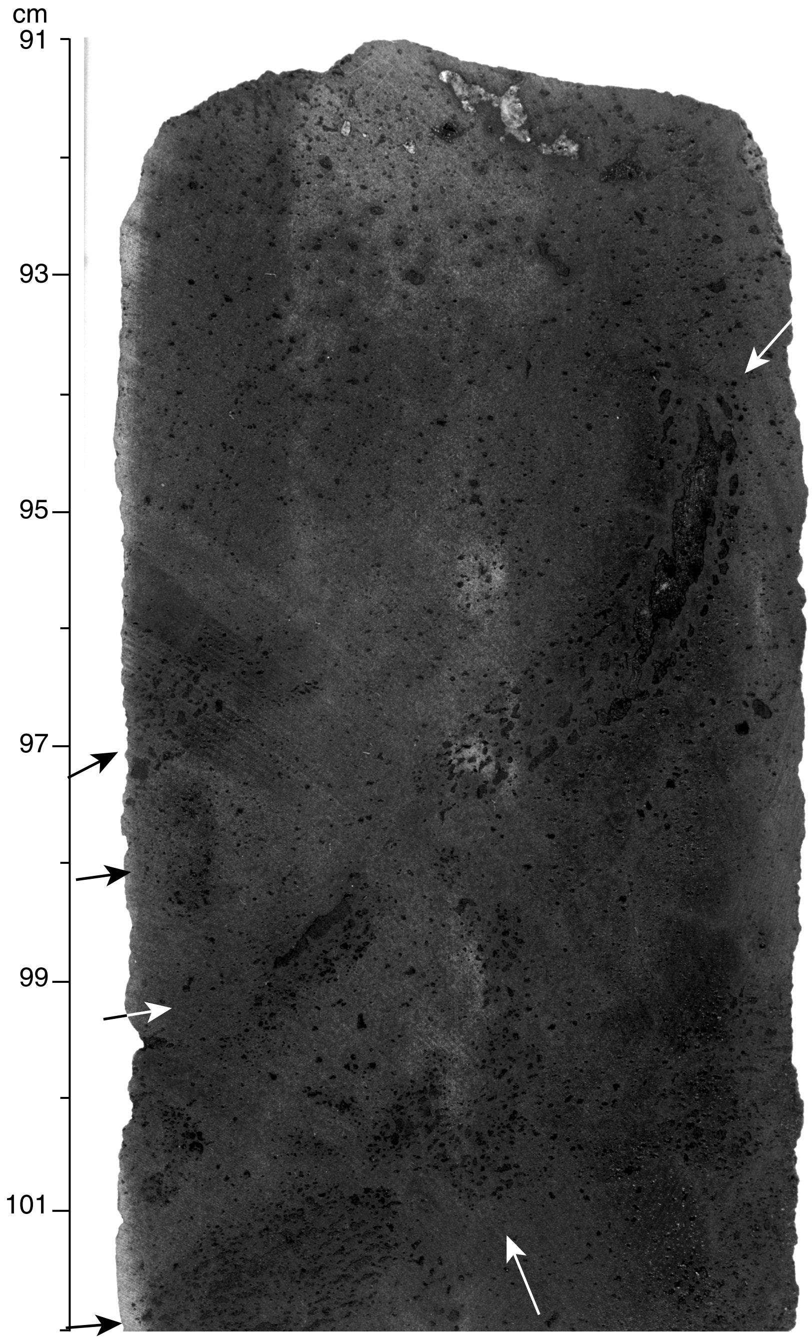

Figure F50. Close-up photograph of Sample 183-1138A-88R-1 (Piece 10, 130–141 cm) showing a bulbous cavity interpreted to be part of the base of a spiracle. The lower margin of basement Unit 20 is mostly planar with a 2- to 3-mm-thick zone of black clays and an ~1-cm-thick slightly oxidized zone with a finer groundmass. In the center of the recovered boundary is a 3 cm × 5 cm bulbous cavity. The zone of finer groundmass wraps up and around the cavity, but the black clays do not follow. Within the cavity, the lava has a vesicularity of 35%–40% with extremely angular and almost rectangular vesicles mostly 1–3 mm in dimension.

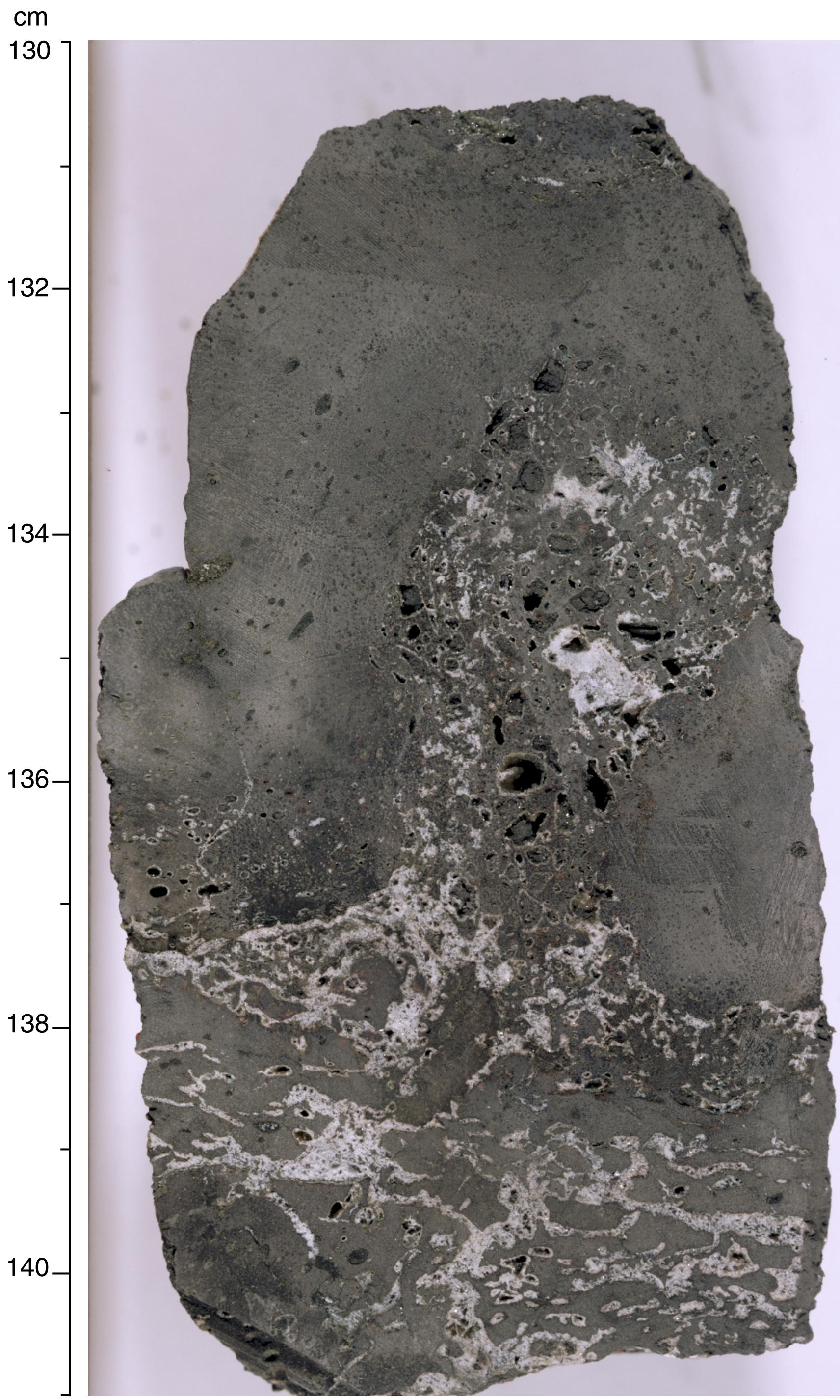

Figure F51. Close-up photograph of Sample 183-1138A-88R-2 (Piece 2, 30–40 cm) showing a dense arm intruding flow-top breccia of basement Unit 21.

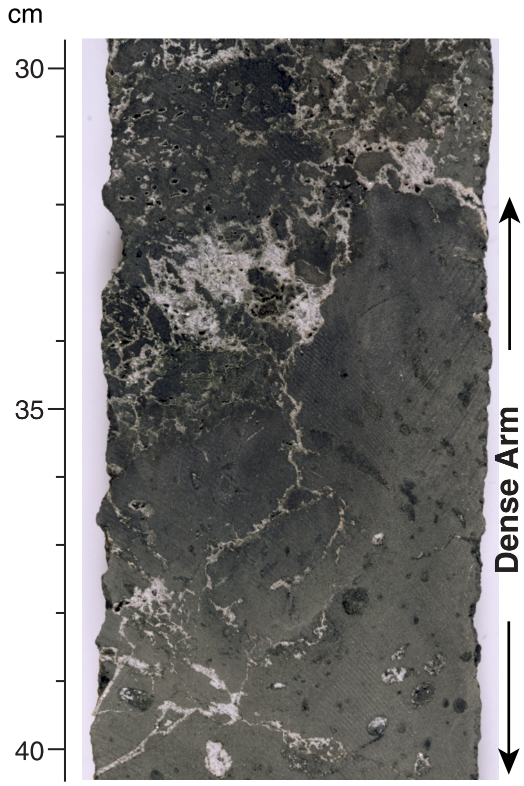

Figure F52. Close-up photograph of Sample 183-1138A-88R-2 (Piece 4, 28–51 cm) showing pahoehoe lobes intruding flow-top breccia of basement Unit 22.

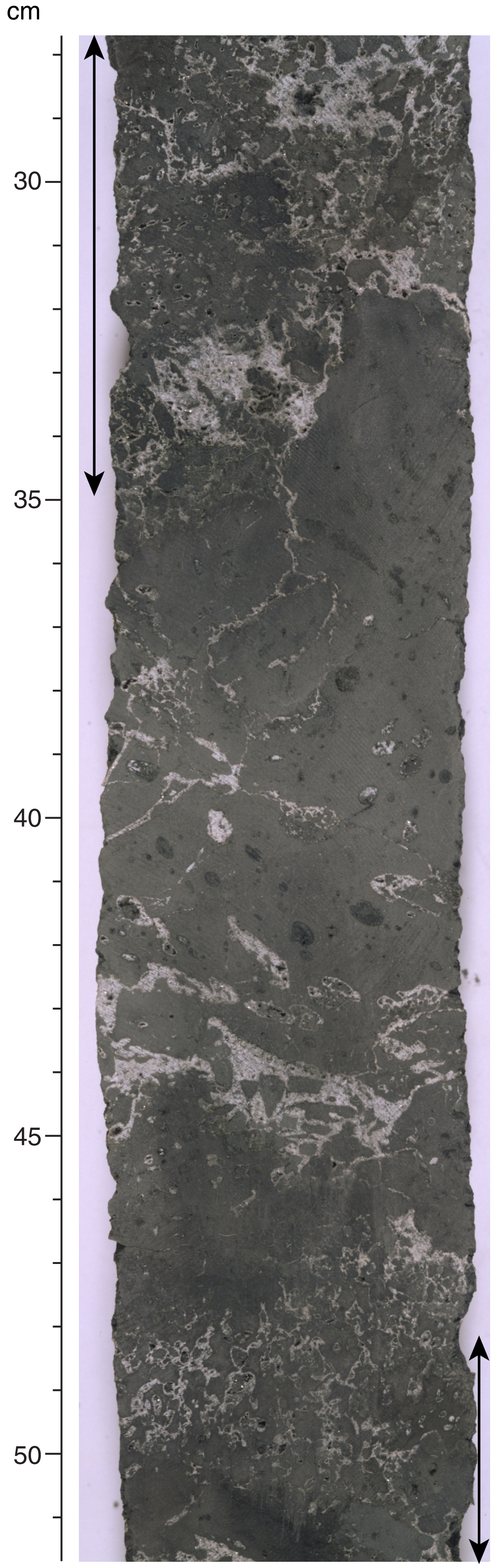

Figure F53. Interpretative summary of the lithology, morphology, and mineralogy of basaltic lava flows sampled in the basement (Unit VI) at Site 1138. Boundaries for igneous Units 3–22 are indicated. We illustrate the structural variations through the section schematically, assigning unrecovered core to the overlying unit. Flow types are pahoehoe (P), aa (A) and transitional (T). The presence of plagioclase (PL), clinopyroxene phenocrysts (CPX), and olivine microphenocrysts (OL) is indicated.

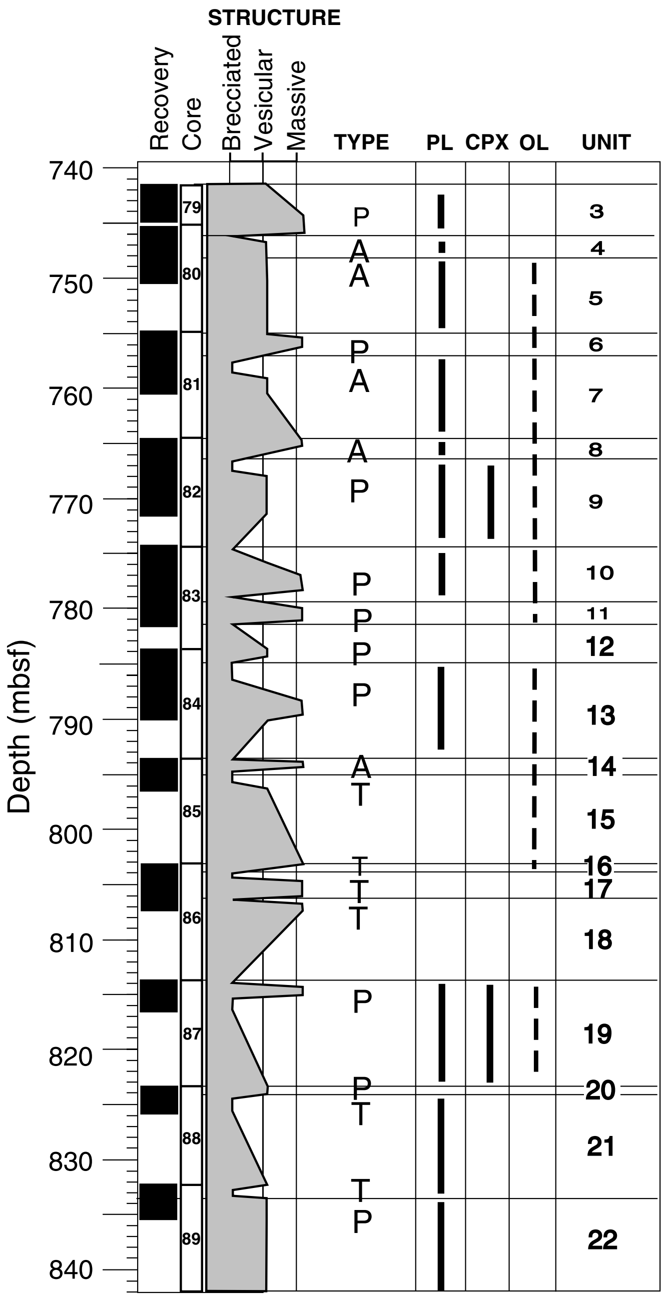

Figure F54. Photomicrograph of alkali feldspar-bearing dacite cobble from Unit 1. Rare subhedral phenocrysts are set in a fine-grained subtrachytic groundmass. Sample 183-1138A-74R-1, 22–29 cm, in cross-polarized light; width of field of view = 1 mm.

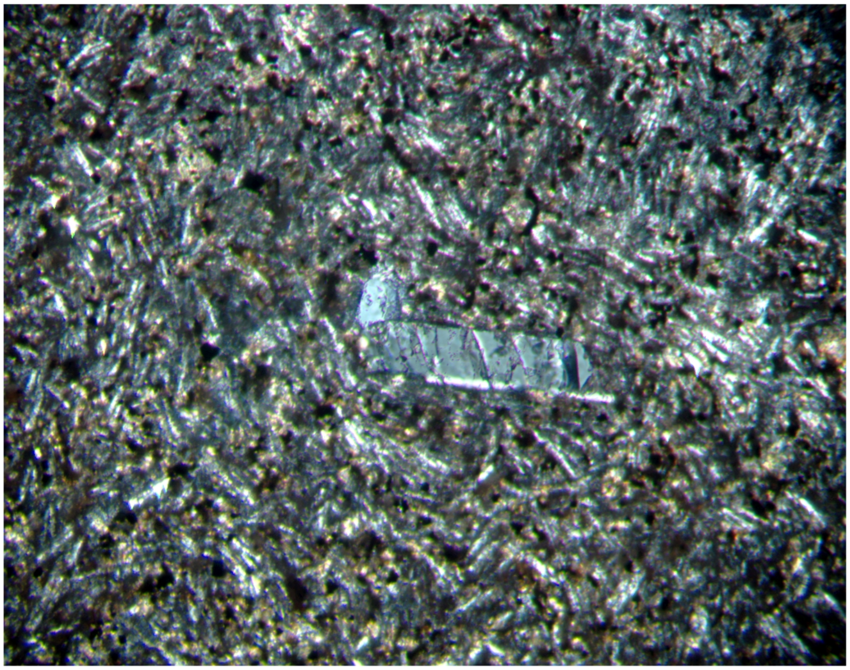

Figure F55. Photomicrograph of typical intergranular to intersertal, subtrachytic texture of Site 1138 basalts. Sample 183-1138-80R-3, 18–27 cm, in cross-polarized light; width of field of view = 2 mm.

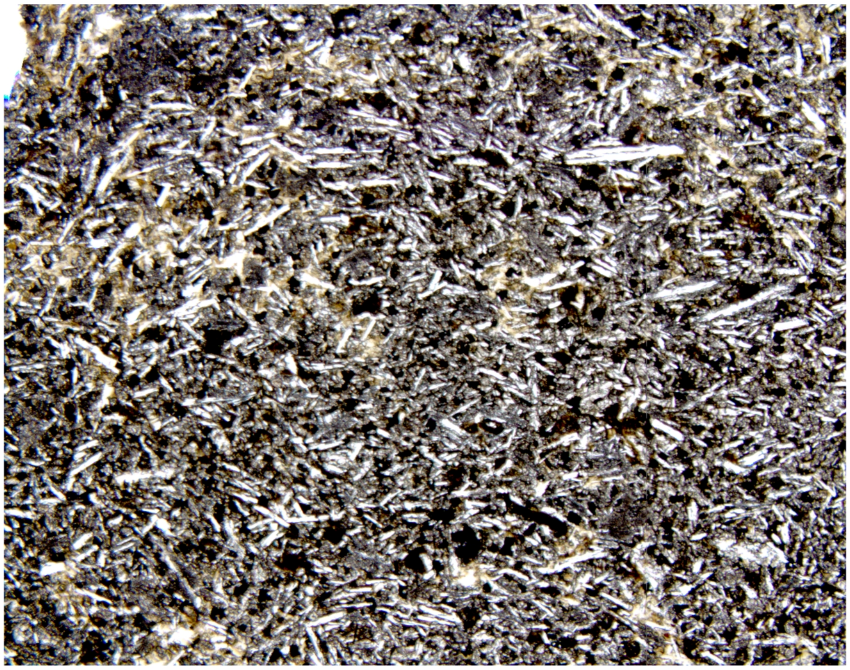

Figure F56. Segregation of glassy mesostasis into millimeter-wide subhorizontal lineaments seen in massive portions of flow interiors, now altered to light brown clay through the center of this photomicrograph. Sample 183-1138-83R-4, 34–37 cm, in cross-polarized light; width of field of view = 2 mm.

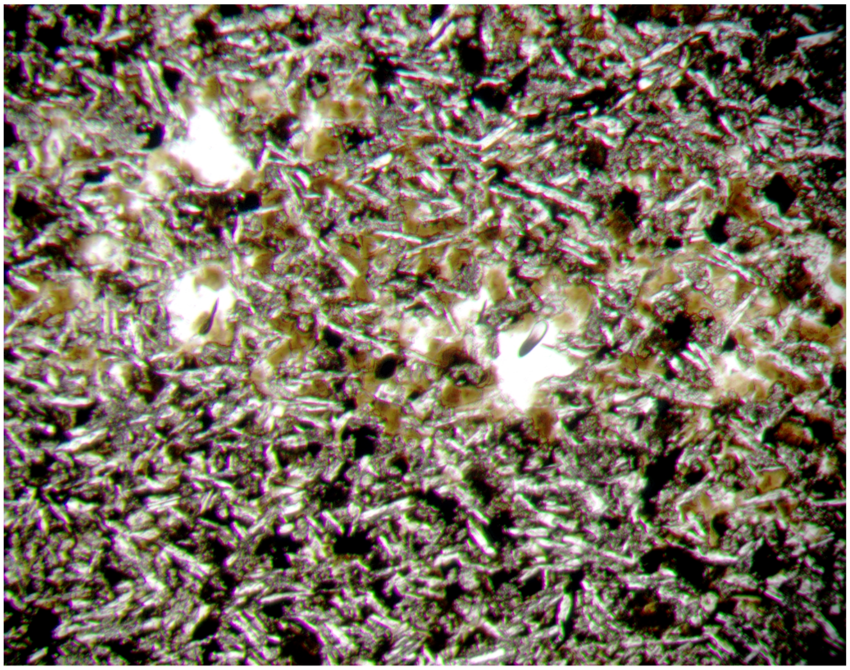

Figure F57. Close-up photomicrograph of skeletal, dendritic titanomagnetite groundmass crystals in flow margin, Unit 6. Sample 183-1138-81R-2, 26–27 cm, in reflected light; width of field of view = 0.5 mm.

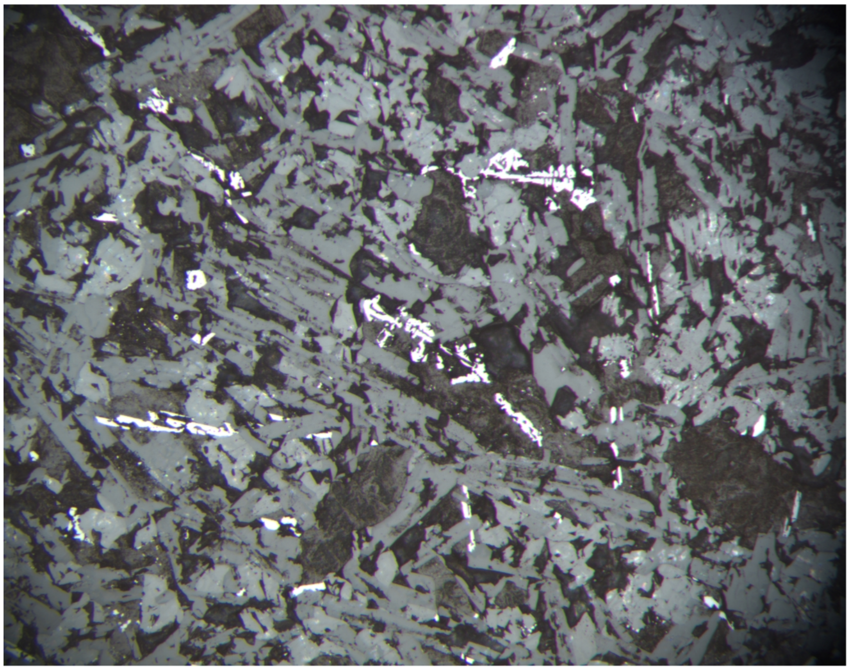

Figure F58. Close-up photomicrograph of skeletal, dendritic titanomagnetite groundmass crystals in the flow margin of Unit 19. Sample 183-1138-87R-2, 110–113 cm, in reflected light; width of field of view = 0.5 mm.

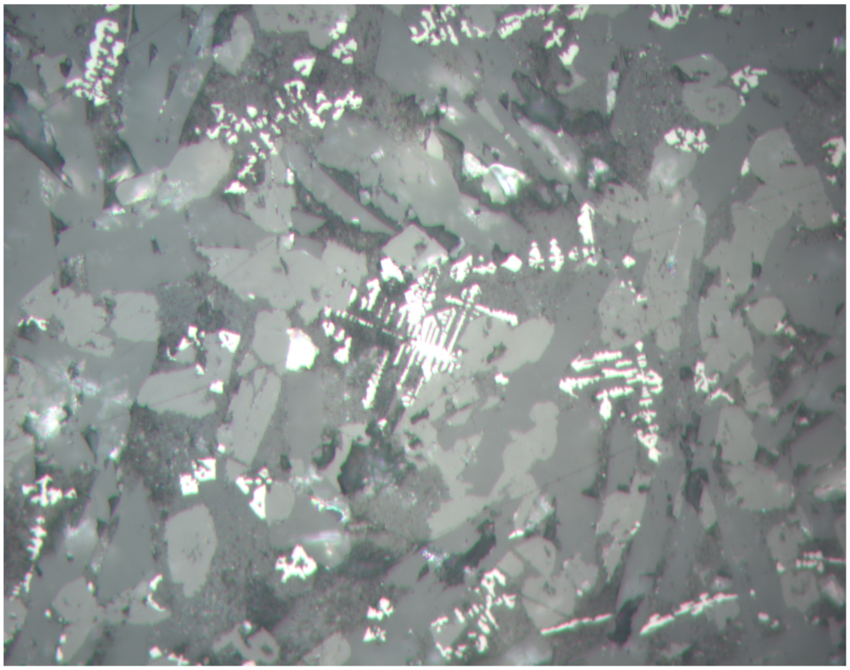

Figure F59. Photomicrograph of a glomerocryst of plagioclase and smaller clinopyroxene in Sample 183-1138A-82R-5, 69–71 cm, in cross-polarized light; width of field of view = 2 mm.

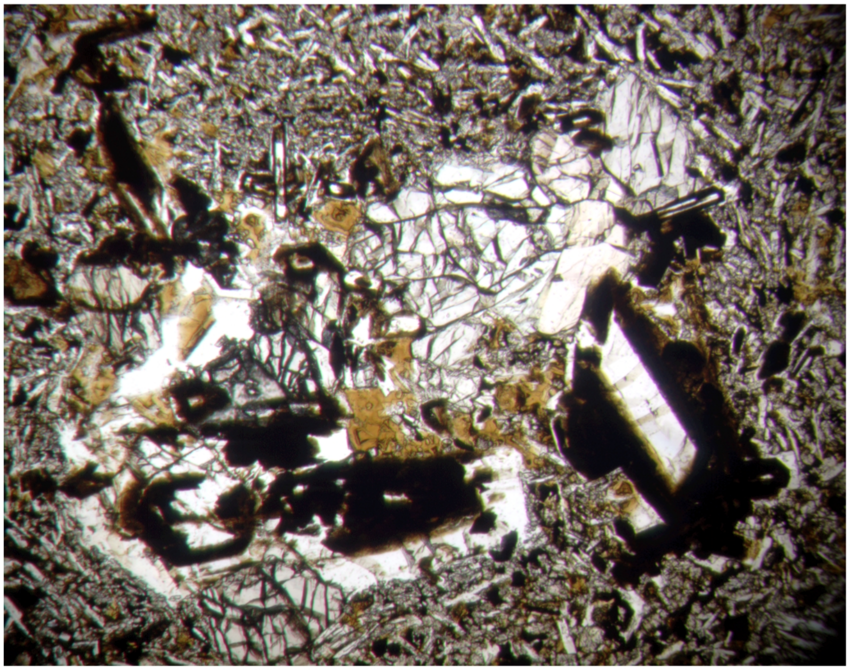

Figure F60. Olivine microphenocrysts in Unit 8. Euhedral to subhedral crystals are now replaced by dark green-brown clays. Sample 183-1138A-82R-1, 126–128 cm, in cross-polarized light; width of field of view = 1 mm.

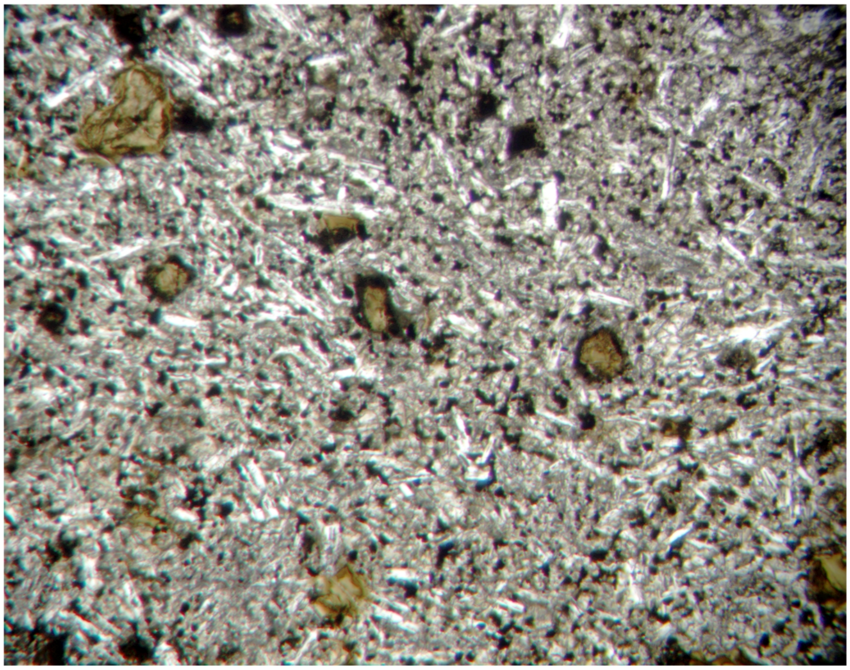

Figure F61. A. Site 1138 igneous rock compositions represented by total alkalis ($Na_2O + K_2O$) vs. SiO_2. Unit 1 cobbles are dacites, whereas the pumice-rich portion of the Unit 2 breccia has a trachytic composition (large solid squares). Units 3–22 are tholeiitic to transitional basalts (diamonds). **B.** Alkalic and tholeiitic basalt fields are distinguished by the Macdonald-Katsura (1964) line. Site 1138 basalts are poorer in silica than those from Sites 1136 and 1137. Solid diamonds = upper series lavas; shaded diamonds = lower series lavas. Open symbols = samples determined from petrography and loss on ignition to have been affected by low-temperature alteration. Compositions for basalts from other southern and central Kerguelen Plateau locations are shown as fields for drilling Sites 738, 747, 749, and 750 and dredge locations reported by Davies et al. (1989) and Weis et al. (1989).

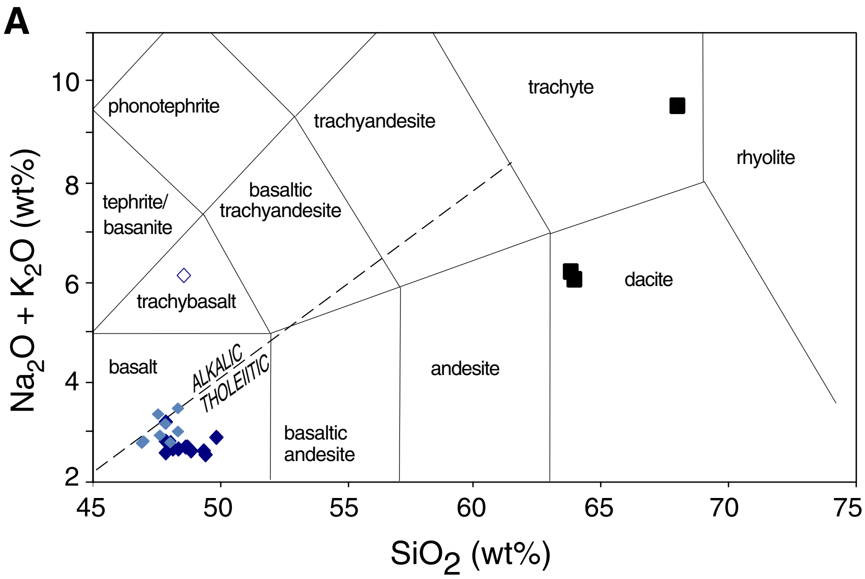

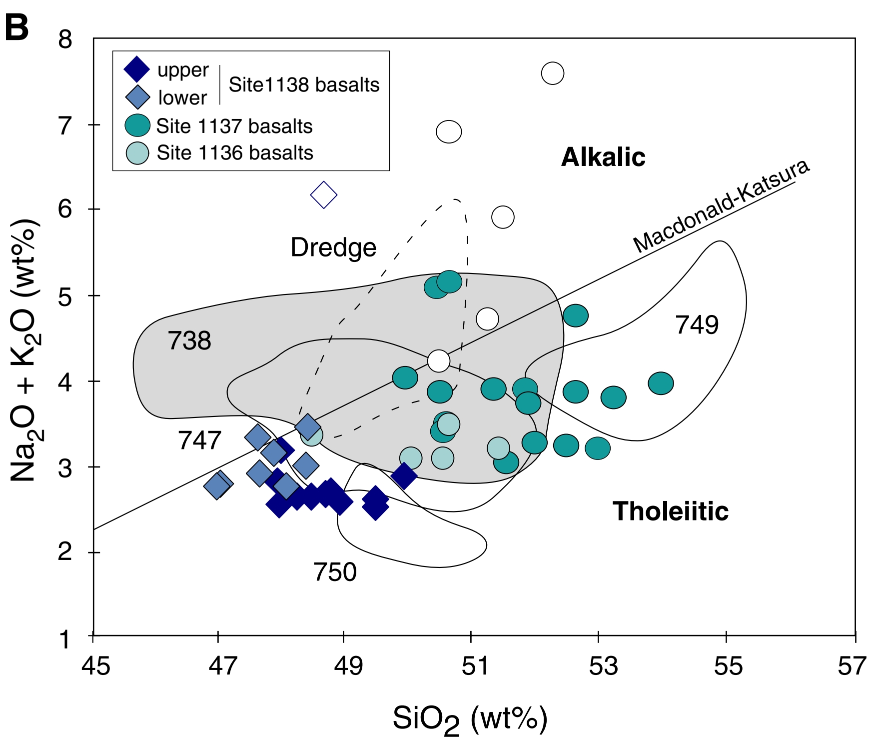

Figure F62. Downhole variations in major element compositions for Site 1138 basalts. Mg# is Mg/(Mg + Fe^{2+}). Basalts are divided into chemically coherent lava-flow series. Units 3–13 form the upper series (solid diamonds) and Units 14–22 form the lower series (shaded diamonds).

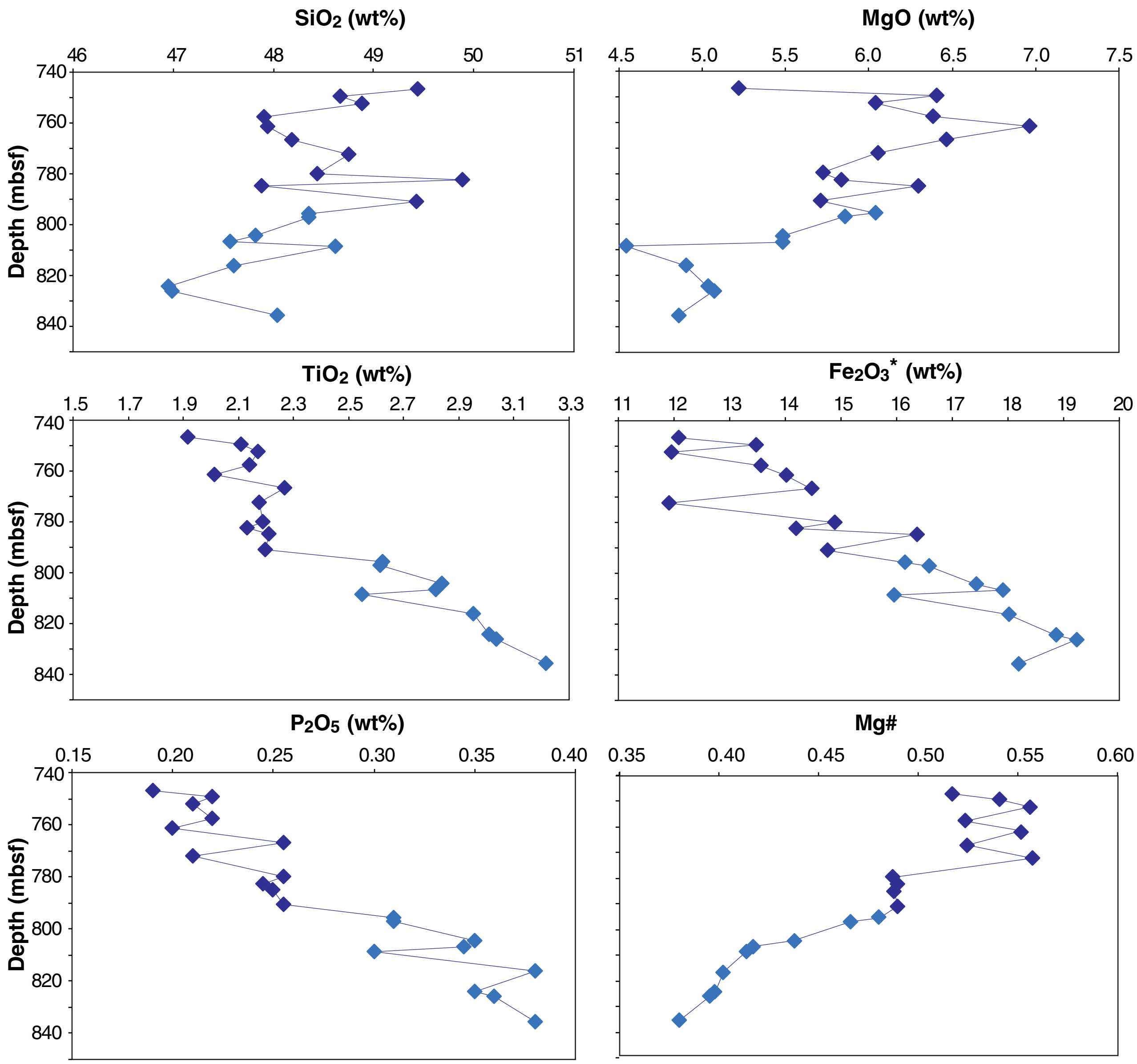

Figure F63. Major element compositional variations plotted against Mg# for Site 1138 basalts. Basalts are divided into chemically coherent lava-flow series. Units 3–13 form the upper series (solid diamonds) and Units 14–22 form the lower series (shaded diamonds).

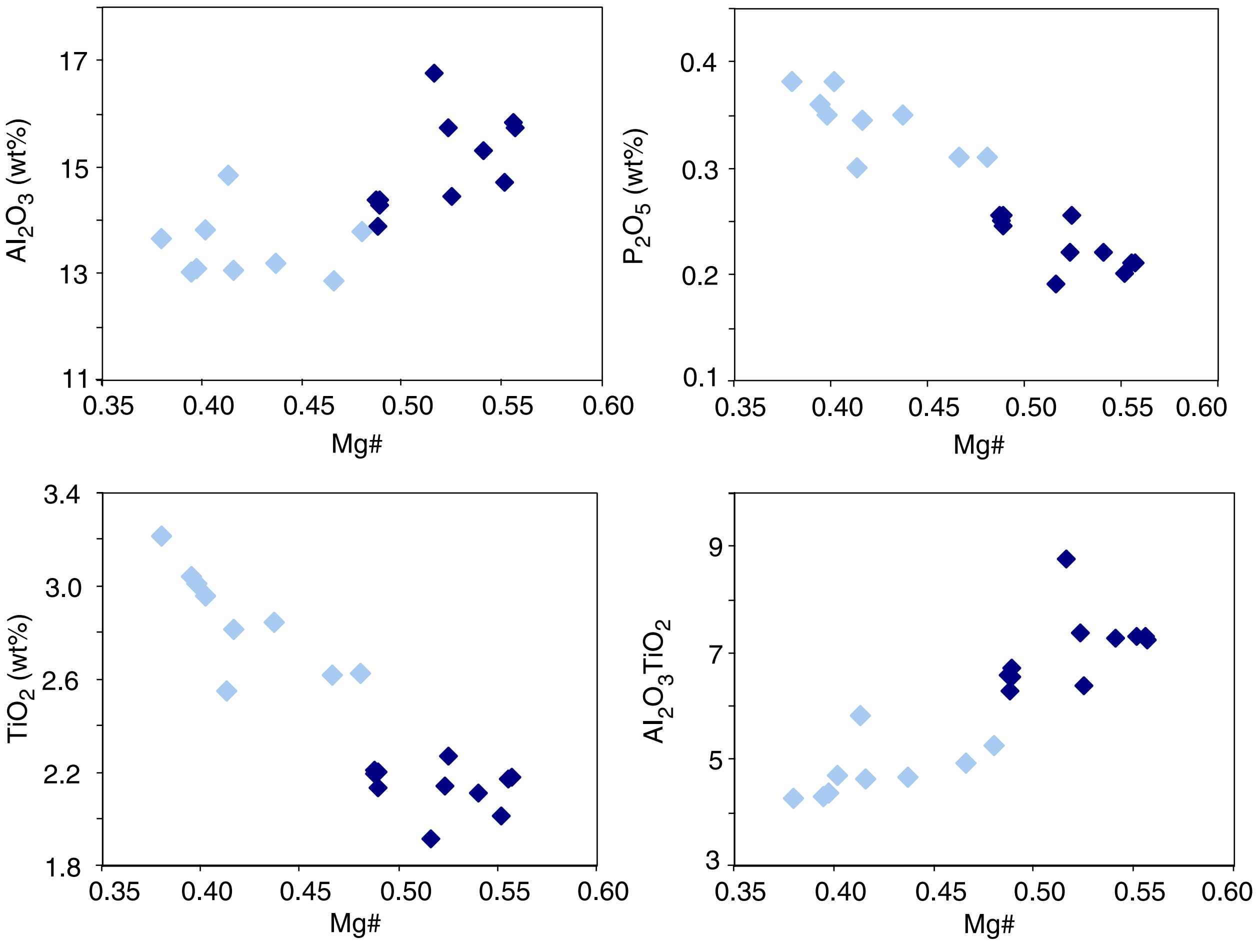

Figure F64. Downhole variations in trace element abundances and primitive mantle–normalized ratios (except for Sr/Zr) for Site 1138 basalts. Basalts are divided into chemically coherent lava-flow series. Units 3–13 form the upper series (solid diamonds) and Units 14–22 form the lower series (shaded diamonds).

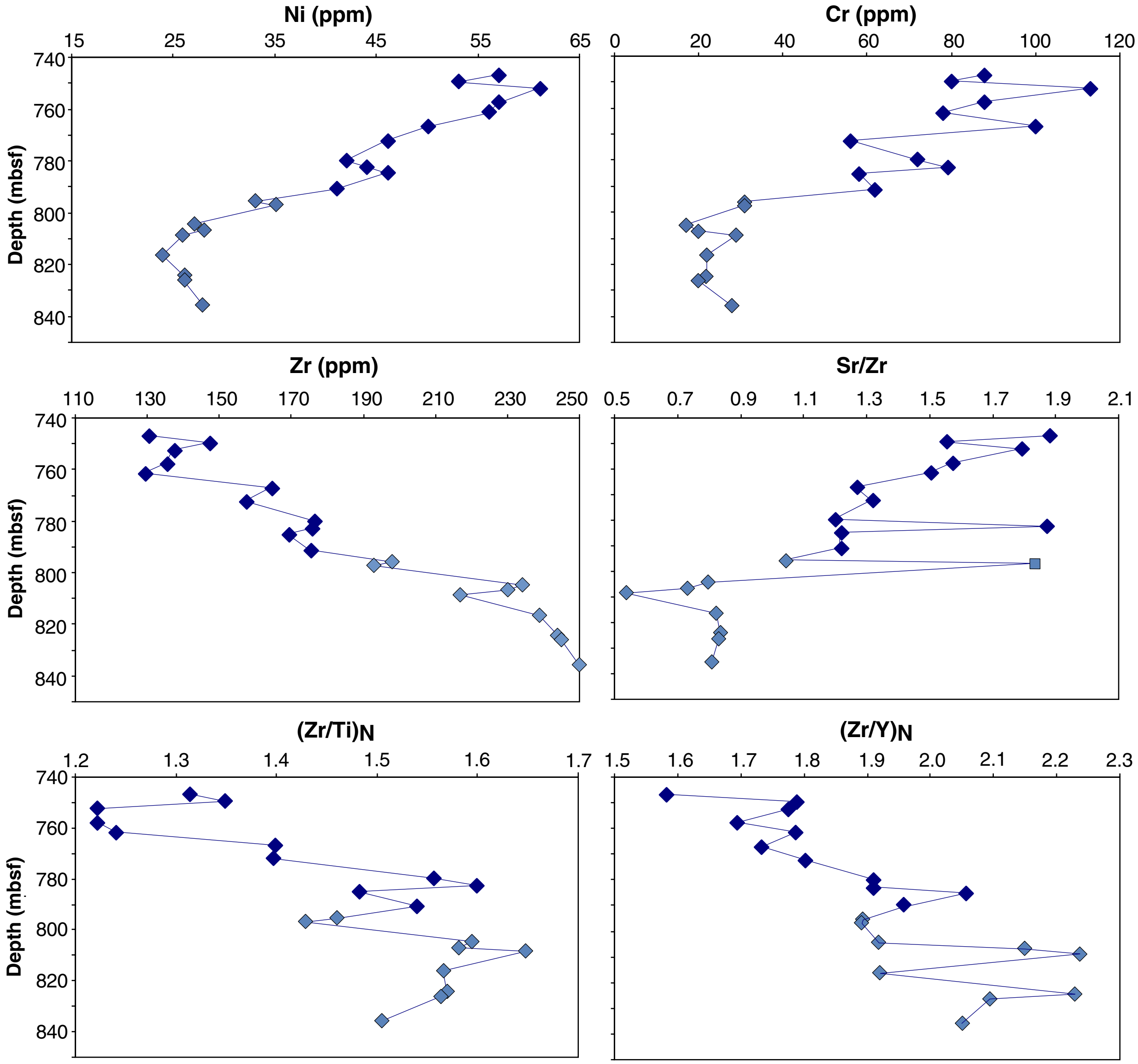

Figure F65. A. Primitive mantle–normalized (Sun and McDonough, 1989), incompatible trace element patterns for Site 1138 basalts. Upper series lavas (solid diamonds) and lower series lavas (shaded diamonds) both show striking Sr depletions, interpreted to reflect plagioclase fractionation. **B.** Patterns for basalt compositions from other Kerguelen Plateau sites. The Site 1138 data are intermediate between those basalts from Sites 1136 and 1137 and most similar to basalts from Site 747.

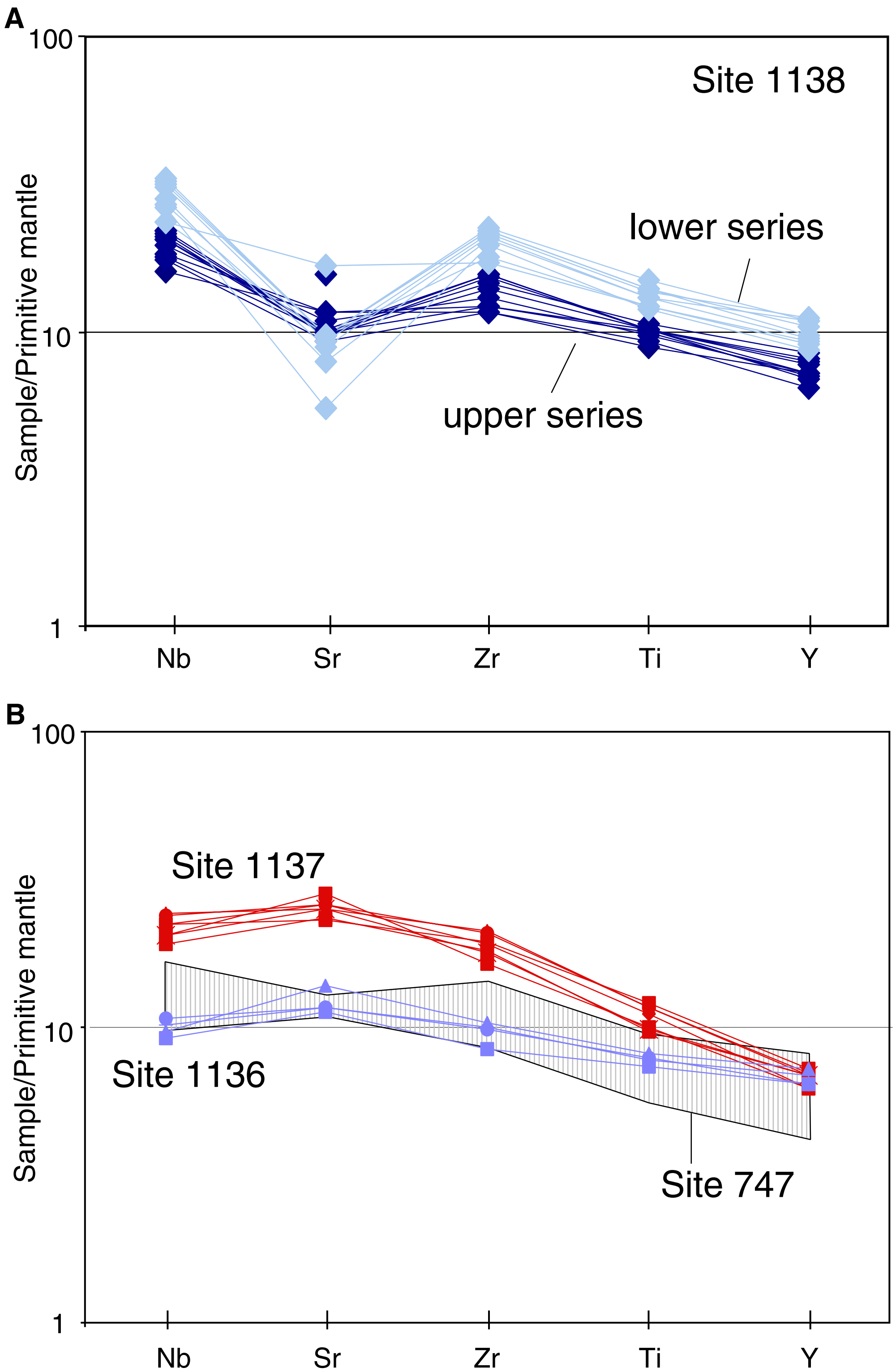

Figure F66. Major element compositional variations for Site 1138 compared with other Kerguelen Plateau sites. The TiO_2 and Fe_2O_3 enrichments in the lower series basalts (shaded diamonds) are the most extreme in the province, whereas Al_2O_3/CaO of Site 1138 basalts are comparable to those of Sites 747 and 749 basalts, but generally higher than those of basalts from Sites 1136 and 1137.

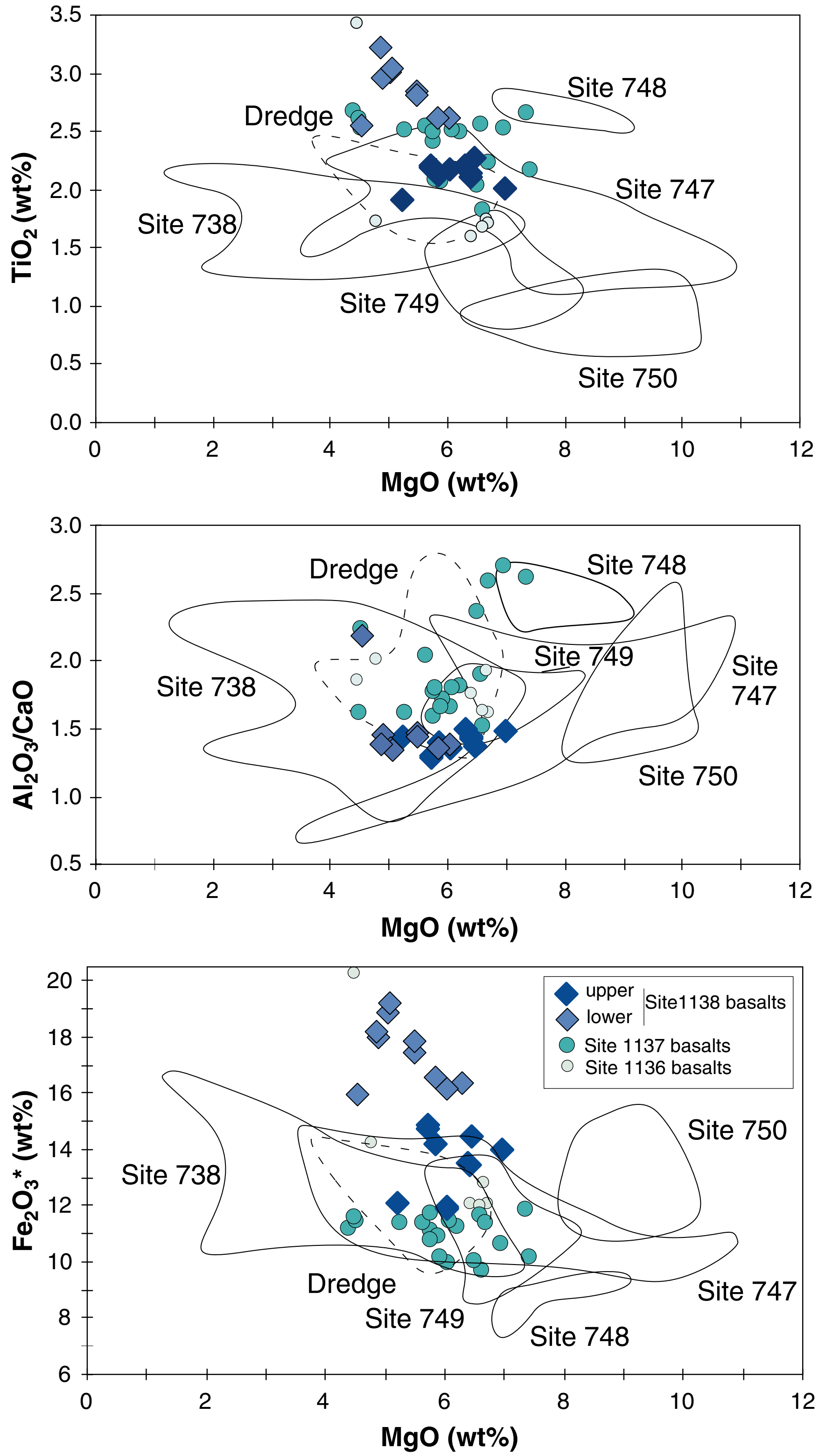

Figure F67. Primitive mantle–normalized Zr/Ti vs. Zr for Site 1138 basalts (upper series = solid diamonds; lower series = shaded diamonds) compared with data for other central and southern Kerguelen Plateau basalts. The upper series lavas are between Site 1136 and 1137 basalt $(Zr/Ti)_N$ values and may represent parental compositions for the lower series lavas. Site 1136 basalts = small shaded circles; Site 1137 basalts = large shaded circles.

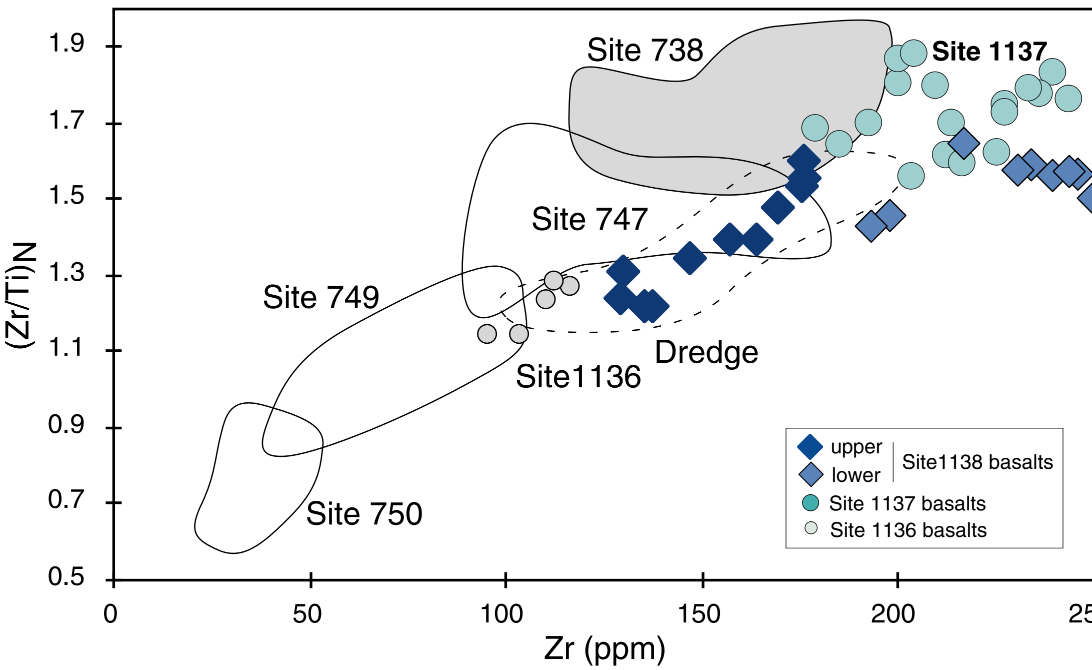

Figure F68. Nb/Y vs. Zr/Y has been proposed as a discriminant between MORB and mantle plume–derived melts. In Iceland, plume-derived melts fall within the two sloping, parallel lines (Fitton et al., 1997, 1998). Fields for compositions from other southern and central Kerguelen Plateau drilling sites are discussed in Figure F31, p. 82, in the "Leg 183 Summary" chapter. The Sun and McDonough (1989) primitive mantle composition is represented by the cross. Continental crustal material typically plots to the right of the plume field. Site 1138 basalt compositions are most similar to those from Site 747 and trend from the mantle array toward Site 1137 basalt compositions, which may contain a continental crust component (see "Igneous Petrology," p. 28, in the "Site 1137" chapter). However, the Site 1138 basalts may reflect crystal fractionation of clinopyroxene.

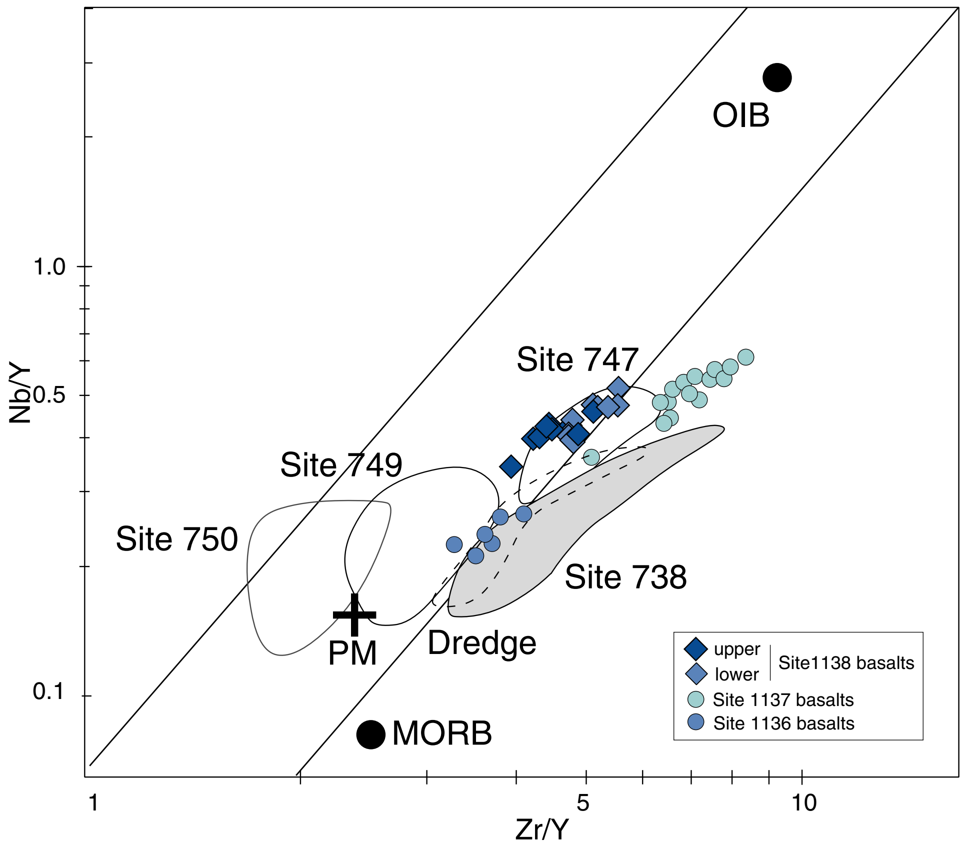

Figure F69. Distribution and abundance of secondary minerals as well as other alteration features in Hole 1138A vs. depth (mbsf), based upon macroscopic features and mineral occurrences we observed in hand specimen from the core. The color is the hue of the bulk rock; dark gray = the least-altered rocks. The sediment/breccia column shows the distribution of clastic flow tops and flow bottoms. Horizontal lines = basement unit boundaries. Colors: Bl = blue-green, Gn = green, G = dark gray, Pk = pink-brown, Bk = black, R = red. Alteration: f = fresh, s = slight, m = moderate, h = high, c = complete. Sediment/Breccia: S = pebbly sandstone and brown clays from above the basement and brown quartz-rich siltstones infilling volcanic breccias; A = igneous rock completely altered to red-brown clays; Vc = volcaniclastic conglomerates, sands, and ashes (basement Unit 2); V = volcanic breccia; T = tectonic breccia. Abundance: 0 = absent, t = trace, c = common, a = abundant. AmSi = amorphous silica.

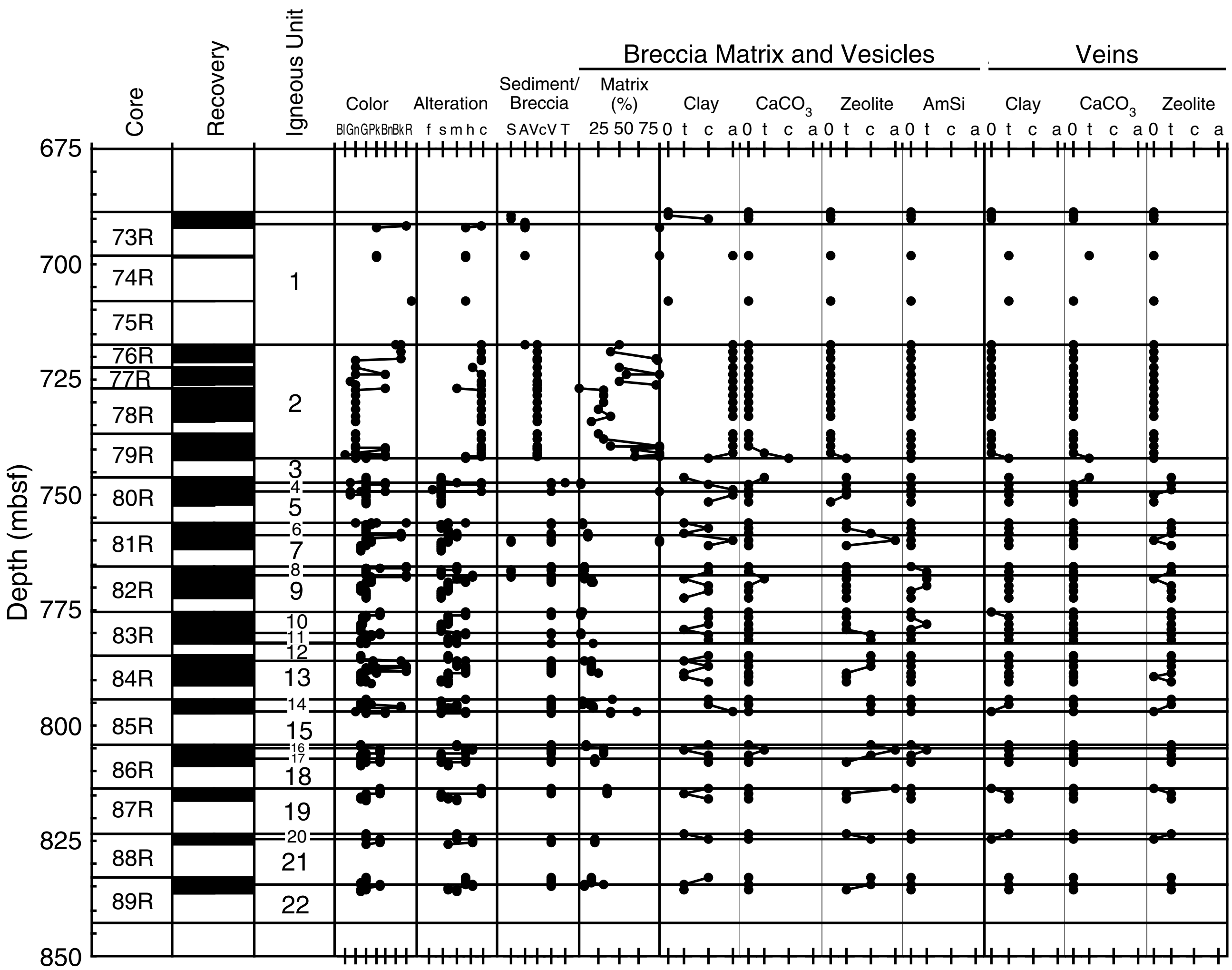

Figure F70. A. Diagram showing the unoriented true dip of veins in basement rocks from Hole 1138A. We subdivide veins by the dominant mineral filling and plot the true dip vs. depth. Zones of igneous brecciation are delineated by horizontal gray bands and abundance of mineral filled veins with depth in Hole 1138A. We subdivide veins by the dominant mineral filling and calculate vein abundance as an equivalent vein thickness in millimeters of vein material per meter of recovered drill core (in millimeters per meter). **B.** Diagram showing the total fracture distribution, which we calculate from the total number of veins of any thickness per meter of recovered core. We present data on a core by core basis. Crosses = clay; open circles = calcium carbonate; solid triangles = zeolites.

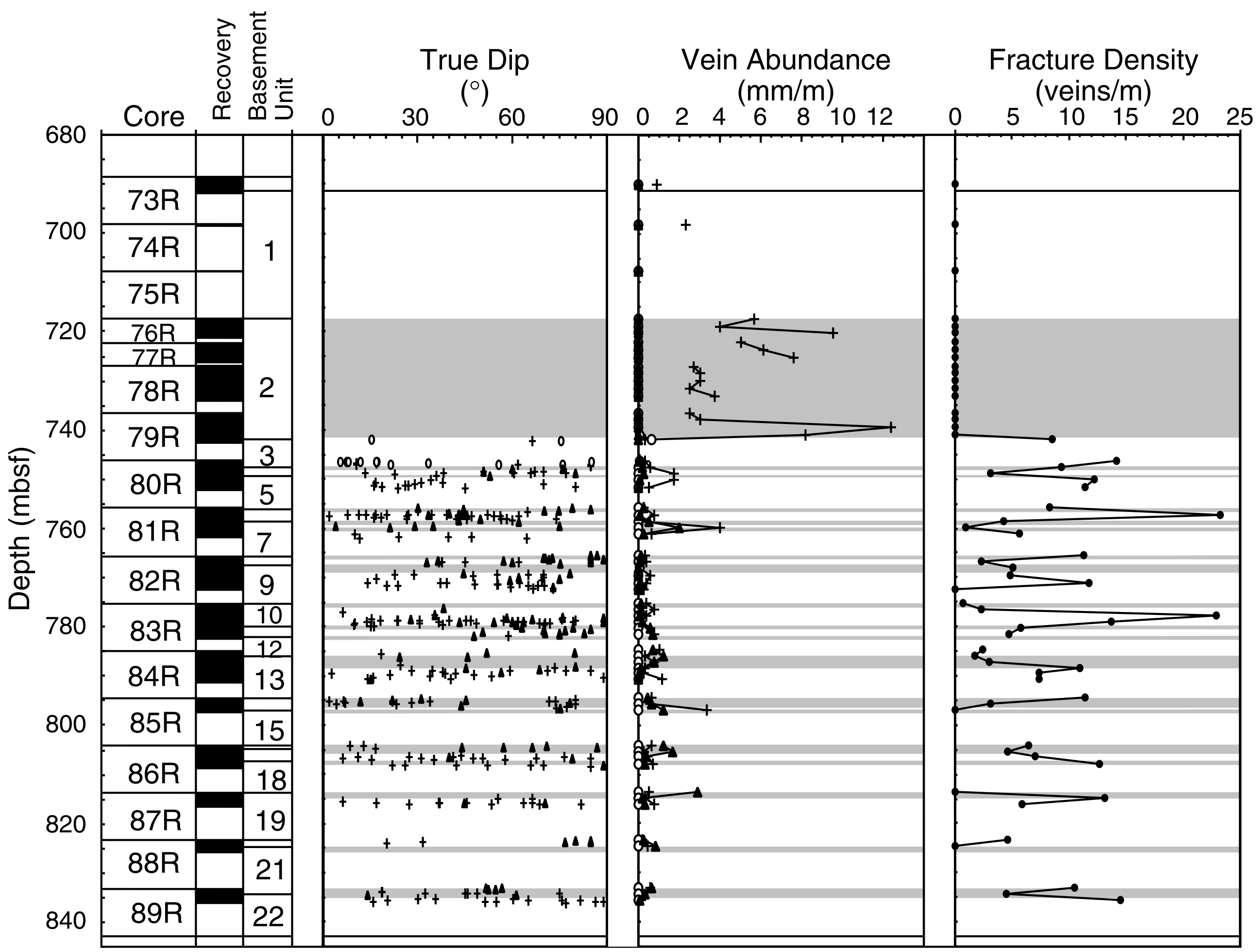

Figure F71. Histogram showing the distribution of vein dips subdivided according to mineral filling in Hole 1138A. Crosses = clay; open circles = calcium carbonate; solid triangles = zeolites.

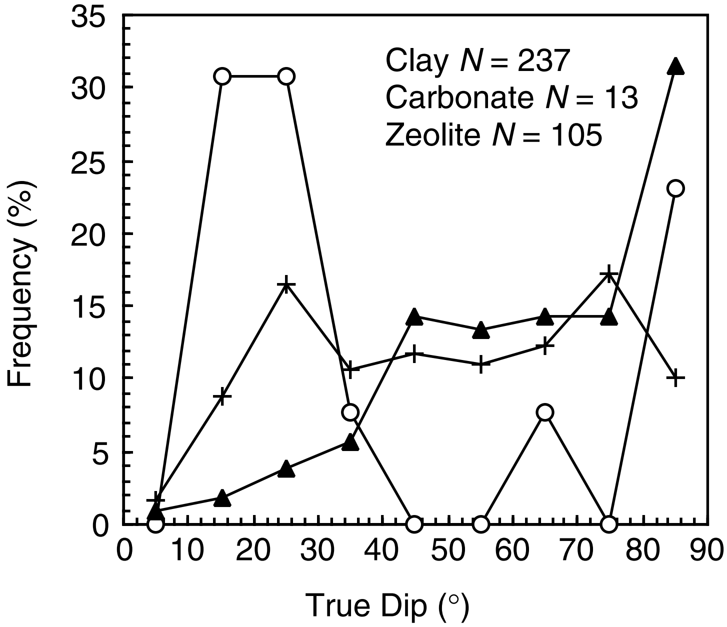

Figure F72. Example of progressive AF demagnetization of a discrete sediment sample. The intensity decay curve is plotted on the left, and the directional change is plotted on an orthogonal vector projection on the right. Magnetic directions that tend toward the origin with high median destructive fields are considered reliable. J_0 is the magnetization intensity before AF treatment.

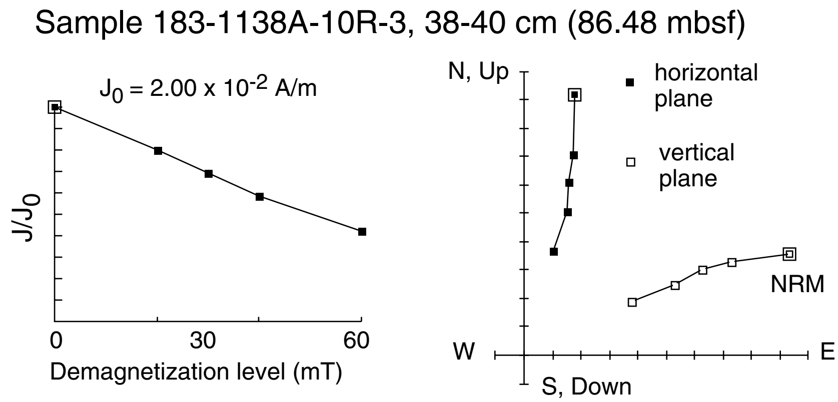

Figure F73. Hole 1138A inclination, intensity of remanent magnetization, and MST susceptibility of sediments from (**A**) 0–140 mbsf, (**B**) 140–280 mbsf, (**C**) 280–420 mbsf, (**D**) 420–560 mbsf, and (**E**) 560–700 mbsf (note change in susceptibility scale between top and bottom). Crosses and lines represent remanent magnetization before and after AF demagnetization at 20 mT, respectively. Inclination data used for polarity interpretations are shown by open circles. Interpreted normal and reversed geomagnetic chrons are shown by black and white rectangles, respectively. Inclinations from discrete samples are shown by solid circles. Lithologic units are shown on the right. (Continued on next four pages.)

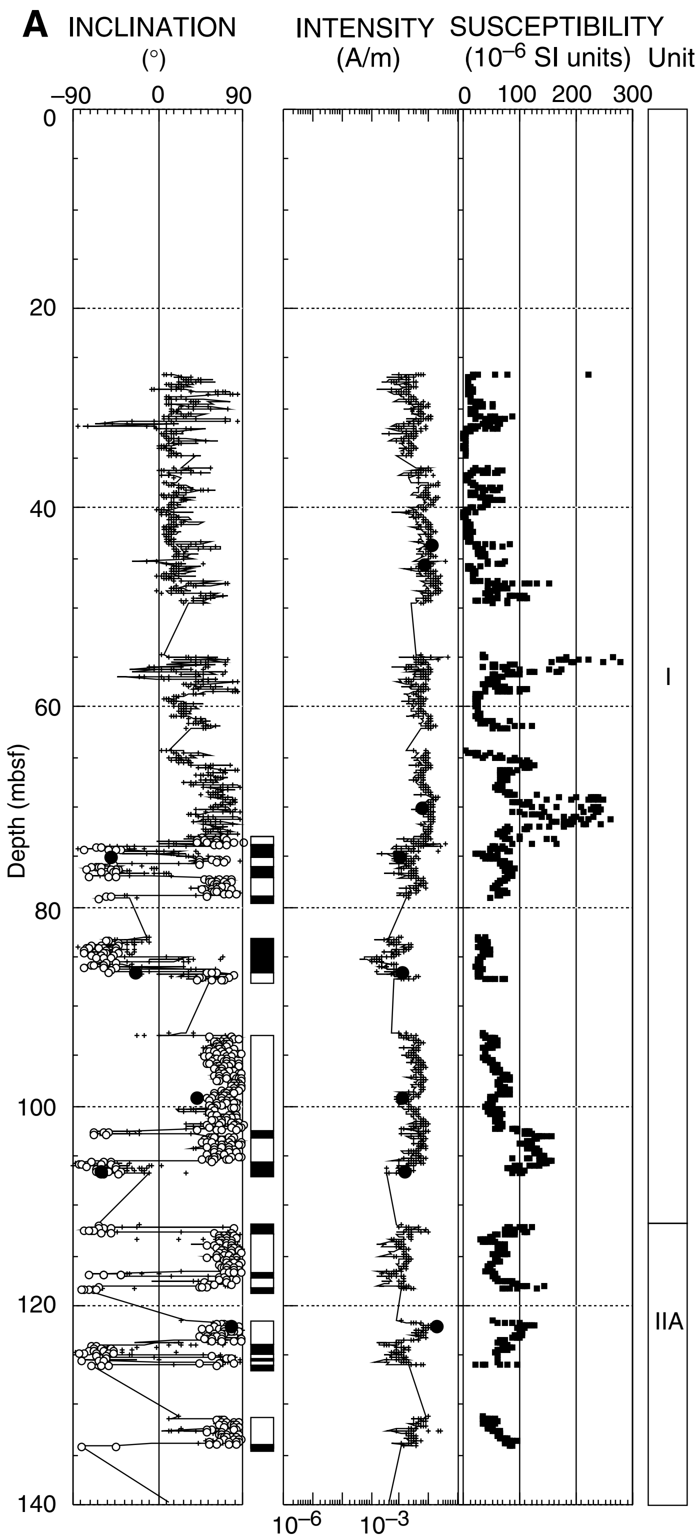

Figure F73 (continued).

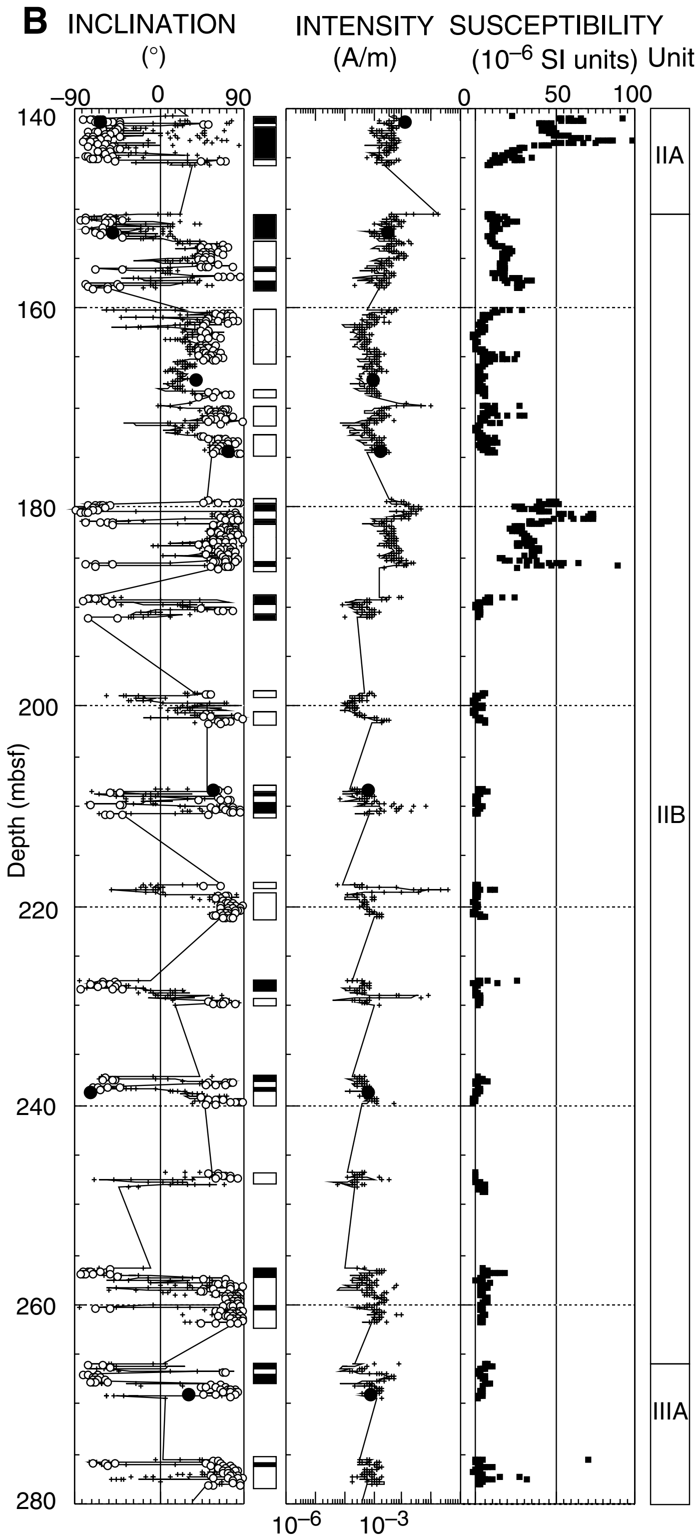

Figure F73 (continued).

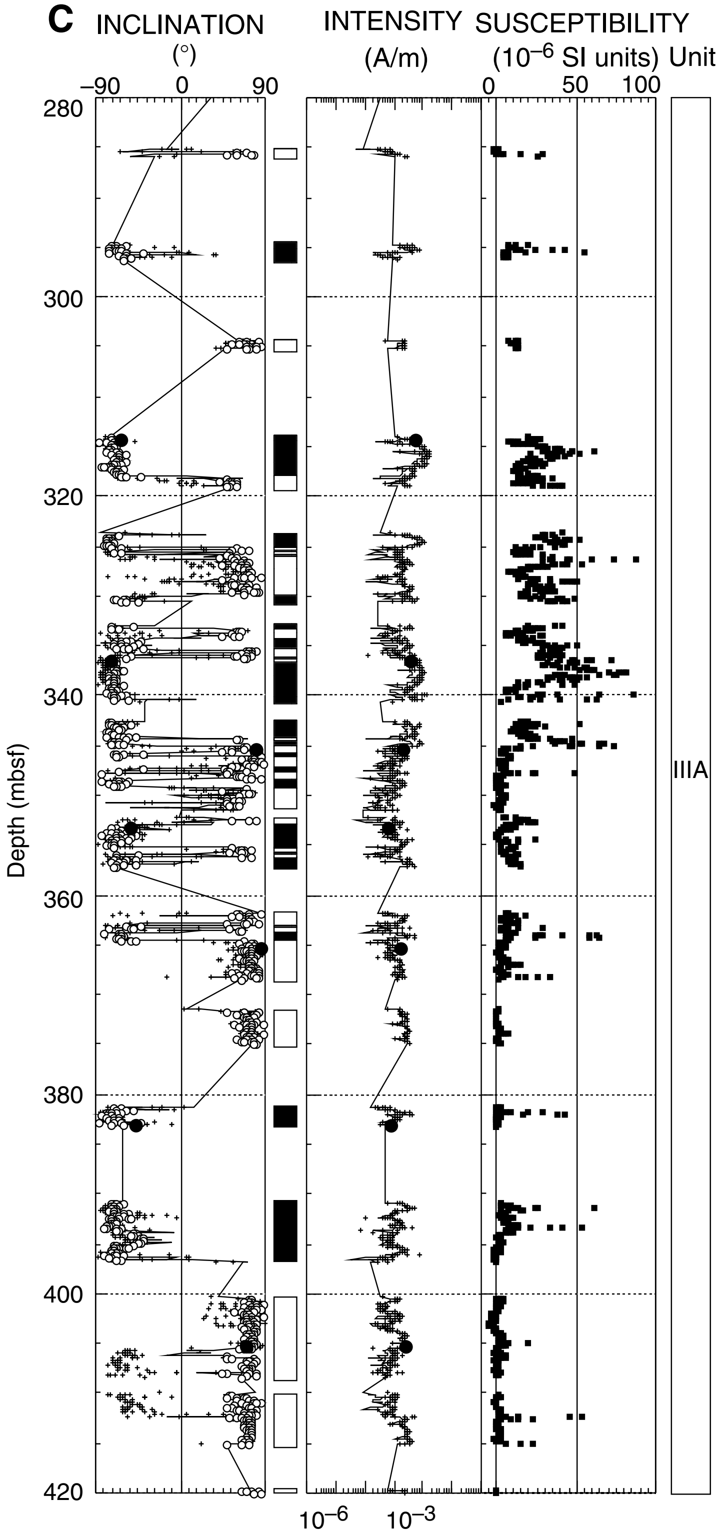

Figure F73 (continued).

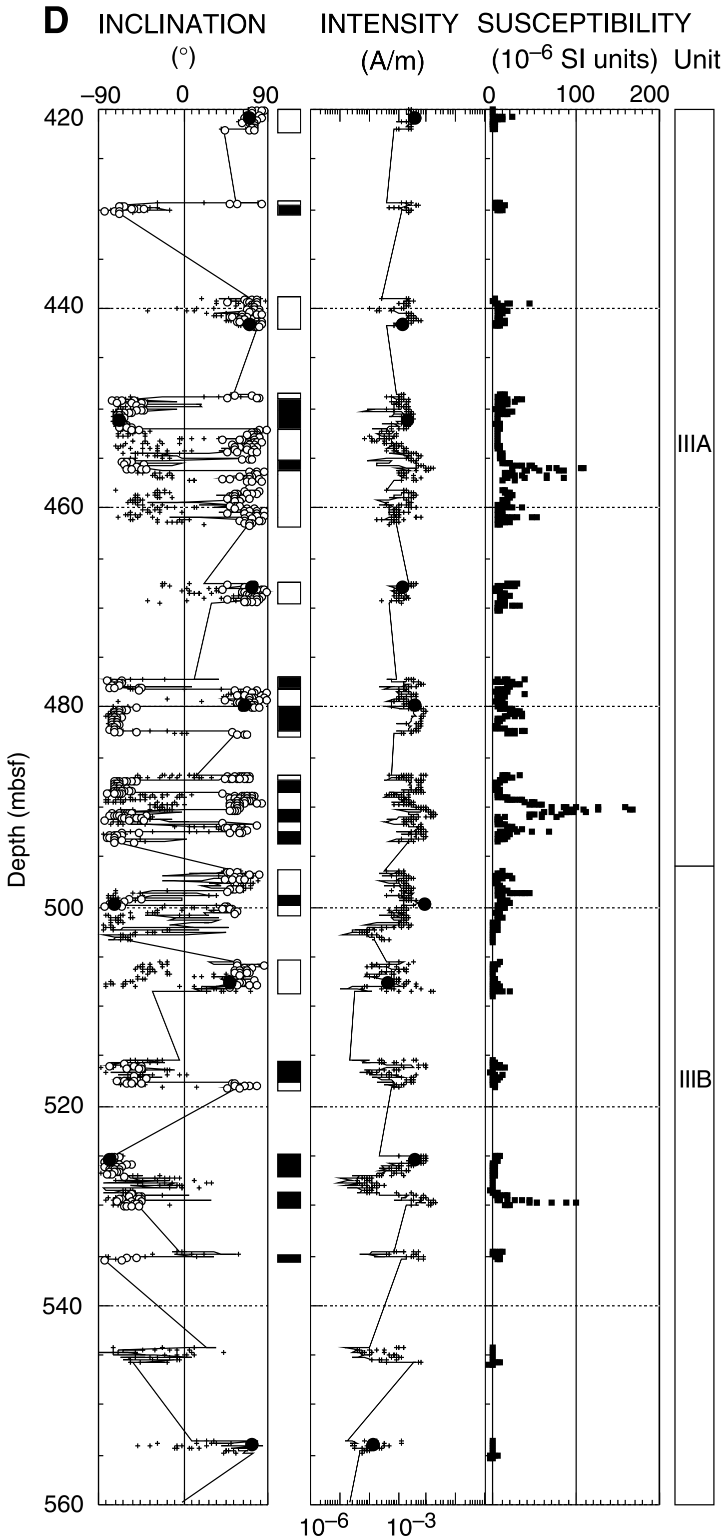

Figure F73 (continued).

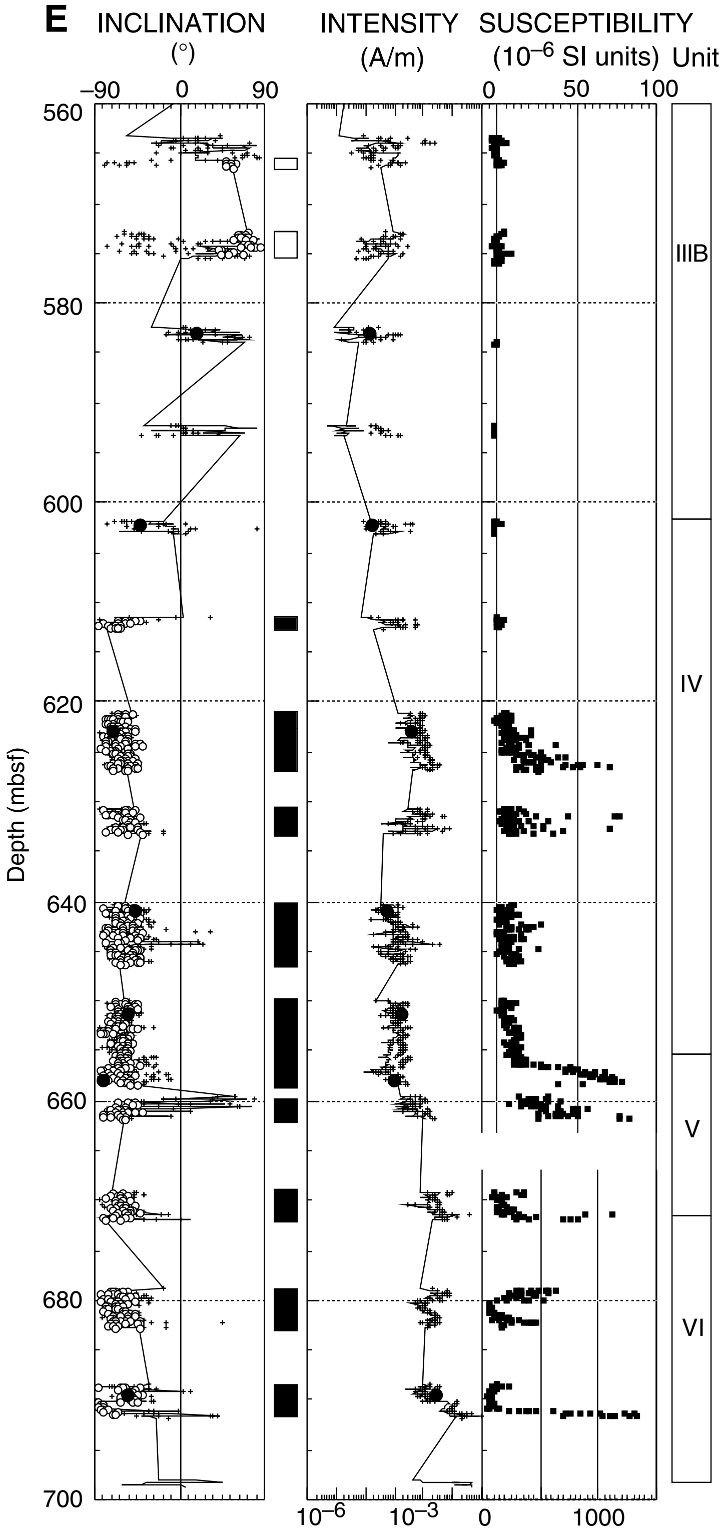

Figure F74. Average natural remanent magnetization intensity and MST susceptibility of each lithologic and basement unit. Open circles represent the average values of subunits. Large solid circles give the average values for all sediments and lavas. The horizontal bars show the range between maximum and minimum values that we obtained in the respective units.

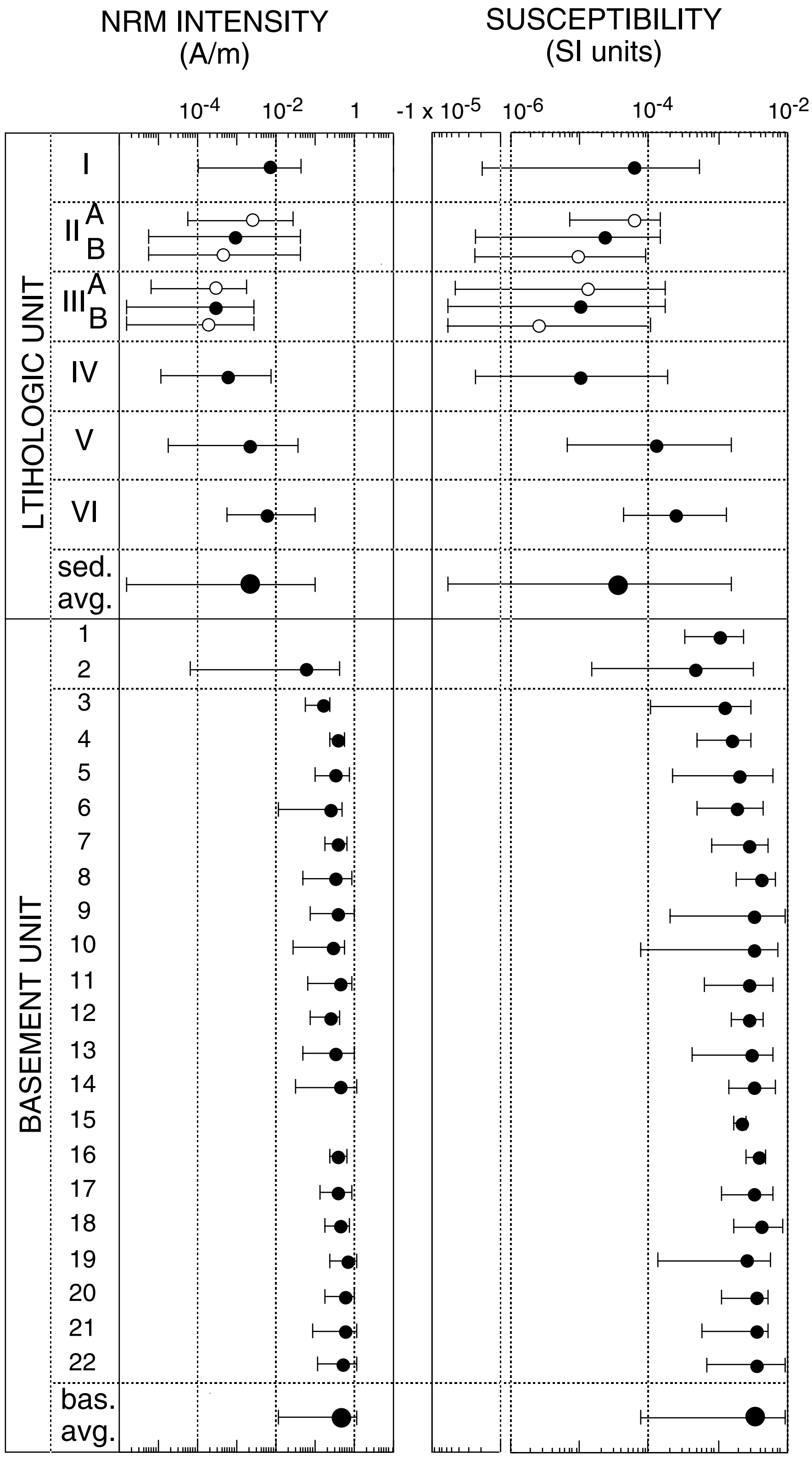

Figure F75. Hole 1138A inclination (left), intensity of remanent magnetization (middle), and susceptibility (right) of basement rocks from (**A**) 697–767 mbsf and (**B**) 767–837 mbsf. Crosses and lines represent remanent magnetization before and after AF demagnetization at 40 mT, respectively. Inclinations of NRM and characteristic inclinations of discrete samples are represented by solid and open circles, respectively. MST, AMST, and discrete-sample susceptibilities are represented by lines, crosses, and open circles, respectively. Basement units are shown on the right. (Continued on next page.)

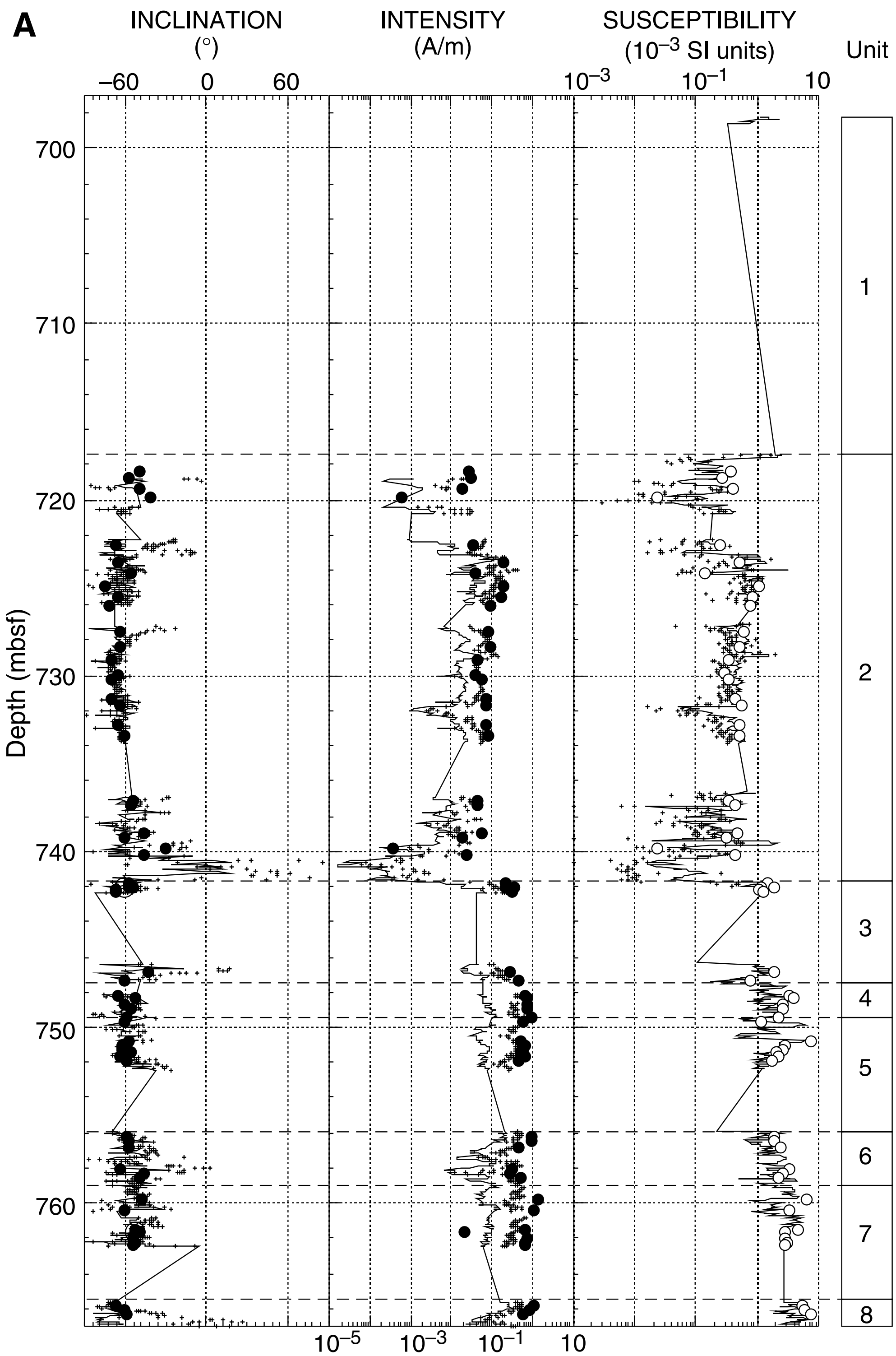

Figure F75 (continued).

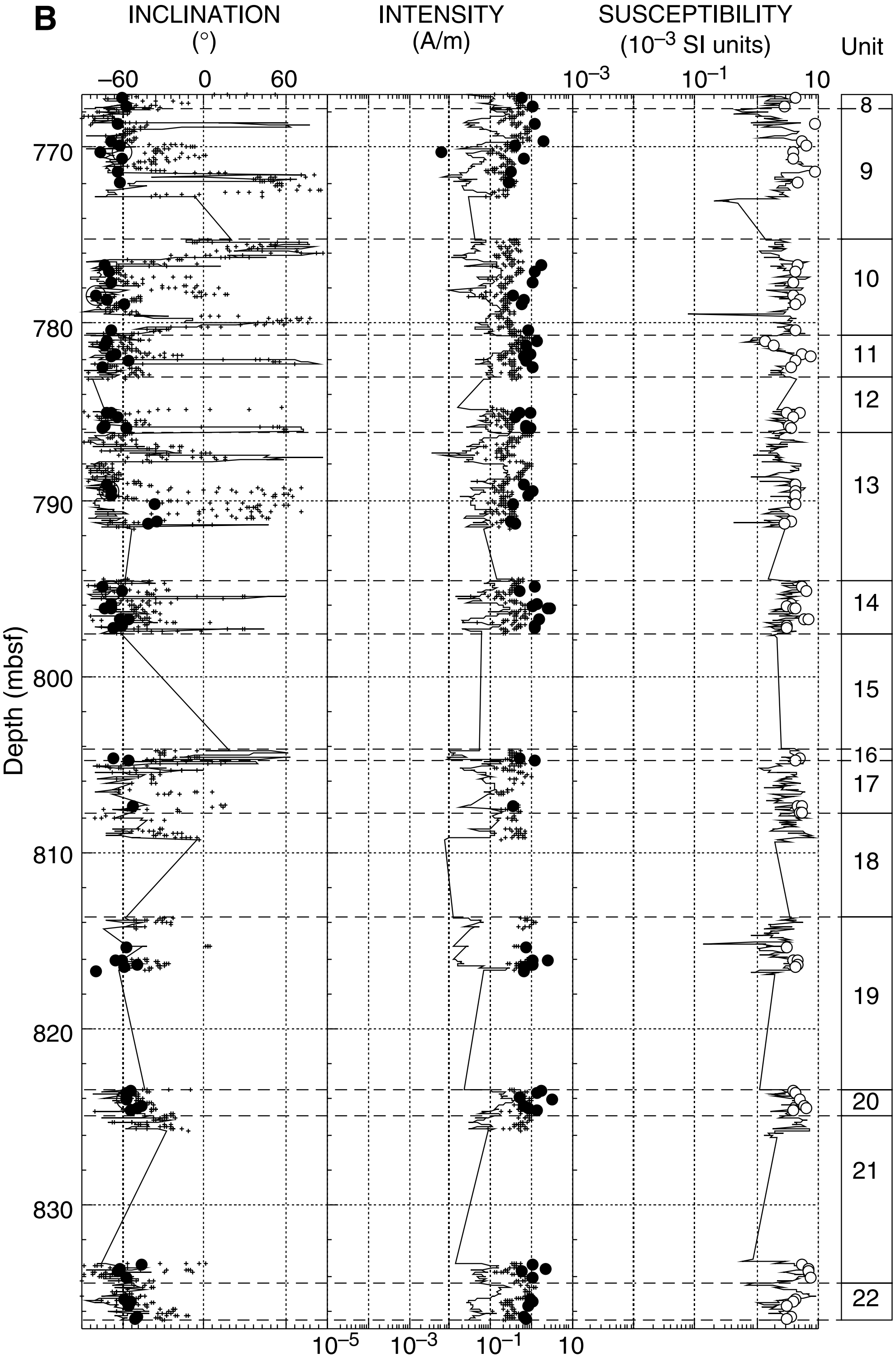

Figure F76. Directional anisotropy data from samples of (**A**) Unit 13 and (**B**) Unit 6 plotted on an equal-area stereographic projection. The directions of maximum principal axes are plotted as open squares, of intermediate principal axes as gray squares, and of minimum principal axes as black squares.

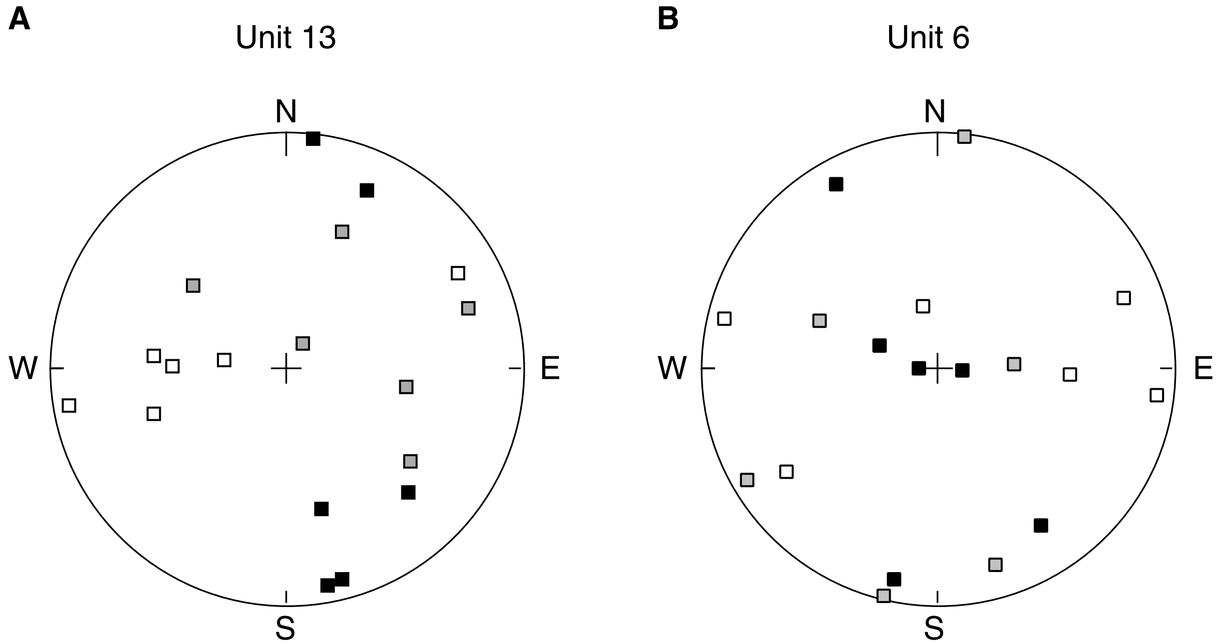

Figure F77. Stepwise AF demagnetization up to 60 mT of Sample 183-1138A-85R-1, 61–63 cm, from basement Unit 14. The sample has a median destructive field of 20 mT and a single-component magnetization as is evident from the straight lines in the orthogonal vector projections. J_0 is the magnetization intensity before AF treatment.

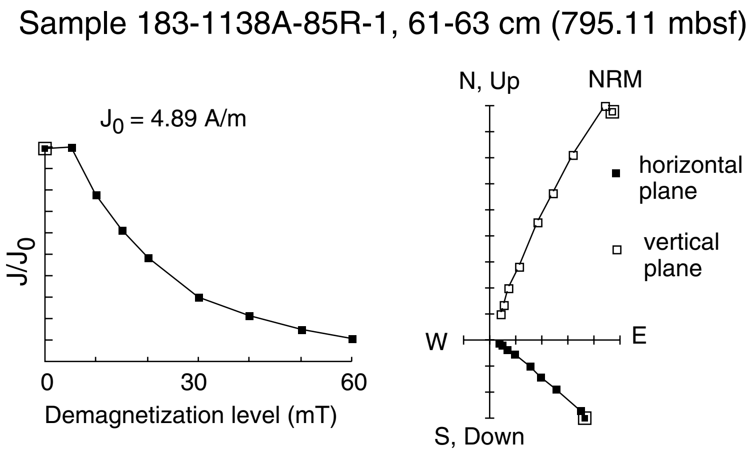

Figure F78. A. Thermal demagnetization of Sample 183-1138A-81R-5, 27–29 cm, from basement Unit 7. The NRM is stable and has a single component. Most unblocking temperatures are above 500°C. The decay curve gives no indication of a second magnetic phase. The magnetic mineral is most likely magnetite, which has a Curie temperature of 580°C. **B.** Thermal demagnetization of Sample 183-1138A-79R-4, 115–117 cm, from basement Unit 3. Unblocking temperatures are ~580°and ~300°C, indicating that both magnetite and titanomaghemite are the magnetic minerals. The NRM is stable and has a single component. J_0 is the magnetization intensity before thermal treatment.

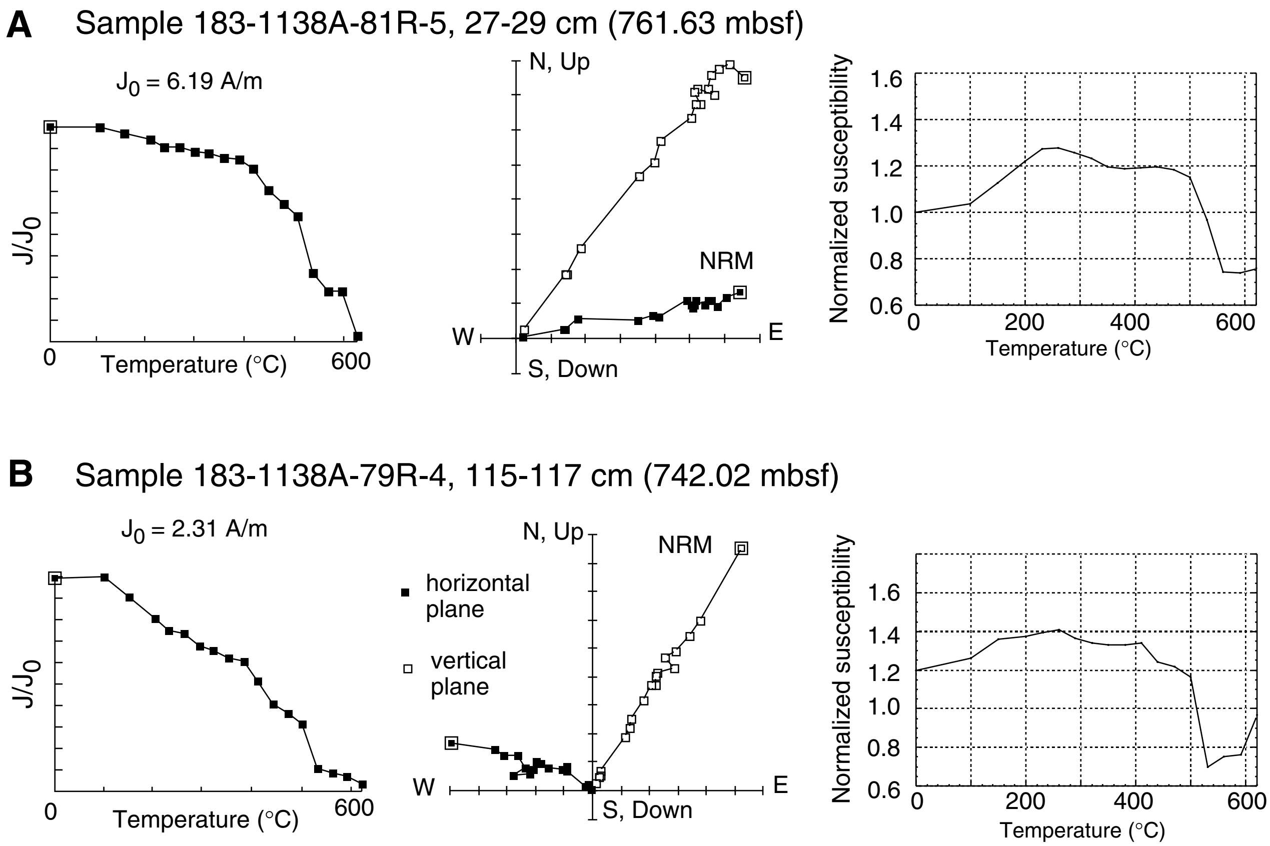

Figure F79. Downhole index properties of (**A**) bulk density, (**B**) grain density, and (**C**) porosity, and (**D**) velocities at Site 1138. Velocities measured in the x, y, and z direction are represented by circles, triangles, and squares, respectively. Open symbols = measurements on split cores. Solid symbols = measurements on cut samples. Lithologic unit boundaries are shown on the right (see **"Lithostratigraphy,"** p. 3).

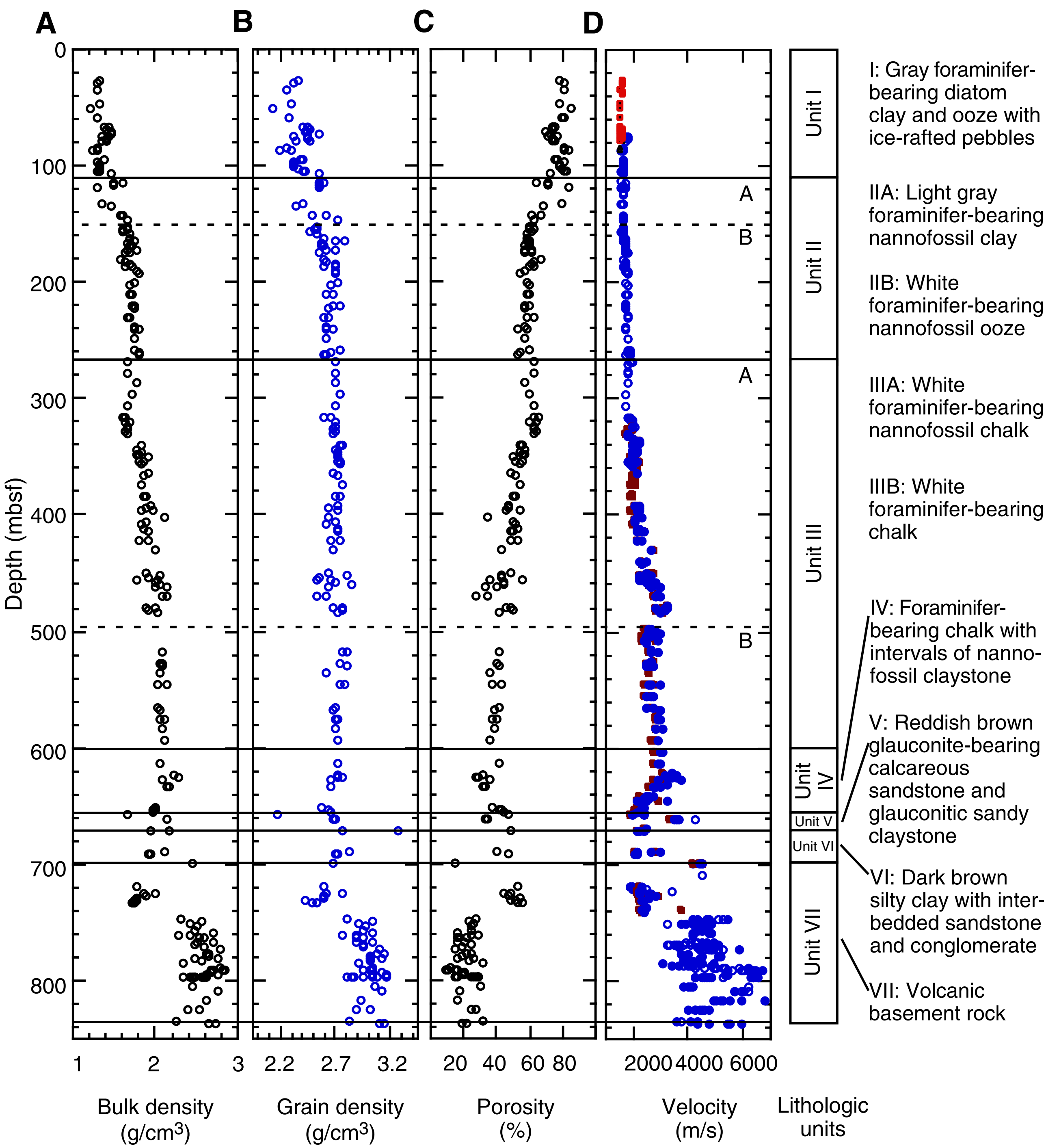

Figure F80. Summary of physical properties measurements in basaltic basement of Hole 1138A. Velocities measured in the x, y, or z direction are represented by circles, triangles, and squares, respectively. Open symbols = measurements on split cores. Solid symbols = measurements on cut samples. Basement unit boundaries are indicated on the right (see "Physical Volcanology," p. 22, and "Igneous Petrology," p. 46).

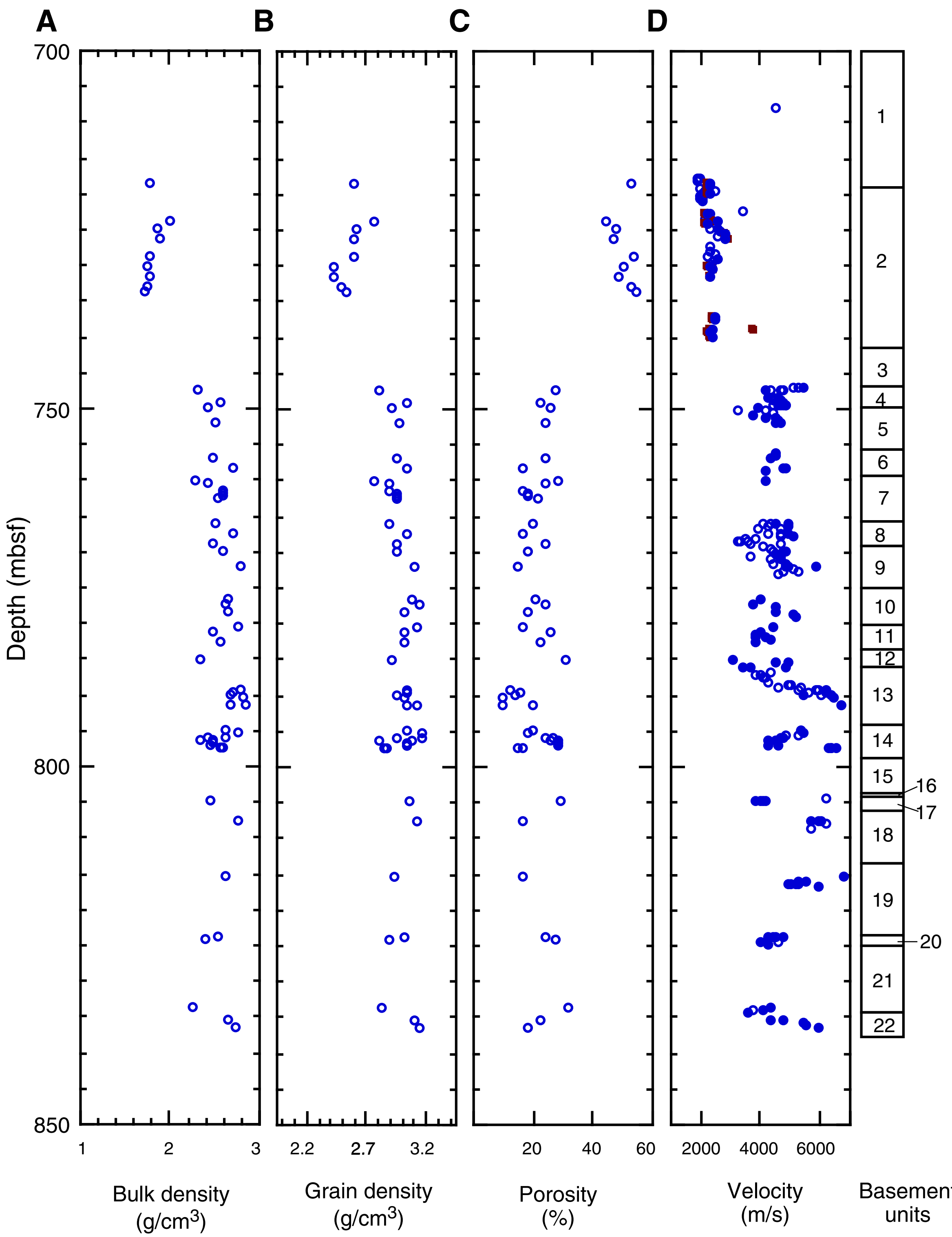

Figure F81. Downhole profiles of whole-core measurements of (**A**) GRAPE bulk density, (**B**) magnetic susceptibility, and (**C**) natural gamma ray from Site 1138. Dark dots and the associated solid line in (A) are the bulk density results from discrete samples.

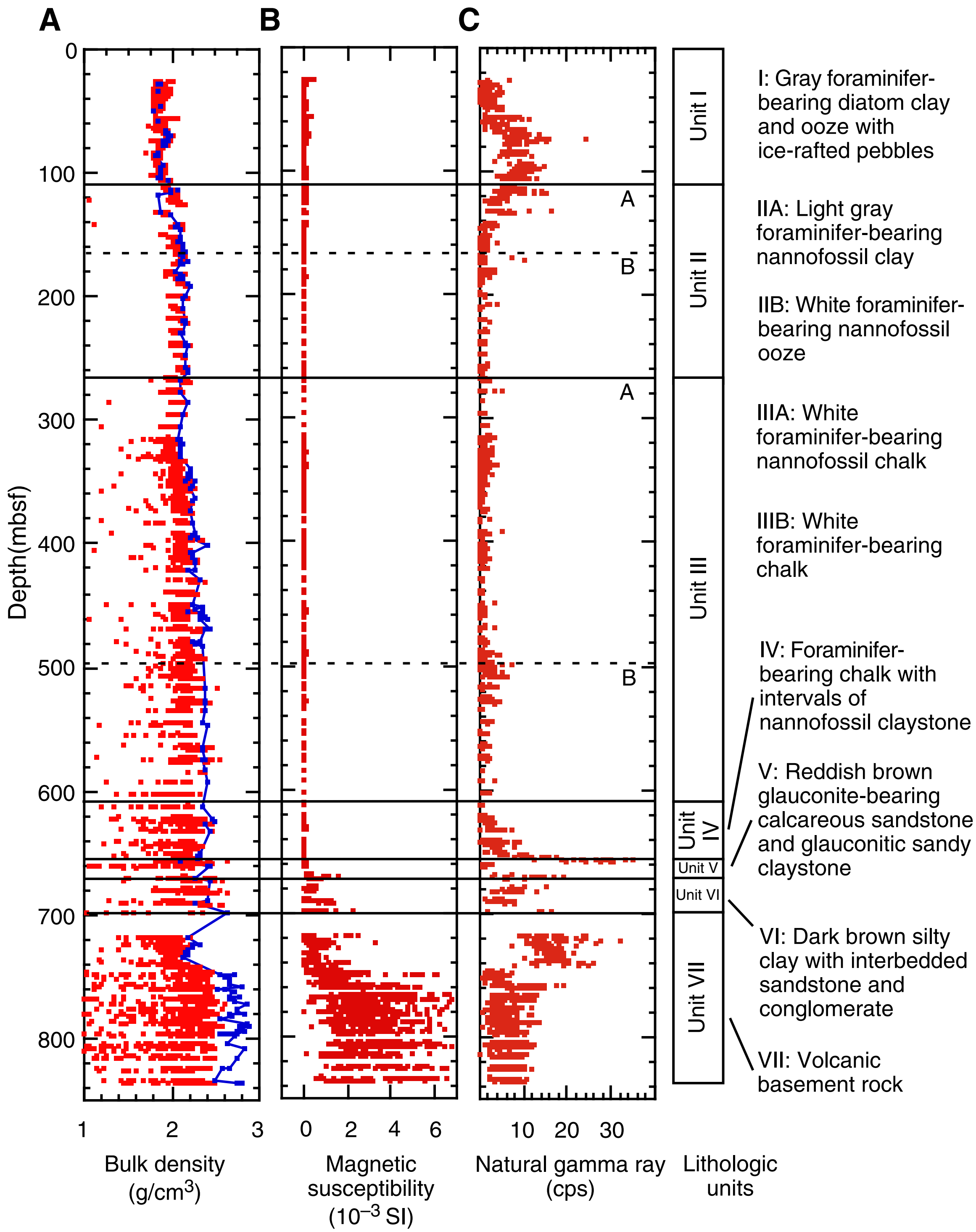

Figure F82. Downhole profiles of thermal conductivity for soft sediments in Units I and II and the upper part of Unit III (upper figure) and basement Unit VII (lower figure) at Site 1138.

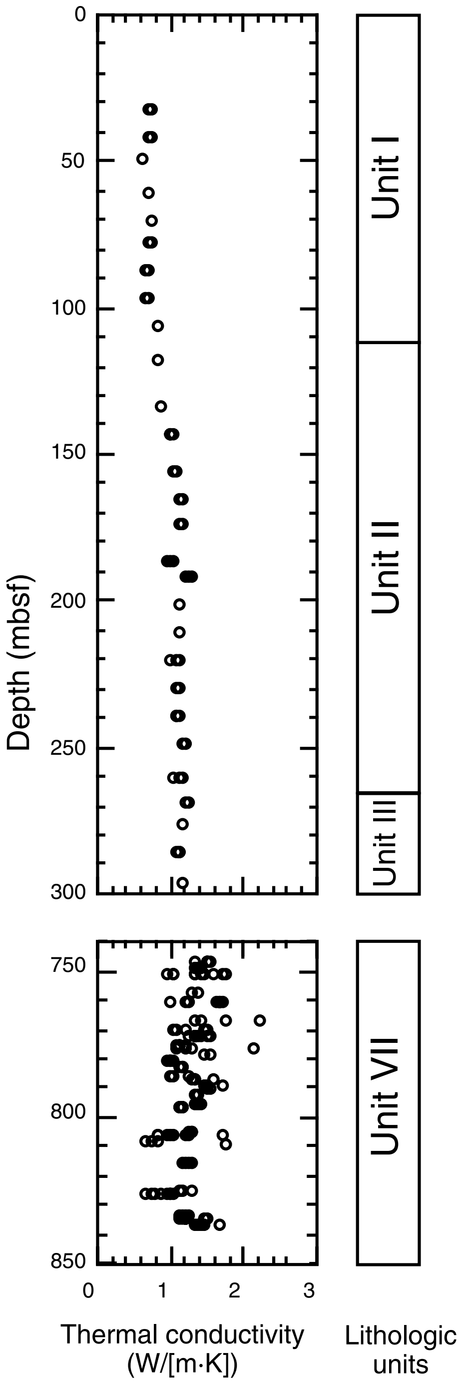

Figure F83. Comparison of densities determined from core samples, gamma-ray attenuation porosity evaluator, multisensor track, and compressional wave velocities from downhole logs and core samples. Raw and robust mode filtered data are shown. Note velocity inversions at 475–505, 625–660, 665–670, 710–720, 780–785, 792.5–795, and 810–835 mbsf. (Continued on next two pages.)

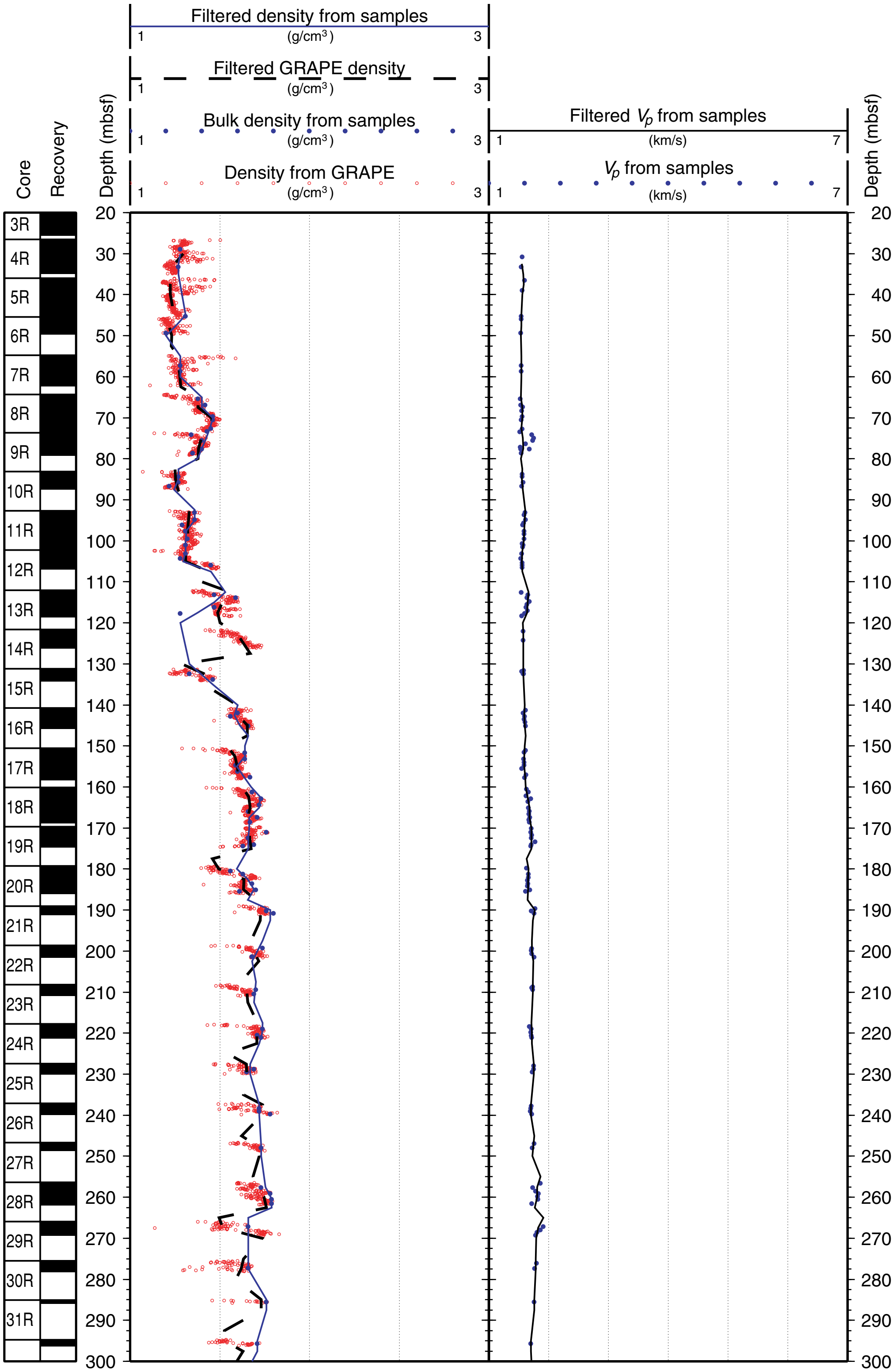

Figure F83 (continued).

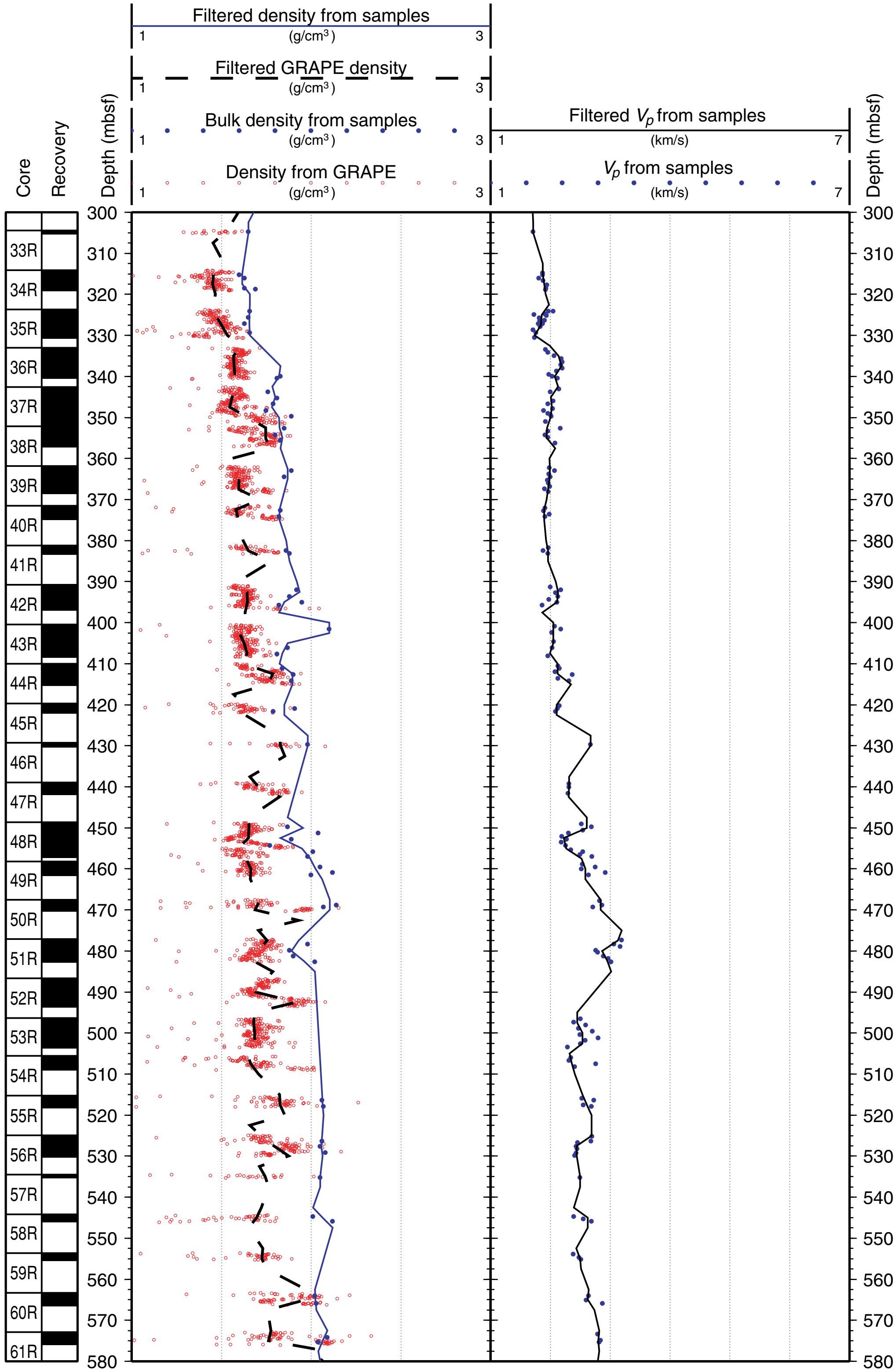

Figure F83 (continued).

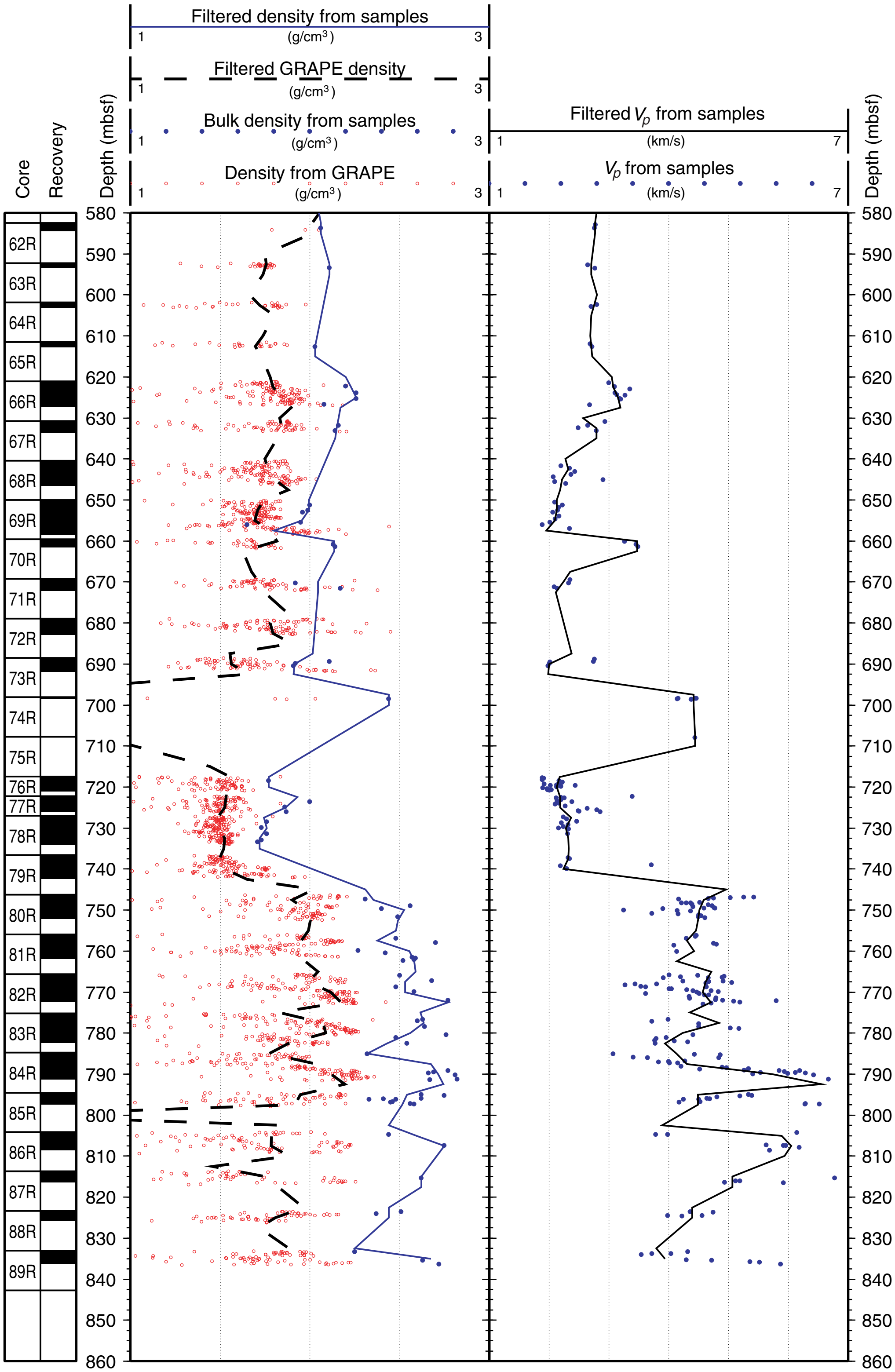

Figure F84. Composite of core recovery, lithostratigraphy, and age and (**A**) density and velocity as a function of depth, (**B**) density and velocity as a function of two-way traveltime (TWT), (**C**) impedance, (**D**) reflection coefficients without interbed multiples and transmission losses, (**E**) reflection coefficients with interbed multiples and transmission losses, and (**F**) synthetic seismograms based on (D) (black) and (E) (red) as a function of TWT. Note that reflections may be at depths where no core has been recovered, as a consequence of linear resampling and subsequent convolution with a wavelet with peak frequency of 40 Hz. This results in "blurring" and phase shifting the boundaries associated with velocities and/or densities of recovered core segments. In terms of signal processing, this is an aliasing effect. sbsf = seconds below seafloor. (**Figure shown on next page.**)

Figure F84. (Caption on previous page.)

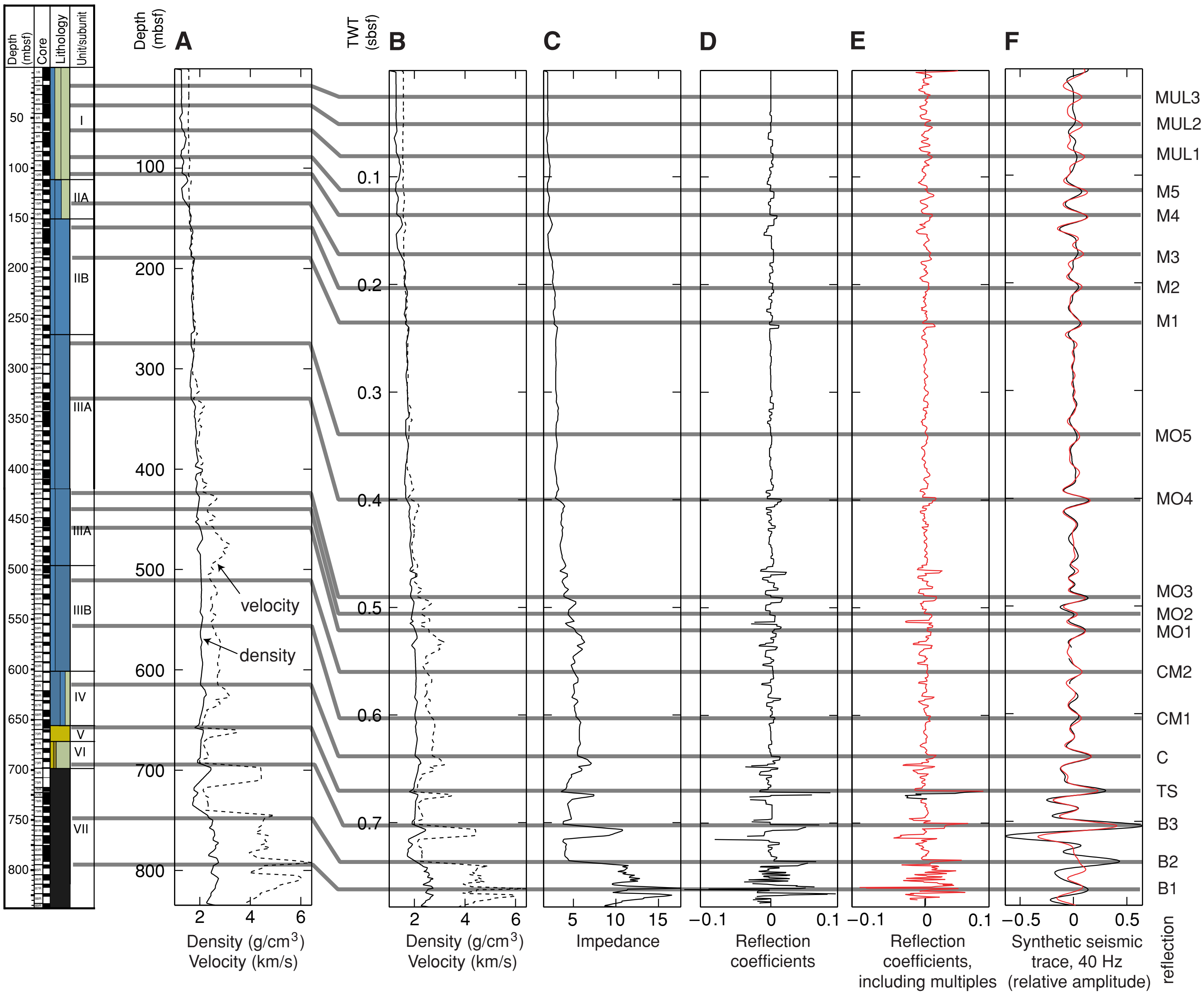

Figure F85. A. Portion of seismic reflection line 101 data from *Rig Seismic* cruise 179, across Site 1138, and a synthetic seismic trace from Figure F84, p. 162, excluding multiples and transmission losses. Reflections tied to the synthetic seismogram are labeled. MUL = multiple, M = Miocene, MO = late Maastrichtian–late Oligocene, CM = mid-Campanian–late Maastrichtian, C = mid-Campanian, TS = Turonian–Santonian, B = basement. (Continued on next page.)

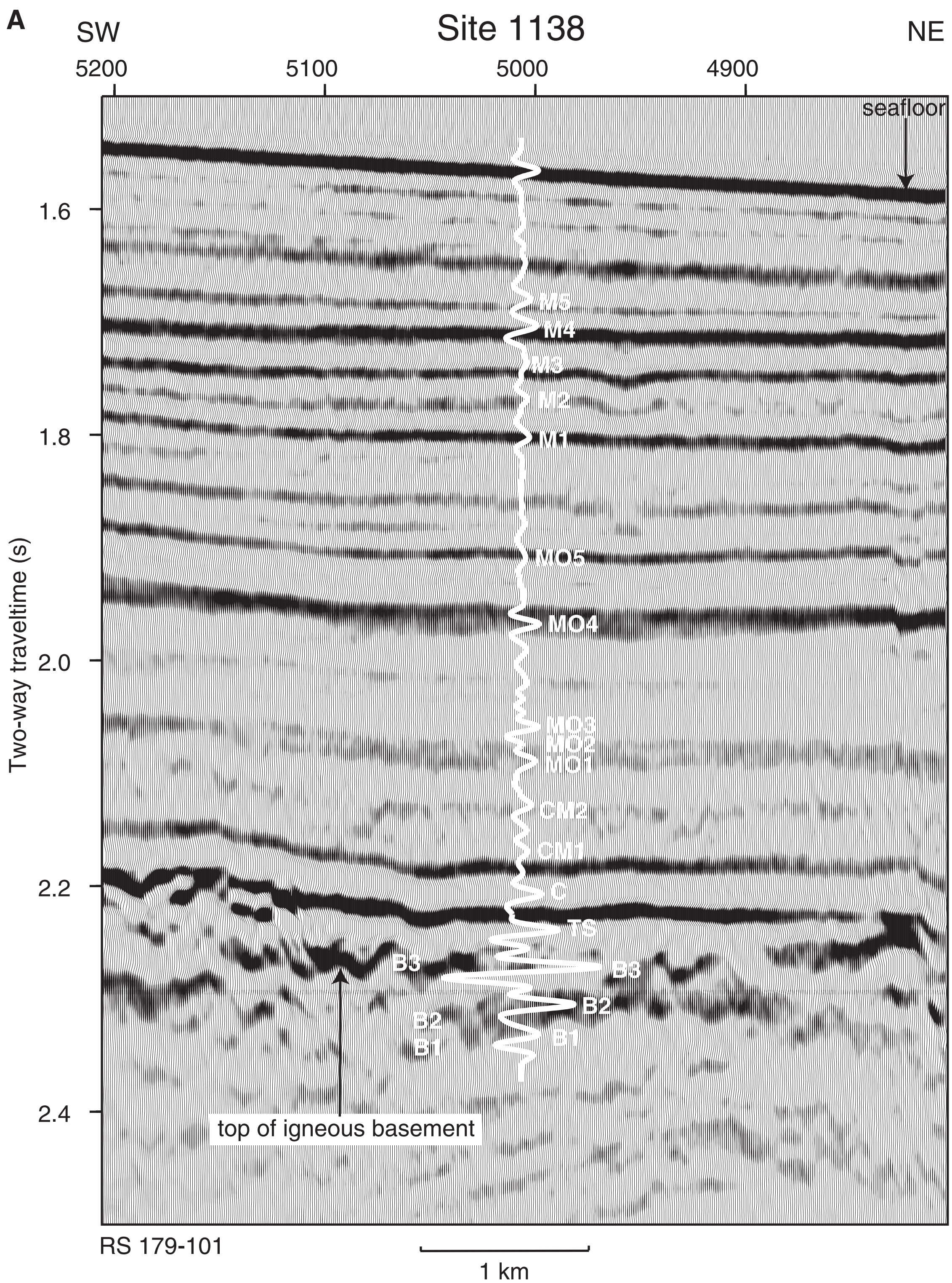

Figure F85 (continued). B. Portion of seismic reflection line 101 from *Rig Seismic* cruise 179, across Site 1138, and a synthetic seismic trace from Figure F84, p. 162, including multiples and transmission losses. Reflections tied to the synthetic seismogram are labeled as in Figure F85A, p. 164. The vertical exaggeration is ~16:1 at the seafloor.

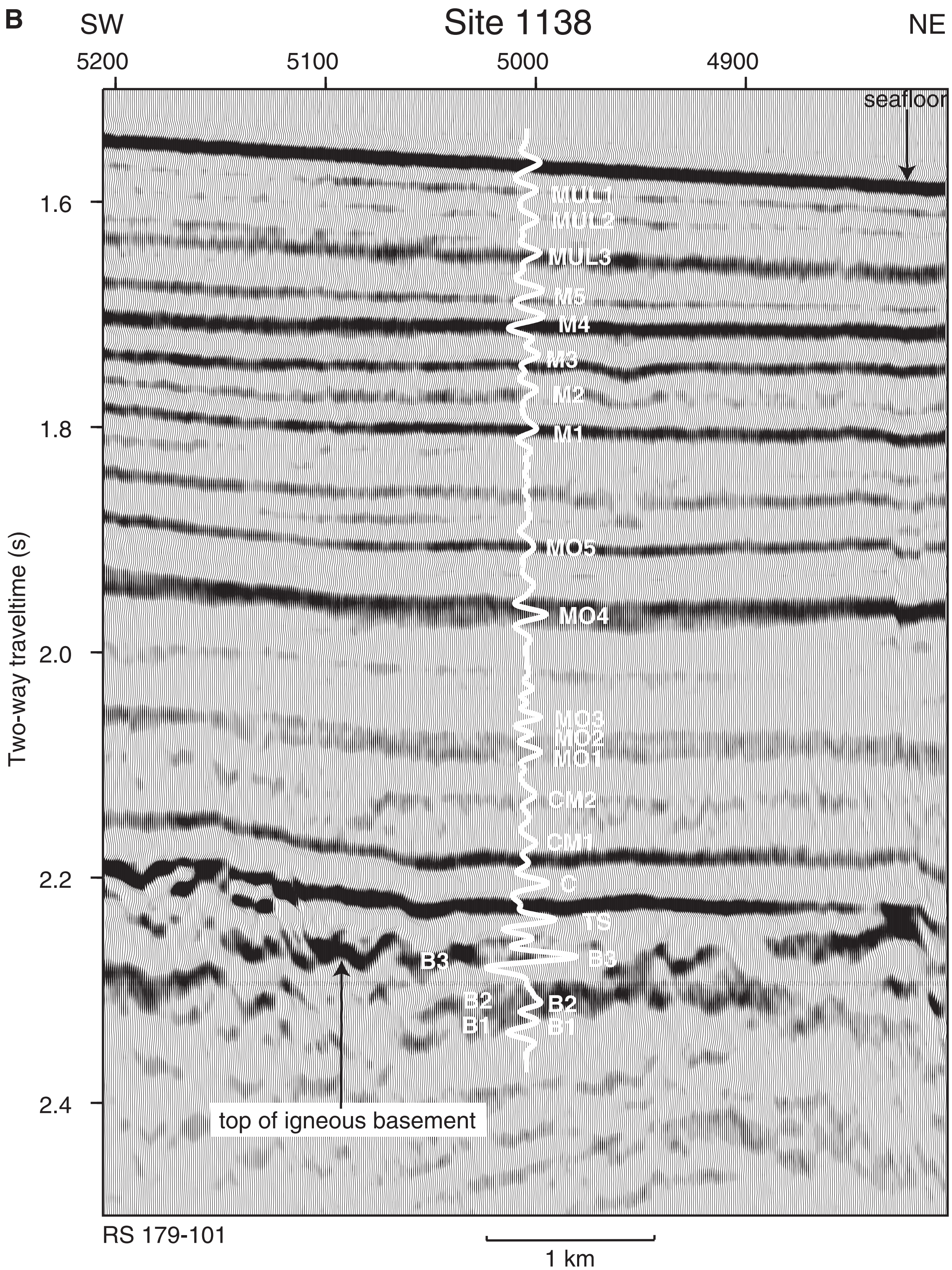

Table T1. Coring summary for Site 1138. (See table note. Continued on next page.)

Continued on next page.

Core	Date (Jan 1999)	Time (UTC)	Depth (mbsf)	Length (m) Cored	Length (m) Recovered	Recovery (%)
183-1138A-						
1R	7	2140	0.0-9.5	9.5	8.58	90.3
2R	7	2230	9.5-17.1	7.6	4.97	65.4
3R	7	2305	17.1-26.5	9.4	8.52	90.6
4R	7	2330	26.5-36.0	9.5	8.49	89.4
5R	8	0000	36-45.4	9.4	9.63	102.4
6R	8	0030	45.4-54.8	9.4	4.30	45.7
7R	8	0100	54.8-64.3	9.5	7.56	79.6
8R	8	0135	64.3-73.7	9.4	9.79	104.1
9R	8	0200	73.7-83.1	9.4	5.56	59.1
10R	8	0230	83.1-92.7	9.6	4.48	46.7
11R	8	0300	92.7-102.3	9.6	9.74	101.5
12R	8	0330	102.3-112.0	9.7	4.78	49.3
13R	8	0405	112.0-121.6	9.6	6.64	69.2
14R	8	0440	121.6-131.2	9.6	4.68	48.8
15R	8	0515	131.2-140.8	9.6	3.08	32.1
16R	8	0555	140.8-150.5	9.7	5.10	52.6
17R	8	0635	150.5-160.1	9.6	7.82	81.5
18R	8	0715	160.1-169.7	9.6	8.81	91.8
19R	8	0745	169.7-179.3	9.6	5.10	53.1
20R	8	0830	179.3-189.0	9.7	6.89	71.0
21R	8	0905	189.0-198.6	9.6	2.31	24.1
22R	8	0940	198.6-208.2	9.6	3.05	31.8
23R	8	1010	208.2-217.8	9.6	2.70	28.1
24R	8	1040	217.8-227.4	9.6	3.59	37.4
25R	8	1120	227.4-237.1	9.7	2.67	27.5
26R	8	1155	237.1-246.7	9.6	2.80	29.2
27R	8	1235	246.7-256.4	9.7	2.06	21.2
28R	8	1305	256.4-265.9	9.5	5.51	58.0
29R	8	1345	265.9-275.5	9.6	3.56	37.1
30R	8	1415	275.5-285.1	9.6	2.76	28.8
31R	8	1510	285.1-294.7	9.6	0.85	8.9
32R	8	1550	294.7-304.4	9.7	1.65	17.0
33R	8	1630	304.4-314.1	9.7	0.98	10.1
34R	8	1720	314.1-323.7	9.6	5.13	53.4
35R	8	1800	323.7-333.0	9.3	7.13	76.7
36R	8	1835	333.0-342.6	9.6	7.65	79.7
37R	8	1905	342.6-352.2	9.6	9.43	98.2
38R	8	1940	352.2-361.8	9.6	5.06	52.7
39R	8	2015	361.8-371.5	9.7	6.77	69.8
40R	8	2050	371.5-381.2	9.7	3.55	36.6
41R	8	2125	381.2-390.8	9.6	2.20	22.9
42R	8	2200	390.8-400.4	9.6	6.25	65.1
43R	8	2235	400.4-410.0	9.6	8.11	84.5
44R	8	2305	410.0-419.7	9.7	5.36	55.3
45R	8	2340	419.7-429.3	9.6	2.46	25.6
46R	9	0010	429.3-438.9	9.6	1.15	12.0
47R	9	0040	438.9-448.6	9.7	3.13	32.3
48R	9	0115	448.6-458.2	9.6	8.77	91.4
49R	9	0150	458.2-467.5	9.3	3.55	38.2
50R	9	0230	467.5-477.1	9.6	2.95	30.7
51R	9	0305	477.1-486.7	9.6	5.70	59.4
52R	9	0350	486.7-496.4	9.7	7.06	72.8
53R	9	0430	496.4-505.6	9.2	7.38	80.2
54R	9	0510	505.6-515.3	9.7	3.62	37.3
55R	9	0550	515.3-524.9	9.6	3.03	31.6
56R	9	0630	524.9-534.5	9.6	5.41	56.4
57R	9	0720	534.5-544.2	9.7	0.99	10.2
58R	9	0815	544.2-553.6	9.4	1.92	20.4
59R	9	1130	553.6-563.3	9.7	1.85	19.1
60R	9	1215	563.3-572.9	9.6	3.24	33.8
61R	9	1305	572.9-582.5	9.6	3.09	32.2
62R	9	1350	582.5-592.2	9.7	1.89	19.5
63R	9	1440	592.2-601.8	9.6	1.37	14.3
64R	9	1610	601.8-611.5	9.7	1.42	14.6
65R	9	1750	611.5-621.1	9.6	1.30	13.5
66R	9	2000	621.1-630.7	9.6	6.10	63.5

Table T1 (continued).

Core	Date (Jan 1999)	Time (UTC)	Depth (mbsf)	Length (m)		Recovery (%)
				Cored	Recovered	
67R	9	2330	630.7-640.4	9.7	2.91	30.0
68R	10	0015	640.4-650.0	9.6	6.12	63.8
69R	10	0145	650.0-659.6	9.6	8.49	88.4
70R	10	0305	659.6-669.2	9.6	1.99	20.7
71R	10	0450	669.2-678.9	9.7	3.02	31.1
72R	10	0705	678.9-688.5	9.6	4.00	41.7
73R	11	0240	688.5-698.1	9.6	3.39	35.3
74R	11	0445	698.1-707.8	9.7	0.45	4.6
75R	11	0650	707.8-717.4	9.6	0.05	0.5
76R	11	1055	717.4-722.2	4.8	3.68	76.7
77R	11	1205	722.2-727.0	4.8	4.01	83.5
78R	11	1325	727.0-736.6	9.6	7.01	73.0
79R	11	1525	736.6-746.3	9.7	5.85	60.3
80R	11	1800	746.3-755.9	9.6	5.87	61.1
81R	11	2025	755.9-765.6	9.7	6.02	62.1
82R	11	2315	765.6-775.2	9.6	6.79	70.7
83R	12	0140	775.2-784.8	9.6	7.17	74.7
84R	12	0515	784.8-794.5	9.7	6.47	66.7
85R	12	0710	794.5-804.1	9.6	2.90	30.2
86R	12	0905	804.1-813.7	9.6	4.50	46.9
87R	12	1035	813.7-823.4	9.7	2.69	27.7
88R	12	1225	823.4-833.1	9.7	2.44	25.2
89R	12	1435	833.1-842.7	9.6	3.13	32.6
			Cored:	842.7	411.98	48.9
			Drilled:	0.0		
			Total:	842.7		

Note: UTC = Universal Time Coordinated. This table is also available in ASCII format.

Table T2. Expanded coring summary for Hole 1138A. (See table note. Continued on next eight pages.)

Core	Date (Jan 1999)	Time (UTC)	Depth (mbsf)	Length (m)		Recovery (%)	Section	Length (m)		Section depth (mbsf)	Catwalk samples	Comment
				Cored	Recovered			Liner	Curated			
183-1138A-												
1R	7	2140	0.0-9.5	9.5	8.58	90.3						
							1	1.50	1.50	0.0-1.5		
							2	1.50	1.50	1.5-3.0		
							3	1.50	1.50	3.0-4.5		
							4	0.96	0.96	4.5-5.46		Other
							5	1.50	1.50	5.46-6.96	HS	
							6	1.41	1.41	6.96-8.37		
							CC(w/CC)	0.21	0.21	8.37-8.58	PAL	
								8.58	8.58			
2R	7	2230	9.5-17.1	7.6	4.97	65.4						
							1	1.05	1.05	9.5-10.55		
							2	1.14	0.32	10.55-10.87		
							3	0.60	0.24	10.87-11.11		
							4	0.98	0.52	11.11-11.63	HS	
							5	1.08	1.08	11.63-12.71		
							CC(w/5)	0.12	0.12	12.71-12.83	PAL	
								4.97	3.33			
3R	7	2305	17.1-26.5	9.4	8.52	90.6						
							1	1.50	1.50	17.1-18.6		
							2	1.50	1.50	18.6-20.1		
							3	1.50	1.50	20.1-21.6		
							4	1.50	1.50	21.6-23.1		
							5	1.50	1.50	23.1-24.6	HS	
							6	0.90	0.90	24.6-25.5		
							CC(w/6)	0.12	0.12	25.5-25.62	PAL	
								8.52	8.52			
4R	7	2330	26.5-36.0	9.5	8.49	89.4						
							1	1.50	1.50	26.5-28.0		
							2	1.50	1.50	28.0-29.5		
							3	1.50	1.50	29.5-31.0		
							4	1.50	1.50	31.0-32.5		
							5	1.50	1.50	32.5-34.0	HS	
							6	0.88	0.88	34.0-34.88		
							CC(w/6)	0.11	0.11	34.88-34.99	PAL	
								8.49	8.49			
5R	8	0000	36.0-45.4	9.4	9.63	102.4						
							1	1.50	1.50	36.0-37.5		
							2	1.50	1.50	37.5-39.0		
							3	1.50	1.50	39.0-40.5		
							4	1.50	1.50	40.5-42.0		
							5	1.50	1.50	42.0-43.5	HS	
							6	1.50	1.50	43.5-45.0		
							7	0.46	0.46	45.0-45.46		
							CC(w/7)	0.17	0.17	45.46-45.63	PAL	
								9.63	9.63			
6R	8	0030	45.4-54.8	9.4	4.3	45.7						
							1	1.50	1.50	45.4-46.9		
							2	1.50	1.50	46.9-48.4		
							3	1.13	1.13	48.4-49.53	HS	
							CC(w/3)	0.17	0.17	49.53-49.7	PAL	
								4.30	4.30			
7R	8	0100	54.8-64.3	9.5	7.56	79.6						
							1	1.50	1.50	54.8-56.3		
							2	1.50	1.50	56.3-57.8		
							3	1.50	1.50	57.8-59.3		
							4	1.50	1.50	59.3-60.8		
							5	1.38	1.38	60.8-62.18	HS	
							CC(w/CC)	0.18	0.18	62.18-62.36	PAL	
								7.56	7.56			
8R	8	0135	64.3-73.7	9.4	9.79	104.1						
							1	1.50	1.50	64.3-65.8		
							2	1.50	1.50	65.8-67.3		
							3	1.50	1.50	67.3-68.8		
							4	1.50	1.50	68.8-70.3	MAI	
							5	1.50	1.50	70.3-71.8	HS	
							6	1.50	1.50	71.8-73.3		
							7	0.64	0.64	73.3-73.94		

Table T2 (continued).

Core	Date (Jan 1999)	Time (UTC)	Depth (mbsf)	Length (m) Cored	Length (m) Recovered	Recovery (%)	Section	Length (m) Liner	Length (m) Curated	Section depth (mbsf)	Catwalk samples	Comment
							CC(w/7)	0.15	0.15	73.94-74.09	PAL	
								9.79	9.79			
9R	8	0200	73.7-83.1	9.4	5.56	59.1						
							1	1.50	1.50	73.7-75.2		
							2	1.50	1.50	75.2-76.7		
							3	1.50	1.50	76.7-78.2	HS	
							4	0.87	0.87	78.2-79.07		
							CC(w/4)	0.19	0.19	79.07-79.26	PAL	
								5.56	5.56			
10R	8	0230	83.1-92.7	9.6	4.48	46.7						
							1	1.50	1.50	83.1-84.6		
							2	1.50	1.50	84.6-86.1		
							3	1.30	1.30	86.1-87.4	HS	
							CC(w/3)	0.18	0.18	87.4-87.58	PAL	
								4.48	4.48			
11R	8	0300	92.7-102.3	9.6	9.74	101.5						
							1	1.50	1.50	92.7-94.2		
							2	1.50	1.50	94.2-95.7		
							3	1.50	1.50	95.7-97.2		
							4	1.50	1.50	97.2-98.7		
							5	1.50	1.50	98.7-100.2	HS	
							6	1.50	1.50	100.2-101.7		
							7	0.60	0.60	101.7-102.3		
							CC(w/7)	0.14	0.14	102.3-102.44	PAL	
								9.74	9.74			
12R	8	0330	102.3-112.0	9.7	4.78	49.3						
							1	1.50	1.50	102.3-103.8		
							2	1.50	1.50	103.8-105.3		
							3	1.50	1.50	105.3-106.8	HS	
							CC(w/CC)	0.28	0.28	106.8-107.08	PAL	
								4.78	4.78			
13R	8	0405	112.0-121.6	9.6	6.64	69.2						
							1	1.50	1.50	112-113.5		
							2	1.50	1.50	113.5-115		
							3	1.50	1.50	115-116.5		
							4	1.50	1.50	116.5-118	HS, MAI	
							5	0.40	0.40	118-118.4		
							CC(w/5)	0.24	0.24	118.4-118.64	PAL	
								6.64	6.64			
14R	8	0440	121.6-131.2	9.6	4.68	48.8						
							1	1.50	1.50	121.6-123.1		
							2	1.50	1.50	123.1-124.6		
							3	1.48	1.48	124.6-126.08	HS	
							CC(w/CC)	0.20	0.20	126.08-126.28	PAL	
								4.68	4.68			
15R	8	0515	131.2-140.8	9.6	3.08	32.1						
							1	1.50	1.50	131.2-132.7		
							2	1.38	1.38	132.7-134.08	HS	
							CC(w/CC)	0.20	0.20	134.08-134.28	PAL	
								3.08	3.08			
16R	8	0555	140.8-150.5	9.7	5.1	52.6						
							1	1.50	1.50	140.8-142.3		
							2	1.50	1.50	142.3-143.8		
							3	1.50	1.50	143.8-145.3	HS	
							4	0.42	0.42	145.3-145.72		
							CC(w/4)	0.18	0.18	145.72-145.9	PAL	
								5.10	5.10			
17R	8	0635	150.5-160.1	9.6	7.82	81.5						
							1	1.50	1.50	150.5-152		
							2	1.50	1.50	152-153.5		
							3	1.50	1.50	153.5-155		
							4	1.50	1.50	155-156.5		
							5	1.50	1.50	156.5-158	HS	
							6	0.22	0.22	158-158.22		
							CC(w/6)	0.10	0.10	158.22-158.32	PAL	
								7.82	7.82			
18R	8	0715	160.1-169.7	9.6	8.81	91.8						
							1	1.50	1.50	160.1-161.6		

Table T2 (continued).

Core	Date (Jan 1999)	Time (UTC)	Depth (mbsf)	Length (m) Cored	Length (m) Recovered	Recovery (%)	Section	Length (m) Liner	Length (m) Curated	Section depth (mbsf)	Catwalk samples	Comment
							2	1.50	1.50	161.6-163.1		
							3	1.50	1.50	163.1-164.6		
							4	1.50	1.50	164.6-166.1		
							5	1.50	1.50	166.1-167.6	HS	
							6	1.24	1.24	167.6-168.84		
							CC(NS)	0.07	0.07	168.84-168.91	PAL	All to PAL
								8.81	8.81			
19R	8	0745	169.7-179.3	9.6	5.1	53.1						
							1	1.50	1.50	169.7-171.2		
							2	1.50	1.50	171.2-172.7	MAI	
							3	1.50	1.50	172.7-174.2	HS	
							4	0.40	0.40	174.2-174.6		
							CC(w/4)	0.20	0.20	174.6-174.8	PAL	
								5.10	5.10			
20R	8	0830	179.3-189.0	9.7	6.89	71						
							1	1.50	1.50	179.3-180.8		
							2	1.50	1.50	180.8-182.3		
							3	1.50	1.50	182.3-183.8		
							4	1.50	1.50	183.8-185.3	HS	
							5	0.72	0.72	185.3-186.02		
							CC(w/5)	0.17	0.17	186.02-186.19	PAL	
								6.89	6.89			
21R	8	0905	189.0-198.6	9.6	2.31	24.1						
							1	1.50	1.50	189-190.5		
							2	0.61	0.61	190.5-191.11	HS	
							CC(w/2)	0.20	0.20	191.11-191.31	PAL	
								2.31	2.31			
22R	8	0940	198.6-208.2	9.6	3.05	31.8						
							1	1.50	1.50	198.6-200.1		
							2	1.50	1.50	200.1-201.6	HS	
							CC(NS)	0.05	0.05	201.6-201.65	PAL	All to PAL
								3.05	3.05			
23R	8	1010	208.2-217.8	9.6	2.7	28.1						
							1	1.50	1.50	208.2-209.7		
							2	1.15	1.15	209.7-210.85	HS	
							CC(NS)	0.05	0.05	210.85-210.9	PAL	All to PAL
								2.7	2.7			
24R	8	1040	217.8-227.4	9.6	3.59	37.4						
							1	1.50	1.50	217.8-219.3	MAI	
							2	1.50	1.50	219.3-220.8	HS	
							3	0.43	0.43	220.8-221.23		
							CC(w/3)	0.16	0.16	221.23-221.39	PAL	
								3.59	3.59			
25R	8	1120	227.4-237.1	9.7	2.67	27.5						
							1	1.50	1.50	227.4-228.9		
							2	1.00	1.00	228.9-229.9	HS	
							CC(w/2)	0.17	0.17	229.9-230.07	PAL	
								2.67	2.67			
26R	8	1155	237.1-246.7	9.6	2.8	29.2						
							1	1.50	1.50	237.1-238.6		
							2	1.25	1.25	238.6-239.85	HS	
							CC(NS)	0.05	0.05	239.85-239.9	PAL	All to PAL
								2.80	2.80			
27R	8	1235	246.7-256.4	9.7	2.06	21.2						
							1	1.50	1.50	246.7-248.2		
							2	0.51	0.51	248.2-248.71	HS	
							CC(NS)	0.05	0.05	248.71-248.76	PAL	All to PAL
								2.06	2.06			
28R	8	1305	256.4-265.9	9.5	5.51	58.0						
							1	1.50	1.50	256.4-257.9		
							2	1.50	1.50	257.9-259.4		
							3	1.50	1.50	259.4-260.9	HS	
							4	0.91	0.91	260.9-261.81		
							CC(NS)	0.10	0.10	261.81-261.91	PAL	All to PAL
								5.51	5.51			
29R	8	1345	265.9-275.5	9.6	3.56	37.1						
							1	1.50	1.50	265.9-267.4		
							2	1.50	1.50	267.4-268.9	HS, MAI	

Table T2 (continued).

Core	Date (Jan 1999)	Time (UTC)	Depth (mbsf)	Length (m) Cored	Length (m) Recovered	Recovery (%)	Section	Length (m) Liner	Length (m) Curated	Section depth (mbsf)	Catwalk samples	Comment
							3	0.43	0.43	268.9-269.33		
							CC(w/3)	0.13	0.13	269.33-269.46	PAL	
								3.56	3.56			
30R	8	1415	275.5-285.1	9.6	2.76	28.8						
							1	1.50	1.50	275.5-277.0		
							2	1.07	1.07	277.0-278.07	HS	
							CC(w/2)	0.19	0.19	278.07-278.26	PAL	
								2.76	2.76			
31R	8	1510	285.1-294.7	9.6	0.85	8.9						
							1	0.75	0.75	285.1-285.85	HS	
							CC(NS)	0.10	0.10	285.85-285.95	PAL	All to PAL
								0.85	0.85			
32R	8	1550	294.7-304.4	9.7	1.65	17						
							1	1.46	1.46	294.7-296.16	HS	
							CC(w/CC)	0.19	0.19	296.16-296.35	PAL	
								1.65	1.65			
33R	8	1630	304.4-314.1	9.7	0.98	10.1						
							1	0.80	0.80	304.4-305.2	HS	
							CC(w/1)	0.18	0.18	305.2-305.38		
								0.98	0.98			
34R	8	1720	314.1-323.7	9.6	5.13	53.4						
							1	1.50	1.50	314.1-315.6		
							2	1.50	1.50	315.6-317.1		
							3	1.50	1.50	317.1-318.6	HS	
							4	0.49	0.49	318.6-319.09		
							CC(w/4)	0.14	0.14	319.09-319.23		
								5.13	5.13			
35R	8	1800	323.7-333.0	9.3	7.13	76.7						
							1	1.50	1.50	323.7-325.2		
							2	1.50	1.50	325.2-326.7		
							3	1.50	1.50	326.7-328.2		
							4	1.50	1.50	328.2-329.7		
							5	0.96	0.96	329.7-330.66	HS	
							CC(w/5)	0.17	0.17	330.66-330.83	PAL	
								7.13	7.13			
36R	8	1835	333.0-342.6	9.6	7.65	79.7						
							1	1.50	1.50	333.0-334.5		
							2	1.50	1.50	334.5-336.0		
							3	1.50	1.50	336.0-337.5		
							4	1.50	1.50	337.5-339.0	HS, MAI	
							5	1.00	1.00	339.0-340.0		
							6	0.60	0.60	340.0-340.6		
							CC(NS)	0.05	0.05	340.6-340.65	PAL	All to PAL
								7.65	7.65			
37R	8	1905	342.6-352.2	9.6	9.43	98.2						
							1	1.50	1.50	342.6-344.1		
							2	1.50	1.50	344.1-345.6		
							3	1.50	1.50	345.6-347.1		
							4	1.50	1.50	347.1-348.6	HS	
							5	1.50	1.50	348.6-350.1		
							6	1.50	1.50	350.1-351.6		
							7	0.25	0.25	351.6-351.85		
							CC(w/7)	0.18	0.18	351.85-352.03	PAL	
								9.43	9.43			
38R	8	1940	352.2-361.8	9.6	5.06	52.7						
							1	1.50	1.50	352.2-353.7		
							2	1.50	1.50	353.7-355.2		
							3	1.50	1.50	355.2-356.7	HS	
							4	0.41	0.41	356.7-357.11		
							CC(w/4)	0.15	0.15	357.11-357.26	PAL	
								5.06	5.06			
39R	8	2015	361.8-371.5	9.7	6.77	69.8						
							1	1.50	1.50	361.8-363.3		
							2	1.50	1.50	363.3-364.8		
							3	1.50	1.50	364.8-366.3		
							4	1.50	1.50	366.3-367.8	HS	
							5	0.61	0.61	367.8-368.41		
							CC(w/5)	0.16	0.16	368.41-368.57	PAL	

Table T2 (continued).

Core	Date (Jan 1999)	Time (UTC)	Depth (mbsf)	Length (m) Cored	Recovered	Recovery (%)	Section	Length (m) Liner	Curated	Section depth (mbsf)	Catwalk samples	Comment
								6.77	6.77			
40R	8	2050	371.5-381.2	9.7	3.55	36.6						
							1	1.50	1.50	371.5-373.0		
							2	1.50	1.50	373.0-374.5	HS	
							3	0.40	0.40	374.5-374.9		
							CC(w/3)	0.15	0.15	374.9-375.05	PAL	
								3.55	3.55			
41R	8	2125	381.2-390.8	9.6	2.2	22.9						
							1	1.50	1.50	381.2-382.7	HS	
							2	0.49	0.49	382.7-383.19		
							CC(w/2)	0.21	0.21	383.19-383.4	PAL	
								2.2	2.2			
42R	8	2200	390.8-400.4	9.6	6.25	65.1						
							1	1.50	1.50	390.8-392.3		
							2	1.50	1.50	392.3-393.8	MAI	
							3	1.50	1.50	393.8-395.3	HS	
							4	1.50	1.50	395.3-396.8		
							CC(w/CC)	0.25	0.25	396.8-397.05	PAL	
								6.25	6.25			
43R	8	2235	400.4-410.0	9.6	8.11	84.5						
							1	1.50	1.50	400.4-401.9		
							2	1.50	1.50	401.9-403.4		
							3	1.50	1.50	403.4-404.9		
							4	1.50	1.50	404.9-406.4		
							5	1.50	1.50	406.4-407.9	HS	
							6	0.42	0.42	407.9-408.32		
							CC(w/6)	0.19	0.19	408.32-408.51	PAL	
								8.11	8.11			
44R	8	2305	410.0-419.7	9.7	5.36	55.3						
							1	1.50	1.50	410.0-411.5		
							2	1.50	1.50	411.5-413.0	HS	
							3	1.50	1.50	413.0-414.5		
							4	0.60	0.60	414.5-415.1		
							CC(w/4)	0.26	0.26	415.1-415.36	PAL	
								5.36	5.36			
45R	8	2340	419.7-429.3	9.6	2.46	25.6						
							1	1.50	1.50	419.7-421.2	HS	
							2	0.80	0.80	421.2-422.0		
							CC(w/2)	0.16	0.16	422-422.16	PAL	
								2.46	2.46			
46R	9	0010	429.3-438.9	9.6	1.15	12.0						
							1	1.0	1.0	429.3-430.3	HS	
							CC(w/1)	0.15	0.15	430.3-430.45	PAL	
								1.15	1.15			
47R	9	0040	438.9-448.6	9.7	3.13	32.3						
							1	1.50	1.50	438.9-440.4		
							2	1.40	1.40	440.4-441.8	HS	
							CC(w/CC)	0.23	0.23	441.8-442.03		
								3.13	3.13			
48R	9	0115	448.6-458.2	9.6	8.77	91.4						
							1	1.50	1.50	448.6-450.1	MAI	
							2	1.50	1.50	450.1-451.6		
							3	1.50	1.50	451.6-453.1		
							4	1.50	1.50	453.1-454.6		
							5	1.50	1.50	454.6-456.1	HS	
							6	1.12	1.12	456.1-457.22		
							CC(w/6)	0.15	0.15	457.22-457.37	PAL	
								8.77	8.77			
49R	9	0150	458.2-467.5	9.3	3.55	38.2						
							1	1.50	1.50	458.2-459.7	HS	
							2	1.50	1.50	459.7-461.2		
							3	0.42	0.42	461.2-461.62		
							CC(w/3)	0.13	0.13	461.62-461.75	PAL	
								3.55	3.55			
50R	9	0230	467.5-477.1	9.6	2.95	30.7						
							1	1.50	1.50	467.5-469		
							2	1.40	1.40	469-470.4	HS	
							CC(NS)	0.05	0.05	470.4-470.45	PAL	All to PAL

Table T2 (continued).

Core	Date (Jan 1999)	Time (UTC)	Depth (mbsf)	Length (m) Cored	Length (m) Recovered	Recovery (%)	Section	Length (m) Liner	Length (m) Curated	Section depth (mbsf)	Catwalk samples	Comment
								2.95	2.95			
51R	9	0305	477.1-486.7	9.6	5.7	59.4						
							1	1.50	1.50	477.1-478.6	MAI	
							2	1.50	1.50	478.6-480.1	HS	
							3	1.50	1.50	480.1-481.6		
							4	1.05	1.05	481.6-482.65		
							CC(w/4)	0.15	0.15	482.65-482.8	PAL	
								5.70	5.70			
52R	9	0350	486.7-496.4	9.7	7.06	72.8						
							1	1.50	1.50	486.7-488.2		
							2	1.50	1.50	488.2-489.7		
							3	1.50	1.50	489.7-491.2	HS	
							4	1.50	1.50	491.2-492.7		
							5	0.80	0.80	492.7-493.5		
							CC(w/5)	0.26	0.26	493.5-493.76	PAL	
								7.06	7.06			
53R	9	0430	496.4-505.6	9.2	7.38	80.2						
							1	1.50	1.50	496.4-497.9		
							2	1.50	1.50	497.9-499.4		
							3	1.50	1.50	499.4-500.9		
							4	1.50	1.50	500.9-502.4	HS, MAI	
							5	1.17	1.17	502.4-503.57		
							CC(w/5)	0.21	0.21	503.57-503.78	PAL	
								7.38	7.38			
54R	9	0510	505.6-515.3	9.7	3.62	37.3						
							1	1.50	1.50	505.6-507.1	MAI	
							2	1.50	1.50	507.1-508.6		
							3	0.45	0.45	508.6-509.05	HS	
							CC(w/3)	0.17	0.17	509.05-509.22	PAL	
								3.62	3.62			
55R	9	0550	515.3-524.9	9.6	3.03	31.6						
							1	1.50	1.50	515.3-516.8		
							2	1.26	1.26	516.8-518.06	HS	
							CC(w/CC)	0.27	0.27	518.06-518.33	PAL	
								3.03	3.03			
56R	9	0630	524.9-534.5	9.6	5.41	56.4						
							1	1.50	1.50	524.9-526.4		
							2	1.50	1.50	526.4-527.9		
							3	1.50	1.50	527.9-529.4		
							4	0.60	0.60	529.4-530	HS	
							CC(w/4)	0.31	0.31	530-530.31	PAL	
								5.41	5.41			
57R	9	0720	534.5-544.2	9.7	0.99	10.2						
							1	0.83	0.83	534.5-535.33	HS	
							CC(w/1)	0.16	0.16	535.33-535.49	PAL	
								0.99	0.99			
58R	9	0815	544.2-553.6	9.4	1.92	20.4						
							1	1.50	1.50	544.2-545.7		
							2	0.37	0.37	545.7-546.07	HS	
							CC(NS)	0.05	0.05	546.07-546.12	PAL	All to PAL
								1.92	1.92			
59R	9	1130	553.6-563.3	9.7	1.85	19.1						
							1	1.38	1.38	553.6-554.98	MAI	
							2	0.42	0.42	554.98-555.4	HS	
							CC(NS)	0.05	0.05	555.4-555.45	PAL	All to PAL
								1.85	1.85			
60R	9	1215	563.3-572.9	9.6	3.24	33.8						
							1	1.51	1.51	563.3-564.81		
							2	1.51	1.54	564.81-566.35	HS	
							CC(w/CC)	0.22	0.22	566.35-566.57	PAL	
								3.24	3.27			
61R	9	1305	572.9-582.5	9.6	3.09	32.2						
							1	1.50	1.50	572.9-574.4		
							2	1.39	1.39	574.4-575.79	HS, MAI	
							CC(w/CC)	0.20	0.20	575.79-575.99	PAL	
								3.09	3.09			
62R	9	1350	582.5-592.2	9.7	1.89	19.5						
							1	1.50	1.50	582.5-584		

Table T2 (continued).

Core	Date (Jan 1999)	Time (UTC)	Depth (mbsf)	Length (m) Cored	Length (m) Recovered	Recovery (%)	Section	Length (m) Liner	Length (m) Curated	Section depth (mbsf)	Catwalk samples	Comment
							2	0.15	0.15	584-584.15	HS	
							CC(w/2)	0.24	0.24	584.15-584.39	PAL	
								1.89	1.89			
63R	9	1440	592.2-601.8	9.6	1.37	14.3						
							1	1.19	1.19	592.2-593.39	HS	
							CC(w/1)	0.18	0.18	593.39-593.57	PAL	
								1.37	1.37			
64R	9	1610	601.8-611.5	9.7	1.42	14.6						
							1	1.37	1.37	601.8-603.17	HS	
							CC(NS)	0.05	0.05	603.17-603.22	PAL	All to PAL
								1.42	1.42			
65R	9	1750	611.5-621.1	9.6	1.3	13.5						
							1	1.16	1.16	611.5-612.66	HS	
							CC(w/1)	0.14	0.14	612.66-612.8	PAL	
								1.30	1.30			
66R	9	2000	621.1-630.7	9.6	6.1	63.5						
							1	1.50	1.50	621.1-622.6		
							2	1.50	1.50	622.6-624.1		
							3	1.50	1.50	624.1-625.6	HS, MAI	
							4	1.39	1.39	625.6-626.99		
							CC(w/CC)	0.21	0.21	626.99-627.2	PAL	
								6.10	6.10			
67R	9	2230	630.7-640.4	9.7	2.91	30						
							1	1.41	1.41	630.7-632.11		
							2	1.25	1.25	632.11-633.36	HS	
							CC(w/CC)	0.25	0.25	633.36-633.61	PAL	
								2.91	2.91			
68R	10	0015	640.4-650.0	9.6	6.12	63.8						
							1	1.35	1.35	640.4-641.75		
							2	1.50	1.50	641.75-643.25		
							3	1.41	1.41	643.25-644.66	HS	
							4	0.90	0.90	644.66-645.56		
							5	0.73	0.73	645.56-646.29		
							CC(w/5)	0.23	0.23	646.29-646.52	PAL	
								6.12	6.12			
69R	10	0145	650.0-659.6	9.6	8.49	88.4						
							1	1.42	1.42	650-651.42		
							2	1.17	1.17	651.42-652.59		
							3	1.50	1.50	652.59-654.09		
							4	1.48	1.48	654.09-655.57		
							5	1.50	1.50	655.57-657.07	HS	
							6	1.29	1.29	657.07-658.36		
							CC(w/6)	0.13	0.13	658.36-658.49	PAL	
								8.49	8.49			
70R	10	0305	659.6-669.2	9.6	1.99	20.7						
							1	0.44	1.50	659.6-661.1		
							2	1.50	0.68	661.1-661.78		
							CC(NS)	0.05	0.05	661.78-661.83	PAL	
								1.99	2.23			
71R	10	0450	669.2-678.9	9.7	3.02	31.1						
							1	1.30	1.30	669.2-670.5		
							2	1.50	1.50	670.5-672	HS	
							CC(w/CC)	0.22	0.22	672-672.22	PAL	
								3.02	3.02			
72R	10	0705	678.9-688.5	9.6	4.0	41.7						
							1	1.50	1.50	678.9-680.4		
							2	1.50	1.50	680.4-681.9	HS	
							3	0.80	0.80	681.9-682.7		
							CC(w/3)	0.20	0.20	682.7-682.9	PAL	
								4.00	4.00			
73R	11	0240	688.5-698.1	9.6	3.39	35.3						
							1	0.73	0.81	688.5-689.31		
							2	0.95	0.95	689.31-690.26		
							3	1.50	1.50	690.26-691.76	HS	
							CC(w/CC)	0.21	0.21	691.76-691.97	PAL	
								3.39	3.47			
74R	11	0445	698.1-707.8	9.7	0.45	4.6						
							1	0.45	0.56	698.1-698.66		

Table T2 (continued).

Core	Date (Jan 1999)	Time (UTC)	Depth (mbsf)	Length (m) Cored	Length (m) Recovered	Recovery (%)	Section	Length (m) Liner	Length (m) Curated	Section depth (mbsf)	Catwalk samples	Comment
								0.45	0.56			
75R	11	0650	707.8-717.4	9.6	0.05	0.5						
							1	0.05	0.07	707.8-707.87		
								0.05	0.07			
76R	11	1055	717.4-722.2	4.8	3.68	76.7						
							1	1.50	1.50	717.4-718.9		
							2	1.50	1.50	718.9-720.4	HS	
							3	0.46	0.46	720.4-720.86		
							CC(w/3)	0.22	0.22	720.86-721.08	PAL	
								3.68	3.68			
77R	11	1205	722.2-727	4.8	4.01	83.5						
							1	1.50	1.50	722.2-723.7		
							2	1.50	1.50	723.7-725.2	HS	
							3	0.85	0.85	725.2-726.05		
							CC(w/3)	0.16	0.16	726.05-726.21		
								4.01	4.01			
78R	11	1325	727.0-736.6	9.6	7.01	73.0						
							1	1.50	1.50	727.00-728.50		
							2	1.50	1.50	728.50-730.00		
							3	1.50	1.50	730.00-731.50	HS	
							4	1.50	1.50	731.50-733.00		
							5	0.89	0.89	733.00-733.89		
							CC(w/5)	0.12	0.12	733.89-734.01		
								7.01	7.01			
79R	11	1525	736.6-746.3	9.7	5.85	60.3						
							1	1.36	1.36	736.6-737.96		
							2	1.41	1.41	737.96-739.37		
							3	1.50	1.50	739.37-740.87	HS	
							4	1.20	1.20	740.87-742.07		
							5	0.38	0.38	742.07-742.45		
								5.85	5.85			
80R	11	1800	746.3-755.9	9.6	5.87	61.1						
							1	1.36	1.47	746.3-747.77		
							2	1.44	1.43	747.77-749.2		
							3	1.48	1.50	749.2-750.7		
							4	1.38	1.34	750.7-752.04		
							5	0.21	0.39	752.04-752.43		
								5.87	6.13			
81R	11	2025	755.9-765.6	9.7	6.02	62.1						
							1	0.55	1.41	755.9-757.31		
							2	1.35	1.34	757.31-758.65		
							3	1.25	1.46	758.65-760.11		
							4	1.41	1.25	760.11-761.36		
							5	1.46	1.16	761.36-762.52		
								6.02	6.62			
82R	11	2315	765.6-775.2	9.6	6.79	70.7						
							1	1.03	1.50	765.6-767.1		
							2	1.41	1.47	767.1-768.57		
							3	1.45	1.47	768.57-770.04		
							4	1.43	1.50	770.04-771.54		
							5	1.47	1.50	771.54-773.04		
							6	0.00	0.21	773.04-773.25		
								6.79	7.65			
83R	12	0140	775.2-784.8	9.6	7.17	74.7						
							1	1.25	1.50	775.2-776.7		
							2	1.50	1.46	776.7-778.16		
							3	1.48	1.35	778.16-779.51		
							4	1.47	1.42	779.51-780.93		
							5	1.47	1.33	780.93-782.26		
							6	0.00	0.93	782.26-783.19		
								7.17	7.99			
84R	12	0515	784.8-794.5	9.7	6.47	66.7						
							1	0.74	1.38	784.8-786.18		
							2	1.44	1.32	786.18-787.5		
							3	1.46	1.47	787.5-788.97		
							4	1.36	0.86	788.97-789.83		
							5	1.47	1.47	789.83-791.3		
							6	0.00	0.32	791.3-791.62		

Table T2 (continued).

Core	Date (Jan 1999)	Time (UTC)	Depth (mbsf)	Length (m) Cored	Length (m) Recovered	Recovery (%)	Section	Length (m) Liner	Length (m) Curated	Section depth (mbsf)	Catwalk samples	Comment
								6.47	6.82			
85R	12	0710	794.5-804.1	9.6	2.9	30.2						
							1	1.54	1.33	794.5-795.83		
							2	1.36	1.50	795.83-797.33		
							3	0.00	0.50	797.33-797.83		
								2.90	3.33			
86R	12	0905	804.1-813.7	9.6	4.5	46.9						
							1	1.50	1.50	804.1-805.6		
							2	1.50	1.50	805.6-807.1		
							3	1.50	1.50	807.1-808.6		
							4	0.00	0.85	808.6-809.45		
								4.50	5.35			
87R	12	1035	813.7-823.4	9.7	2.69	27.7						
							1	0.40	1.46	813.7-815.16		
							2	1.21	1.36	815.16-816.52		
							3	1.08	0.42	816.52-816.94		
								2.69	3.24			
88R	12	1225	823.4-833.1	9.7	2.44	25.2						
							1	1.13	1.41	823.4-824.81		
							2	1.31	1.38	824.81-826.19		
								2.44	2.79			
89R	12	1435	833.1-842.7	9.6	3.13	32.6						
							1	1.50	1.48	833.1-834.58		
							2	1.40	1.28	834.58-835.86		
							3	0.23	0.73	835.86-836.59		
								3.13	3.49			
			Totals:	842.7	411.98	48.9						

Notes: UTC = Universal Time Coordinated. CC = core catcher (number in parenthesis indicates which section the core catcher is stored with), NS = all of the core catcher was used for paleontology sample. HS = headspace gas sample, PAL = paleontology sample, MAI = whole-round sample for shore-tossed physical properties study. This table is also available in **ASCII format.**

Table T3. Summary of lithologic units at Site 1138.

Lithologic unit/subunit	Basement unit	Core interval	Depth (mbsf)	Thickness (m)	Age	Lithology	Interpretation
I		1R–1, 0 cm, to 12R–CC, 28 cm	0.00–112.00	112.00	late Pleistocene to late Miocene	Gray foraminifer-bearing diatom clay and ooze with scattered ice-rafted pebbles	Continuous pelagic with intermittent sediment gravity flows of terrigenous sediment; bathyal
IIA		13R–1, 0 cm, to 16R–CC, 18 cm	112.00–150.50	38.50	late Miocene	Light gray foraminifer-bearing nannofossil clay	Continuous pelagic with intermittent sediment gravity flows of terrigenous sediment; bathyal
IIB		17R–1, 0 cm, to 28R–CC, 10 cm	150.50–265.90	115.40	late to early Miocene	White foraminifer-bearing nannofossil ooze	Pelagically deposited sediment; bathyal environment
IIIA		29R–1, 0 cm, to 52R–CC, 26 cm	265.90–496.40	230.50	late Oligocene to late Maastrichtian	White foraminifer-bearing nannofossil chalk	Pelagically deposited sediment; bathyal environment
IIIB		53R–1, 0 cm, to 63R–CC, 18 cm	496.40–601.80	105.40	late Maastrichtian to middle Campanian	White foraminifer-bearing chalk	Pelagically deposited sediment; bathyal environment
IV		64R–1, 0 cm, to 69R–5, 112 cm	601.80–656.69	54.89	mid-Campanian to Turonian	Interbedded light gray chalk and dark gray nannofossil claystone; black, organic-rich claystone	Pelagically deposited sediment; bathyal environment
V		69R–5, 112 cm, to 71R–2, 138 cm	656.69–671.88	15.19	Santonian-Turonian	Reddish brown glauconite-bearing calcareous sandstone and glauconitic sandy claystone	Neritic (shallow marine) deposit
VI		71R–2, 138 cm, to 74R–1, 13 cm	671.88–698.23	26.35	Late Cretaceous	Dark brown silty clay with interbedded sandstone and conglomerate	Fluvial and possibly neritic (shallow marine)
VII	1–22	74R–1, 13 cm, to 89R–3, 73 cm	698.23–842.70	144.47	Cretaceous(?)	Basalt flows capped by volcaniclastic rocks and minor sediments	Volcanic lava flows and pyroclastics

Table T4. X-ray diffraction results, carbonate contents, and total and organic carbon contents expressed as $CaCO_3$ and C for Hole 1138A. (See table note. Continued on next page.)

Unit, core, section, interval (cm)	Depth (mbsf)	Minerals	$CaCO_3$ (wt%)	Total carbon (wt%)	Organic carbon (wt%)
Unit I					
183-1138A-					
1R-3, 69	3.69	Calcite, clay (montmorillonite?), opal-A, quartz, K-feldspar	18	2.35	0.24
3R-4, 17	21.77	Calcite, clay (montmorillonite?), opal-CT, K-feldspar, glauconite, (opal-A, quartz)	44		
4R-4, 92	31.92	Calcite, opal-A, quartz, K-feldspar, clay (montmorillonite?)	46	5.69	0.19
5R-1, 92	36.92	Opal-A, calcite, (quartz)	19		
6R-1, 92	46.32	Calcite, opal-A, K-feldspar, (clay)	11		
7R-1, 92	55.72	Calcite, opal-A, (feldspar)	23	2.92	0.12
8R-1, 92	65.22	Calcite, opal-A, feldspar, clay (montmorillonite?), (quartz, opal-CT)	14		
9R-1, 92	74.62	Calcite, opal-A, (opal-CT, feldspar)	39	4.75	0.11
10R-1, 92	84.02	Opal-A, calcite, (feldspar, clay, opal-CT)	4	0.63	0.13
11R-1, 92	93.62	Opal-A, calcite, (feldspar, clay, pyrite)	20		
12R-1, 91	103.21	Opal-A, opal-CT, calcite, K-feldspar, clay, (quartz)	13		
Unit II					
183-1138A-					
13R-1, 92	112.92	Calcite, K-feldspar, (opal-A, clay)	57	6.80	0.00
14R-1, 92	122.52	Calcite, K-feldspar, (clay)	62		
15R-1, 91	132.11	Calcite, opal-A, K-feldspar, clay	24	2.92	0.00
16R-1, 91	141.71	Calcite, (feldspar)	76		
17R-1, 92	151.42	Calcite, (feldspar)	84		
18R-1, 92	161.02	Calcite	87	10.41	0.02
19R-1, 92	170.62	Calcite	91		
20R-1, 92	180.22	Calcite, (feldspar, clay, glass)	69		
21R-1, 91	189.91	Calcite	94	11.27	0.00
22R-1, 89	199.49	Calcite	95		
23R-1, 91	209.11	Calcite, (quartz?)	90		
24R-1, 91	218.71	Calcite	94	11.32	0.00
26R-1, 92	238.02	Calcite	93		
27R-1, 92	247.62	Calcite	94		
28R-1, 92	257.32	Calcite	94	11.30	0.00
Unit III					
183-1138A-					
29R-1, 92	266.82	Calcite	92		
30R-1, 92	276.42	Calcite	91		
33R-1, 71	305.11	Calcite, (clay, opal?)	80	9.65	0.00
34R-1, 92	315.02	Calcite, (clay, opal?)	74		
35R-1, 92	324.62	Calcite, (clay, opal?)	72	8.60	0.00
36R-1, 92	333.92	Calcite	92		
37R-2, 65	344.75	Calcite, (clinoptilolite, glauconite)			
37R-2, 67	344.77	Calcite	92		
38R-1, 91	353.11	Calcite	93	11.24	0.07
39R-1, 92	362.72	Calcite	92		
40R-1, 91	372.41	Calcite	96		
41R-1, 91	382.11	Calcite			
42R-1, 92	391.72	Calcite	93	11.13	0.00
43R-1, 92	401.32	Calcite	93		
44R-1, 91	410.91	Calcite	96		
46R-1, 91	430.21	Calcite	95	11.43	0.00
47R-1, 91	439.81	Calcite	94		
48R-1, 92	449.52	Calcite	92		
49R-1, 91	459.11	Calcite, (clinoptilolite)	93	11.18	0.00
50R-1, 91	468.41	Calcite	95		
51R-1, 92	478.02	Calcite	87		
53R-1, 92	497.32	Calcite	95	11.39	0.00
54R-1, 92	506.52	Calcite	93		
55R-1, 92	516.22	Calcite	93		
56R-1, 82	525.72	Calcite	94	11.34	0.02
59R-1, 91	554.51	Calcite	93		
61R-2, 83	575.23	Calcite	95		
62R-1, 91	583.41	Calcite	92	11.26	0.17
63R-1, 90	593.10	Calcite	96		
Unit IV					
138-1139A-					

Table T4 (continued).

Unit, core, section, interval (cm)	Depth (mbsf)	Minerals	$CaCO_3$ (wt%)	Total carbon (wt%)	Organic carbon (wt%)
64R-1, 91	602.71	Calcite	93		
66R-1, 91	622.01	Calcite	96	11.56	0.04
67R-1, 90	631.60	Calcite, opal-CT, opal-A, quartz	77		
68R-1, 85	641.25	Calcite, opal-CT, opal-A, (quartz)	61		
69R-1, 91	650.91	Calcite, opal-CT, opal-A, (quartz)	58	6.94	0.00
69R-5, 90	656.47	Clinoptilolite, pyrite, quartz, montmorillonite	1	2.38	2.24
Unit V					
69R-6, 91	657.98	Glauconite, calcite, clay	7		
70R-1, 92	660.52	Calcite, opal-CT, opal-A, clinoptilolite	55	6.73	0.07
71R-2, 17	670.67	Calcite, glauconite, clinoptilolite,	12		
Unit VI					
72R-2, 60	680.98	Siderite, kaolinite, pyrite, gibbsite(?)	12	6.99	5.55
73R-2, 65	689.96	Siderite, kaolinite, gibbsite(?), (pyrite)	14		
73R-3, 136	691.62	Kaolinite, hematite, quartz, goethite	1		

Note: Minerals listed in parentheses are present only in trace amounts. See **"Organic and Inorganic Geochemistry,"** p. 59.

Table T5. Summary of thin sections at Site 1138.

Core, section, interval (cm)	Lithologic unit	Lithology	Mineral components	Lithic components	Bioclastic components	Matrix and cement	Texture
183-1138A-							
70R-2, 46–50 cm	V	Bioclastic packstone	Glauconite (1-2), opaque grains (1), brown translucent grains (1)	None	Bivalves, crinoids, echinoids, benthic foraminifers, ostracodes, bryozoans	Syntaxial overgrowths on echinoderms	Poorly sorted, high matrix content
71R-2, 92–95 cm	V	Glauconite-bearing sandstone	Glauconite (20), Fe oolites (1), pyroxene (<1)	Altered plagioclase-phyric lavas (1), brown translucent grains	Ostracodes, pectinid bivalves, benthic foraminifers, echinoderms, bryozoans	Brown ferruginous matrix	Fine grained; most bioclasts reworked, partially rounded, and broken
73R-1, 24–28 cm	VI	Sandstone	Plagioclase-phyric lavas	None	None	Carbonate cement	Moderately well-sorted sand, subangular sand, well-rounded pebbles

Note: Number in parentheses indicates abundance in vol%.

Table T6. Summary of volcaniclastic components at Site 1138.

Unit/ Subunit	Core, section, interval	Depth to top of unit (mbsf)	Thickness (m)	Age	Lithologies with volcanic components	Volcanic components	Authigenic and secondary minerals
Lithologic:							
I	1R-1, 0 cm, to 13R, 0 cm	0-112.00	112.00	late Miocene to late Pleistocene	Foraminifer-bearing diatom clay and ooze	Mixed disseminated volcanic ash with feldspar crystals, pumice lapilli, broken pumice (forming shards), brown (basaltic) glass, and lithic fragments.	Green clay (nontronite?) forming on basaltic glass rims, brown volcanic clay.
I, II, and IIIA	1R-1, 0 cm, to 53R, 0 cm	0-496.40	496.40	late Maastrichtian to late Pleistocene	Foraminifer-bearing diatom clay and ooze; foraminifer-bearing nannofossil clay, ooze, and chalk	Discrete pyroclastic fall deposits forming cm thick tephra layers. Some are dominated by brown (basaltic) glass ± lithic fragments, and others by pumice ± feldspar crystals (see Table T10, p. 185).	Green clay (nontronite?) forming on basaltic glass rims, brown clay in matrix of glassy intervals. Glauconite in lowermost discrete basaltic ashes.
Basement:							
1	74R-1, 0 cm, to 76R-1, 0 cm	698.10-717.40	19.30	Cretaceous	Aphyric dacite	Abraded, flow-banded, aphyric, dacite cobbles with spherulitic texture.	Spherulitic alteration (silicification) and pale brown clay minerals along flow banding.
2	76R-1, 0 cm, to 79R-4, 87 cm	717.40-741.89	24.49	Cretaceous	Trachytic pumice lithic breccias and ash deposits	Pumice lithic breccia, lithic breccia with pumice, ash-fall deposits with accretionary lapilli, highly altered pumice-rich clays, massive volcanic clays (see Figure F13, p. 82).	A wide variety of alteration from red to pale green, abundant smectite, and minor kaolinite clay minerals.

Table T7. Hole 1138A lava-flow units.

Basement unit	Curated position of top (cm)	Depth of top (mbsf)	Thickness* (m)	Interpreted lava type
	182-1138A-			
3	79R-4, 102	741.89	5.68	Slab pahoehoe?
4	80R-1, 119	747.57	2.39	Aa?
5	80R-3, 48	749.68	6.28	Aa?
6	81R-1, 6	755.96	2.84	Inflated pahoehoe
7	81R-3, 10-17	758.80	6.80	Transitional breccia top (aa-like)
8	82R-1, 0	765.60	2.20	Transitional breccia top (aa-like)
9	82R-2, 70	767.80	7.42	Aa and slab pahoehoe
10	83R-1, 2	775.22	5.44	Transitional breccia top (slab-like)
11	83R-4, 115	780.66	2.41	Elongated vesicle pahoehoe (spatter fed?)
12	83R-6, 81	783.07	3.05	Welded spongy pahoehoe lobes
13	84R-1, 130-133	786.12	8.38	Slab pahoehoe and aa
14	85R-1, 0	794.50	3.17	Transitional?
15	85R-3, 34	797.67	6.43	Transitional? + additional flows?
16	86R-1, 0	804.10	0.73	Massive interior only, flow type unknown
17	86R-1, 73	804.83	3.03	Transitional (reactivated pahoehoe?)
18	86R-3, 76	807.86	5.84	Transitional (reactivated pahoehoe?)
19	87R-1, 0	813.70	9.70	Transitional (reactivated pahoehoe)
20	88R-1, 0	823.40	1.36	Rootless vent
21	88R-1, 136	824.76	9.64	Transitional (breccia with intruding pahoehoe)
22	89R-1, 130	834.40	8.30	Transitional (breccia with intruding pahoehoe)

Note: * = thicknesses are based on curated depths and may differ from true unit thicknesses by as much as ±5 m.

Table T8. Summary of curated positions of contacts and internal boundaries for Hole 1138A lava-flow units.

Boundary	Curated position	Lava structure from boundary downward
Unit 2/3	79R-4, 102 cm (Piece 1)	Coherent vesicular
Unit 3 internal	79R-5, 0 cm (Piece 1)	Massive
Unit 3/4	80R-1, 119 cm (Piece 16)	Altered breccia
Unit 4 internal	80R-2, 35 cm (Piece 3)	Coherent vesicular
Unit 4/5	80R-3, 48 cm (Piece 5)	Altered black breccia
Unit 5 internal	80R-3, 60 cm (Piece 6)	Coherent vesicular
Unit 5/6	81R-1, 6 cm (Piece 2)	Coherent vesicular
Unit 6 internal	81R-1, 133 cm (Piece 15)	Massive
Unit 6 internal	81R-2, 50 cm (Piece 2)	Vesicular
Unit 6/7	81R-3, 10-17 cm (Piece 1)	Breccia
Unit 7 internal	81R-4, 53 cm (Piece 6)	Coherent vesicular
Unit 7/8	82R-1, 0 cm, (Piece 1)	Altered breccia
Unit 8 internal	82R-1, 67-84 cm (Pieces 6&7)	Massive
Unit 8 internal	82R-1, 140 cm (Piece 13)	Vesicular
Unit 8/9	82R-2, 70 cm (Piece 8)	Breccia
Unit 9 internal	82R-3, 110 cm (Piece 8)	Coherent vesicular
Unit 9/10	83R-1, 2 cm (Piece 2)	Breccia
Unit 10 internal	83R-1, 138 cm (Piece 11)	Coherent vesicular
Unit 10 internal	83R-3, 35-40 cm (Piece 4)	Massive
Unit 10 internal	83R-4, 50-55 cm (Piece 4A)	Coherent vesicular
Unit 10 internal	83R-4, 94 cm (Piece 7)	Welded breccia
Unit 10/11	83R-4, 115 cm (Piece 9)	Vesicular
Unit 11 internal	83R-5, 60 cm (Piece 5)	Massive
Unit 11 internal	83R-6, 53 cm (Piece 4)	Welded breccia
Unit 11/12	83R-6, 81 cm (Piece 7)	Vesicular
Unit 12/13	84R-1, 130-133 cm (Piece 7)	Breccia
Unit 13 internal	84R-3, 137 cm (Piece 9)	Coherent vesicular
Unit 13 internal	84R-5, 26 cm (Piece 1)	Massive
Unit 13 internal	84R-6, 12 cm (Piece 2)	Vesicular
Unit 13/14	85R-1, 0 cm (Piece 1)	Breccia
Unit 14 internal	85R-1, 18 cm (Piece 2)	Massive
Unit 14 internal	85R-2, 0 cm (Piece 1)	Welded breccia
Unit 14/15	85R-3, 34 cm (Piece 2)	Breccia
Unit 15 internal	85R-3, 75 cm (Piece 7)	Coherent vesicular
Unit 15/16	86R-1, 0 cm (Piece 1)	Coherent vesicular
Unit 16 internal	86R-1, 15 cm (Piece 2)	Massive
Unit 16 internal	86R-1, 51 cm (Piece 2)	Vesicular
Unit 16/17	86R-1, 73 cm (Piece 4)	Altered breccia
Unit 17 internal	86R-2, 92 cm (Piece 13)	Massive
Unit 17/18	86R-3, 76 cm (Piece 9)	Altered breccia
Unit 18 internal	86R-3, 145 cm (Piece 15)	Massive
Unit 18/19	87R-1, 0 cm (Piece 1)	Breccia
Unit 19 internal	87R-1, 137 cm (Piece 16)	Massive
Unit 19 internal	87R-3, 15 cm, (Piece 2)	Altered breccia
Unit 19/20	88R-1, 0 cm (Piece 1)	Coherent vesicular
Unit 20/21	88R-1, 136 cm (Piece 10)	Breccia
Unit 21 internal	89R-1, 97 cm (Piece 5B)	Coherent vesicular
Unit 21/22	89R-1, 130 cm (Piece 7)	Breccia
Unit 22 internal	89R-2, 80 cm (Piece 5)	Coherent vesicular

Table T9. Summary of internal textures of Site 1138 lava-flow units.

Basement unit	Pahoehoe top	Pahoehoe base	Breccia top	Breccia base	Aa clasts	Pahoehoe slabs	Pahoehoe lobes	Pahoehoe fragments	Sediment fill	Peperitic parts	Jigsaw-fit clasts	Welding in upper breccia	Welding in basal breccia	Spatter in basal breccia	Dense arms in breccia	Lower vesicular crust	Upper vesicular crust	Massive interior	Entrained crusts	Round vesicles	Irregular angular vesicles	Horizontal elongate vesicles	Vertical elongate vesicles	Horizontal vesicle sheet	Megavesicle	Mesostasis blebs	Oxidized tops
3	–	–	–	y	–	–	–	–	–	–	–	–	–	–	–	–	?	Y	–	y	Y	y	n	n	n	n	–
4	N	N	Y	?	Y	n	n	?	?	–	–	–	–	–	–	Y	Y	N	Y	y	Y	N	N	N	Y	n	–
5	N	N	Y	?	?	n	n	?	?	–	–	–	–	–	–	n	Y	N	Y	y	Y	n	n	N	Y	Y	–
6	?	Y	y	N	N	N	N	y	N	N	N	N	N	N	N	Y	Y	Y	N	Y	N	N	N	N	N	N	Y
7	N	–	Y	–	?	n	n	?	Y	y	y	n	–	–	N	–	Y	n	Y	n	Y	n	n	n	n	Y	Y
8	N	n	Y	?	n	n	n	?	Y	N	Y	n	–	–	?	Y	N	Y	?	N	Y	n	n	N	N	N	y
9	N	n	Y	?	?	Y	n	y	Y	y	?	n	–	–	Y	?	Y	n	Y	Y	Y	n	n	?	N	N	Y
10	N	N	Y	?	?	?	n	Y	y	N	Y	n	y	?	Y	Y	Y	Y	Y	Y	Y	y	n	?	Y	Y	y
11	?	n	n	?	N	N	N	N	N	N	N	N	Y	?	N	Y	Y	Y	?	Y	n	Y	Y	n	?	n	Y
12	?	Y	n	N	N	N	Y	N	N	N	N	N	N	N	N	N	N	N	N	N	y	N	N	N	N	N	Y
13	N	N	Y	?	Y	Y	Y	Y	y	N	Y	Y	Y	?	Y	Y	Y	Y	Y	Y	Y	Y	Y	N	N	Y	Y
14	N	N	Y	Y	?	–	–	–	–	–	–	–	Y	?	–	Y	–	Y	Y	Y	?	n	n	–	–	n	–
15	N	N	Y	?	n	?	n	?	n	n	?	n	–	–	n	–	Y	n	Y	Y	Y	n	n	n	n	n	–
16	–	–	–	?	–	–	–	–	–	–	–	–	?	–	–	Y	?	Y	–	Y	–	Y	–	n	n	n	–
17	N	–	Y	–	N	y	n	Y	N	N	y	N	–	–	N	–	–	Y	?	Y	Y	n	n	n	n	n	y
18	N	–	Y	–	N	?	n	?	N	N	y	N	–	–	N	–	?	?	–			n	n	n	n	Y	–
19	N	N	Y	Y	n	n	n	Y	y	y	n	Y	?	N	N	Y	N	Y	N	Y	N	Y	y	N	N	N	y
20	–	Y	–	N	–	–	–	–	–	–	–	–	N	?	–	Y	–	–	Y	Y	n	n	n	?	n	n	–
21	y	–	Y	–	N	?	Y	Y	N	N	y	y	–	–	Y	–	–	–	Y	Y	Y	?	n	–	–	–	y
22	N	–	Y	–	N	n	Y	Y	N	N	y	y	–	–	n	–	Y	Y	y	Y	N	Y	n	n	?	n	N

Note: – = cannot tell from the recovered rocks; y = identified, but only a minor component; ? = debatable identification; Y = major component; n = questionable lack of feature; N = definite lack of feature.

Table T10. Distribution of volcanic components in core catcher samples from lithologic Units I, II, and III at Hole 1138A.

Unit/ Subunit	Lithologies with volcanic components	Core, section	Depth (mbsf)	Feldspar	Glass (brown)	Pumice	Lithics	Biotite	Tephra layer	Age (Ma)
I	Foraminifer-bearing diatom clay and ooze	1R-CC	8.53	R		R				<0.6
		2R-CC	12.78							<0.6
		3R-CC	25.57							1.9-0.6
		4R-CC	34.94							1.9-0.6
		5R-CC	45.58	R		P				1.9-0.6
		6R-CC	49.65				R	R		1.9-0.6
		7R-CC	62.31	R		R				1.9-0.6
		8R-CC	74.04	P		P		R		3.2-2.6
		9R-CC	79.21			R				3.8-3.2
		10R-CC	87.53							3.8-3.2
		11R-CC	102.39	R		A		R		3.8-3.2
		12R-CC	107.03	P		P	P	P	T	6.4-5.6
IIA	Foraminifer-bearing nannofossil clay	13R-CC	118.59						TT	6.4-5.6
		14R-CC	126.23		A					10.6-8.9
		15R-CC	134.23		A		P		T	10.6-8.9
		16R-CC	145.85				C			10.6-8.9
IIB	Foraminifer-bearing nannofossil ooze	17R-CC	158.27		R		C			10.6-8.9
		18R-CC	168.84							11.7-10.6
		19R-CC	174.75					R	T	12.2-11.7
		20R-CC	186.14				R			13.5-12.8
		21R-CC	191.26							17.0-15.4
IIIA	Foraminifer-bearing nannofossil chalk	30R-CC	278.21						TT	31.0-26.5
		31R-CC	285.85		A					31.0-26.5
		32R-CC	296.3		A				T	31.0-26.5
		33R-CC	305.2		A				T	31.0-26.5
		34R-CC	319.09		A					31.0-26.5
		35R-CC	330.78							31.0-26.5
		36R-CC	340.6						T	35.5-33.0
		37R-CC	351.98							43.6-38.0
		38R-CC	357.21							43.6-38.0
		39R-CC	368.52							43.6-38.0
		40R-CC	375							43.6-38.0
		41R-CC	383.19	R		R				43.6-38.0
		42R-CC	397							43.6-38.0

Notes: Age determined from **"Biostratigraphy,"** p. 10. Volcanic components in >63 µm fraction of core catcher sample are represented by A = abundant, C = common, P = present, and R = rare. Volcanic components are not abundant in core catcher samples from 183-1138A-22R-CC through 29R-CC and below 42R-CC in Subunit IIIA. Blank = not detected. T = a discrete tephra layer was present in the core from which the core catcher was examined. TT = two tephra layers were present.

Table T11. Pyroclastic ash-fall deposits identified at Site 1138.

Lithologic unit/ subunit	Core, section, interval (cm)	Depth (mbsf)	Age (Ma)	Age type	Color	Volcanic components	Composition
I	12R-3, 5-7	105.35	6.4-5.6	D+F+N	Dark gray	Brown glass, minor clinopyroxene	Mafic
IIA	13R-1, 22-24	112.22	6.4-5.6	D+F+N	Dark brownish gray	Brown glass, felsic glass and feldspar	Bimodal
IIA	13R-5, 17-19	118.17	6.4-5.6	D+F+N	Pale brown	Brown glass and clay-sized matrix material	Mafic
IIB	15R-1, 73-75	131.93	10.0-8.9	D+F+N	Dark gray	Translucent pumice fragments	Felsic
IIIA	19R-1, 110-112	170.80	12.2-11.7	D+F+N	Light gray	Blocky translucent glass shards	Felsic
IIIA	30R-2, 34-35	277.34	27.0-26.5	F+N	Light gray	Translucent glass shards	Felsic
IIIA	30R-2, 40-42	277.40	27.0-26.5	F+N	Gray	Translucent glass shards	Felsic
IIIA	32R-1, 73-75	295.43	27.0-26.5	F+N	Light gray	Brown glass, minor clinopyroxene	Mafic
IIIA	33R-1, 26-28	304.66	27.0-26.5	F+N	Pale green	Brown glass and lithic fragments	Mafic
IIIA	36R-6, 41-43	340.41	34.3-33.5	F+N	Green	Brown glass ± glauconite	Mafic

Note: D = diatoms, F = foraminifer, N = nannofossils.

Table T12. Petrographic summary of Site 1138 basement units.

Basement Unit	Rock type	Thickness (m)	Phenocrysts	Rock (%)	Groundmass	Core, section, interval (cm)
						183-1138A-
1	Aphyric trachyte	19.50	PL	<1	PL, CPX, GL, OPQ	74R-1, 27-29; 75R-1, 5-6
2	Bedded pumice lithic breccia	24.29				
3	Moderately plagioclase-phyric basalt	5.98	PL	10	PL, CPX, GL, OPQ	80R-1, 52-56
4	Moderately plagioclase-phyric basalt	2.39	PL	3	PL, CPX, GL, OPQ	80R-2, 101-103; 80R-3, 18-22
5	Sparsely plagioclase-phyric basalt	6.28	PL	3	PL, CPX, GL, OPQ, OL	80R-5, 17-20
6	Aphyric basalt	2.84			PL, CPX, GL, OL, OPQ	81R-2, 26-27; 81R-2, 129-132
7	Sparsely plagioclase-phyric basalt	6.80	PL	4	PL, CPX, GL, OL, OPQ	81R-5, 2-5
8	Sparsely plagioclase-phyric basalt	2.20	PL	1	PL, CPX, GL, OL, OPQ	82R-1, 126-128
9	Sparsely plagioclase-phyric basalt	7.42	PL, CPX	2	PL, CPX, GL, OPQ, OL	82R-5, 69-71
10	Aphyric basalt	5.44	PL	1	PL, CPX, GL, OL, OPQ	83R-4, 34-37
11	Aphyric basalt	2.41	PL	<1	PL, CPX, GL, OL, OPQ	83R-6, 22-23
12	Aphyric basalt	3.05	PL	<1	PL, CPX, GL, OPQ	84R-1, 7-8; 84R-1, 30-34
13	Sparsely plagioclase-phyric basalt	8.38	PL	1	PL, CPX, GL, OPQ, OL	84R-5, 13-15; 84R-5, 100-101
14	Aphyric basalt	3.17			PL, CPX, GL, OL, OPQ	85R-1, 107-110
15	Aphyric basalt	6.43	PL	<1	PL, CPX, GL, OPQ, OL	85R-2, 123-124
16	Aphyric basalt	0.73			PL, CPX, GL, OPQ, OL	86R-1, 44-46
17	Aphyric basalt	3.03	PL	<1	PL, CPX, GL, OPQ	86R-2, 115-118; 86R-3, 32-34
18	Aphyric basalt	5.84			PL, CPX, GL, OPQ	86R-3, 148-149
19	Sparsely plagioclase-phyric basalt	9.70	PL, CPX	3	PL, CPX, GL, OL, OPQ	87R-2, 110-113; 87R-3, 10-13
20	Aphyric basalt	1.36			PL, CPX, GL, OPQ	88R-1, 87-89
21	Aphyric basalt	9.64	PL	<1	PL, CPX, GL, OPQ	88R-2, 126-129
22	Aphyric basalt	8.30	PL	<1	PL, CPX, GL, OPQ	89R-2, 119-122

Note: PL = plagioclase, CPX = clinopyroxene, GL = glass, OPQ = opaques, OL = olivine.

Table T13. X-ray fluorescence analyses of major and trace elements for Site 1138 igneous units. (Continued on next page.)

Hole:	1138	1138	1138	1138	1138	1138	1138	1138	1138	1138	1138
Core, section:	74R-1	74R-1	78R-3	80R-1	80R-3	80R-5	81R-2	81R-5	82R-1	82R-5	83R-4
Interval (cm):	13-16	24-30	50-54	53-56	19-23	17-20	23-25	2-5	127-131	69-72	33-37
Piece:	1	4	—	8	2	3	1B	1A	12	6B	2
Unit:	1	1	2	3	4	5	6	7	8	9	10
Rock type:	Dacite	Dacite	Pumice lithic breccia	Plagioclase-phyric basalt	Plagioclase-phyric basalt	Basalt	Basalt	Plagioclase-phyric basalt	Basalt	Basalt	Basalt
Depth (mbsf):	698.23	698.34	730.50	746.83	749.39	752.21	757.54	761.38	766.87	772.23	779.84
Major element oxides (wt%):											
SiO_2	63.97	63.85	68.06	49.45	48.67	48.89	47.91	47.95	48.19	48.75	48.44
TiO_2	1.57	1.53	0.52	1.92	2.11	2.17	2.14	2.02	2.27	2.18	2.19
Al_2O_3	14.77	14.76	15.11	16.76	15.30	15.81	15.73	14.70	14.42	15.72	14.38
Fe_2O_3	9.40	9.33	5.13	12.07	13.46	11.93	13.54	14.01	14.47	11.90	14.88
MnO	0.04	0.04	0.05	0.26	0.30	0.22	0.28	0.34	0.35	0.22	0.26
MgO	0.34	0.25	1.32	5.21	6.40	6.03	6.38	6.96	6.46	6.05	5.72
CaO	3.43	3.58	0.86	11.59	10.69	11.62	10.92	9.93	10.55	11.58	11.05
Na_2O	3.40	3.53	2.62	2.33	2.45	2.38	2.20	2.15	2.31	2.48	2.41
K_2O	2.65	2.70	6.92	0.22	0.24	0.23	0.38	1.07	0.37	0.23	0.26
P_2O_5	0.59	0.58	0.02	0.19	0.22	0.21	0.22	0.20	0.26	0.21	0.26
Total:	100.13	100.13	100.58	99.96	99.84	99.48	99.68	99.31	99.62	99.31	99.84
LOI	2.25	1.69	2.52	1.09	0.49	0.43	1.04	0.80	0.18	0.89	0.41
Mg#*	0.08	0.06	0.39	0.52	0.54	0.56	0.52	0.55	0.52	0.56	0.49
Trace elements (ppm):											
Rb	69	73	187	3	4	2	5	12	3	11	2
Sr	182	198	173	243	227	244	211	193	207	206	210
Nb†	51	48	116	11	14	13	13	12	15	15	16
Zr	673	711	1016	130	147	137	135	129	164	157	176
Y	67	73	39	33	33	31	32	29	38	35	37
V	36	46	21	385	413	452	417	401	460	390	401
Cr	10	2	11	88	80	113	88	78	100	56	72
Ni	6	9	22	57	53	61	57	56	50	46	42
Cu	29	35	9	120	124	119	194	114	170	154	170
Zn	147	143	115	96	108	110	104	106	125	111	116
Normative mineralogy: Fe^{2+}:Fe^{3+} = 0.8											
Q	24.2	22.0	19.7	2.1	0.1	1.0	0.0	7.0	0.1	0.4	0.6
Or	15.7	15.6	40.1	1.2	1.4	1.3	2.1	6.6	2.1	1.3	1.5
Ab	28.9	29.1	21.7	19.1	20.1	19.6	18.1	21.5	18.9	20.5	19.7
An	13.2	13.6	4.0	33.6	29.1	31.0	31.0	23.2	27.0	30.4	26.7
Cor	1.5	0.9	1.8	0.0	0.0	0.0	0.0	0.0	0.0	0.0	0.0
Wo (Di)	0.0	0.0	0.0	8.7	8.7	10.0	8.4	7.1	9.2	10.2	10.3
En (Di)	0.0	0.0	0.0	3.8	3.8	4.3	3.6	3.1	4.0	4.4	4.4
Fs (Di	0.0	0.0	0.0	3.5	3.2	3.3	3.0	2.4	3.6	3.3	4.7
En (Hy)	0.8	0.6	3.2	8.8	11.6	10.3	11.3	9.6	11.6	10.3	9.3
Fs (Hy)	8.4	8.8	5.4	8.2	9.9	7.9	9.6	7.5	10.5	7.8	9.9
Ol (Fo)	0.0	0.0	0.0	0.0	0.0	0.0	0.3	0.0	0.0	0.0	0.0
Ol (Fa)	0.0	0.0	0.0	0.0	0.0	0.0	0.5	0.0	0.0	0.0	0.0
Ilmenite	3.0	2.8	1.0	3.5	3.9	4.0	4.0	4.7	4.2	4.0	4.0
Magnetite	2.7	5.3	2.9	6.8	7.6	6.8	7.6	6.5	8.1	6.8	8.4
Apatite	1.3	1.2	0.0	0.4	0.5	0.4	0.5	0.8	0.5	0.4	0.5
Total:	99.8	99.9	99.9	99.9	99.9	99.9	99.9	99.9	99.9	99.9	99.9

Table T13 (continued).

Hole:	1138	1138	1138	1138	1138	1138	1138	1138	1138	1138	1138	1138
Core, section:	83R-6	84R-1	84R-5	85R-1	85R-2	86R-1	86R-2	86R-3	87R-2	88R-1	88R-2	89R-2
Interval (cm):	22-25	3-7	98-100	106-111	120-124	42-48	113-119	148-150	110-114	82-88	126-130	120-127
Piece:	2	2	6B	12	13	2B	14	15	15	6B	9	9
Unit:	11	12	13	14	15	16	17	18	19	20	21	22
Rock type:	Basalt	Basalt	Basalt	Basalt	Basalt	Basalt	Basalt	Basalt	Plagioclase-clinopyroxene-olivine-phyric basalt	Basalt	Basalt	Basalt
Depth (mbsf):	782.48	784.83	790.81	795.56	797.03	804.52	806.73	808.58	816.26	824.22	826.07	835.78
Major element oxides (wt%):												
SiO_2	49.89	47.89	49.44	48.35	48.36	47.83	47.58	48.63	47.61	46.95	46.99	48.04
TiO_2	2.13	2.21	2.20	2.63	2.62	2.84	2.82	2.55	2.96	3.01	3.04	3.22
Al_2O_3	14.26	13.87	14.36	13.77	12.85	13.17	13.04	14.85	13.80	13.09	13.01	13.65
Fe_2O_3	14.18	16.35	14.73	16.13	16.57	17.42	17.89	15.94	18.01	18.84	19.21	18.18
MnO	0.26	0.28	0.24	0.34	0.31	0.33	0.32	0.19	0.32	0.31	0.32	0.29
MgO	5.83	6.29	5.71	6.03	5.85	5.48	5.48	4.54	4.90	5.03	5.07	4.85
CaO	10.22	9.27	11.18	9.88	9.47	8.97	9.05	6.79	9.48	9.60	9.68	9.88
Na_2O	2.51	2.34	2.39	2.50	2.99	2.75	3.08	5.72	2.47	2.47	2.49	2.53
K_2O	0.40	0.50	0.23	0.52	0.48	0.42	0.28	0.41	0.48	0.32	0.33	0.27
P_2O_5	0.25	0.25	0.26	0.31	0.31	0.35	0.35	0.30	0.38	0.35	0.36	0.38
Total	99.91	99.23	100.72	100.45	99.79	99.54	99.86	99.91	100.39	99.97	100.48	101.27
LOI	1.98	0.49	0.72	0.87	2.16	1.49	1.60	4.12	1.61	0.24	0.25	0.65
Mg#*	0.49	0.49	0.49	0.48	0.47	0.44	0.42	0.41	0.40	0.40	0.39	0.38
Trace elements (ppm):												
Rb	5	5	1	5	6	14	3	8	16	2	3	2
Sr	329	205	212	206	353	186	168	116	196	203	203	202
Nb†	16	15	15	17	17	19	20	19	22	23	22	23
Zr	176	169	175	198	193	234	230	217	239	244	245	250
Y	37	33	36	42	41	49	43	39	50	44	47	49
V	428	403	422	503	445	424	446	392	442	465	467	515
Cr	79	58	62	31	31	17	20	29	22	22	20	28
Ni	44	46	41	33	35	27	28	26	24	26	26	28
Cu	140	88	155	190	166	175	160	148	190	199	187	201
Zn	111	112	117	133	131	137	139	111	145	146	136	153
Normative mineralogy: $Fe^{2+}:Fe^{3+}$ = 0.8												
Q	2.2	0.2	1.7	0.0	0.0	7.0	0.0		0.9	0.4	0.1	7.0
Or	2.3	2.8	1.3	2.9	2.7	6.6	1.6		2.7	1.8	1.9	6.6
Ab	20.5	19.1	19.3	20.2	24.3	21.5	25.0		19.9	20.0	20.0	21.5
An	25.6	25.1	26.6	23.8	19.5	23.2	20.1		24.0	22.6	22.2	23.2
Cor	0.0	0.0	0.0	0.0	0.0	0.0	0.0		0.0	0.0	0.0	0.0
Wo (Di)	9.1	7.5	10.4	8.8	9.9	7.1	8.7		7.7	8.6	8.8	7.1
En (Di)	3.9	3.2	4.5	3.8	4.3	3.1	3.7		3.3	3.7	3.8	3.1
Fs (Di	3.9	3.5	4.7	4.1	4.1	2.4	4.1		4.9	5.6	5.8	2.4
En (Hy)	10.1	11.9	9.1	10.5	7.8	9.6	7.0		8.3	8.2	8.1	9.6
Fs (Hy)	10.0	12.9	9.5	11.3	9.4	7.5	10.1		12.1	12.3	12.4	7.5
Ol (Fo)	0.0	0.0	0.0	0.0	1.3	0.0	1.6		0.0	0.0	0.0	0.0
Ol (Fa)	0.0	0.0	0.0	0.0	1.9	0.0	2.3		0.0	0.0	0.0	0.0
Ilmenite	3.9	4.1	4.0	4.8	4.8	4.7	5.1		5.4	5.5	5.5	4.7
Magnetite	8.0	9.2	8.2	9.0	9.3	6.5	10.0		10.0	10.5	10.6	6.5
Apatite	0.5	0.5	0.5	0.6	0.7	0.8	0.7		0.8	0.7	0.7	0.8
Total	99.9	99.9	99.9	99.9	99.9	99.9	99.9		99.9	99.9	99.9	99.9

Notes: * = (Mg# = Mg/[Mg+Fe^{2+}]), where $Fe^{2+}:Fe^{3+}$ = 0.8. LOI = loss on ignition at 1025°C for 4 hr. † = analyzed Nb concentrations were adjusted using BHVO-1 as a secondary standard.

Table T14. Alteration minerals within basement units in Hole 1138A identified by X-ray diffraction.

Core, section, piece, interval (cm)	Depth (mbsf)	Description	XRD identification
183-1138A-			
80R-1 (Piece 6, 36-37)	746.66	Prismatic crystals in vug	Calcite
80R-1 (Piece 15, 120)	747.50	Prismatic crystals in vug	Calcite, clinoptilolite
81R-1 (Piece 11, 102-104)	756.92	White porcelain zeolite in vug	Clinoptilolite, smectite
81R-1 (Piece 14, 132-135)	757.22	Dark equant zeolite lining vesicle	Clinoptilolite, smectite
81R-3 (Piece 3A, 61-65)	759.26	White porcelain solid in vesicular clast within breccia	Quartz
81R-4 (Piece 11, 97-98)	761.08	Mucous-like green tendrils in vesicle	Clinoptilolite
82R-3 (Piece 4, 28-45)	768.85	Well-indurated brown sediment in breccia matrix	Quartz
82R-4 (Piece 3, 74-75)	770.78	Equant crystals in vesicle	Quartz, clinoptilolite
82R-5 (Piece 9, 136-138)	772.90	Amber equant zeolite in vug	Clinoptilolite
83R-1 (Piece 3B, 33-34)	775.53	Green equant zeolite in vesicle	Quartz, clinoptilolite
83R-1 (Piece 3B, 42-43)	775.62	White platy zeolite in vesicle within breccia	Clinoptilolite
83R-2 (Piece 5B, 47-48)	777.17	White platy zeolite in vesicle	Clinoptilolite
83R-2 (Piece 5B, 48-49)	777.18	Zeolite + clay in vesicle	Clinoptilolite, smectite
83R-4 (Piece 9, 112-114)	780.63	Green equant zeolite in vug	Clinoptilolite
83R-5 (Piece 2, 15-16)	781.08	Tan zeolite blades in vesicle	Clinoptilolite
84R-2 (Piece 10, 98-101)	787.16	Amber zeolite in breccia matrix	Clinoptilolite
84R-3 (Piece 1, 12-13)	787.62	White zeolite in breccia matrix	Clinoptilolite
85R-1 (Piece 10, 94-94)	795.44	Equant zeolite in vesicle	Clinoptilolite
86R-1 (Piece 8, 110-111)	805.20	Platy white zeolite in vesicle	Clinoptilolite
86R-3 (Piece 7, 60-61)	807.70	White zeolite vein	Clinoptilolite
87R-1 (Piece 2, 11-13)	813.81	Large zeolite crystal in center of vug	Analcime
87R-1 (Piece 13, 105-106)	814.75	Platy zeolite in breccia vug	Clinoptilolite
89R-1 (Piece 5, 84-85)	833.94	Zeolite crystals in vug	Clinoptilolite
89R-3 (Piece 1B, 20-21)	836.06	White zeolite in vesicle	Clinoptilolite

Table T15. True dips of intact basement unit boundaries in Hole 1138A.

Boundary	Core, section, piece, interval (cm)	Depth (mbsf)	Description	True dip (°)
	183-1138A-			
Unit 5/6	81R-1 (Piece 2, 6-7)	755.96	Chilled contact between coherent vesicular basalts	30
Unit 6/7	81R-3 (Piece 1, 12-13)	758.77	Vesicular flow base over flow top breccia	62
Unit 9 internal	82R-3 (Piece 8, 107-110)	769.64	Flow top breccia to vesicular coherent interior	45

Note: For basement unit descriptions, see **"Physical Volcanology,"** p. 22.

Table T16. Characteristic inclinations and natural remanent magnetization intensities of discrete basalt samples from Hole 1138A.

Core, section, interval (cm)	Basement unit	Inclination (°)	NRM intensity (A/m)	Depth (mbsf)	Demagnetization range (° or mT)
183-1138A-					
79R-4,115-117	3	–61	3.28	742.02	TH 290-620
81R-5,27-29	7	–53	8.81	761.63	TH 260-620
82R-4,19-21	9	–61	7.31	770.23	TH 260-620
83R-3,13-15	10	–80	3.22	778.29	AF 30-60
84R-4,47-49	13	–71	9.83	789.44	TH 290-590
85R-1,61-63	14	–68	4.89	795.11	AF 20-60
88R-1,53-55	20	–59	30.5	823.93	TH 230-620

Notes: NRM = natural remanent magnetization. Inclination = characteristic inclination determined from progressive demagnetization. Demagnetization range = demagnetization method and characteristic inclination is determined from the component in this range. TH = thermal demagnetization, AF = alternating field demagnetization.

Table T17. Index properties data from Site 1138. (See table note. Continued on next three pages.)

Core, section interval (cm)	Depth (mbsf)	Water content (%)		Density (g/cm³)			Porosity (%)	Void ratio
		Wet	Dry	Bulk	Dry	Grain		
183-1138A-								
4R-1, 51-53	27.01	60.8	155.0	1.32	0.52	2.37	78.2	3.59
4R-2, 85-87	28.85	64.7	183.5	1.28	0.45	2.34	80.8	4.20
4R-5, 71-73	33.21	65.0	185.9	1.27	0.44	2.27	80.5	4.12
5R-7, 23-25	45.23	61.3	158.1	1.31	0.51	2.31	78.1	3.57
6R-3, 84-86	49.24	72.7	266.9	1.20	0.33	2.16	84.9	5.64
7R-2, 94-96	57.24	63.6	175.0	1.28	0.47	2.29	79.6	3.91
7R-3, 77-79	58.57	64.0	177.9	1.28	0.46	2.30	80.0	3.99
8R-1, 110-112	65.40	55.0	122.0	1.38	0.62	2.41	74.2	2.87
8R-2, 114-116	66.94	52.5	110.6	1.42	0.67	2.46	72.7	2.66
8R-3, 101-103	68.31	53.2	113.5	1.41	0.66	2.47	73.3	2.74
8R-4, 91-93	69.71	48.7	95.0	1.46	0.75	2.45	69.4	2.27
8R-5, 25-27	70.55	48.3	93.5	1.46	0.76	2.44	69.0	2.23
8R-6, 87-89	72.67	51.3	105.2	1.45	0.71	2.56	72.4	2.63
8R-7, 7-9	73.37	50.9	103.6	1.43	0.70	2.45	71.2	2.48
9R-1, 45-47	74.15	58.1	138.6	1.34	0.56	2.34	76.0	3.17
9R-2, 38-40	75.58	53.5	115.2	1.40	0.65	2.45	73.4	2.76
9R-3, 98-100	77.68	54.1	117.9	1.40	0.64	2.47	74.0	2.85
9R-4, 39-41	78.59	57.0	132.8	1.35	0.58	2.36	75.4	3.06
10R-1, 118-120	84.28	64.6	182.6	1.27	0.45	2.27	80.2	4.04
10R-2, 110-112	85.70	65.0	185.4	1.27	0.45	2.32	80.7	4.19
10R-3, 56-58	86.66	70.4	238.0	1.22	0.36	2.22	83.7	5.15
11R-1, 37-39	93.07	57.2	133.7	1.36	0.58	2.39	75.7	3.12
11R-2, 56-58	94.76	56.6	130.3	1.36	0.59	2.41	75.4	3.07
11R-3, 31-33	96.01	63.5	174.2	1.29	0.47	2.33	79.8	3.96
11R-4, 35-37	97.55	60.8	155.3	1.31	0.51	2.34	78.0	3.55
11R-5, 70-72	99.40	60.3	152.2	1.32	0.52	2.34	77.7	3.48
11R-6, 77-79	100.97	61.3	158.3	1.31	0.51	2.37	78.6	3.67
12R-1, 81-83	103.11	62.3	165.4	1.31	0.49	2.43	79.7	3.93
12R-2, 39-41	104.19	65.0	185.8	1.28	0.45	2.42	81.5	4.40
12R-3, 59-61	105.89	51.3	105.5	1.45	0.70	2.55	72.5	2.63
13R-1, 114-116	113.14	49.1	96.4	1.47	0.75	2.55	70.6	2.40
13R-2, 31-33	113.81	41.4	70.5	1.59	0.93	2.59	64.1	1.79
13R-3, 113-115	116.13	49.5	98.2	1.47	0.74	2.55	71.0	2.45
13R-4, 114-116	117.64	66.7	200.0	1.28	0.43	2.56	83.3	4.99
15R-1, 115-117	132.35	60.5	153.2	1.33	0.52	2.41	78.3	3.61
15R-2, 110-112	133.80	47.3	89.7	1.46	0.77	2.35	67.3	2.06
16R-1, 109-111	141.89	38.8	63.5	1.60	0.98	2.49	60.7	1.54
16R-2, 42-44	142.72	43.7	77.6	1.56	0.88	2.62	66.5	1.99
16R-3, 127-129	145.07	38.3	62.0	1.66	1.03	2.72	62.2	1.65
17R-1, 111-113	151.61	37.4	59.7	1.64	1.02	2.54	59.7	1.48
17R-2, 107-109	153.07	37.2	59.2	1.64	1.03	2.53	59.3	1.46
17R-3, 118-120	154.68	39.7	65.8	1.59	0.96	2.51	61.7	1.61
17R-4, 112-114	156.12	38.8	63.4	1.60	0.98	2.48	60.6	1.54
17R-5, 110-112	157.60	35.3	54.6	1.67	1.08	2.53	57.4	1.35
18R-1, 105-107	161.15	35.4	54.7	1.68	1.09	2.59	58.0	1.38
18R-2, 123-125	162.83	35.5	55.0	1.73	1.11	2.77	59.8	1.49
18R-3, 126-128	164.36	34.8	53.4	1.72	1.12	2.70	58.4	1.41
18R-4, 130-132	165.90	36.3	57.0	1.66	1.06	2.57	58.8	1.43
18R-5, 121-123	167.31	34.1	51.7	1.71	1.12	2.60	56.7	1.31
18R-6, 95-97	168.55	36.0	56.2	1.67	1.07	2.58	58.6	1.42
19R-1, 129-131	170.99	32.7	48.5	1.76	1.18	2.69	56.0	1.28
19R-2, 113-115	172.33	37.1	58.9	1.66	1.04	2.62	60.1	1.51
19R-3, 125-127	173.95	34.2	52.0	1.69	1.11	2.56	56.5	1.30
19R-4, 16-18	174.36	38.2	61.7	1.63	1.01	2.56	60.7	1.54
20R-1, 111-113	180.41	43.6	77.4	1.56	0.88	2.60	66.3	1.97
20R-2, 39-41	181.19	38.6	62.9	1.63	1.00	2.61	61.6	1.60
20R-3, 130-132	183.60	37.0	58.7	1.68	1.06	2.69	60.6	1.54
20R-4, 125-127	185.05	35.9	56.1	1.70	1.09	2.69	59.6	1.47
20R-5, 15-17	185.45	39.5	65.2	1.61	0.98	2.59	62.2	1.65
21R-1, 120-122	190.20	32.5	48.2	1.76	1.19	2.69	55.8	1.26
21R-2, 30-32	190.80	30.6	44.1	1.80	1.25	2.70	53.8	1.16
22R-1, 64-66	199.24	34.3	52.2	1.74	1.14	2.72	58.1	1.39
22R-2, 125-127	201.35	36.2	56.8	1.68	1.07	2.65	59.5	1.47
23R-1, 117-119	209.37	35.4	54.9	1.70	1.10	2.68	58.9	1.44
23R-2, 68-70	210.38	35.1	54.2	1.69	1.10	2.62	58.1	1.38
24R-1, 108-110	218.88	33.5	50.4	1.74	1.16	2.68	56.9	1.32

Table T17 (continued).

Core, section interval (cm)	Depth (mbsf)	Water content (%)		Density (g/cm³)			Porosity (%)	Void ratio
		Wet	Dry	Bulk	Dry	Grain		
24R-2, 118-120	220.48	35.8	55.7	1.71	1.10	2.73	59.7	1.48
24R-3, 21-23	221.01	33.1	49.5	1.73	1.16	2.64	56.1	1.28
25R-1, 131-133	228.71	34.9	53.6	1.69	1.10	2.60	57.6	1.36
25R-2, 55-58	229.45	38.3	62.0	1.65	1.02	2.64	61.5	1.60
26R-1, 117-119	238.27	33.6	50.6	1.72	1.14	2.61	56.3	1.29
26R-2, 39-41	238.99	34.2	52.1	1.72	1.13	2.67	57.6	1.36
26R-2, 103-105	239.63	30.0	42.9	1.78	1.25	2.61	52.2	1.09
27R-1, 122-124	247.92	33.2	49.8	1.73	1.15	2.62	56.0	1.28
28R-1, 123-125	257.63	34.8	53.5	1.73	1.13	2.74	58.8	1.43
28R-2, 112-114	259.02	31.0	45.0	1.78	1.22	2.65	53.8	1.16
28R-3, 110-112	260.50	29.5	41.9	1.79	1.26	2.59	51.5	1.06
28R-4, 58-60	261.48	29.7	42.2	1.79	1.26	2.61	51.8	1.08
29R-1, 124-126	267.14	38.2	61.7	1.66	1.03	2.69	61.8	1.62
30R-2, 30-32	277.30	38.4	62.4	1.66	1.02	2.69	62.1	1.64
31R-1, 48-50	285.58	32.7	48.5	1.76	1.19	2.70	56.1	1.28
32R-1, 97-99	295.67	35.9	56.0	1.71	1.09	2.73	59.9	1.49
33R-1, 30-32	304.70	38.7	63.2	1.65	1.01	2.70	62.5	1.67
34R-1, 109-110	315.19	41.9	72.0	1.60	0.93	2.66	65.2	1.87
34R-2, 34-36	315.94	38.9	63.6	1.63	1.00	2.60	61.8	1.62
34R-3, 129-131	318.39	39.8	66.1	1.63	0.98	2.69	63.5	1.74
34R-4, 10-12	318.70	36.3	56.9	1.69	1.08	2.69	59.9	1.50
35R-1, 37-39	324.07	37.9	61.1	1.66	1.03	2.69	61.6	1.61
35R-2, 40-42	325.60	38.6	62.9	1.65	1.01	2.68	62.2	1.65
35R-3, 41-43	327.11	40.2	67.2	1.63	0.97	2.69	63.8	1.76
35R-4, 110-112	329.30	38.1	61.7	1.66	1.02	2.67	61.7	1.61
36R-5, 89-91	339.89	29.6	42.1	1.83	1.29	2.73	52.9	1.12
36R-6, 31-33	340.31	30.8	44.4	1.81	1.26	2.76	54.5	1.20
37R-1, 111-113	343.71	32.6	48.3	1.76	1.19	2.69	55.9	1.27
37R-2, 111-113	345.21	30.4	43.7	1.81	1.26	2.72	53.7	1.16
37R-3, 108-110	346.68	31.4	45.9	1.79	1.23	2.72	54.9	1.22
37R-4, 118-120	348.28	33.3	49.9	1.75	1.17	2.71	56.9	1.32
37R-5, 111-113	349.71	26.6	36.2	1.89	1.39	2.72	49.1	0.96
38R-1, 43-45	352.63	28.2	39.2	1.85	1.33	2.72	51.0	1.04
38R-2, 51-53	354.21	31.2	45.3	1.80	1.24	2.73	54.7	1.21
38R-3, 29-31	355.49	29.6	42.1	1.83	1.29	2.74	53.0	1.13
39R-1, 109-111	362.89	25.6	34.4	1.89	1.41	2.68	47.3	0.90
39R-2, 111-113	364.41	28.3	39.5	1.85	1.33	2.72	51.2	1.05
40R-1, 112-114	372.62	29.9	42.7	1.83	1.28	2.76	53.6	1.15
40R-2, 107-109	374.07	30.1	43.2	1.82	1.27	2.75	53.6	1.16
41R-1, 115-117	382.35	28.0	38.8	1.86	1.34	2.73	50.9	1.04
41R-2, 41-43	383.11	26.7	36.4	1.88	1.38	2.70	49.0	0.96
42R-1, 111-113	391.91	25.0	33.4	1.92	1.44	2.72	47.0	0.89
42R-2, 126-128	393.56	25.6	34.4	1.88	1.40	2.64	47.0	0.89
42R-3, 115-117	394.95	23.8	31.2	1.95	1.49	2.72	45.3	0.83
42R-4, 40-42	395.70	29.9	42.6	1.82	1.27	2.71	53.0	1.13
43R-1, 110-112	401.50	16.6	19.8	2.10	1.75	2.64	33.9	0.51
43R-4, 115-117	406.05	27.2	37.3	1.87	1.36	2.69	49.5	0.98
43R-5, 111-113	407.51	28.4	39.6	1.81	1.30	2.61	50.2	1.01
44R-1, 110-112	411.10	29.0	40.8	1.84	1.30	2.72	52.0	1.08
44R-2, 113-115	412.63	26.2	35.6	1.90	1.40	2.72	48.6	0.94
44R-3, 111-113	414.11	26.4	35.9	1.89	1.39	2.71	48.7	0.95
45R-1, 112-114	420.82	26.0	35.1	1.91	1.41	2.74	48.4	0.94
45R-2, 38-40	421.58	30.1	43.1	1.79	1.25	2.66	52.8	1.12
46R-1, 34-36	429.64	21.6	27.6	1.98	1.55	2.67	41.8	0.72
48R-1, 111-113	449.71	26.2	35.5	1.87	1.38	2.64	47.7	0.91
48R-2, 107-109	451.17	21.2	27.0	2.04	1.61	2.79	42.4	0.74
48R-3, 112-114	452.72	23.3	30.3	1.89	1.45	2.55	43.0	0.76
48R-4, 116-118	454.26	31.7	46.5	1.77	1.21	2.66	54.7	1.21
48R-5, 113-115	455.73	18.0	21.9	2.01	1.65	2.54	35.2	0.54
48R-6, 86-88	456.96	22.5	29.0	1.98	1.53	2.70	43.3	0.77
49R-1, 129-131	459.49	21.6	27.6	2.05	1.60	2.83	43.2	0.76
49R-2, 120-122	460.90	15.5	18.3	2.12	1.79	2.64	32.1	0.47
49R-3, 24-26	461.44	20.1	25.2	2.00	1.60	2.64	39.4	0.65
50R-1, 128-130	468.78	12.9	14.8	2.14	1.86	2.54	26.9	0.37
50R-2, 23-25	469.23	16.7	20.1	2.07	1.73	2.61	33.9	0.51
51R-1, 112-114	478.22	23.1	30.0	1.98	1.52	2.75	44.7	0.81
51R-2, 115-117	479.75	26.3	35.6	1.88	1.39	2.67	48.2	0.93
51R-3, 110-112	481.20	26.4	35.9	1.90	1.40	2.76	49.2	0.97
51R-4, 94-96	482.54	20.9	26.4	2.02	1.59	2.71	41.1	0.70

Table T17 (continued).

Core, section interval (cm)	Depth (mbsf)	Water content (%)		Density (g/cm³)			Porosity (%)	Void ratio
		Wet	Dry	Bulk	Dry	Grain		
55R-1, 100-102	516.30	20.1	25.2	2.06	1.65	2.76	40.4	0.68
55R-2, 96-98	517.76	20.4	25.6	2.07	1.65	2.79	41.1	0.70
56R-1, 139-141	526.29	19.6	24.3	2.06	1.66	2.73	39.3	0.65
56R-2, 125-127	527.65	20.0	25.1	2.05	1.64	2.74	40.2	0.67
56R-3, 129-131	529.19	19.9	24.8	2.08	1.66	2.78	40.3	0.68
57R-1, 65-67	535.15	17.8	21.6	2.05	1.69	2.62	35.6	0.55
58R-1, 42-44	544.62	21.2	27.0	2.01	1.59	2.73	41.8	0.72
58R-2, 9-11	545.79	17.8	21.7	2.12	1.75	2.77	37.0	0.59
60R-1, 76-78	564.06	20.5	25.8	2.02	1.60	2.69	40.4	0.68
60R-2, 111-113	565.92	19.4	24.1	2.03	1.64	2.67	38.5	0.63
61R-1, 121-123	574.11	18.0	22.0	2.09	1.72	2.71	36.8	0.58
61R-2, 91-93	575.31	19.8	24.6	2.04	1.64	2.70	39.4	0.65
62R-1, 112-114	583.62	18.8	23.1	2.06	1.67	2.69	37.7	0.61
63R-1, 115-117	593.35	17.4	21.1	2.11	1.74	2.71	35.8	0.56
65R-1, 104-106	612.54	20.6	25.9	2.03	1.61	2.72	40.7	0.69
66R-1, 119-121	622.29	14.3	16.7	2.20	1.89	2.72	30.7	0.44
66R-2, 121-123	623.81	12.7	14.6	2.26	1.97	2.75	28.1	0.39
66R-3, 111-113	625.21	12.2	13.8	2.26	1.99	2.72	26.9	0.37
66R-4, 112-114	626.72	17.3	20.8	2.08	1.72	2.65	35.1	0.54
67R-1, 114-116	631.84	14.4	16.8	2.16	1.85	2.66	30.4	0.44
67R-2, 96-98	633.07	15.4	18.1	2.14	1.81	2.66	32.0	0.47
69R-1, 114-116	651.14	19.0	23.4	2.00	1.62	2.58	37.1	0.59
69R-2, 103-105	652.45	20.8	26.3	1.99	1.57	2.64	40.4	0.68
69R-3, 28-30	652.87	21.8	27.8	1.96	1.54	2.64	41.8	0.72
69R-4, 131-133	655.40	22.7	29.3	1.95	1.51	2.66	43.2	0.76
69R-5, 35-37	655.92	29.2	41.2	1.65	1.17	2.20	46.9	0.89
70R-1, 113-115	660.73	16.3	19.4	2.13	1.78	2.69	33.8	0.51
70R-2, 23-25	661.33	15.4	18.3	2.14	1.81	2.67	32.3	0.48
71R-1, 94-96	670.14	25.5	34.3	1.92	1.43	2.75	47.9	0.92
71R-2, 98-100	671.48	22.5	29.1	2.17	1.68	3.23	47.8	0.92
73R-1, 76-78	689.26	19.0	23.5	2.11	1.71	2.81	39.3	0.65
73R-2, 51-53	689.82	24.9	33.1	1.92	1.44	2.71	46.7	0.88
73R-3, 14-16	690.40	25.1	33.6	1.91	1.43	2.69	46.8	0.88
74R-1, 26-28	698.36	6.1	6.5	2.44	2.29	2.68	14.5	0.17
76R-1, 97-99	718.37	30.3	43.4	1.77	1.24	2.60	52.4	1.10
77R-1, 126-128	723.46	22.4	28.9	2.00	1.55	2.75	43.7	0.78
77R-2, 113-115	724.83	26.1	35.3	1.86	1.38	2.62	47.4	0.90
77R-3, 73-75	725.93	25.4	34.0	1.87	1.39	2.59	46.3	0.86
78R-1, 137-139	728.37	31.1	45.1	1.76	1.21	2.59	53.3	1.14
78R-2, 135-137	729.85	29.9	42.6	1.73	1.21	2.44	50.3	1.01
78R-3, 129-131	731.29	27.8	38.4	1.76	1.28	2.44	47.8	0.92
78R-4, 128-130	732.78	30.9	44.8	1.73	1.19	2.49	52.1	1.09
78R-5, 33-35	733.33	32.6	48.4	1.71	1.15	2.53	54.5	1.20
80R-1, 99-101	747.29	11.9	13.5	2.31	2.04	2.78	26.8	0.37
80R-2, 114-116	748.91	8.8	9.7	2.56	2.34	3.00	22.1	0.28
80R-3, 40-42	749.60	11.0	12.3	2.40	2.14	2.88	25.7	0.35
80R-4, 95-97	751.65	9.8	10.8	2.49	2.24	2.94	23.7	0.31
81R-1, 92-94	756.82	9.6	10.7	2.48	2.24	2.92	23.4	0.31
81R-2, 66-68	757.97	6.0	6.3	2.70	2.54	3.01	15.7	0.19
81R-3, 111-113	759.76	12.6	14.4	2.27	1.98	2.75	27.9	0.39
81R-4, 27-29	760.38	9.9	11.0	2.42	2.18	2.86	23.5	0.31
81R-5, 9-11	761.45	6.4	6.9	2.57	2.41	2.87	16.1	0.19
81R-5, 27-29	761.63	6.9	7.4	2.59	2.41	2.92	17.4	0.21
81R-5, 61-63	761.97	7.0	7.5	2.58	2.40	2.92	17.6	0.21
81R-5, 82-84	762.18	8.7	9.5	2.52	2.30	2.93	21.4	0.27
82R-1, 21-23	765.81	8.1	8.8	2.50	2.30	2.86	19.8	0.25
82R-2, 9-11	767.19	6.1	6.5	2.68	2.52	3.00	16.0	0.19
82R-3, 8-10	768.65	9.7	10.8	2.48	2.24	2.92	23.5	0.31
82R-3, 128-130	769.85	7.0	7.6	2.58	2.40	2.92	17.8	0.22
82R-5, 43-45	771.97	5.4	5.7	2.77	2.62	3.07	14.5	0.17
83R-1, 139-141	776.59	8.0	8.7	2.63	2.42	3.05	20.6	0.26
83R-2, 29-31	776.99	9.4	10.4	2.60	2.36	3.10	23.9	0.31
83R-3, 13-15	778.29	6.9	7.4	2.64	2.45	2.99	17.8	0.22
83R-4, 79-81	780.30	5.8	6.2	2.76	2.60	3.09	15.8	0.19
83R-5, 6-8	780.99	10.5	11.7	2.48	2.22	2.98	25.4	0.34
83R-6, 15-17	782.41	8.9	9.8	2.54	2.32	2.98	22.2	0.29
84R-1, 15-17	784.95	13.5	15.6	2.32	2.01	2.89	30.5	0.44
84R-4, 12-14	789.09	4.4	4.6	2.77	2.64	3.00	11.8	0.13
84R-4, 47-49	789.44	5.9	6.3	2.69	2.54	3.00	15.5	0.18

Table T17 (continued).

Core, section interval (cm)	Depth (mbsf)	Water content (%)		Density (g/cm³)			Porosity (%)	Void ratio
		Wet	Dry	Bulk	Dry	Grain		
84R-4, 67-69	789.64	5.2	5.5	2.66	2.53	2.92	13.5	0.16
84R-5, 30-32	790.13	3.3	3.4	2.81	2.72	2.99	9.1	0.10
84R-5, 128-130	791.11	3.5	3.6	2.82	2.72	3.01	9.6	0.11
84R-6, 4-6	791.34	7.6	8.2	2.67	2.47	3.08	19.9	0.25
85R-1, 37-39	794.87	7.5	8.1	2.62	2.42	3.00	19.2	0.24
85R-1, 61-63	795.11	6.7	7.2	2.75	2.56	3.13	18.1	0.22
85R-2, 4-6	795.87	9.4	10.3	2.62	2.37	3.12	23.9	0.32
85R-2, 11-13	795.94	11.2	12.7	2.41	2.14	2.92	26.5	0.36
85R-2, 21-23	796.04	11.6	13.1	2.48	2.19	3.04	27.9	0.39
85R-2, 27-29	796.10	11.3	12.8	2.33	2.07	2.79	25.8	0.35
85R-2, 84-86	796.67	11.5	13.0	2.46	2.17	3.01	27.7	0.38
85R-2, 89-91	796.72	11.6	13.2	2.45	2.17	3.01	27.9	0.39
85R-2, 128-130	797.11	6.4	6.8	2.56	2.40	2.85	15.9	0.19
85R-2, 138-140	797.21	5.6	5.9	2.58	2.44	2.83	14.0	0.16
86R-1, 55-57	804.65	12.2	13.9	2.44	2.14	3.02	29.1	0.41
86R-3, 25-27	807.35	6.1	6.5	2.75	2.59	3.09	16.4	0.20
87R-2, 14-16	815.30	6.2	6.6	2.62	2.45	2.91	15.8	0.19
88R-1, 8-10	823.48	9.8	10.9	2.51	2.27	2.99	24.1	0.32
88R-1, 53-55	823.93	11.5	13.0	2.37	2.10	2.87	26.7	0.37
89R-1, 20-22	833.30	14.3	16.7	2.25	1.93	2.81	31.4	0.46
89R-2, 77-79	835.35	8.5	9.3	2.63	2.40	3.07	21.7	0.28
89R-3, 40-42	836.26	6.8	7.3	2.72	2.54	3.10	18.1	0.22

Note: This table is also available in **ASCII format.**

Table T18. Compressional wave velocity discrete measurements, Site 1138. (See table note. Continued on next five pages.)

Core, section, interval (cm)	Depth (mbsf)	Direction	Velocity (m/s)
183-1138A-			
4R-1, 26	26.76	LZ	1557
4R-2, 85	28.85	LZ	1567
4R-2, 85	28.85	LY	1561
4R-3, 121	30.71	LZ	1560
4R-3, 122	30.72	LY	1559
4R-5, 72	33.22	LZ	1547
4R-5, 72	33.22	LY	1550
5R-1, 46	36.46	LZ	1599
5R-1, 46	36.46	LY	1620
5R-2, 140	38.90	LY	1572
5R-2, 140	38.90	LZ	1562
5R-7, 24	45.24	LY	1545
5R-7, 24	45.24	LZ	1543
6R-1, 47	45.87	LZ	1545
6R-1, 72	46.12	LY	1542
6R-3, 87	49.27	LY	1534
6R-3, 87	49.27	LZ	1538
7R-2, 96	57.26	LY	1543
7R-2, 96	57.26	LZ	1541
7R-3, 76	58.56	LZ	1546
7R-3, 77	58.57	LY	1545
8R-1, 110	65.40	LY	1531
8R-1, 113	65.43	LZ	1529
8R-2, 115	66.95	LZ	1537
8R-2, 115	66.95	LY	1547
8R-3, 11	67.41	LZ	1565
8R-3, 36	67.66	LY	1565
8R-3, 102	68.32	LY	1540
8R-3, 102	68.32	LZ	1553
8R-4, 92	69.72	LY	1562
8R-4, 93	69.73	LZ	1560
8R-5, 25	70.55	LY	1541
8R-5, 25	70.55	LZ	1544
8R-6, 83	72.63	LY	1563
8R-6, 88	72.68	LZ	1562
8R-7, 8	73.38	LY	1518
8R-7, 10	73.40	LZ	1521
9R-1, 45	74.15	LY	1514
9R-1, 46	74.16	LX	1718
9R-1, 120	74.90	LX	1751
9R-2, 39	75.59	LX	1733
9R-2, 39	75.59	LY	1546
9R-2, 39	75.59	LZ	1569
9R-2, 111	76.31	LX	1619
9R-3, 47	77.17	LZ	1528
9R-3, 47	77.17	LY	1534
9R-3, 47	77.17	LX	1678
9R-3, 98	77.68	LZ	1532
9R-3, 99	77.69	LX	1684
9R-3, 99	77.69	LY	1542
9R-4, 40	78.60	LZ	1540
9R-4, 40	78.60	LY	1555
9R-4, 40	78.60	LX	1691
10R-1, 56	83.66	LY	1541
10R-1, 57	83.67	LX	1557
10R-1, 120	84.30	LY	1536
10R-1, 121	84.31	LX	1556
10R-2, 112	85.72	LY	1552
10R-2, 113	85.73	LX	1578
10R-3, 57	86.67	LX	1551
10R-3, 57	86.67	LY	1528
11R-1, 38	93.08	LX	1607
11R-1, 97	93.67	LX	1593
11R-2, 57	94.77	LX	1614
11R-2, 143	95.63	LX	1580
11R-3, 32	96.02	LX	1566
11R-4, 36	97.56	LX	1588
11R-4, 106	98.26	LX	1595
11R-5, 71	99.41	LX	1588
11R-6, 45	100.65	LX	1557
11R-6, 79	100.99	LX	1575
11R-6, 121	101.41	LX	1566
12R-1, 82	103.12	LX	1554
12R-2, 40	104.20	LX	1539
12R-2, 146	105.26	LX	1556
12R-3, 60	105.90	LX	1562
12R-3, 116	106.46	LX	1556
13R-1, 51	112.51	LX	1541
13R-1, 115	113.15	LX	1657
13R-2, 32	113.82	LX	1643
13R-2, 118	114.68	LX	1679
13R-3, 45	115.45	LX	1638
13R-3, 114	116.14	LX	1625
13R-4, 44	116.94	LX	1650
13R-4, 115	117.65	LX	1600
13R-5, 28	118.28	LX	1553
14R-1, 41	122.01	LX	1575
14R-2, 111	124.21	LX	1572
15R-1, 30	131.50	LX	1585
15R-1, 54	131.74	LX	1553
15R-1, 110	132.30	LX	1582
15R-1, 117	132.37	LX	1572
16R-1, 41	141.21	LX	1617
16R-1, 111	141.91	LX	1576
16R-2, 43	142.73	LX	1596
16R-2, 114	143.44	LX	1589
16R-3, 38	144.18	LX	1609
16R-3, 127	145.07	LX	1616
17R-1, 46	150.96	LX	1612
17R-1, 101	151.51	LX	1591
17R-2, 109	153.09	LX	1586
17R-3, 43	153.93	LX	1588
17R-3, 118	154.68	LX	1595
17R-4, 43	155.43	LX	1550
17R-4, 43	155.43	LX	1593
17R-5, 42	156.92	LX	1623
17R-5, 111	157.61	LX	1597
18R-1, 39	160.49	LX	1632
18R-1, 106	161.16	LX	1662
18R-2, 46	162.06	LX	1620
18R-2, 125	162.85	LX	1703
18R-3, 37	163.47	LX	1655
18R-3, 37	163.47	LX	1615
18R-4, 36	164.96	LX	1667
18R-4, 128	165.88	LX	1676
18R-5, 43	166.53	LX	1675
18R-5, 124	167.34	LX	1685
18R-6, 38	167.98	LX	1672
18R-6, 96	168.56	LX	1678
19R-1, 36	170.06	LX	1714
19R-1, 129	170.99	LX	1703
19R-2, 44	171.64	LX	1717
19R-2, 114	172.34	LX	1713
19R-3, 57	173.27	LX	1776
19R-3, 125	173.95	LX	1713
19R-4, 17	174.37	LX	1707
20R-1, 39	179.69	LX	1629
20R-1, 39	179.69	LX	1564
20R-2, 40	181.20	LX	1665
20R-2, 127	182.07	LX	1668
20R-3, 50	182.80	LX	1651
20R-3, 130	183.60	LX	1657
20R-4, 34	184.14	LX	1650
20R-4, 125	185.05	LX	1685
20R-5, 17	185.47	LX	1617

Table T18 (continued).

Core, section, interval (cm)	Depth (mbsf)	Direction	Velocity (m/s)
21R-1, 58	189.58	LX	1773
21R-1, 121	190.21	LX	1716
21R-2, 31	190.81	LX	1761
22R-1, 66	199.26	LX	1722
22R-1, 124	199.84	LX	1712
22R-2, 50	200.60	LX	1718
22R-2, 126	201.36	LX	1764
23R-1, 46	208.66	LX	1736
23R-1, 70	208.90	LX	1719
23R-1, 117	209.37	LX	1733
24R-1, 49	218.29	LX	1684
24R-1, 110	218.90	LX	1713
24R-2, 44	219.74	LX	1705
24R-2, 120	220.50	LX	1714
24R-3, 22	221.02	LX	1721
25R-1, 47	227.87	LX	1752
25R-1, 131	228.71	LX	1754
25R-2, 55	229.45	LX	1729
26R-1, 55	237.65	LX	1709
26R-1, 119	238.29	LX	1706
26R-2, 40	239.00	LX	1695
26R-2, 104	239.64	LX	1723
27R-1, 24	246.94	LX	1759
27R-1, 121	247.91	LX	1731
28R-1, 16	256.56	LX	1865
28R-1, 124	257.64	LX	1736
28R-2, 61	258.51	LX	1783
28R-2, 113	259.03	LX	1830
28R-3, 35	259.75	LX	1817
28R-3, 110	260.50	LX	1820
28R-4, 58	261.48	LX	1723
29R-1, 125	267.15	LX	1914
29R-2, 51	267.91	LX	1862
29R-2, 108	268.48	LX	1806
29R-3, 28	269.18	LX	1785
30R-1, 60	276.10	LX	1800
30R-1, 60	276.10	LX	1767
30R-2, 32	277.32	LX	1770
31R-1, 49	285.59	LX	1760
32R-1, 96	295.66	LX	1700
33R-1, 32	304.72	LX	1716
34R-1, 56	314.66	LX	1870
34R-1, 108	315.18	LX	1868
34R-2, 36	315.96	LX	1804
34R-2, 92	316.52	LX	1883
34R-3, 47	317.57	LX	1945
34R-3, 129	318.39	LX	1928
34R-4, 13	318.73	LX	1916
35R-1, 37	324.07	LX	2048
35R-1, 38	324.08	CY	1893
35R-1, 38	324.08	CZ	1965
35R-1, 102	324.72	LX	1910
35R-1, 110	324.80	CZ	1729
35R-1, 141	325.11	LX	1932
35R-2, 42	325.62	LX	1813
35R-2, 107	326.27	CZ	1902
35R-2, 108	326.28	LX	1823
35R-3, 41	327.11	LX	1801
35R-3, 42	327.12	CZ	1872
35R-3, 110	327.80	LX	1835
35R-3, 111	327.81	LX	1830
35R-4, 40	328.60	CZ	1712
35R-4, 111	329.31	CY	1771
35R-4, 111	329.31	CZ	1757
35R-5, 75	330.45	CY	1765
35R-5, 75	330.45	CZ	1732
36R-1, 41	333.41	CY	1968
36R-1, 41	333.41	CZ	1922
36R-1, 111	334.11	CY	1942

Core, section, interval (cm)	Depth (mbsf)	Direction	Velocity (m/s)
36R-1, 111	334.11	CZ	1958
36R-2, 42	334.92	CY	2065
36R-2, 42	334.92	CZ	2066
36R-2, 111	335.61	CY	2173
36R-2, 111	335.61	CZ	2183
36R-3, 40	336.40	CY	2168
36R-3, 40	336.40	CZ	2200
36R-3, 112	337.12	CY	2137
36R-3, 112	337.12	CZ	2172
36R-4, 41	337.91	CY	2146
36R-4, 41	337.91	CY	2147
36R-4, 41	337.91	CY	2174
36R-4, 41	337.91	CZ	2201
36R-4, 111	338.61	CY	2083
36R-4, 111	338.61	CZ	2100
36R-5, 41	339.41	CY	1920
36R-5, 41	339.41	CZ	1975
36R-5, 90	339.90	CY	2077
36R-5, 90	339.90	CZ	2028
36R-6, 31	340.31	CY	2080
36R-6, 31	340.31	CZ	2118
37R-1, 42	343.02	CY	2102
37R-1, 42	343.02	CZ	2142
37R-1, 42	343.02	CZ	2110
37R-1, 112	343.72	CY	1918
37R-1, 112	343.72	CZ	1996
37R-2, 42	344.52	CY	2088
37R-2, 112	345.22	CY	2108
37R-2, 112	345.22	CY	2043
37R-3, 42	346.02	CY	1962
37R-3, 42	346.02	CZ	2051
37R-3, 109	346.69	CZ	1961
37R-4, 70	347.80	CY	1911
37R-4, 70	347.80	CZ	2041
37R-4, 120	348.30	CZ	1889
37R-5, 42	349.02	CY	1920
37R-5, 42	349.02	CZ	1956
37R-5, 49	349.09	CY	1918
37R-5, 59	349.19	CZ	1999
37R-5, 112	349.72	CZ	2012
37R-6, 90	351.00	CZ	1918
38R-1, 44	352.64	CY	2124
38R-1, 44	352.64	CZ	2170
38R-1, 111	353.31	CZ	1962
38R-2, 52	354.22	CY	1780
38R-2, 52	354.22	CZ	1911
38R-2, 112	354.82	CZ	1962
38R-3, 30	355.50	CY	1876
38R-3, 108	356.28	CY	1971
38R-3, 108	356.28	CZ	2079
39R-1, 41	362.21	CZ	1985
39R-1, 110	362.90	CY	2085
39R-1, 110	362.90	CZ	2072
39R-2, 42	363.72	CZ	1978
39R-2, 112	364.42	CZ	2001
39R-3, 43	365.23	CZ	1953
39R-3, 112	365.92	CZ	1972
39R-4, 42	366.72	CZ	1994
39R-4, 102	367.32	CZ	1901
39R-5, 22	368.02	CZ	1964
40R-1, 52	372.02	CZ	1908
40R-1, 113	372.63	CZ	1886
40R-2, 45	373.45	CZ	1985
40R-2, 109	374.09	CZ	1908
41R-1, 42	381.62	CZ	1967
41R-1, 115	382.35	CZ	1883
41R-2, 42	383.12	CZ	1959
42R-1, 42	391.22	CY	2031
42R-1, 42	391.22	CZ	2002

Table T18 (continued).

Core, section, interval (cm)	Depth (mbsf)	Direction	Velocity (m/s)
42R-1, 112	391.92	CY	2204
42R-1, 112	391.92	CZ	2175
42R-2, 39	392.69	CY	2148
42R-2, 39	392.69	CZ	2086
42R-2, 127	393.57	CY	2130
42R-2, 127	393.57	CZ	2131
42R-3, 44	394.24	CY	2070
42R-3, 44	394.24	CZ	1974
42R-3, 44	394.24	CZ	2098
42R-3, 116	394.96	CY	2164
42R-3, 116	394.96	CZ	2109
42R-3, 127	395.07	CY	2130
42R-4, 41	395.71	CZ	1867
42R-4, 41	395.71	CZ	1847
43R-1, 42	400.82	CY	2079
43R-1, 42	400.82	CZ	2070
43R-1, 111	401.51	CY	2250
43R-1, 111	401.51	CZ	2174
43R-2, 39	402.29	CY	2024
43R-2, 39	402.29	CZ	2021
43R-2, 116	403.06	CY	2000
43R-3, 108	404.48	CY	2054
43R-3, 108	404.48	CZ	2056
43R-4, 116	406.06	CZ	2032
43R-5, 113	407.53	CZ	1959
44R-1, 50	410.50	CY	2165
44R-1, 50	410.50	CZ	2131
44R-1, 112	411.12	CY	2114
44R-1, 112	411.12	CZ	2155
44R-2, 38	411.88	CY	2071
44R-2, 38	411.88	CZ	2083
44R-2, 114	412.64	CY	2352
44R-2, 114	412.64	CZ	2368
44R-3, 46	413.46	CY	2101
44R-3, 46	413.46	CZ	2126
44R-3, 112	414.12	CY	2314
44R-3, 112	414.12	CZ	2314
45R-1, 43	420.13	CY	2132
45R-1, 43	420.13	CZ	2152
45R-1, 113	420.83	CY	2262
45R-1, 113	420.83	CZ	2116
45R-2, 38	421.58	CY	2091
45R-2, 38	421.58	CZ	2086
46R-1, 35	429.65	CY	2611
46R-1, 35	429.65	CZ	2668
47R-1, 30	439.20	CY	2219
47R-1, 30	439.20	CZ	2309
47R-1, 110	440.00	CY	2407
47R-1, 110	440.00	CZ	2309
47R-2, 108	441.48	CY	2304
47R-2, 108	441.48	CZ	2294
48R-1, 40	449.00	CY	2434
48R-1, 40	449.00	CZ	2523
48R-1, 111	449.71	CZ	2689
48R-1, 111	449.71	CZ	2598
48R-2, 39	450.49	CY	2634
48R-2, 39	450.49	CZ	2547
48R-2, 108	451.18	CY	2345
48R-2, 108	451.18	CZ	2306
48R-3, 36	451.96	CY	2213
48R-3, 36	451.96	CZ	2193
48R-3, 113	452.73	CY	2245
48R-3, 113	452.73	CZ	2270
48R-4, 36	453.46	CY	2219
48R-4, 36	453.46	CZ	2180
48R-4, 118	454.28	CY	2280
48R-4, 118	454.28	CZ	2260
48R-5, 63	455.23	CY	2213
48R-5, 63	455.23	CZ	2341
48R-5, 114	455.74	CY	2639
48R-5, 114	455.74	CZ	2542
48R-6, 39	456.49	CY	2468
48R-6, 39	456.49	CZ	2499
48R-6, 87	456.97	CY	2765
48R-6, 87	456.97	CZ	2696
49R-1, 56	458.76	CY	2524
49R-1, 56	458.76	CZ	2535
49R-1, 130	459.50	CY	2768
49R-1, 130	459.50	CZ	2756
49R-2, 30	460.00	CY	2546
49R-2, 30	460.00	CZ	2523
49R-2, 122	460.92	CY	2939
49R-2, 122	460.92	CZ	2919
49R-3, 25	461.45	CY	2627
49R-3, 25	461.45	CZ	2638
50R-1, 25	467.75	CY	2862
50R-1, 25	467.75	CZ	2822
50R-1, 129	468.79	CY	2964
50R-1, 129	468.79	CZ	2865
50R-2, 24	469.24	CY	2796
50R-2, 24	469.24	CZ	2713
51R-1, 20	477.30	CY	3187
51R-1, 20	477.30	CZ	3188
51R-1, 112	478.22	CY	3190
51R-1, 112	478.22	CZ	3062
51R-2, 12	478.72	CY	3124
51R-2, 12	478.80	CZ	3166
51R-2, 117	479.77	CY	2793
51R-2, 117	479.77	CZ	2764
51R-3, 17	480.27	CY	2851
51R-3, 17	480.27	CZ	2792
51R-3, 112	481.22	CY	2902
51R-3, 112	481.22	CZ	2890
51R-4, 16	481.76	CY	3153
51R-4, 16	481.76	CZ	2967
51R-4, 96	482.56	CY	2967
51R-4, 96	482.56	CZ	3014
53R-1, 11	496.51	CY	2612
53R-1, 11	496.51	CZ	2502
53R-1, 90	497.30	CY	2523
53R-1, 90	497.30	CZ	2395
53R-2, 12	498.02	CY	2787
53R-2, 12	498.02	CZ	2595
53R-2, 91	498.81	CY	2546
53R-2, 91	498.81	CZ	2469
53R-3, 13	499.53	CY	2808
53R-3, 13	499.53	CZ	2704
53R-3, 93	500.33	CY	2561
53R-3, 93	500.33	CZ	2493
53R-4, 18	501.08	CY	2917
53R-4, 18	501.08	CZ	2797
53R-4, 84	501.74	CY	2654
53R-4, 84	501.74	CZ	2584
53R-5, 18	502.58	CY	2634
53R-5, 18	502.58	CZ	2505
53R-5, 90	503.30	CY	2431
53R-5, 90	503.30	CZ	2288
54R-1, 32	505.92	CY	2438
54R-1, 32	505.92	CZ	2344
54R-1, 104	506.64	CY	2374
54R-1, 104	506.64	CZ	2312
54R-2, 31	507.41	CY	2887
54R-2, 31	507.41	CZ	2760
54R-2, 108	508.18	CY	2476
54R-2, 108	508.18	CZ	2411
55R-1, 57	515.87	CY	2600
55R-1, 57	515.87	CZ	2531
55R-1, 101	516.31	CY	2847

Table T18 (continued).

Core, section, interval (cm)	Depth (mbsf)	Direction	Velocity (m/s)
55R-1, 101	516.31	CZ	2726
55R-2, 69	517.49	CY	2579
55R-2, 69	517.49	CZ	2548
55R-2, 98	517.78	CY	2838
55R-2, 98	517.78	CZ	2685
56R-1, 31	525.21	CY	2628
56R-1, 31	525.21	CZ	2692
56R-1, 139	526.29	CY	2635
56R-1, 139	526.29	CZ	2677
56R-2, 26	526.66	CY	2432
56R-2, 26	526.66	CZ	2456
56R-2, 126	527.66	CY	2482
56R-2, 126	527.66	CZ	2430
56R-3, 26	528.16	CY	2425
56R-3, 26	528.16	CZ	2448
56R-3, 130	529.20	CY	2663
56R-3, 130	529.20	CZ	2430
56R-4, 42	529.82	CY	2503
56R-4, 42	529.82	CZ	2404
57R-1, 66	535.16	Z	2499
58R-1, 40	544.60	CY	2544
58R-1, 40	544.60	CZ	2395
58R-1, 98	545.18	CY	2609
58R-1, 98	545.18	CZ	2555
58R-2, 10	545.80	CY	2909
58R-2, 10	545.80	CZ	2688
59R-1, 26	553.86	CY	2433
59R-1, 26	553.86	CZ	2384
59R-1, 111	554.71	CY	2600
59R-1, 111	554.71	CZ	2481
59R-2, 20	555.18	CY	2662
59R-2, 20	555.18	CZ	2511
60R-1, 77	564.07	CY	2697
60R-1, 77	564.07	CZ	2640
60R-2, 28	565.09	CY	2468
60R-2, 28	565.09	CZ	2601
60R-2, 113	565.94	CY	2964
60R-2, 113	565.94	CZ	2868
61R-1, 49	573.39	CY	2880
61R-1, 49	573.39	CZ	2789
61R-1, 122	574.12	CY	2873
61R-1, 122	574.12	CY	2884
61R-2, 52	574.92	CY	2894
61R-2, 52	574.92	CZ	2843
61R-2, 92	575.32	CY	2976
61R-2, 92	575.32	CZ	2813
62R-1, 33	582.83	CY	3071
62R-1, 33	582.83	CZ	2777
62R-1, 113	583.63	CY	2805
62R-1, 113	583.63	CZ	2757
63R-1, 41	592.61	CY	2862
63R-1, 41	592.61	CZ	2645
63R-1, 116	593.36	CZ	2769
64R-1, 46	602.26	CY	3045
64R-1, 46	602.26	CZ	2796
64R-1, 98	602.78	CY	2950
64R-1, 98	602.78	CZ	2703
65R-1, 40	611.90	CY	2900
65R-1, 40	611.90	CZ	2686
65R-1, 105	612.55	CY	2977
65R-1, 105	612.55	CZ	2717
66R-1, 34	621.44	CY	3333
66R-1, 34	621.44	CZ	3003
66R-1, 120	622.30	CY	3132
66R-1, 120	622.30	CZ	3094
66R-2, 28	622.88	CY	3526
66R-2, 28	622.88	CZ	3350
66R-2, 122	623.82	CY	3232
66R-2, 122	623.82	CZ	3107
66R-3, 29	624.39	CY	3259
66R-3, 29	624.39	CZ	3136
66R-3, 33	624.43	CZ	3271
66R-3, 112	625.22	CY	3329
66R-3, 112	625.22	CZ	3180
66R-3, 133	625.43	CY	3530
66R-3, 133	625.43	CZ	3197
66R-4, 33	625.93	CY	3733
66R-4, 113	626.73	CY	2859
66R-4, 113	626.73	CZ	2680
67R-1, 11	630.81	CY	3186
67R-1, 11	630.81	CZ	2937
67R-1, 115	631.85	CY	2744
67R-1, 115	631.85	CZ	2650
67R-2, 30	632.41	CY	2708
67R-2, 30	632.41	CZ	2485
67R-2, 98	633.09	CY	2964
67R-2, 98	633.09	CZ	2794
68R-1, 42	640.82	CY	2529
68R-1, 42	640.82	CY	2697
68R-1, 118	641.58	CY	2482
68R-1, 118	641.58	CZ	2202
68R-2, 38	642.13	CY	2487
68R-2, 38	642.13	CZ	2340
68R-2, 125	643.00	CY	2353
68R-2, 125	643.00	CZ	2434
68R-3, 41	643.66	CY	2420
68R-3, 41	643.66	CZ	2365
68R-3, 105	644.30	CY	2134
68R-3, 105	644.30	CZ	2074
68R-4, 33	644.99	CY	3228
68R-4, 33	644.99	CZ	2903
68R-4, 80	645.46	CY	2328
68R-4, 80	645.46	CZ	2095
68R-5, 37	645.93	CY	2393
68R-5, 37	645.93	CZ	2279
69R-1, 43	650.43	CY	2253
69R-1, 43	650.43	CZ	2097
69R-1, 117	651.17	CY	2388
69R-1, 117	651.17	CZ	2227
69R-2, 31	651.73	CY	2238
69R-2, 31	651.73	CZ	2159
69R-2, 102	652.44	CY	2306
69R-2, 102	652.44	CZ	2145
69R-3, 29	652.88	CY	2251
69R-3, 29	652.88	CZ	2060
69R-3, 125	653.84	CY	2352
69R-3, 125	653.84	CZ	2171
69R-4, 44	654.53	CY	2122
69R-4, 44	654.53	CZ	2102
69R-4, 132	655.41	CY	2252
69R-4, 132	655.41	CZ	2017
69R-5, 37	655.94	CY	1946
69R-5, 37	655.94	CZ	1891
69R-5, 136	656.93	CY	2387
69R-5, 136	656.93	CZ	2343
70R-1, 47	660.07	CZ	3261
70R-1, 114	660.74	CY	3455
70R-1, 114	660.74	CZ	3455
70R-1, 114	660.74	X	3640
70R-2, 24	661.34	CY	3505
70R-2, 24	661.34	CZ	3484
70R-2, 24	661.34	X	4253
71R-1, 14	669.34	CY	2441
71R-1, 14	669.34	CZ	2349
71R-1, 95	670.15	CY	2362
71R-1, 95	670.15	CZ	2331
71R-2, 58	671.08	CY	2128
71R-2, 58	671.08	CZ	2084

Table T18 (continued).

Core, section, interval (cm)	Depth (mbsf)	Direction	Velocity (m/s)
71R-2, 98	671.48	CY	2200
71R-2, 98	671.48	CZ	2138
73R-1, 25	688.75	CY	2646
73R-1, 25	688.75	CZ	2762
73R-1, 78	689.28	CY	2917
73R-1, 78	689.28	CZ	2745
73R-2, 8	689.39	CY	2079
73R-2, 8	689.39	CZ	2017
73R-2, 51	689.82	CY	2064
73R-2, 51	689.82	CZ	2011
73R-3, 14	690.40	CY	2051
73R-3, 14	690.40	CZ	1985
74R-1, 15	698.25	Z	4159
74R-1, 22	698.32	X	4446
74R-1, 22	698.32	Z	4375
74R-1, 25	698.35	CY	4402
74R-1, 25	698.35	CZ	4464
74R-1, 37	698.47	X	4148
74R-1, 41	698.51	X	4382
74R-1, 47	698.57	X	4375
75R-1, 3	707.83	X	4436
76R-1, 28	717.68	X	1891
76R-1, 33	717.73	X	1915
76R-1, 68	718.08	X	1884
76R-1, 98	718.38	CY	2279
76R-1, 98	718.38	CZ	2170
76R-1, 119	718.59	X	2180
76R-1, 132	718.72	CY	2268
76R-1, 132	718.72	CZ	2225
76R-1, 141	718.81	X	2213
76R-2, 28	719.18	X	1916
76R-2, 40	719.30	X	2151
76R-2, 51	719.41	X	2125
76R-2, 61	719.51	X	2439
76R-2, 68	719.58	X	2025
76R-2, 68	719.58	X	2262
76R-2, 92	719.82	CY	2232
76R-2, 92	719.82	CZ	2197
76R-2, 98	719.88	X	2130
76R-2, 125	720.15	X	1898
76R-2, 147	720.37	X	1971
76R-3, 13	720.53	X	2043
76R-3, 19	720.59	X	1977
76R-3, 34	720.74	X	2011
77R-1, 6	722.26	X	3391
77R-1, 22	722.42	X	2196
77R-1, 37	722.57	CY	2216
77R-1, 37	722.57	CZ	2123
77R-1, 42	722.62	X	2254
77R-1, 84	723.04	X	2201
77R-1, 115	723.35	X	2133
77R-1, 127	723.47	CY	2499
77R-1, 127	723.47	CZ	2387
77R-2, 14	723.84	X	2158
77R-2, 43	724.13	CY	2150
77R-2, 43	724.13	CZ	2100
77R-2, 43	724.13	CZ	2151
77R-2, 85	724.55	X	2274
77R-2, 113	724.83	CY	2516
77R-2, 146	725.16	X	2639
77R-3, 30	725.50	CY	2808
77R-3, 30	725.50	CZ	2798
77R-3, 50	725.70	X	2489
77R-3, 66	725.86	X	2502
77R-3, 73	725.93	CY	2814
77R-3, 73	725.93	CZ	2856
78R-1, 22	727.22	X	2242
78R-1, 67	727.67	X	2295
78R-1, 132	728.32	X	2463
78R-2, 14	728.64	X	2205
78R-2, 14	728.64	Z	2384
78R-2, 38	728.88	CY	2555
78R-2, 62	729.12	X	2316
78R-2, 101	729.51	X	2242
78R-2, 136	729.86	CY	2297
78R-2, 136	729.86	CZ	2156
78R-3, 20	730.20	CY	2331
78R-3, 20	730.20	CZ	2325
78R-3, 130	731.30	CY	2305
78R-3, 130	731.30	CZ	2314
79R-1, 53	737.13	CY	2402
79R-1, 53	737.13	CZ	2321
79R-1, 76	737.36	CY	2471
79R-1, 76	737.36	CZ	2342
79R-2, 91	738.87	CY	2318
79R-2, 91	738.87	CZ	3714
79R-2, 91	738.87	CZ	2289
79R-2, 121	739.17	CY	2256
79R-2, 121	739.17	CZ	2190
79R-3, 42	739.79	CY	2338
79R-3, 42	739.79	CZ	2294
80R-1, 49	746.79	X	5258
80R-1, 50	746.80	MX	5425
80R-1, 60	746.90	X	5032
80R-1, 74	747.04	X	4752
80R-1, 92	747.22	X	4662
80R-1, 100	747.30	MX	4167
80R-1, 100	747.30	X	4298
80R-2, 38	748.15	MX	4518
80R-2, 41	748.18	X	4367
80R-2, 47	748.24	X	4292
80R-2, 52	748.29	MX	4219
80R-2, 82	748.59	X	4390
80R-2, 94	748.71	MX	4664
80R-2, 115	748.92	MX	4728
80R-2, 115	748.92	X	4582
80R-2, 139	749.16	X	4411
80R-3, 15	749.35	X	4757
80R-3, 20	749.40	CX	4796
80R-3, 20	749.40	CY	4629
80R-3, 26	749.46	MX	4777
80R-3, 27	749.47	X	4595
80R-3, 42	749.62	MX	3900
80R-3, 79	749.99	X	3244
80R-3, 94	750.14	X	4147
80R-3, 104	750.24	X	4366
80R-4, 5	750.75	MX	3717
80R-4, 25	750.95	MX	4156
80R-4, 50	751.20	MX	4506
80R-4, 67	751.37	MX	4540
80R-4, 95	751.65	MX	4492
80R-4, 115	751.85	MX	4611
81R-1, 25	756.15	MX	4464
81R-1, 45	756.35	MX	4445
81R-1, 94	756.84	MX	4294
81R-2, 68	757.99	MX	4751
81R-2, 95	758.26	MX	4801
81R-2, 116	758.47	MX	4092
81R-3, 112	760.02	MX	4140
82R-1, 10	765.70	X	4007
82R-1, 22	765.82	MX	4491
82R-1, 22	765.82	X	4302
82R-1, 43	766.03	MX	4929
82R-1, 55	766.15	X	4201
82R-1, 71	766.31	MX	4898
82R-1, 80	766.40	X	3915
82R-1, 88	766.48	X	4661
82R-2, 10	767.20	MX	4914

Table T18 (continued).

Core, section, interval (cm)	Depth (mbsf)	Direction	Velocity (m/s)
82R-2, 11	767.21	X	4242
82R-2, 32	767.42	X	4675
82R-2, 54	767.64	MX	5056
82R-2, 59	767.69	X	4625
82R-2, 81	767.91	X	3803
82R-2, 90	768.00	X	3438
82R-2, 107	768.17	X	3272
82R-2, 107	768.17	X	3194
82R-2, 140	768.50	X	3532
82R-3, 9	768.66	X	3613
82R-3, 10	768.67	X	4634
82R-3, 51	769.08	X	4049
82R-3, 60	769.17	X	4010
82R-3, 82	769.39	X	4308
82R-3, 100	769.57	X	4410
82R-3, 106	769.63	MX	4714
82R-3, 129	769.86	MX	4834
82R-3, 136	769.93	X	4468
82R-4, 21	770.25	MX	4511
82R-4, 24	770.28	X	3614
82R-4, 54	770.58	X	4673
82R-4, 58	770.62	MX	4601
82R-4, 90	770.94	X	4342
82R-4, 134	771.38	MX	4791
82R-4, 144	771.48	X	4355
82R-5, 30	771.84	X	4780
82R-5, 43	771.97	X	4900
82R-5, 44	771.98	MX	5797
82R-5, 60	772.14	X	5087
82R-5, 89	772.43	X	5194
82R-5, 105	772.59	X	4710
82R-5, 135	772.89	X	4579
83R-1, 140	776.60	MX	3989
83R-2, 30	777.00	MX	3717
83R-2, 94	777.64	MX	4507
83R-3, 14	778.30	MX	4505
83R-3, 47	778.63	MX	5030
83R-3, 69	778.85	MX	5178
83R-4, 80	780.31	MX	4410
83R-5, 7	781.00	MX	3956
83R-5, 29	781.22	MX	3796
83R-5, 74	781.67	MX	3766
83R-5, 88	781.81	MX	4099
83R-5, 116	782.09	MX	4319
83R-6, 16	782.42	MX	3779
84R-1, 16	784.96	MX	3070
84R-1, 26	785.06	MX	4432
84R-1, 45	785.25	MX	4867
84R-1, 45	785.25	MX	4438
84R-1, 97	785.77	MX	3405
84R-1, 107	785.87	MX	4841
84R-1, 111	785.91	MX	3644
84R-2, 54	786.72	X	4274
84R-2, 67	786.85	X	3997
84R-2, 75	786.93	X	3831
84R-2, 101	787.19	X	4016
84R-2, 106	787.24	X	4152
84R-3, 51	788.01	X	4212
84R-3, 77	788.27	X	4892
84R-3, 86	788.36	X	4966
84R-3, 112	788.62	X	5336
84R-3, 126	788.76	X	4520
84R-3, 143	788.93	X	5267
84R-4, 8	789.05	X	5845
84R-4, 13	789.10	MX	6192
84R-4, 29	789.26	X	5934
84R-4, 51	789.48	X	5536
84R-4, 59	789.56	X	6120
84R-4, 68	789.65	MX	6291
84R-4, 81	789.78	X	5991
84R-5, 5	789.88	MX	5406
84R-5, 31	790.14	MX	6427
84R-5, 129	791.12	MX	6675
85R-1, 38	794.88	MX	5338
85R-1, 62	795.12	MX	5390
85R-1, 78	795.28	X	5188
85R-1, 102	795.52	X	4804
85R-2, 5	795.88	MX	4637
85R-2, 12	795.95	MX	4687
85R-2, 22	796.05	MX	4507
85R-2, 28	796.11	MX	4245
85R-2, 85	796.68	MX	4531
85R-2, 90	796.73	MX	4175
85R-2, 129	797.12	MX	6288
85R-2, 136	797.19	X	6283
85R-2, 136	797.19	X	6304
85R-2, 139	797.22	MX	6517
86R-1, 9	804.19	X	6143
86R-1, 56	804.66	MX	3984
86R-1, 57	804.67	CX	4156
86R-1, 65	804.75	CX	4081
86R-1, 65	804.75	MX	3787
86R-3, 16	807.26	CX	5647
86R-3, 16	807.26	MX	5631
86R-3, 25	807.35	X	5917
86R-3, 26	807.36	MX	5959
86R-3, 74	807.84	X	6182
86R-3, 141	808.51	X	5688
87R-2, 14	815.30	CX	7491
87R-2, 14	815.30	CX	7357
87R-2, 15	815.31	MX	6777
87R-2, 85	816.01	CX	5461
87R-2, 85	816.01	MX	5193
87R-2, 91	816.07	CX	5238
87R-2, 91	816.07	MX	5116
87R-2, 119	816.35	MX	4935
87R-2, 119	816.35	MX	4896
87R-2, 129	816.45	MX	5919
88R-1, 9	823.49	MX	4359
88R-1, 9	823.49	MX	4210
88R-1, 23	823.63	MX	4746
88R-1, 23	823.63	X	4488
88R-1, 98	824.38	X	4557
88R-1, 107	824.47	MX	3986
88R-1, 115	824.55	MX	4224
89R-1, 21	833.31	MX	4320
89R-1, 62	833.72	MX	4040
89R-1, 67	833.77	X	3720
89R-1, 91	834.01	MX	3545
89R-2, 72	835.30	MX	4297
89R-2, 78	835.36	MX	4716
89R-2, 112	835.70	MX	5363
89R-3, 3	835.89	MX	5521
89R-3, 41	836.27	MX	5870

Notes: Type of samples is denoted by prefix: L = split-core section with core liner, C = oriented cubes, M = oriented minicore, and no prefix = split-core sections without core liner. The directions of the velocity measurements are represented by Z (along the core), Y (across the core), and X (into the core). This table is also available in **ASCII format.**

Table T19. Thermal conductivity values for Site 1138.

Core, section, interval (cm)	Depth (mbsf)	Thermal conductivity (W/[m·K])
183-1138A-		
4R-4, 75	31.75	0.68
5R-4, 75	41.25	0.70
6R-3, 75	49.15	0.60
7R-4, 75	60.05	0.68
8R-4, 75	69.55	0.73
9R-3, 75	77.45	0.70
10R-3, 75	86.85	0.67
11R-3, 75	96.45	0.64
12R-3, 75	106.05	0.81
13R-4, 75	117.25	0.81
15R-2, 69	133.39	0.85
16R-2, 75	143.05	1.00
17R-4, 75	155.75	1.06
18R-4, 75	165.35	1.13
19R-3, 75	173.45	1.12
20R-5, 35	185.65	0.97
21R-2, 30	190.80	1.23
22R-2, 30	200.40	1.11
23R-2, 58	210.28	1.09
24R-2, 75	220.05	1.04
25R-2, 50	229.40	1.07
26R-2, 62	239.22	1.08
27R-2, 26	248.46	1.17
28R-3, 75	260.15	1.10
29R-2, 75	268.15	1.20
30R-1, 75	276.25	1.15
31R-1, 40	285.50	1.10
32R-1, 110	295.80	1.14
80R-1, 40-52	746.76	1.45
80R-2, 118-136	749.04	1.36
80R-3, 130-140	750.55	1.39
80R-4, 0-10	750.75	1.65
80R-4, 1-10	750.76	1.20
81R-1, 113-125	757.09	1.31
81R-3, 107-115	759.76	1.43
82R-1, 76-83	766.40	1.66
82R-3, 65-74	769.27	1.28
82R-4, 138-146	771.46	1.35
82R-5, 35-48	771.96	1.38
83R-1, 10-24	775.37	1.11
83R-1, 108-123	776.36	1.42
83R-3, 21-33	778.43	1.50
83R-4, 59-69	780.15	0.96
83R-5, 96-110	781.96	1.12
84R-1, 63-75	785.49	1.05
84R-2, 1-20	786.29	1.37
84R-3, 83-95	788.39	1.53
84R-4, 77-86	789.79	1.51
84R-5, 1-10	789.89	1.53
84R-6, 21-31	791.56	1.32
85R-1, 71-80	795.26	1.37
85R-2, 52-64	796.41	1.12
86R-1, 30-44	804.47	1.26
86R-2, 40-50	806.05	1.08
86R-3, 101-113	808.17	0.72
86R-4, 31-44	808.98	1.72
87R-2, 45-50	815.64	1.20
88R-1, 110-125	824.58	1.15
88R-2, 54-64	825.40	0.86
89R-1, 18-30	833.34	1.17
89R-2, 1-15	834.66	1.25
89R-3, 1-17	835.95	1.44

Note: This table is also available in ASCII format.

Table T20. Carbon, nitrogen, sulfur, and hydrogen analyses of sediments from Site 1138.

Core, section	Depth (mbsf)	$CaCO_3$ (wt%)	IC (wt%)	OC (wt%)	N (wt%)	S (wt%)	H (wt%)
183-1138A							
1R-3	3.68-3.69	17.55	2.11	0.24	0.07	0.21	0.52
3R-4	21.77-21.78	44.23	5.31				
4R-4	31.89-31.90	45.79	5.50	0.19	0.05	BD	0.38
5R-1	36.89-36.90	19.23	2.31				
6R-1	46.29-46.30	11.36	1.36				
7R-1	55.69-55.70	23.34	2.80	0.12	0.04	0.19	0.68
8R-1	65.19-65.20	14.44	1.73				
9R-1	74.59-74.60	38.59	4.63	0.11	0.02	0.13	0.42
10R-1	83.99-84.00	4.17	0.50	0.13	0.05	0.27	0.83
11R-1	93.59-93.60	19.78	2.37				
12R-1	103.19-103.20	12.51	1.50				
13R-1	112.89-112.90	56.68	6.80	BD	0.02	0.11	0.24
14R-1	122.49-122.50	62.28	7.48				
15R-1	132.09-132.10	24.32	2.92	BD	0.02	0.18	0.55
16R-1	141.69-141.70	76.12	9.14				
17R-1	151.39-151.40	84.18	10.11				
18R-1	160.99-161.00	86.53	10.39	0.02	BD	0.11	0.07
19R-1	170.59-170.60	90.55	10.87				
20R-1	180.19-180.20	68.82	8.26				
21R-1	189.89-189.90	93.88	11.27	BD	BD	0.06	BD
22R-1	199.47-199.48	94.52	11.35				
23R-1	209.09-209.10	89.92	10.80				
24R-1	218.69-218.70	94.27	11.32	BD	BD	0.09	0.03
26R-1	237.99-238.00	93.23	11.19				
27R-1	247.59-247.60	94.10	11.30				
28R-1	257.29-257.30	94.12	11.30	BD	BD	0.07	0.03
29R-1	266.79-266.80	92.26	11.08				
30R-1	276.39-276.40	91.37	10.97				
33R-1	305.10-305.11	80.39	9.65	BD	0.01	0.11	0.13
34R-1	314.99-315.00	73.82	8.86				
35R-1	324.59-324.60	71.65	8.60	BD	BD	0.10	0.18
36R-1	333.89-333.90	92.41	11.09				
37R-2	344.76-344.77	92.46	11.10				
38R-1	353.09-353.10	93.01	11.17	0.07	0.01	BD	0.06
39R-1	362.69-362.70	92.35	11.09				
40R-1	372.39-372.40	95.53	11.47				
42R-1	391.69-391.70	92.74	11.13	BD	0.01	BD	0.06
43R-1	401.29-401.30	93.24	11.19				
44R-1	410.89-410.90	95.60	11.48				
46R-1	430.19-430.20	95.20	11.43	BD	0.01	BD	0.04
47R-1	439.79-439.80	93.51	11.23				
48R-1	449.49-449.50	92.30	11.08				
49R-1	459.09-459.10	93.13	11.18	BD	BD	BD	0.05
50R-1	468.40-468.41	94.72	11.37				
51R-1	477.99-478.00	87.29	10.48				
53R-1	497.29-497.30	94.86	11.39	BD	0.01	BD	0.04
54R-1	506.49-506.50	92.50	11.10				
55R-1	516.20-516.21	92.99	11.16				
56R-1	525.70-525.71	94.30	11.32	0.02	0.01	BD	0.03
59R-1	554.49-554.50	92.86	11.15				
61R-2	575.21-575.22	95.13	11.42				
62R-1	583.39-583.40	92.35	11.09	0.17	BD	0.06	0.01
63R-1	593.08-593.09	95.98	11.52				
64R-1	602.69-602.70	93.15	11.18				
66R-1	621.99-622.00	95.96	11.52	0.04	BD	BD	0.02
67R-1	631.59-631.60	77.28	9.28				
68R-1	641.25-641.26	61.24	7.35				
69R-1	650.88-650.89	57.83	6.94	BD	BD	BD	0.13
69R-5	656.46-656.47	1.18	0.14	2.24	0.09	5.01	1.02
69R-6	657.95-657.96	6.53	0.78				
70R-1	660.53-660.56	55.47	6.66	0.07	BD	BD	0.16
71R-2	670.65-670.66	11.88	1.43				
72R-2	680.96-681.00	12.00	1.44	5.55	0.08	1.00	1.50
73R-2	689.96-689.97	13.92	1.67				
73R-3	691.61-691.62	0.62	0.07				
76R-1	717.53-717.54	0.55	0.07	BD	BD	BD	1.37

Note: BD = below detection limit. This table is also available in **ASCII format.**

Table T21. Carbon, nitrogen, sulfur, and hydrogen analyses of volcanic and volcaniclastic rocks from Site 1138.

Core, section, piece	Depth (mbsf)	TC (wt%)	N (wt%)	S (wt%)	H (wt%)
183-1138A-					
74R-1	698.23-698.26	0.03	0.01	BD	0.24
74R-1	698.34-698.40	0.01	BD	BD	0.15
78R-3	730.50-730.54	0.02	BD	BD	0.26
80R-1 (Piece 8)	746.83-746.86	0.01	BD	BD	0.15
80R-3 (Piece 2)	749.39-749.43	0.03	BD	BD	0.15
80R-5 (Piece 3)	752.21-752.24	0.02	BD	BD	0.12
81R-2 (Piece 1B)	757.54-757.56	0.02	BD	BD	0.23
81R-5 (Piece 1A)	761.38-761.41	0.02	BD	BD	0.19
82R-1 (Piece 12)	766.87-766.91	0.02	BD	BD	0.14
82R-5 (Piece 6B)	772.23-772.26	0.02	BD	BD	0.17
83R-6 (Piece 2)	782.48-782.51	0.04	BD	BD	0.21
83R-4 (Piece 2)	779.84-779.88	0.02	BD	BD	0.15
84R-1 (Piece 2)	784.83-784.87	0.03	BD	BD	0.16
84R-5 (Piece 6)	790.81-790.83	0.00	BD	BD	0.11
85R-1 (Piece 12)	795.56-795.61	0.01	BD	BD	0.13
85R-2 (Piece 13)	797.03-797.07	0.05	BD	BD	0.55
86R-1 (Piece 2B)	804.52-804.58	0.01	BD	BD	0.17
86R-2 (Piece 14)	806.73-806.79	0.01	BD	BD	0.21
86R-3 (Piece 15)	808.58-808.60	0.02	BD	BD	0.42
87R-2 (Piece 15)	816.26-816.30	0.04	BD	BD	0.23
88R-1 (Piece 6C)	824.22-824.28	0.01	BD	BD	0.08
88R-2 (Piece 9)	826.07-826.11	0.01	BD	BD	0.07
89R-2 (Piece 9)	835.78-835.85	0.02	BD	BD	0.11

Notes: BD = below detection limit. This table is also available in **ASCII format.**